ON HYDROCRACKING OF VACUUM RESIDUES IN SLURRY REACTORS

by

Mariela Sanoja

B.S. in Chemistry, Universidad Central de Venezuela (UCV), Caracas, Venezuela, 2002

Submitted to the Graduate Faculty of

Swanson School of Engineering in partial fulfillment

of the requirements for the degree of

Doctor of Philosophy in Chemical Engineering

University of Pittsburgh

2012

UNIVERSITY OF PITTSBURGH

SWANSON SCHOOL OF ENGINEERING

This dissertation was presented

by

Mariela Sanoja

It was defended on

May 18th, 2012

and approved by

Shiao-Hung Chiang, Ph.D., Professor Emeritus, Department of Chemical and Petroleum Engineering

Badie I. Morsi, Professor, Ph.D., Department of Chemical and Petroleum Engineering

George E. Klinzing, Ph.D., Professor, Department of Chemical and Petroleum Engineering

Rachid Oukaci, Ph.D., Associate Professor, Department of Chemical and Petroleum Engineering

Brian Gleeson, Ph.D., Professor, Department of Mechanical Engineering and Material Science

Dissertation Director: Badie I. Morsi, Ph.D., Professor, Department of Chemical and Petroleum Engineering

ON HYDROCRACKING OF VACUUM RESIDUES IN SLURRY REACTORS

Mariela Sanoja, PhD

University of Pittsburgh, 2012

The equilibrium solubility (C^*) and liquid-side mass transfer coefficient (k_La) were measured for H_2 in four liquids, two vacuum residues (A and B); and two mixtures (vacuum residue B + liquid paraffins and vacuum residue B + liquid paraffins + molten wax). The data were measured in the presence and absence of solid particles (activated carbon) in one-liter agitated autoclave operating in a gas-inducing mode. The effect of operating variables, including pressure (27.5–55bar), temperature (423–623K), mixing speed (20–33Hz), and activated carbon concentration (0-40wt.%) on k_La and C^* values were statistically investigated using the Central Composite Statistical Design technique. The k_La values were obtained using the Transient Physical Gas Absorption technique and the C^* values were calculated at the thermodynamic equilibrium.

The experimental data showed that C^* values of hydrogen in the four liquids increase linearly with pressure at constant temperature following Henry's law. The C^* values also increased with temperature at constant pressure and the temperature effect was modeled using an Arrhenius-type equation.

The k_La values of H_2 in the four liquids strongly increased with temperature and mixing speed, and slightly increased with H_2 partial pressure. The k_La values, however, decreased with increasing solid concentrations in the vacuum residues A and B. Statistical correlations and

empirical correlations, using dimensionless numbers, were developed to predict k_La values of H_2 in the liquids used in the presence and absence of solid particles in the gas-inducing slurry agitated reactor.

The kinetic rate constants proposed by Sanchez at al.[1] for hydrocracking of vacuum residue at 380, 400 and 420^oC were used in a simple kinetic model using a series of CSTRs to calculate the residue conversion and the VGO, distillate, naphtha and gaseous products concentrations and molar flow rates. For a series arrangements of 4-CSTRs(3-m inside diameter and 3-m height), operating at 400 ^oC with an LHSV of 0.33h^{-1} corresponding to an inlet liquid superficial velocity of 0.99 m s^{-1}, the residue conversion reached 91.8%. However, for the same arrangement at 400^oC with an LHSV of 1.5h^{-1} corresponding to an inlet liquid superficial velocity of 4.5m s^{-1}, the residue conversion was only 50.36%.

DESCRIPTORS

Absorption

Agitated Reactor

Gas Inducing Reactor

Hydrocracking

Hydrodynamics

Hydrogen

Multiphase reactors

Slurry

Solubility

Statistical Experimental Design

Vacuum Residue

Volumetric Liquid-Side Mass Transfer Coefficient

TABLE OF CONTENTS

LIST OF TABLES

LIST OF FIGURES

NOMENCLATURE

a	Gas-liquid interfacial area per unit volume, m^{-1}
a_s	Specific interfacial area of particle, m^{-1}
C	Concentration, mol m^{-3} or specific heat, BTU lb^{-1} $°F^{-1}$
C^*	Solubility of gas at equilibrium, mol m^{-3} or mol kg^{-1}
C_G	Gas concentration, mol m^{-3}
C_L	Concentration of gas in the liquid bulk, mol m^{-3}
Cs	Solid concentration, wt. %
C_p	Heat capacity, J kg^{-1} K^{-1}
C_V	Volumetric solid concentration, %
D	Diameter of reactor, m or diffusivity in Equations (1-4), m s^{-1}
D_{AB}	Diffusion coefficient, m s^{-1}
D_{eff}	Effective diffusion, m s^{-1}
d_{imp}	Impeller diameter, m
D_K	Knudsen diffusivity, m s^{-1}
d_p	Particle diameter, m
d_s	Sauter mean particle diameter, m
d_T	Diameter of reactor, m
d_W	Width of the impeller blade, m
E	Activation energy, J mol^{-1}
F	Mass flow rate, mol h^{-1}
g	Gravitational constant, 9.81 m^2 s^{-1}
H	Liquid height above the bottom of the reactor, m
H_L	Liquid height above impeller, m

He_0	Pre-exponential constant in Equation (4-2), Pa m^3 mol^{-1}
He	Henry's law constant, Pa m^3 mol^{-1}
J	Molar flux, mol s^{-1} m^{-2}
k	Phase mass-transfer coefficient, m s^{-1} or rate constant
k_0	Pre-exponential factor or pseudo-kinetic constant for a first order expression
k_i	First order rate constant, h^{-1}
k_{ij}^c, k_{ij}^t	Kinetic constant in catalytic and thermal processes
K_W	Watson characterization factor
k_La	Volumetric liquid-side mass transfer coefficient, s^{-1}
L	Reactor length, m
m	Mass, kg
MW	Molecular weight, kg $kmol^{-1}$
n	Number of mol, mol
N	Mixing speed, Hz or rpm
N_{CRI}	Critical mixing speed for gas induction, Hz or rpm
$n_{i,F}$	Number of mols of species i at equilibrium, mol
$n_{i,I}$	Number of mols of species i at initial time, mol
P	Pressure, bar
P_C	Critical pressure, bar
P^*	Total power input, W
P^S	Saturated vapor pressure, bar
Q	Heat of combustion, cal. g^{-1}
Q_{GI}	Gas volumetric flowrate, m^3 s^{-1}
R	Ideal gas constant, 8.314 J mol^{-1} K^{-1}
R^2	Regresion coefficient = $\frac{\sum\left(\Omega_{Exp.}-\overline{\Omega}_{Exp.}\right)\left(\Omega_{\Pr ed.}-\overline{\Omega}_{\Pr ed.}\right)}{\sqrt{\sum\left(\Omega_{Exp.}-\overline{\Omega}_{Exp.}\right)^2\sum\left(\Omega_{\Pr ed.}-\overline{\Omega}_{\Pr ed.}\right)^2}}$ x100, %
r	Reaction rate, mol kg^{-1} s^{-1} or mol m^{-3} s^{-1}
r_R	Reaction rate of residue, wt% h^{-1}
r_N	Reaction rate of naphta, wt% h^{-1}
r_D	Reaction rate of distillates, wt% h^{-1}

r_{VGO}	Reaction rate of VGO, wt% h^{-1}
r_G	Reaction rate of gases, wt% h^{-1}
r_{ij}^c, r_{ij}^t	Kinetic reaction rate in catalytic and thermal processes, mol kg^{-1} s^{-1} or mol m^{-3} s^{-1}
r_p	Catalyst pore radius, m
s	Surface renewal frecuency
t	Time, s
T	Temperature, K
T_b	Boiling-point temperature, K
T_r	Reduced temperature
T_C	Critical temperature, K
U_G	Superficial gas velocity, m s^{-1}
U_L	Liquid velocity, m s^{-1}
V	Volume, m^3
V_C	Critical molar volume, m^3 $kmol^{-1}$
W	Baffle width, m
x_i	Mass fraction
y_i	Mole fraction
z	Axial position in the reactor, m
Z	Compressibility factor
Z_c	Critical compressibility factor

Greek Letters

δ	Film thickness, m
ΔH^0	Heat of solution, J mol^{-1}
ε	Phase holdup
ε_{cat}	Catalyst void fraction
η	Effectiveness factor
θ	Residence time
λ	Association factor of solvent

μ	Dynamic viscosity, kg m^{-1} s^{-1}
ν	Kinematic viscosity, m^2 s^{-1}
ρ	Density, kg m^{-3}
σ	Surface tension, N m^{-1}
τ_{cat}	Tortuosity factor of particle
υ	Molar volume at normal boiling temperature, m^3 $kmol^{-1}$
ϕ	Thiele module
ω	Acentric factor

Superscripts

c	Catalytic
t	Thermal

Subscripts

b	Boiling point
c	Critical point
cat	Catalyst
D	Distillate
F	Final
G	Gas phase
i	Component i
I	Initial
j	Component j
L	Liquid phase
m	Mean
N	Naphta
pre	Pre-heater
R	Reactor or residue
S	Solid phase
SL	Slurry phase

VGO	Vacuum Gas Oil

Acronyms

AARE	Absolute average relative error = $\frac{1}{n}\sum_{1}^{n}\left\|\frac{\mathrm{Pr}ed.-Exp.}{Exp.}\right\|$ x100,%
amu	Atomic Mass Unit
API	American Petroleum Institute
AR	Atmospheric Residue
ARDS	Atmospheric Residue Desulfurization
CASH	Chevron's trade mark for a particular hydrocracking process
CCSD	Central Composite Statistical Design
CSTR	Continuous Stirred Tank Reactor
EBR	Ebulating-Bed Reactor
FBR	Fixed-Bed Reactor
F-T	Fischer-Tropsch
GIR	Gas-Inducing Reactor
GP	Gas product
GSR	Gas-Sparging Reactor
H/C	Hydrogen/Carbon
HC	Hydrocarbons
HDC	Hydrocracking
HDM	Hydrodemetallization
HDN	Hydrodenitrogenation
HDO	Hydrodeoxigenation
HDS	Hydrodesulfurization
HPLC	High-performance liquid chromatography
IFP	Institut Français du Pétrole
LHSV	Liquid Hourly Space Velocity
LPG	Liquefied Petroleum Gas
MBR	Moving Bed Reactor
NPT	Normal pressure and temperure, 1.01bar and 293.15K

PC	Personal Computer
PR-EOS	Peng-Robinson Equation of State
RDS	Residue Desulfurization
rpm	revolution per minute
SAR	Saturates, Aromatics, Resins/ Surface Aeration Reactor
SBCR	Slurry bubble column reactor
SFB	Swing Fixed Bed
SG	Specific Gravity
SPR	Slurry Phase Reactor
TPGA	Transient Physical Gas Absorption
UOP	Universal Oil Products
VGO	Vacuum Gas Oil
VRDS	Vacuum Residue Desulfurization

Dimensionless Numbers

Euler Number $$Eu = \frac{P_m}{d_{imp}^2 \times \rho_L \times N^2}$$

Reynolds Number $$\mathrm{Re} = \frac{d_{imp}^2 \times \rho_L \times N}{\mu_L}$$

Schmidt Number $$S_C = \frac{\mu_L}{\rho_L \times D_{AB}}$$

Sherwood Number $$Sh = \frac{d_{imp}^2 \times k_L a}{D_{AB}}$$

Weber Number $$We = \frac{d_{imp}^3 \times \rho_L \times N^2}{\sigma_L}$$

ACKNOWLEDGMENTS

My sincere gratitude and appreciation go to my advisor Professor Badie I. Morsi for his expert guidance and support throughout this study. I would also like to extend my thanks to Professor Shiao-Hung Chiang, Professor George E. Klinzing, Professor Rachid Oukaci, and Professor Brian Gleeson for serving on my committee.

In addition, I would like to acknowledge the financial support of Pequiven (Petrochemical of Venezuela), Venezuela. I am especially grateful to my research group mates, for their constructive comments and help during this study.

My deepest appreciation goes to my mother, family and friends for their continuous moral support, encouragement, and sacrifices.

I dedicate this thesis to my mother, Nelida Serrano “Nina”, and to one person who is not with us anymore, my grandmother Maria Perdomo, whose memory will be with me always.

1.0 INTRODUCTION AND BACKGROUND

Crude oil is a complex mixture of hydrocarbons and non-hydrocarbons. The major hydrocarbon groups in the crude oil are straight-chain paraffins and their isomers, naphthenes and aromatics; and the non-hydrocarbons are mainly sulfur-, nitrogen-, and oxygen-containing compounds. It could also contain metals, such as nickel, iron, and vanadium. The hydrocarbon components can range from those with low molecular weights and boiling points, such as methane, to those with high molecular weights and boiling points, such as asphaltenes. In fact, it is impossible to identify all the components present in the crude oil [2].

Liquid hydrocarbons "conventional oil," which flow easily through reservoirs is usually produced using conventional oil production methods; whereas heavy oil, extra heavy oil or bitumen "unconventional oil," would not flow through reservoirs and would require the use of unconventional production methods. Thermal recovery, steam stimulation, or even mining are among such unconventional production methods of those heavy hydrocarbons.

It has been forecasted that fossil fuels will continue to be the main source of energy for at least 50 years[2]. Figure 1.1 shows the current oil reserve by country which totals about 1.5 trillion barrels. The countries with the largest reserve are Saudi Arabia, Venezuela, Canada, Iran, and Iraq.

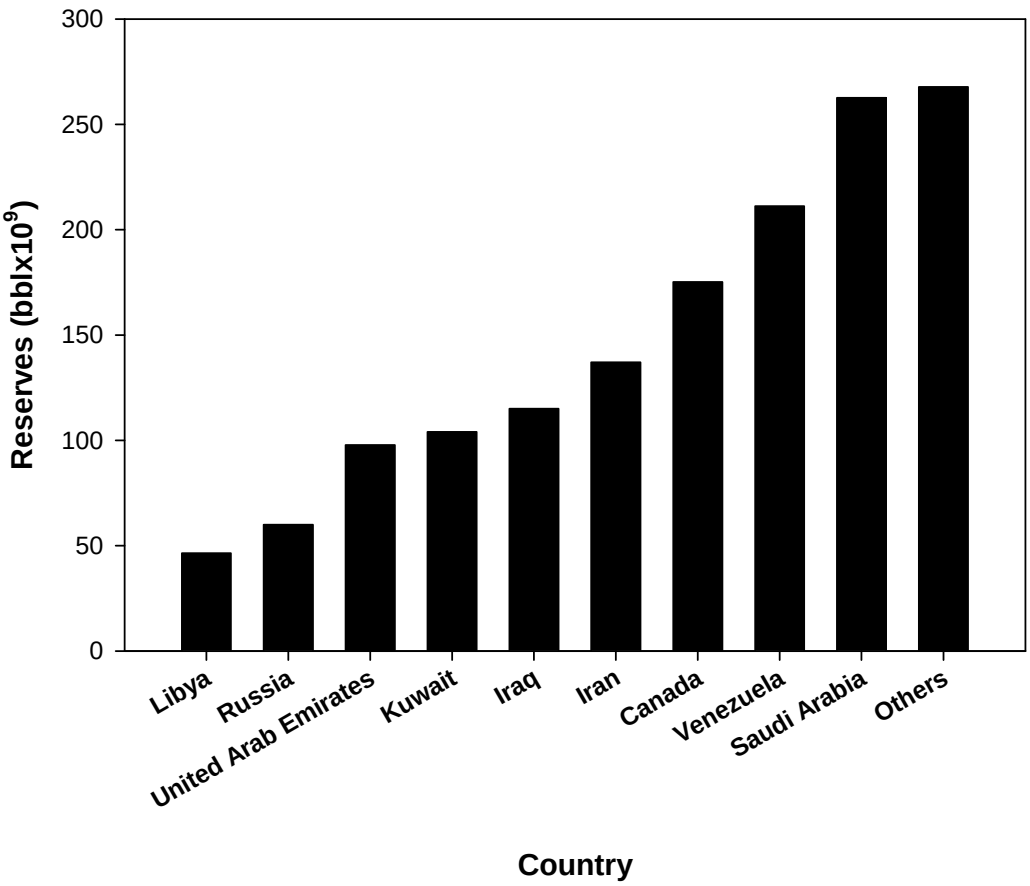

Figure 1.1. Conventional oil reserves by country[3]

The world's demand for oil has been steadily increasing over the last decades [4]. As a consequence, there has been a continuous decrease in the world's conventional oil reserve, making the energy supply for the future decades a major concern around the world. In recent years, however, new reserve of unconventional oil, representing 70% of the total reserve[5], has been discovered as shown in Figure 1.2. This unconventional oil reserve is estimated to be at least about 4 trillion barrels; with the largest reserves in Venezuela and then Canada[2]. If only 10% to 15% of the total unconventional heavy oil reserve were recovered, it would represent approximately 600 billion barrels; and given the current world consumption of about 30 billion

barrels/year, this means that unconventional oil could meet the world's oil needs for about 20 years.

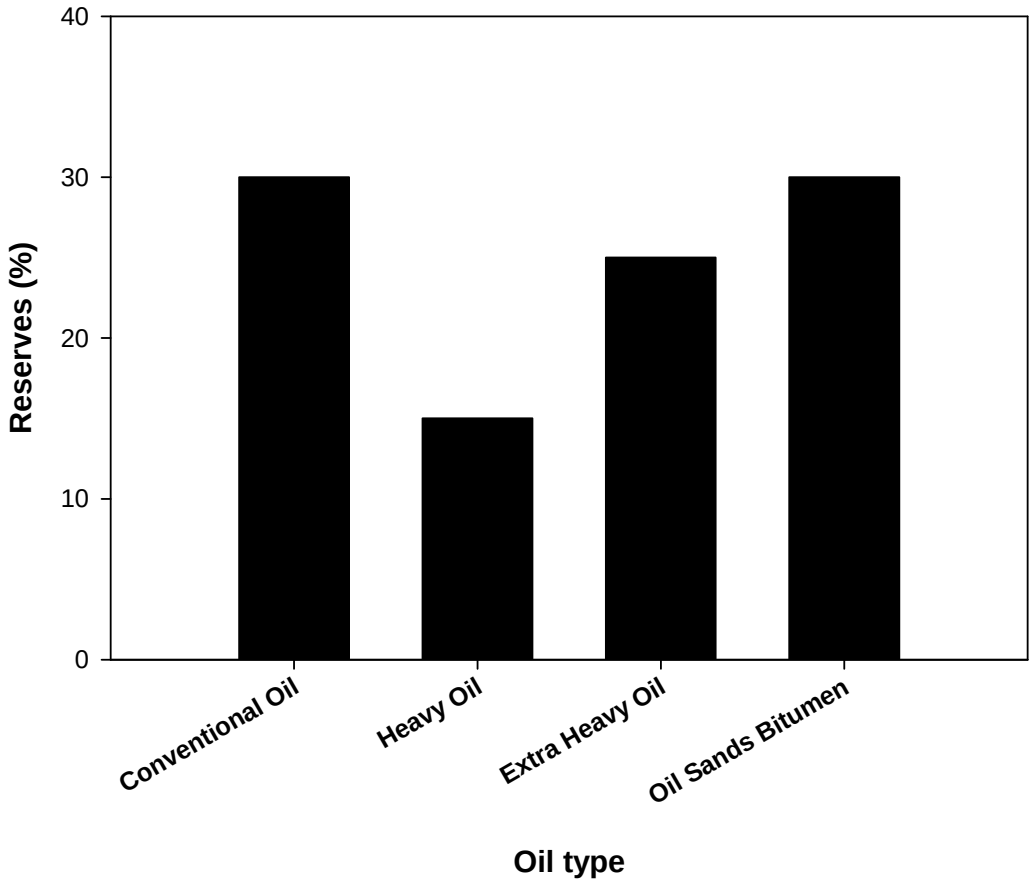

Figure 1.2. Major global reserves of conventional vs. unconventional oil[5]

The conventional oil often contains about 10-30% heavy residue and when it is refined in atmospheric and vacuum distillation towers, it produces useful products, such as liquefied petroleum gases, gasoline, kerosene, jet fuel, gas oil, diesel, residual fuel, lubricants, and asphalt, as illustrated in Figure 1.3. Since many useful products derived from crude oil are used as transportation fuels (see Figure 1.4), it is important to recover as many of these products as possible. The unconventional oil, which often contains 40-85% residue, is more difficult to refine than the conventional oil as it requires more severe conditions due to its high percentage of

asphaltenes and non-hydrocarbon impurities. Table 1.1 and 1.2 compare some properties of various oils.

Table 1.1. Range of properties of various types of oil[6]

	Extra-Light Crude Oil	Light Crude Oil	Heavy Crude Oil	Extra-Heavy Crude Oil
API gravity	>50	22-32	10-22	<10
Hydrocarbons (wt. %):				
- Asphaltenes	0-<2	<0.1-12	11-25	15-40
- Resins	0.05-3	3-22	14-39	
- Oils	-	67-97	24-64	
Impurities (wt. %):				
- Total sulfur	0.02-2	0.05-4.0	0.1-5.0	0.8-6.0
- Total nitrogen	0.0-0.01	0.02-0.5	0.2-0.8	0.1-1.3
- Ni+V(wppm)	<10	10-200	50-500	200-600

Table 1.2. Properties of various crude oils[6]

Crude Oil	Lagrave	Isthmus	Maya	Lloydminster	Athabasca
Country	France	Mexico	Mexico	Canada	Canada
API gravity	43	33.34	21.31	15.0	8.0
Sulfur (wt. %)	-	1.46	3.57	-	1.25
Nitrogen (wt. %)	-	0.1467	0.32	4.30	7.95
Insoluble in nC_7 (wt. %)	4	1.65	11.32	12.9	15.0

Typically, the residue from atmospheric distillation is sent to vacuum distillation towers in order to recover any remaining light cuts in the form of heavy distillates. The properties of some atmospheric residues are shown in Table 1.3. The residue from the vacuum distillation towers, known as vacuum residue, is further sent for processing, as discussed in the following sections. Figure **1.5** shows a schematic of a process for processing vacuum residue in order to produce coke and other useful products.

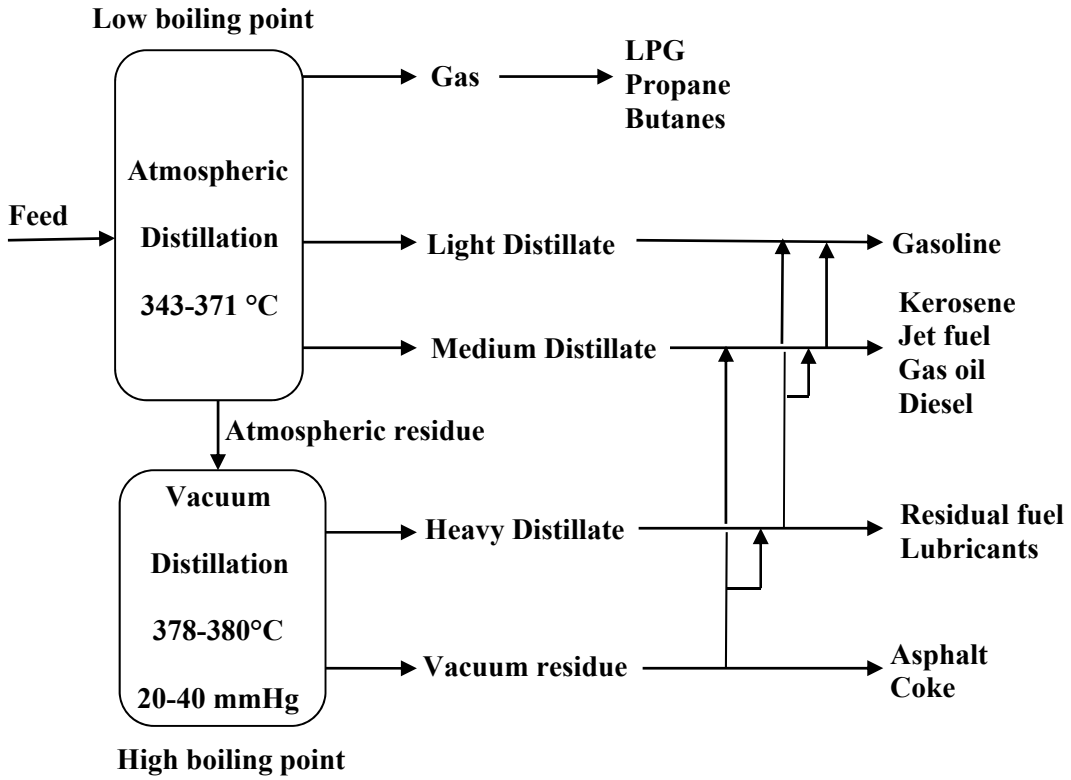

Figure 1.3. Refined products

Table 1.3. Properties of various atmospheric residues (AR), 343 °C+

Crude Oil	Origin	API gravity	Sulfur (wt. %)	Ni+V (wppm)	Carbon residue (wt. %)	Yield of AR (vol. %)
Ekofisk	North Sea	20.9	0.4	6	4.3	25.2
Arabian Light	Arabia	17.2	3.1	50	7.2	44.6
West Texas Sour	United States	15.5	3.4	29	9.0	41.6
Isthmus	Mexico	15.5	2.9	82	8.1	40.4
Export	Kuwait	15.0	4.1	75	-	45.9
North Slope	Alaska	14.9	1.8	71	9.2	51.5
Arabian Heavy	Arabia	13.0	4.3	125	12.8	53.8
Bachaquero	Venezuela	9.4	3.0	509	14.1	70.2
Maya	Mexico	7.9	4.7	620	15.3	56.4
Hondo	United States	7.5	5.8	489	12.0	67.2
Cold Lake	Canada	6.8	5.0	333	15.1	83.7
Athabasca	Canada	5.8	5.4	374	-	85.3
Ku-Maloob-Zaap	Mexico	3.7	5.8	640	20.4	73.7

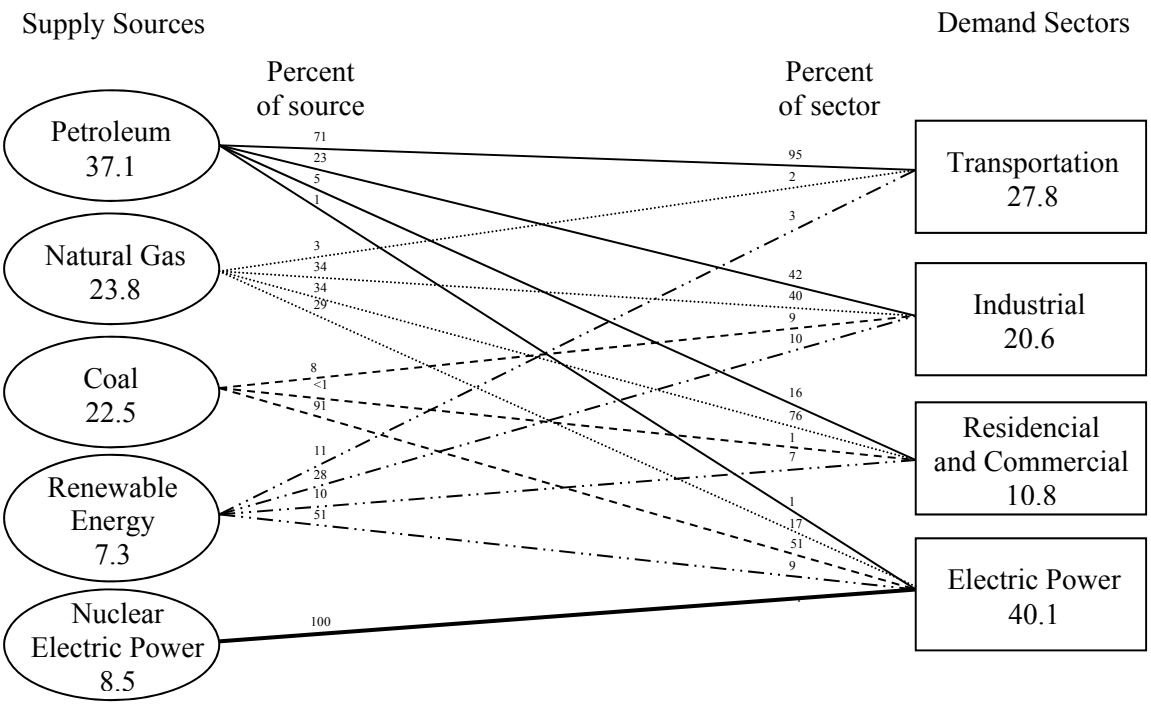

Figure 1.4. Primary energy consumption worldwide by source and sector, 2008[7]

Vacuum residue (low-value product) has an API gravity on the order of 5 to 10°, high viscosity, boiling point over 525+ ºC, high coke-forming potential, and it also contains high concentrations of heteroatoms. The main technologies used for processing vacuum residue involve carbon rejection (the most common method used commercially) or hydrogen addition. The main goal of both technologies is to remove impurities and produce more distillates.

1.1 CARBON REJECTION TECHNOLOGY

Carbon rejection technology, which is carried out at moderate pressures and temperatures between 480 and 550 °C [6], produces a small amount of distillates, and a high yield of gases such as methane, ethane, propene, and butane, as well as coke. The carbon-rejection technology includes two main processes: (1) removal of carbon in the form of coke; and (2) removal of

carbon in the form of asphalt (in the case of deasphalting). The first includes thermal cracking processes such as coking (i.e., delayed coking, fluid coking, and flexicoking), visbreaking, and catalytic cracking of residue [R].

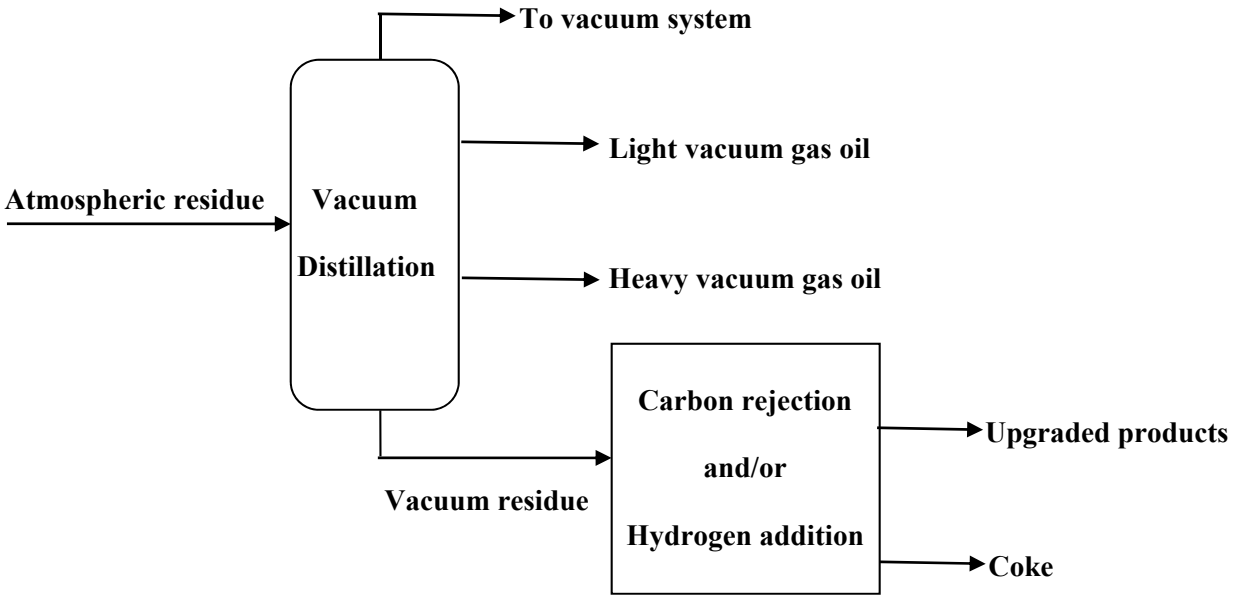

Figure 1.5. Processing of vacuum residue

The second includes solvent deasphalting[6], in which the vacuum residue is physically separated into various fractions using a solvent as an absorption medium in order to obtain high quality products. Although this technology enjoys high feedstock flexibility, it produces uneconomical large amounts of coke [2] and generates low quality distillates and large amount of by-products, such as fuel oil and pet-coke, which are currently of decreasing demand.

1.2 HYDROGEN ADDITION TECHNOLOGY: HYDROCRACKING OF VACUUM RESIDUE

Hydrocracking or hydrogenation of vacuum residue is used to convert high molecular weight feedstocks into more valuable low molecular weight products. Also, hydrogenation removes any heteroatoms, such as sulfur, oxygen or nitrogen which are present in the feedstock, thus producing cleaner products. Depending on the nature of the feedstock to be treated, different catalysts, reactors, and reactor configurations are used.

Hydrocracking of vacuum residue is carried out at elevated pressures (35 – 200 bar), temperatures (260 - 425 °C) and liquid hourly space velocities (LHSV) of 0.3 – 2.0 h^{-1} [8]. In this process, a large amount of hydrogen is required to hydrogenate the feed in order to prevent the formation of coke (H_2/oil: 505 – 1685(NPT) m^3/m^3), which is an undesirable product [9]. The major components of vacuum residue are asphaltenes, which can undergo different reactions to produce mainly coke. It was reported that heavy oils containing more than 5% asphaltenes and 150 wppm metals will produce coke and the metal will deposit on the catalyst surface, causing deactivation and serious plugging problems[2].

The chemical reactions which take place during the hydrocracking of vacuum residue involve hydrogen transfer[2]. The high temperatures used helps cracking the residue molecules and cause the formation of radicals in the presence of a catalyst. The high hydrogen partial pressure leads to the hydrogenation of the radicals, which both stabilize the products and prevent condensation, which lead to coke formation. Therefore, the higher the hydrogen partial pressure is, the better the hydrocracking performance will be. Besides hydrocracking of heavy feed, the heteroatoms are also hydrogenated, producing hydrogen sulfide (H_2S), ammonia (NH_3), and water (H_2O) as secondary products, which could be removed from the products. The elimination

of these heteroatoms is critical because sulfur-containing fuels do not meet environmental fuel specifications, nitrogen-containing compounds have a pronounced negative effect on the storage stability of products and can poison the catalyst, and oxygen-containing compounds are corrosive and can promote gum formation. Therefore, hydrocracking of vacuum residue not only allows better product selectivity, but can also produces cleaner fuels. The degree of residue conversion and, consequently, the cost of the process are strongly affected by the amount of low-value by-products produced and the amount of hydrogen required [10].

The hydrogen-addition technology, which includes hydrovisbreaking (non-catalytic), hydrotreating and hydrocracking, produces a high yield of upgraded products and requires the extensive use of catalysts due to metal, carbonaceous material deposition, and/or sintering which produce permanent catalyst deactivation. In addition, the removal of heteroatoms and metals is expensive. Thus, this technology requires a large capital investment and huge quantities of natural gas in order to produce the required hydrogen and steam. Despite its disadvantages, however, the hydrogen-addition technology is preferred for processing vacuum residue as it produces greater yields of high-value products than the carbon-rejection technology. In the following sections, only hydrocracking, a type of hydrogen-addition technology used to upgrade vacuum residue will be discussed.

1.2.1 Hydrocracking catalyst

The catalysts used for the hydrocracking of vacuum residue are specifically designed to fit the nature of the feedstock and the desired end-product. Usually a combination of several catalysts is used to carry out hydrocracking (HDC) or hydrodemetallization (HDM), hydrodesulfurization (HDS), hydrodenitrogenation (HDN) or hydrogenation to prevent coke formation. The catalysts

commercially used in the hydroprocessing of heavy feedstocks are sulfide of cobalt-molybdenum, nickel-molybdenum, or nickel-tungsten, supported by either coke, alumina, or mixed oxides (Al_2O_3-TiO_2, Al_2O_3-SiO_2, Al_2O_3-MgO, Al_2O_3-ZrO_2); or a finely dispersed catalyst, which forms an emulsion with the residue (catalytic emulsions)[2]. The use of such dispersed catalysts has been reported to be very effective in preventing coke formation and insuring good control of the sediments with only minimal fouling[2]. The criteria used to choose the metal function in the supported catalysts for hydrocracking of vacuum residue strongly depends on the feed composition, while the criteria used to choose the support strongly depends on the metal-phase to be used, and on the textural and extrusion properties, stability and cost [2].

1.2.2 Hydrocracking kinetics

There are only few studies on the reaction kinetics of hydrocracking of heavy feedstocks available in the literature. This can be attributed to the fact that during hydrocracking there are many different reactions that simultaneously occur making it difficult to obtain an accurate understanding of the overall reaction kinetics of the process. Also, during the hydrocracking of vacuum residue, catalytic and thermal cracking can occur due to the high process temperature. Jacob et al.[11] developed two lumped kinetic schemes for catalytic and thermal cracking, respectively as shown in Figure 1.6.

Catalytic cracking **Thermal cracking**

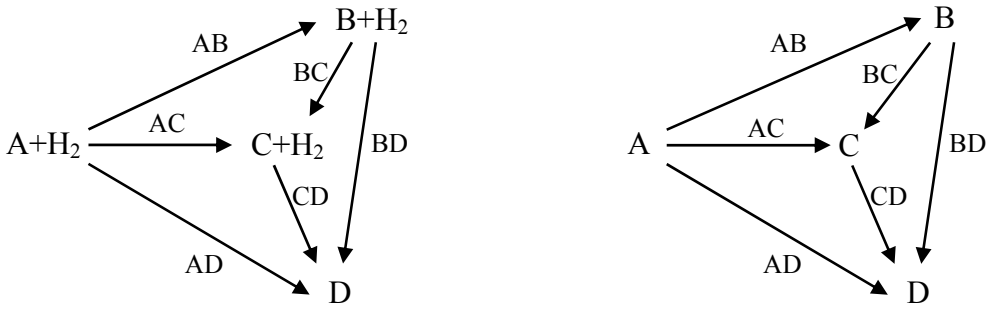

Figure 1.6. Kinetic reaction schemes[12]

Each pseudo-component can be cracked catalytically or thermally to produce lighter components. The kinetic expressions for both catalytic and thermal cracking, where the reactant *i* is converted in the product *j* can be express as follow [12]:

$$r_{ij}^{c} = k_{ij}^{c} C_i C_{H2}^{0.5} \tag{1-1}$$

$$r_{ij}^{t} = k_{ij}^{t} C_i \tag{1-2}$$

where i = A, B, C, D; j = A, B, C, D; i is heavier than j; and $k = k_0 e^{-E/RT}$ (Arrhenius law).

The formation rate of each component can be written as follows:

Catalytic cracking:

$$r_A^c = (-r_{AB}^c - r_{AC}^c - r_{AD}^c)$$

$$r_B^c = (r_{AB}^c - r_{BC}^c - r_{BD}^c)$$

$$r_C^c = (r_{AC}^c + r_{BC}^c - r_{CD}^c)$$

$$r_D^c = (r_{AD}^c + r_{BD}^c + r_{CD}^c)$$

$$r_{H2}^c = -(r_{AB}^c + r_{AC}^c + r_{AD}^c + r_{BC}^c + r_{BD}^c + r_{CD}^c)$$

Thermal cracking:

$$r_A^t = (-r_{AB}^t - r_{AC}^t - r_{AD}^t)$$

$$r_B^t = (r_{AB}^t - r_{BC}^t - r_{BD}^t)$$

$$r_C^t = (r_{AC}^t + r_{BC}^t - r_{CD}^t)$$

$$r_D^t = (r_{AD}^t + r_{BD}^t + r_{CD}^t)$$

The assumptions made for the equations written above were: (1) the reaction rate follows a power law kinetics; (2) the stoichiometric coefficient of hydrogen for the whole set of catalytic reactions is 3; (3) a heavier cut could be converted only to lighter cuts; (4) the reaction orders are the same for all reactions; and (5) the HDO, HDS, HDN, and HDM reactions are not included[12]. The reported optimized values of the dimensionless kinetic constant for the catalytic process at the operating conditions are: k^c_{AB} = 8x10^8, k^c_{AC} = k^c_{AD}= k^c_{CD} =2x10^8, k^c_{BC} = k^c_{BD}=3x10^8; and the activation energy was 200 kJ/mol[13].

Sanchez et al.[1] proposed a kinetic model for a moderate hydrocracking of heavy oils with a Ni/Mo catalyst at 380-420 °C, as shown in Figure 1.7. The model includes five lumps (unconverted residue, VGO, distillates, naphtha, and gases) reactions, and they estimated the kinetic parameters shown in Table 1.4 for the following kinetic expressions from their experimental results obtained in a fixed-bed downflow reactor:

$$r_R = -(k_1 + k_2 + k_3 + k_4)y_R$$

$$r_{VGO} = k_1 y_R - (k_5 + k_6 + k_7)y_{VGO}$$

$$r_D = k_2 y_R + k_5 y_{VGO} - (k_8 + k_9)y_D$$

$$r_N = k_3 y_R + k_6 y_{VGO} + k_8 y_D - k_{10} y_N$$

$$r_G = k_4 y_R + k_7 y_{VGO} + k_9 y_D + k_{10} y_N$$

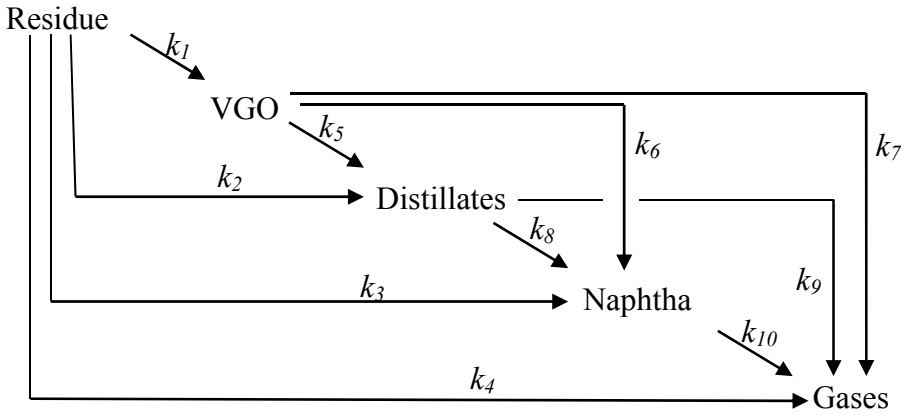

Figure 1.7. Proposed kinetic models by Sanchez[1]

Table 1.4. Kinetic parameters of Satchez's model[1]

Kinetic constant (h^{-1})	Temperature			Activation energy E_A (kcal/mol) 380 °C
	380 °C	400 °C	420°C	
Residue				
k_1	0.042	0.147	k_1	0.042
k_2	0.008	0.022	k_2	0.008
k_3	0.008	0.020	k_3	0.008
k_4	0.041	0.098	k_4	0.041
VGO				
k_5	0.018	0.057	k_5	0.018
k_6	0	0.007	k_6	0
k_7	0	0	k_7	0
Distillate				
k_8	0	0.003	k_8	0
k_9	0	0	k_9	0
Naphtha				
k_{10}	0	0	k_{10}	0

Sanchez et al.[1] found that at higher the temperature and lower the space velocity, the conversion and products yields increase; and as the operation conditions severity increases, the conversion was greater than 50%.

Also, Loria et al.[14] proposed a kinetic model for ultra-dispersed catalytic hydroprocessing of bitumen and they adapted the high severity hydrocracking of heavy oils proposed by Sanchez et al.[1] Their new kinetic model and kinetics constants are shown in Figure 1.8 and Table 1.5, respectively.

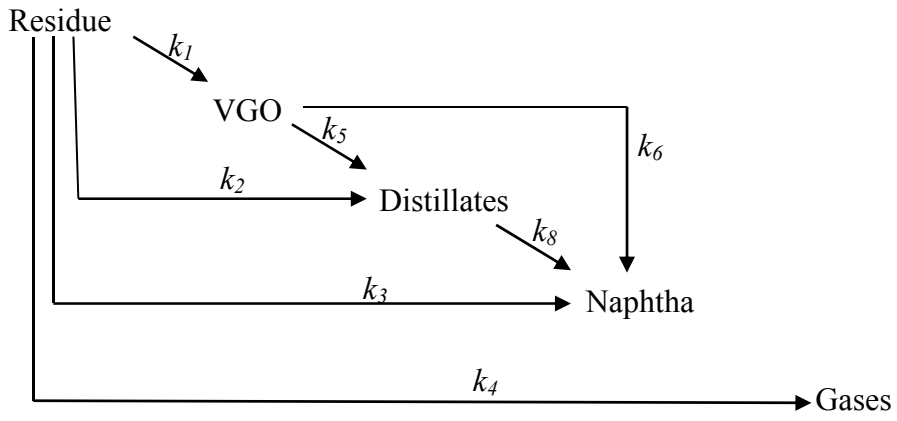

Figure 1.8. Proposed kinetic models by Loria et al.[14]

Table 1.5. Rate constants of Loria et al. model[14]

T, °C	k_1, h^{-1}	k_2, h^{-1}	k_3, h^{-1}	k_4, h^{-1}	k_5, h^{-1}	k_6, h^{-1}	k_8, h^{-1}
320	0.00214	0.00131	0.00030	0.00006	0.00670	0.00491	0.00105
350	0.00845	0.00610	0.00113	0.00073	0.00282	0.00141	0.00046
360	0.01324	0.00951	0.00251	0.00085	0.00181	0.00073	0.00032
380	0.02650	0.03093	0.1130	0.00902	0.00045	0.00014	0.00007

1.2.3 Technologies for hydrocracking of heavy feedstocks

Table 1.6 shows several hydroprocessing technologies for heavy feedstocks. At present, few are in the pilot-stage, and others have been used on an industrial-scale [9].

Table 1.6. Processes for hydrocracking of heavy feedstocks

Process	Licensor/Inventor	Operating conditions	Catalyst/Reactor
Hydrocracking/HDS[2]	-	Low temperatures	Catalytic process / Fixed-bed
RESIDFINING[2]	Exxon-Mobil	380-430 ºC, 100-200 bar	Catalytic process / Fixed-bed
HYVAHL-S Process[2]	IFP/Axens	380-430 ºC, 100-200 bar	Dual catalyst/Swing Fixed-bed
HYCON[10]	Shell	380-430 ºC, 100-200 bar	Catalytic process / Moving-bed
Chevron RDS Isomax and ARDS/VRDS[2]	Chevron	380-430 ºC, 100-200 bar	Catalytic process/Fixed-bed
RCD UNIBON[2]	UOP	380-430 ºC, 100-200 bar	Catalytic process / Fixed-bed
Hydrovisbreaking (HYCAR)[2]	Showa Shell Sekiyu	380-430 ºC, 100-200 bar	Catalytic process / Fixed-bed
H-Oil[2]	IFP/Axen	410-450 ºC, 100-210 bar LHSV 0.15-1.3 h^{-1} 0.8 mm catalyst diameter	Catalytic-process/Ebullated-bed
LC-Fining[2]	Chevron Lummus Global	410-450 ºC, 100-210 bar	Catalytic-process /Ebullated- bed
$(HC)_3$ technology[10]	Canada Alberta Research Co.	410-450 ºC, 100-210 bar	Iron pentacarbonyl or Molybdenum 2-ethyl (liquid catalyst) hexanoate catalyst /Ebullated-bed reactor
VEBA COMBI CRACKING[2]	Veba Oel	440 to 485 ºC, 150-270 bar	Iron/fine coke powder catalyst /Slurry-phase reactor
HDH Plus[10]	PDVSA Intevep	420-480 ºC, 130-300 bar	Catalytic-process /Slurry-phase reactor
EST, Eni slurry technology[10]	Eni Technologies Snamprogetti	420-480 ºC, 130-300 bar	Molybdenum-based catalyst / Slurry-phase reactor
CASH[10]	Chevron	420-480 ºC, 130-300 bar	Catalytic-process /Slurry-phase reactor
MRH[2]	Idemitsu / Kellog	420-480 ºC, 130-300 bar	Fine-powder catalyst / Slurry-phase reactor
CANMET [2]	Petrocanada/Lavalin	420-480 ºC, 130-300 bar	$FeSO_4$ (no catalytic, additive) / Slurry-phase reactor
Micro-cat[2]	ExxonMobil	440 ºC, 170 bar 10^{-6} m catalyst diameter	Phosphomolydic acid and Molybdenum naphthenate / Slurry-phase reactor

1.2.4 Vacuum residue hydrocracking reactors

Depending on the nature of the feedstock, different types of reactors are used for hydrocracking vacuum residue. The reactors used for this process are fixed-bed reactors (FBRs), moving-bed reactors (MBRs), expanded- or ebulating-bed reactors (EBRs), and slurry-phase reactors (SPRs) or some combination of these rectors [2]. Figure 1.9 shows a schematic of these types of reactors. Vacuum residue feed with a high degree of impurities is usually processed in a moving-bed, ebulating-bed, or slurry-phase reactor since in these reactors, the catalyst can continuously be regenerated, thus maintaining the activity and selectivity of the reaction and reaching a minimum conversion of 60% and coke production of less than 8 wt.%. The operating conditions for each hydroprocessing technologies are given in Table 1.7.

The use of fixed-bed reactors for hydrocracking of vacuum residue is very limited because the catalyst deactivates very quickly; this is why in some cases, a dual or triple catalyst system or a combination of different reactors is used[2]. The advantages of fixed-bed reactors are: low back-mixing, low catalytic attrition, no moving parts, flexible operation at high pressure and temperature, and low investment and operation cost. The disadvantages of fixed-bed reactors, however, include low catalyst effectiveness due to the use of large catalytic particles, high pressure drop, possibility of liquid mal-distribution, hot spots, and short catalyst lifecycle[2].

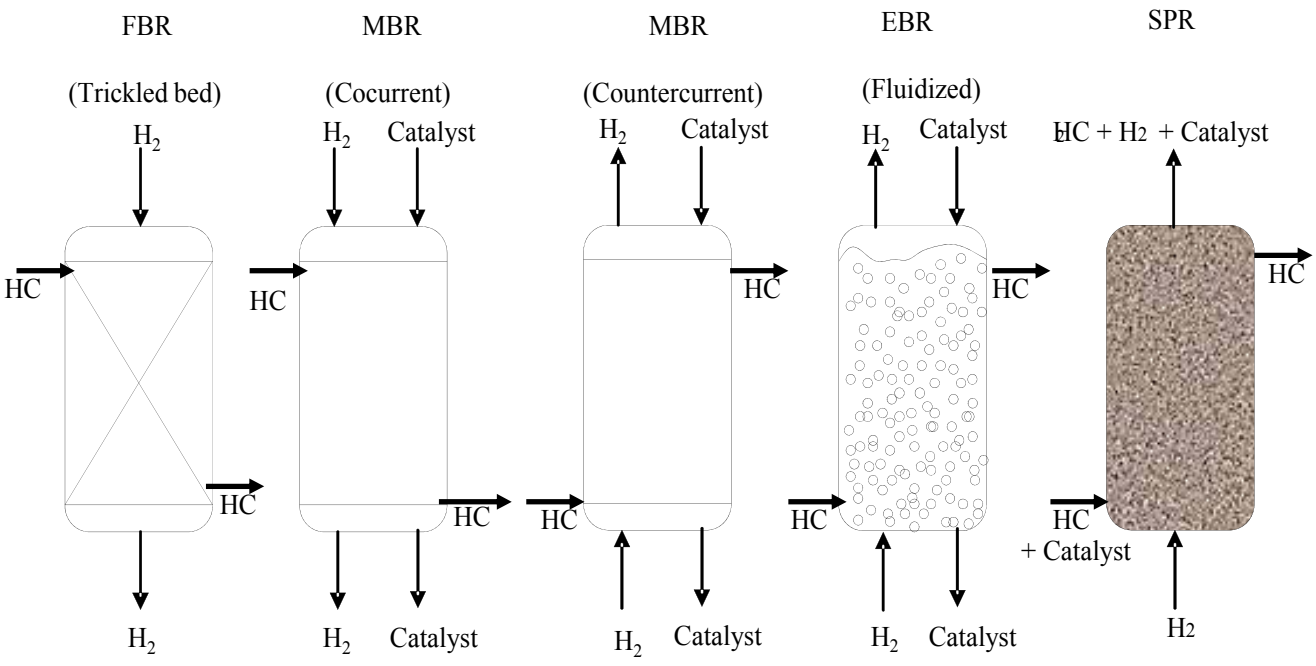

Figure 1.9. Types of reactors used to process heavy oil[2]

Table 1.7. Operating conditions for residue hydrocracking[2]

	FBR	SFB*	MBR	EBR	SPR
Pressure, bar	100-200	100-200	100-200	100-200	100-300
Temperature, ºC	380-420	380-420	380-420	400-440	420-480
Unit LHSV, h^{-1}	0.1-0.5	0.1-0.5	0.1-0.5	0.2-1.0	0.2-1.0
Max. Conv. at 550 ºC, wt%	50-70	60-70	60-70	70-80	80-95
Unit cycle length, month	6-12	Continuous operation	12	Continuous operation	Continuous operation

*SFB: Swing Fixed Bed

Moving-bed reactors have the advantage that deactivated catalyst can continuously be withdrawn from the reactor while fresh catalyst can be added, thus keeping the conversion and selectivity constant for a longer period of time [2]. The main disadvantage of moving-bed reactors, however, is that the co-current and counter-current movement of the gas-phase and slurry-phase (liquid + solid) is difficult to control.

In the ebulating-bed and slurry-phase reactors, the deactivated catalyst can continuously be withdrawn from the reactor while fresh catalyst can be added online in order to keep the hydrogen conversion constant; however, when the conversion of residue exceeds 50%, the sediment formation and equipment fouling becomes important. In order to avoid these problems, the hydrocracking of vacuum residue units are often operated at low conversion. The catalyst fluidization and mixing in SPRs mainly occurs as a result of the gas-phase (hydrogen) sparged from the bottom of the bed, whereas catalyst fluidization and mixing in EBRs occurs primarily as a result of the recycled oil and, and to a lesser extent to the sparged hydrogen. Also, EBRs allow the use of larger catalyst particles (~0.8 mm) than those used in SPRs. The advantages of using EBRs or SPRs over FBRs and MBRs in processing vacuum residue are [2]: (1) constant withdrawal and addition of catalyst, thus maintaining a steady level of catalytic activity, (2) lower pressure drop since bed plugging and channeling are eliminated, (3) high reaction rate due to the small size of the catalyst particles, and (4) better temperature control. The disadvantages of EBRs or SPRs, however, are: (1) strong back-mixing, (2) high catalyst attrition, (3) sediment formation, and (4) difficulty in scaling up.

The product composition of three different ebullating bed processes (H-Oil, LC-fining and T-Star) is summarized in Table 1.8. Table 1.7 indicates that SPRs provide the maximum conversion (80-95%) of all reactors. Therefore, the focus of this study is on SPRs operating with actual heavy residue.

Table 1.8. Product composition resulting from H-Oil, LC-fining and T-Star processes[15]

Parameter	H-Oil	LC-Fining		T-Star	
C_1-C_4	3.5	C_4	2.35	C_1-C_5	10.74
C_4-204°C	17.6	C_5-177°C	12.6	C_6-182°C	14.6
204-371°C	22.1	177-371°C	30.6	182°C-343°C	35.68
371-565°C	34.0	371-550°C	21.5	343-380°C	3.01
565°C+	22.8	550°C+	32.9	380-566°C	23.72
-	-	-		566°C+	11.63

1.3 GAS-LIQUID-SOLID MASS TRANSFER IN SLURRY REACTORS

In multiphase reactors, there are several transport steps which must be followed before the reaction can take place on the active catalyst sites. The reaction may take place in the liquid-phase, as is the case with some hydrogenation processes[16], or in the liquid-phase which may improve the heat and mass transfer between species, such as in Fischer-Tropsch synthesis in Slurry Bubble Column Reactors (SBCRs).

In general, for 3-phase systems, such as the hydrocracking process, the following steps, schematically illustrated in Figure 1.10, have to be followed before the reaction takes place on the active catalyst sites.

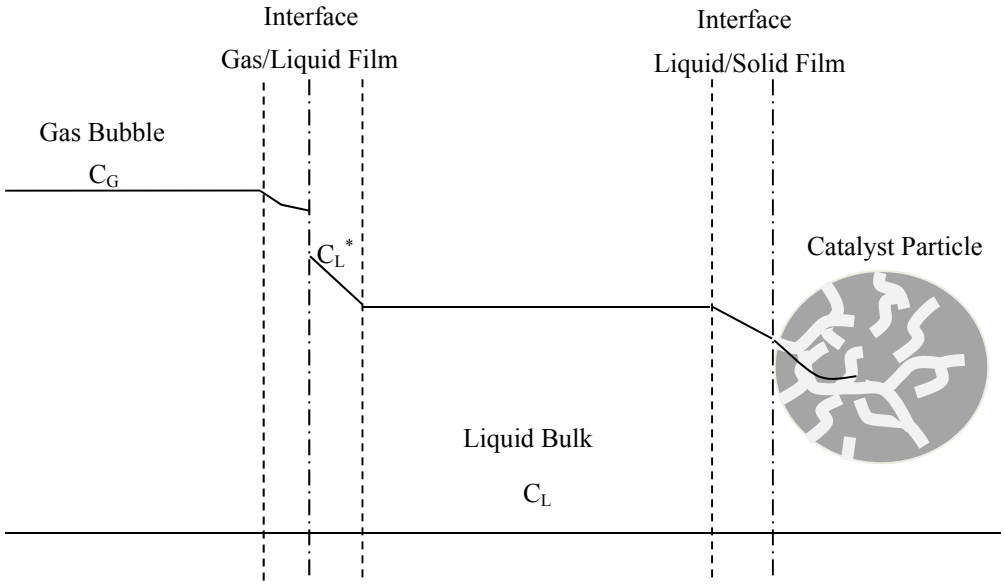

Figure 1.10. Schematic of concentration profile for 3-phase system, film model

1. Transport of hydrogen within the gas bulk.
2. Transport of hydrogen from the gas-phase bulk to the gas-liquid interface through the gas film.
3. Transport of hydrogen from the gas-liquid interface to the liquid bulk through the liquid film.
4. Transport of hydrogen within the liquid bulk.
5. Transport of hydrogen from the liquid bulk to the liquid-solid interface through a liquid film.
6. Transport of hydrogen through the catalyst pores.
7. Adsorption, reaction, and desorption of hydrogen on the active catalyst sites.

If the products are not accumulated in the catalyst pores, they have to travel back to the gas bulk, and the following steps have to be considered:

8. Transport of the products from the catalyst pores to the solid-liquid interface.

9. Transport of the products from the solid-liquid interface to the liquid bulk.
10. Transport of the products within the liquid bulk
11. Transport of the products from the liquid bulk through the liquid film to the liquid-gas interface.
12. Transport of the gaseous products from the liquid-gas interface to the gas bulk through the gas film.
13. Transport of the light products within the gas bulk.

In Steps 1 and 2, if pure hydrogen is used and the vapor pressure of the liquid (heavy residue) is low, the resistance due to the gas-film can be considered negligible.

Step 3: representing the non-negligible resistance in the liquid-film can be described by the following equation:

$$\frac{dC_{L,i}}{dt} = k_{L,i}a\left(C^*_{L,i} - C_{L,i}\right) \tag{1-3}$$

For step 4, Fick's law can be applied as:

$$J_i = - D_{ij}\frac{\partial C_{L,i}}{\partial z} \tag{1-4}$$

where D_{AB} can be estimated using Equation (4-6). There is no resistance in the liquid bulk and liquid-solid interface due to mixing.

Step 5: since the solid particles used are generally of the micron-size, the specific interfacial area of the particle (a_s), which is inversely proportional to its diameter, becomes significant and, accordingly, the resistance to mass transfer ($1/k_s a_s$) becomes negligible.

Step 6 and 8: is determined by surface diffusivity, Knudsen diffusivity, D_K (Equation (1-5), molecular diffusivity (Equation (1-6)) and the effective diffusion, D_{eff} (Equation (1-7) in the catalyst particle [17].

$$D_K = 97 r_p \sqrt{\frac{T}{MW_L}} \tag{1-5}$$

$$D \propto \sqrt{\frac{T^3}{P_{total}}} \tag{1-6}$$

where r_p represents the catalyst particle radius, and MW_L is the molecular weight of the fluid phase.

$$D_{eff} = \varepsilon_{cat} \frac{D}{\tau_{cat}} \tag{1-7}$$

where ε_{cat} is the catalyst void fraction, τ_{cat} is the tortuosity of the particle.

Usually reactions in these two steps are quantified through catalyst studies by the Thiele module (Equation(1-8), and the effectiveness factor η (Equation (1-9)) as:

$$\phi = f(D_{eff}) \tag{1-8}$$

$$\eta = \frac{\tanh \phi}{\phi} \tag{1-9}$$

For practical purposes, the effectiveness factor η is considered to be close to unity [18].

Step 7: represents the chemical reaction (adsorption, reaction, and desorption) of hydrogen on the surface of the catalyst. This chemical reaction could be slow, rapid or instantaneous, depending on the system used. A typical type of a first order reaction (usually found in hydrogenation process) is [18]:

$$r_i = A \cdot \eta \cdot \exp\left(\frac{-E_{app}}{RT}\right) \cdot C_{L,H_2} \tag{1-10}$$

Considering all the above steps, it can be concluded that the steps affecting the overall reaction rate of the process are the gas-liquid mass transfer (step 3) and the chemical reaction (step 7).

Thus, the factors affecting the gas-liquid mass transfer and the reaction kinetics must be carefully considered in the selection, design and scale-up of the reactor to be used for the hydrocracking process.

As mentioned above, the focus of this study is on the use of SPRs for the hydrocracking process; unfortunately, literature data on the liquid-side mass transfer coefficient and reaction kinetics of hydrogen in vacuum residue or even in heavy oil are scanty, which makes the proper design and scale-up of SPRs for such a process somewhat difficult.

1.4 STIRRED REACTORS

Stirred reactors are commonly used for gas/liquid/solid system applications. Their initial costs are not high, and they provide great flexibility and control of the degree of mixing through the use of particular type of the impellers and mixing speeds. The type of impeller can be changed, and the liquid circulation can also be altered from radial to axial by changing the impeller configuration. The use of stirred reactors in large throughput processes, however, is limited due to the restriction on the L/D ratio. As the volume of the reactor increases, its diameter (D) should also increase. Few stirred reactors have large L/D ratios; however, these ratios are kept close to unity. It is worth mentioning that the larger the diameter of the reactor is, the thicker the vessel wall should be and that multiple impellers are required. Also, the level of conversion in stirred tank reactors is lower when compared with that of plug flow reactors for most of the kinetics and mass transfer coefficients of different processes. In spite of these limitations, several applications routinely employ stirred reactors, such as the manufacture of polypropylene, polyvinylchloride (PVC), oxidation of cyclohexane, and synthesis of specialty chemicals[19].

The performance of the processes carried out in stirred reactors depends on a number of specific variables which control the degree of mixing and hydrodynamics within the reactor. Such variables include: the size, number, shape, and axial/radial position of the impeller, and number, size, and position of the baffles, etc... Thus, one can expect that the implementation of the studies conducted in these reactors is limited since the results obtained are often reactor- and/or process-dependent.

1.5 EFFECT OF OPERATING PARAMETERS ON THE SOLUBILITY

As can be seen in Equation (1-3), the equilibrium solubility, C^* is of prime importance for determining the rate of mass transfer in gas-liquid and gas-liquid-solid processes. Different studies showed that, for most of these gas-liquid systems, the gas solubility values increase linearly with pressure and therefore follow Henry's Law within the pressures investigated. The C^* of gases in organic liquids was also reported[20, 21] to decrease with increasing the molecular weight/carbon number of organic liquid in homologous hydrocarbon series. Depending on the gas-liquid system considered as well as the temperature range studied, C^* values were found to either increase or decrease with increasing temperature. For example, the solubilities for Ar, H_2, N_2, He and CO in n-paraffins were reported[22-30] to increase with increasing temperature, whereas those for CO_2, CH_4, C_2H_6, C_2H_4, and C_3H_8 were reported to decrease[21, 22, 27, 29]. Several investigators[27, 29, 31-35] measured the solubility of different gases in the same organic liquid (mostly in n-paraffins) and reported the following order for the solubility values:

$$C^*_{He}<C^*_{H2}<C^*_{N2}<C^*_{CO}<C^*_{CH4}<C^*_{CO2}<C^*_{C2H4}<C^*_{C2H6}<C^*_{C3H8}$$

1.6 MASS TRANSFER IN STIRRED REACTORS

Several studies were conducted in stirred reactors to determine the effect of different operating variables on k_La values. A literature review on the mass transfer studies in stirred reactors is given in Appendix A. The only common finding of these studies is that k_La values increase with the mixing speed of the impeller used[36, 37]. Generally, k_La values were correlated with the solute diffusivity (D_A) and power consumption per unit liquid or slurry volume. A number of investigators found that the effect of diffusivity is related to the k_L values [38-40] and others reported relations between k_L and D_A in the form of $k_L \alpha D_A^m$, as given in Table 1.9. It is important to mention that based on the definition of k_L, the diffusivity exponent should ranges between 0.5 and 1.0, based on the Film theory (Equation (1-11)), The Penetration theory (Equation (1-12)), or Surface-renewal theory (Equation (1-13)) as follow:

$$k_L = \frac{D_{A,B}}{\delta_L} \tag{1-11}$$

$$k_L = 2\left(\frac{D_{A,B}}{\pi\theta}\right)^{0.5} \tag{1-12}$$

$$k_L = \left(D_{A,B}s\right)^{1/2} \tag{1-13}$$

Table 1.9. Relationships between k_L and diffusivity

Author	Variable	Diffusivity Exponent	System
Versteeg et al.[41]	k_L	0.33-0.5	Gases in water
Davies et al. [42]	k_L	0.46-0.60	H_2, He, O_2, CO and CO_2 in protein and water
Kuthan and Broz [43]	k_L	0.51-0.64	He, N_2, and C_3H_8 in ethylene glycol
Kozinski and King [44]	k_L	0.5-0.6	He, H_2, Ar, and CO_2 in distilled water
Linek et al. [45]	k_L	0.46-0.66	O_2, N_2, Ar, and He in water and water solutions of Na_2SO_4, KI and Na_2SO_3

1.6.1 Effect of pressure and temperature on gas-liquid mass transfer

The effect of pressure on k_La in agitated reactors has been shown in the literature to be system-dependent. A number of authors reported that k_La values increase with pressure[28, 39, 46, 47], while others showed either no effect or a decreasing trend[39, 40, 48, 49]. Similar situations concerning the effect of temperature on k_La were also reported. It certain cases, k_La values were found to be independent of temperature[39, 50] while in other cases, an increasing trend[28, 39, 46, 47] or a decreasing trend[39, 40, 47, 49] was reported. In addition, one study[51] used a statistical approach to obtain k_La values, however, the correlations obtained were only applicable to the data obtained in is study.

1.6.2 Effect of solids on gas-liquid mass transfer

The effect of solid concentrations on mass-transfer characteristics was studied in stirred reactors. Small concentration of certain solids were found to increase k_La values by as much as two- to three- fold[52-55]. The general trend, however, is that k_La values decrease with increasing the solid

concentration[46, 56]. The initial increase of k_La values with solid concentrations was attributed to the intermittent adhesion of some particles to the gas/liquid interface[57]. These particles carried the adsorbed solute into the liquid bulk, enhancing the k_La value. Particles with high adsorption characteristics were found to show such behavior. For instance, activated carbon appeared to increase the mass transfer of oxygen in the oxidation of SO_2[58].

1.6.3 Effect of mixing speed on gas-liquid mass transfer in gas inducing reactors

Increasing mixing speed in gas inducing stirred tank reactors, was reported[20, 35, 47, 59-72] to strongly enhance the volumetric liquid-side mass transfer coefficient. This behavior can be explained by the increased amount of gas induced into the liquid and therefore higher gas holdup and gas-liquid interfacial area were obtained with increasing mixing speed. Also, increasing mixing speed increases the shear rate applied at the gas-liquid interface which can reduce the liquid film thickness and, according to the two-film model (Equation (1-11), it will increase k_L. Several investigators[35, 59, 60, 62], however, noticed that no significant k_La enhancement was provided when reaching high mixing speeds (> 1200 rpm) in small size reactors. This observed asymptotic trend of k_La at high mixing speed in those systems was attributed to the fact that the pumping capacity of the impeller reached a maximum and would not produce further change in gas holdup and therefore no further enhancement of k_La values.

2.0 OBJECTIVES

The main objectives of this study are:

1. To obtain the volumetric liquid-side mass transfer coefficient (k_La) and solubility (C^*) for hydrogen (H_2) in four liquids, two vacuum residues (A and B); and two mixtures (vacuum residue B + liquid paraffins and vacuum residue B + liquid paraffins + molten wax). All the liquids will be tested in a one-liter, high-pressure, high-temperature, agitated slurry reactor. The effect of the main process variables, including pressure, temperature, solid loading, and mixing speed, on both k_La and C^* for H_2 in the two vacuum residues and the mixture will be investigated.
2. To develop statistical and empirical correlations that model k_La with the main process variables.
3. To build a kinetic model using a series of CSTRs to calculate the residue conversion and the VGO, distillate, naphtha and gaseous products concentrations and molar flow rates, using the kinetic rate constants proposed by Sanchez at al. [1] for hydrocracking of vacuum residue at 380, 400 and 420 ^oC.

3.0 EXPERIMENTAL

3.1 GAS-PHASE

The gas-phase used in this study was H_2 (99% purity), which was purchased from Valley National Gases LLC (USA). Some relevant thermodynamics properties of H_2 are given in Table 3.1.

Table 3.1. Thermodynamic properties of hydrogen [73]

Gas	MW (kg kmol^{-1})	T_b (K)	T_C (K)	P_C (bar)	V_C (m^3 kmol^{-1})	Z_C -	ω -
H_2	2.016	20.39	33.18	13.13	0.0642	0.305	-0.220

The viscosity (μ) of H_2 in kg m^{-1} s^{-1} is calculated using the following equation[73]:

$$\mu_G = A + BT + CT^2 \tag{3-1}$$

The parameters used in this equation are given in Table 3.2.

Table 3.2. Parameters for correlation of gas viscosity in Equation (3-1)[73]

Gas	A	B	C	μ_{298K} (kg m^{-1} s^{-1})
H_2	27.76	2.12x10^{-1}	-3.28x10^{-5}	8.80x10^{-5}

It should be mentioned that Equation (3-1) shows the pressure has a negligible effect on H_2 viscosity within the range of the applicability of this equation. Figure 3.1 shows the viscosity of H_2 as a function of temperature.

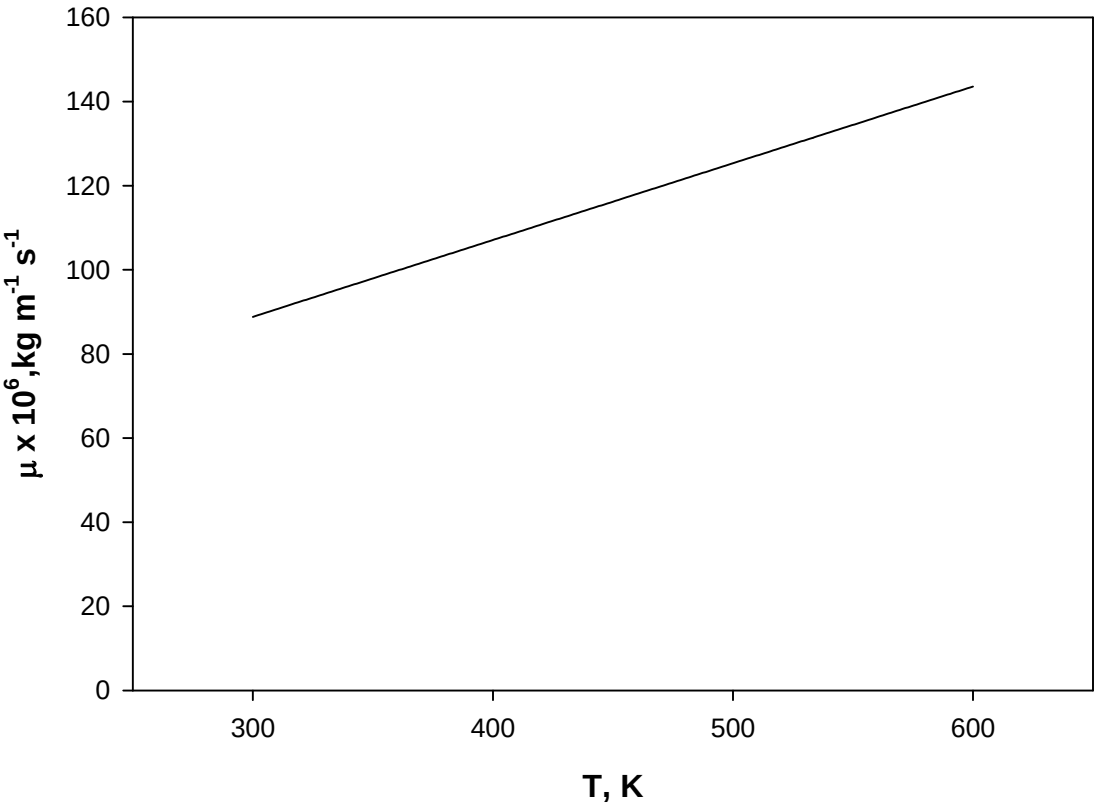

Figure 3.1. Viscosity of H_2 as function of temperature

3.2 LIQUID-PHASE

The four liquids used in this study were vacuum residues A (1.3 API 530+ ºC), and B (4.4 API 500+ ºC), C_{12}-C_{13} paraffins mixture, and C_{17}-C_{79}, wax produced by Sasol, South Africa using the Fischer Tropsch process. The vacuum residues A and B as well as mixtures of 60 wt. % vacuum residue B + 40 wt. % paraffins mixture, and 20 wt. % vacuum residue B + 40 wt. % paraffins mixture + 40 wt. % Sasol wax were used in this study. The residues were obtained from vacuum

distillation and their composition appeared to depend on the feedstock used and the cut point. The vacuum residues A and B compositions, elemental analysis, and metal content are shown in Table 3.3 through 3.5, respectively; the composition of the paraffins mixture composition provided by Sasol is shown in Table 3.6. The Sasol wax consisted mainly of saturated and straight chains of hydrocarbons with almost no branches which is a solid at room temperature and has a melting point around 83 °C.

Table 3.3. Composition of vacuum residues A and B

SAR (HPLC)	Residue B, %	Residue A, %
Saturates	10.0	4.8
Aromatics	31.0	28.2
Resins	38.4	43.6
Asphaltenes	17.6	20.8
Loss	3.0	2.7
Total	97.0	97.4
Sat/As	0.57	0.23
Aro/As	1.76	1.36
Resi/As	2.18	2.10

Table 3.4. Elemental analysis of vacuum residues A and B

Element	wt.%	
	Residue B	Residue A
C	84.96	84.03
H	10.18	9.73
N	0.85	1.00
O	0.70	0.72
S	3.22	3.91
H/C(at)	1.438	1.390
N/C(at)	0.009	0.010
O/C(at)	0.006	0.006
S/C(at)	0.101	0.124

at = atomic

Table 3.5. Metal content of residues A and B

	Residue B	Residue A
Nickel(mg kg^{-1})	125	164
Vanadium(mg kg^{-1})	468	726
Ni/V	0.23	0.20

Table 3.6. Composition of paraffins mixture

C_{11} and lighter	~3 wt.%
C_{12}	50 wt.%
C_{13}	47 wt.%
C_{14+}	<1 wt.%

3.2.1 Thermodynamic properties of paraffins mixture and Sasol wax

The thermodynamic properties of the paraffins mixture, estimated from its composition[74], as well as the thermodynamic properties of Sasol wax are given in Table 3.7.

Table 3.7. Thermodynamic properties of paraffins mixture and Sasol wax

	MW, kg $kmol^{-1}$	T_b, K	T_c, K	P_c, bar	Z_c, -	ω, -
Paraffins mixture	176	224	666	17.8	0.25	0.6
Sasol wax	568	794	883	4.2	0.21	1.5

3.2.2 Molecular weight distribution of vacuum residues A and B, Sasol wax, and liquid mixtures

The averaged molecular weights if the vacuum residues A and B were about 5000 kg/kmol and the molecular weight distribution of Sasol wax was 568 kg/kmol. The average molecular weight of the mixtures of 60 wt. % vacuum residue B + 40 wt. % paraffins mixture, and 20 wt. % vacuum residue B + 40 wt. % paraffins mixture + 40 wt. % Sasol wax along with the product composition for three different types of hydrocracking of vacuum residue technologies were calculated using appropriate mixing rules.

3.2.3 Liquid density and specific gravity

The liquid density (ρ_L) for the vacuum residues A and B, and the density of Athabasca bitumen vacuum found in the literature are presented in Figure 3.2. Both residues A and B densities were modeled with regression coefficient > 0.99 using Equations ((**3-2**) and ((**3-3**). It should be noted that the data obtained for residue B are very close to the data reported for Athabasca bitumen vacuum residue[75].

$$\rho_{L(A)} = 1199.1 - 0.40T \qquad ((3\text{-}2)$$

$$\rho_{L(B)} = 1062.7 - 0.56\,(T - 273.15) \qquad ((3\text{-}3)$$

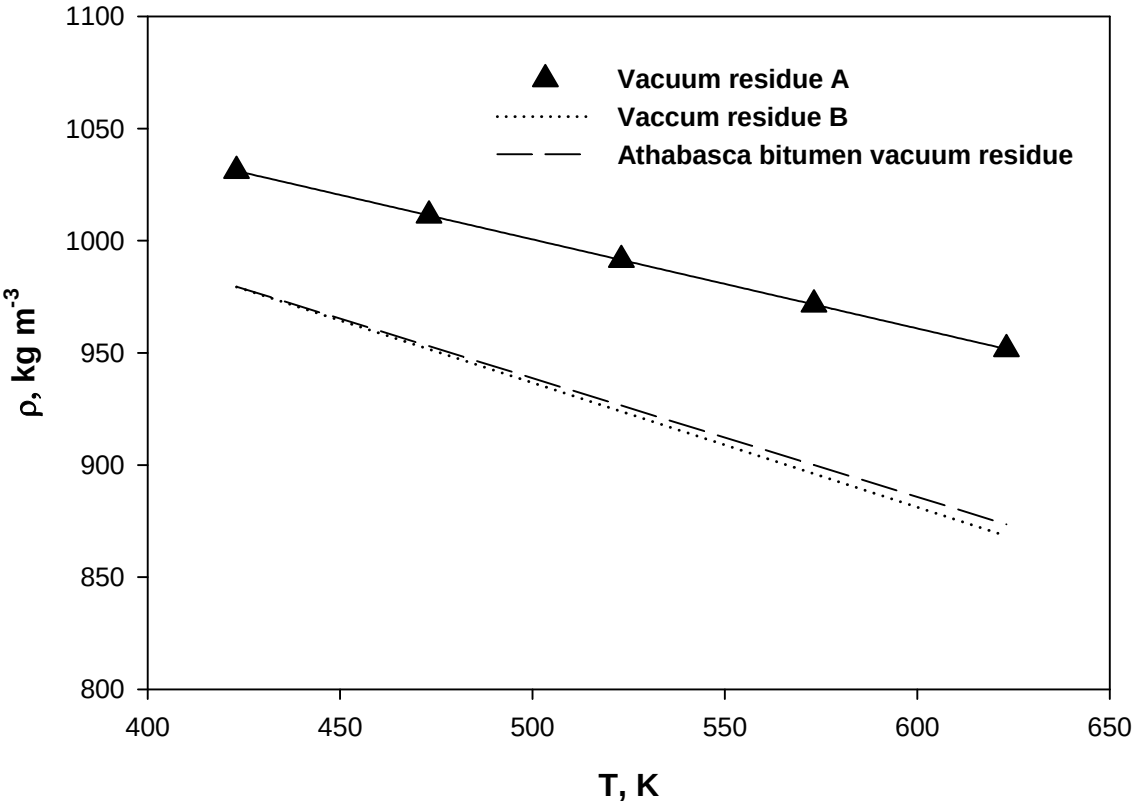

Figure 3.2. Effect of temperature on density of vacuum residues A and B and Athabasca bitumen vacuum residue

The specific gravity (60/60 ºF) values for vacuum residues A and B were calculated using Equation (3-4)[2].

$$SG \quad at \quad 60°F = \frac{141.5}{API \quad gravity + 131.5} \tag{3-4}$$

Since, the (API) gravity for residues A and B are 1.3 and 4.4, respectively, the corresponding specific gravity for vacuum residues A and B are 1.07 and 1.04, respectively, which indicates that the vacuum residue A is slightly heavier than vacuum residue B.

The density of the paraffins mixture and Sasol wax were measured in our laboratory at different temperatures, from 290 K to 500 K for paraffins mixture and 400 K to 480 K for Sasol wax, and correlated as a function of temperature using the following equations with a regression coefficient equal to 1:

$$\rho_{L(paraffins \quad mixture)} = 958.8 - 0.71\,T \tag{3-5}$$

$$\rho_{L(Sasol \quad wax)} = 959.1 - 0.51\,T \tag{3-6}$$

The density of the paraffins mixture and Sasol wax are shown as a function of temperature in Figure 3.3.

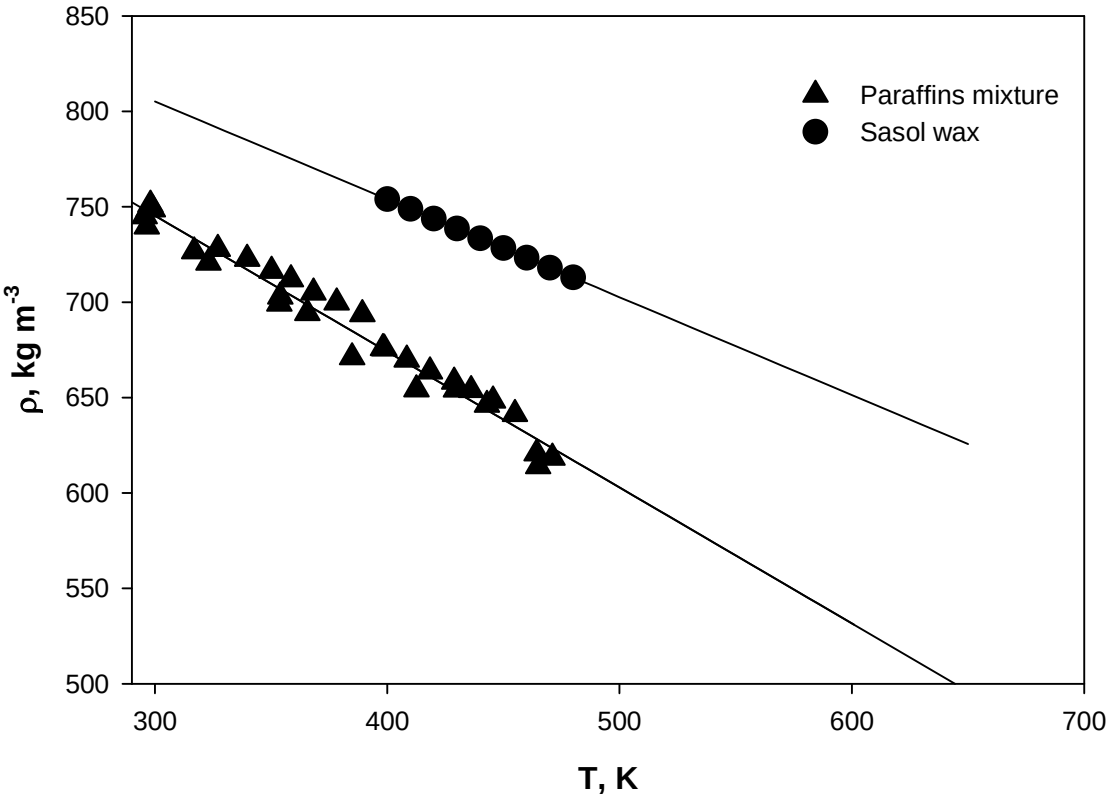

Figure 3.3. Effect of temperature on density of paraffins mixtures and Sasol wax

The liquid mixtures densities, $\rho_{L\ \ mixture}$, were estimated using Equations (3-7) and (3-8), respectively:

$$\rho_{L\ \ B/paraffins} = \frac{m_B + m_{paraffins\ \ mixture}}{\left(\frac{m_B}{\rho_B}\right) + \left(\frac{m_{paraffins\ \ mixture}}{\rho_{paraffins\ \ mixture}}\right)} \tag{3-7}$$

$$\rho_{L\ \ B/paraffins/wax} = \frac{m_B + m_{paraffins\ \ mixture} + m_{Sasol\ \ wax}}{\left(\frac{m_B}{\rho_B}\right) + \left(\frac{m_{paraffins\ \ mixture}}{\rho_{paraffins\ \ mixture}}\right) + \left(\frac{m_{Sasol\ \ wax}}{\rho_{Sasol\ \ wax}}\right)} \tag{3-8}$$

The liquid density for residue B, paraffins mixture, and Sasol wax were calculated from Equations ((3-3) through (3-6), respectively. Figure 3.4 shows different density values for liquid mixtures.

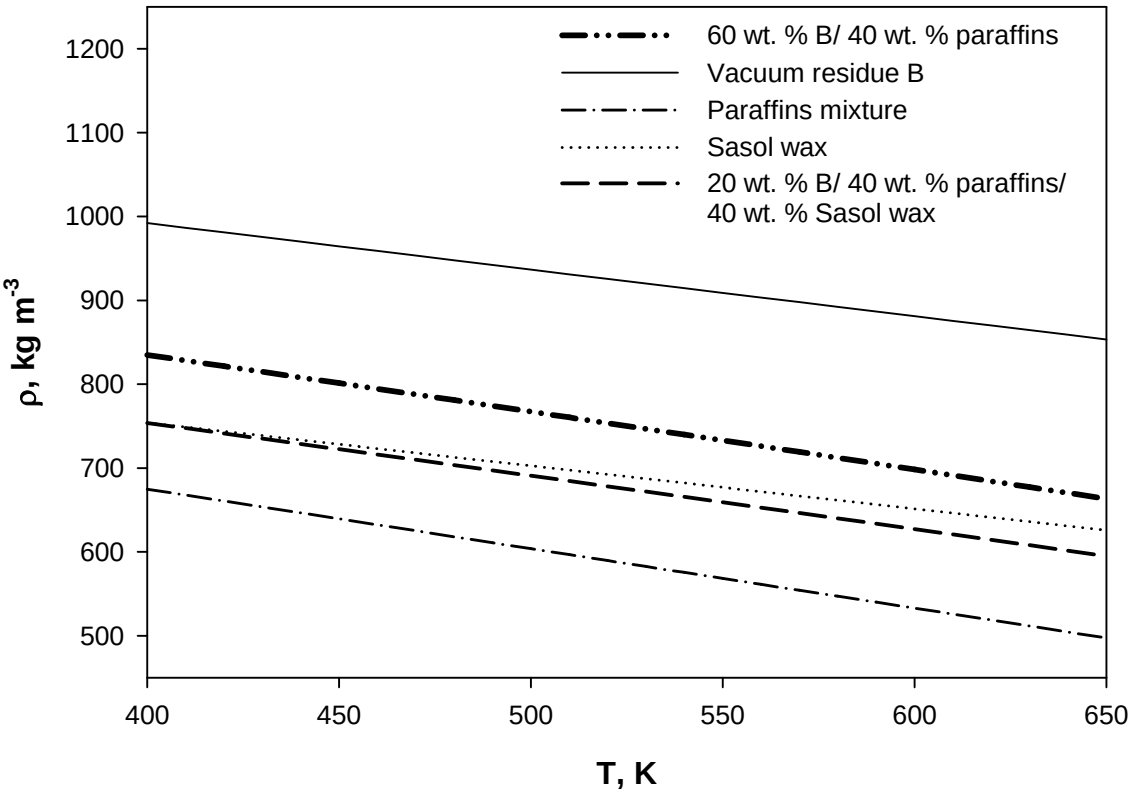

Figure 3.4. Effect of temperature on liquid mixture density

3.2.4 Liquid viscosity

The viscosity values for molten vacuum residues A and B at 398 K and 423 K are given in Table 3.8 below. The liquid kinematic viscosity (ν_L) for both residues were correlated as a function of temperature using Equation (3-9)[76]. This type of equation is often used to calculate the viscosity of vacuum residues. The corresponding dynamic viscosity (μ_L) was then calculated using Equation (3-10).

Table 3.8. Viscosity of vacuum residues A and B

A Vacuum Residue	
Kinematic viscosity at 398 K, $m^2 s^{-1}$	21527.2×10^{-6}
Kinematic viscosity at 423 K, $m^2 s^{-1}$	3176.9×10^{-6}
B Vacuum Residue	
Kinematic viscosity at 398 K, $m^2 s^{-1}$	2356.3×10^{-6}
Kinematic viscosity at 423 K, $m^2 s^{-1}$	516.0×10^{-6}

$$\nu_L = [\exp(\exp(A - B * \ln(T)))] - 0.7 \tag{3-9}$$

$$\mu_L = \nu_L \rho_L \tag{3-10}$$

Using the two viscosity measurements for 398 and 423 K, it was possible to determine the constants in Equation (3-9), and the following equations for kinematic viscosity were obtained for vacuum residues A and B.

$$\nu_{L_{(A)}} = \{[\exp(\exp(23.22 - 3.49 * \ln(T)))] - 0.7\} x (10)^{-6} \tag{3-11}$$

$$\nu_{L(B)} = \{[\exp(\exp(23.42 - 3.57 * \ln(T)))] - 0.7\} x (10)^{-6} \tag{3-12}$$

The kinematic viscosity in the above equations is in m^2/s.

Figure 3.5 shows the effect of temperature on the viscosity of the vacuum residues A and B and includes the values available in the literature[75] for the Athabasca bitumen vacuum residue.

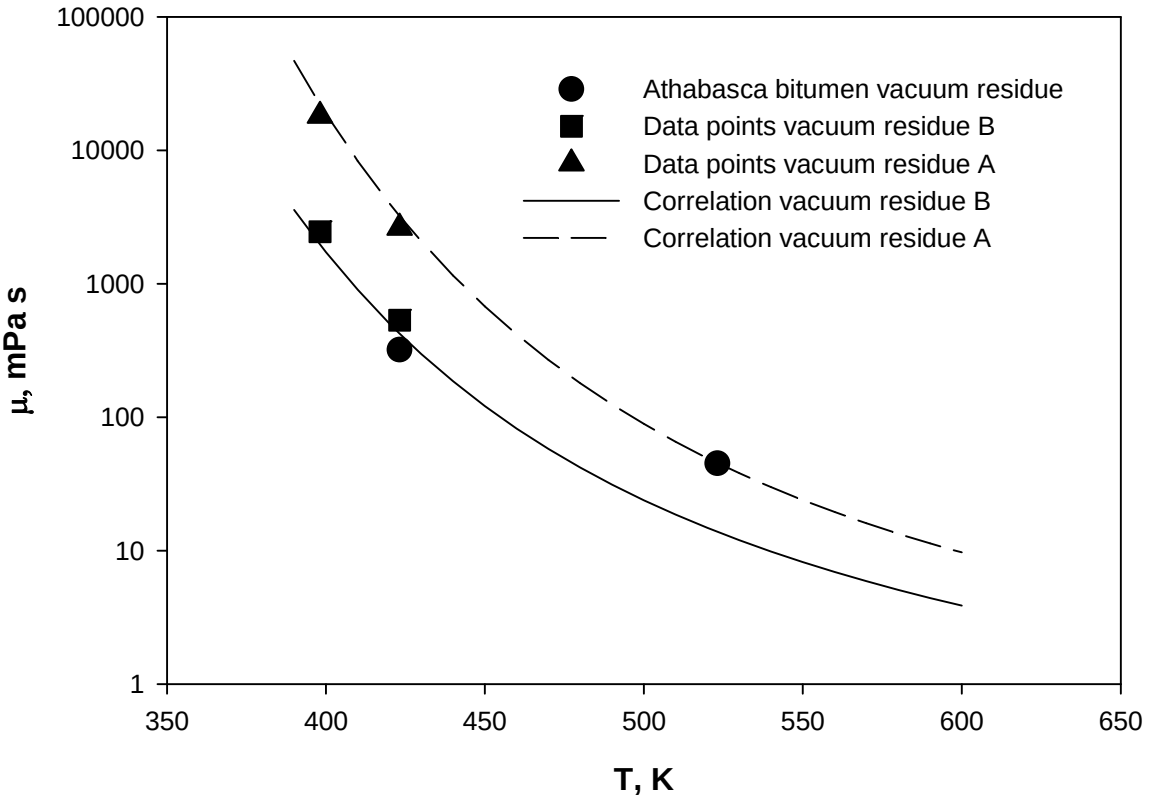

Figure 3.5. Effect of temperature on viscosity of the vacuum residues A and B

The viscosity of the paraffins mixture was measured in our laboratory for a wide range of temperatures (290 to 500 K) using Cannon-Fenske routine viscometers and was correlated as a function of temperature using the following equation:

$$\mu_{L\ paraffins\ \ mixtures} = \frac{\exp\left(\frac{8.321x10^4}{T^2} + \frac{1043.0}{T} - 3.9708\right)}{1000} \tag{3-13}$$

For Sasol wax, the liquid viscosity was calculated using the following equation from Soriano[77]:

$$\mu_{L\,Sasol\quad wax} = \exp\left(-7.71 + \frac{1127.58}{T}\right) \tag{3-14}$$

The liquid viscosity for paraffins mixture and Sasol wax are shown in Figure 3.6 as a function of temperature.

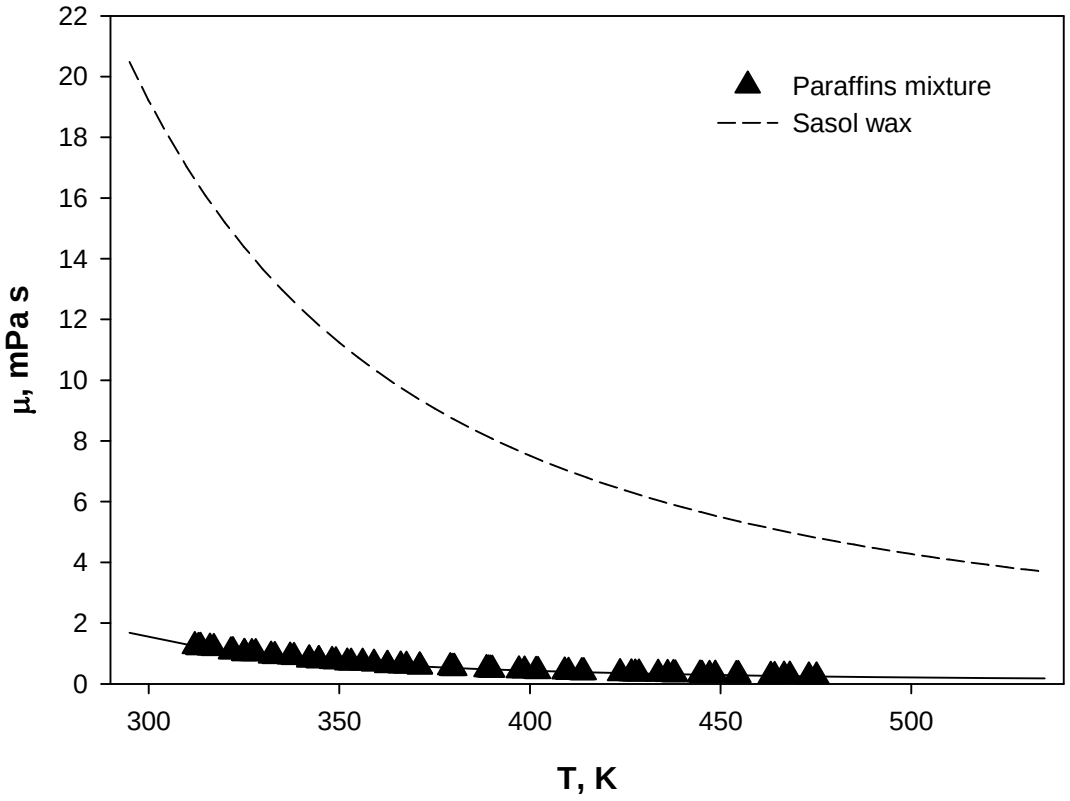

Figure 3.6. Effect of temperature on viscosity of paraffins mixture and Sasol wax

The ideal mixing rule, Equation (3-15), was used to predict the viscosities, μ_L, of both liquid mixtures.

$$Y = \sum_{i=1}^{k} y_i Y_i \tag{3-15}$$

In this equation, Y represents the property to be predicted and y_i is the mole fraction of component i. The effect of temperature on viscosity is presented in Figure 3.7 for the paraffins mixture, Sasol wax, vacuum residue B, and the two liquid mixtures.

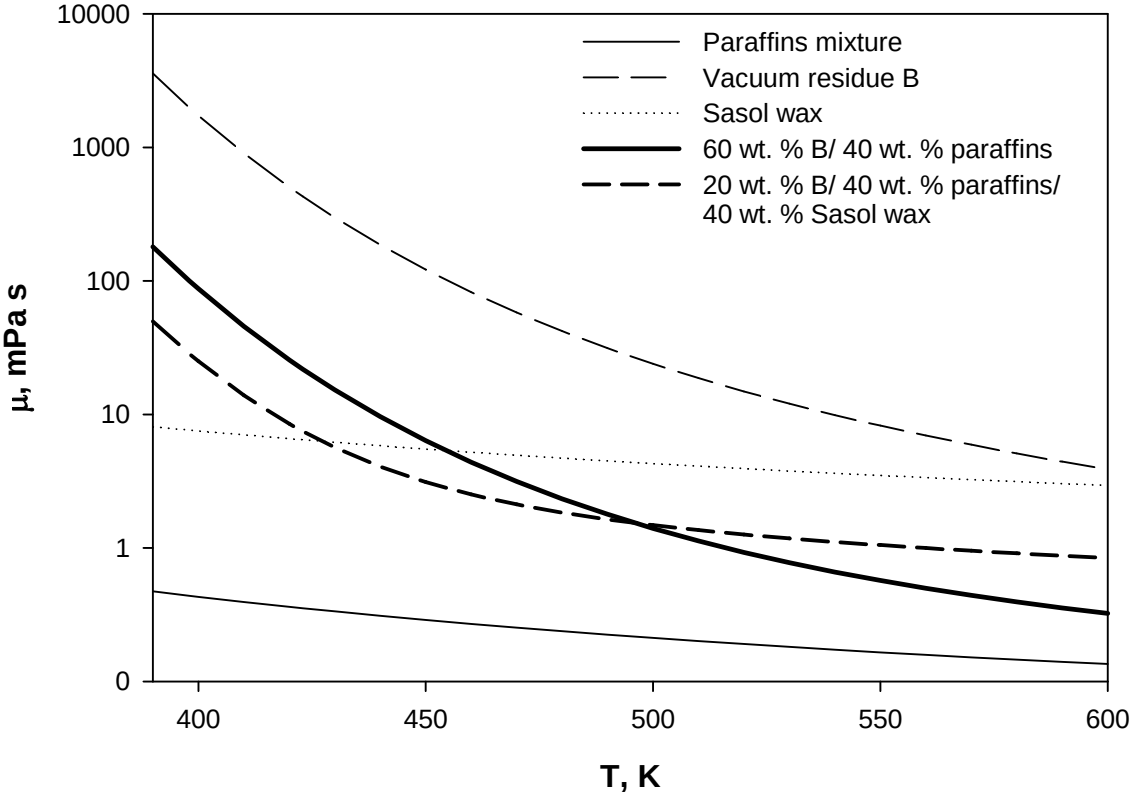

Figure 3.7. Effect of temperature on liquid-mixture viscosity

3.2.5 Vapor pressure

At low temperatures, the vapor pressures of heavy residues are negligible when compared with hydrogen partial pressures employed in the hydrocracking process. The vapor pressure of vacuum residues B and A, were measured in our laboratory from 423 K to 673 K in a one liter reactor (described in the experimental set-up section) equipped with a 5.45 bar pressure transducer.

Figure 3.8 and 3.9 illustrate the vapor pressure and temperature as a function of time for vacuum residue A, respectively. As can be seen in these figures for 423 K, 473 K, 523 K and 573 K, the vapor pressure for each temperature remains independent of time, indicating that the gas and liquid phases are in thermodynamic equilibrium. However, at 623 and 673 K, the pressure in the reactor continues to increase with time, suggesting that thermal cracking and/or hydroconversion of the residue is taking place under these high temperatures. In fact, at these temperatures, the pressure in the reactor continued to increase until it reached approximately the 207 bar, and then the system was shut down and cooled for safety reasons. This is not surprising since Gentzis and Rahimi[78] had reported thermal cracking of heavy feedstock into a wide range of gaseous, liquid and solid products to occur above 623 K. Cai et al.[79] also found that hydrogen appears to react significantly with heavy virgin gas-oil and atmospheric residue at temperatures greater than 603 K.

Thermal cracking of petroleum residue was reported to follow a free-radical chain reaction mechanism, in which the molecules either break down into products with a desirable H/C ratio or condense to form undesirable coke products. Although most of the molecules are initiated by heating or are attacked by free radicals to produce new free radicals, some may react in a slightly different manner, as with hydrogen transfer reaction between cycloalkyl aromatics and aromatic nucleus under mild thermal treatment. Such a reaction, however, represents a more molecular nature rather than a free radical one [80].

In order to further investigate this behavior, during the vapor pressure measurement at 673 K, a portion of the vapor-phase was condensed using a dry-ice trap (-78.5 °C), and the resulting gas and liquid samples were analyzed using a mass spectrometer. As can be seen in Figure 3.10, the mass spectrum of the gas-phase indicates the presence of methane, ethane,

propane and n-butane, as evidenced by the presence of high intensity peaks at the amus of 16, 28, 29, and 43 m/z, respectively, which correspond to these components. The other high intensity peaks, at 55 and 57, could also be due to the presence of other unknown light hydrocarbon components. The liquid mass spectrum depicted in Figure 3.11 shows a number of high intensity peaks between 119.3 and 564.7 m/z, which indicate the presence of liquid hydrocarbons. Unfortunately, such hydrocarbons could not be identified in this study due to the complexity of the liquid mixture. It should be mentioned that even though quantitative analysis of the gas and liquid phases at 673 K was not possible, the qualitative results are consistent with the fact that thermal cracking and/or hydroconversion has occurred at such high temperatures.

Thus, as shown in Figure 3.9, only the vapor-phase pressure (P^S) values of the vacuum residues A and B for temperatures between 423 K and 573 K were correlated using Equations (3-16) and (3-17), respectively, where P^S is in bar and T is in K, with a regression coefficient $R^2 > 0.99$. Figure 3.12 represents the vapor pressure as a function of temperature for A and B residues.

$$\ln\left(P^S\right)_A = 0.003(T) - 2.94 \tag{3-16}$$

$$\ln\left(P^S\right)_B = 0.02(T) - 9.80 \tag{3-17}$$

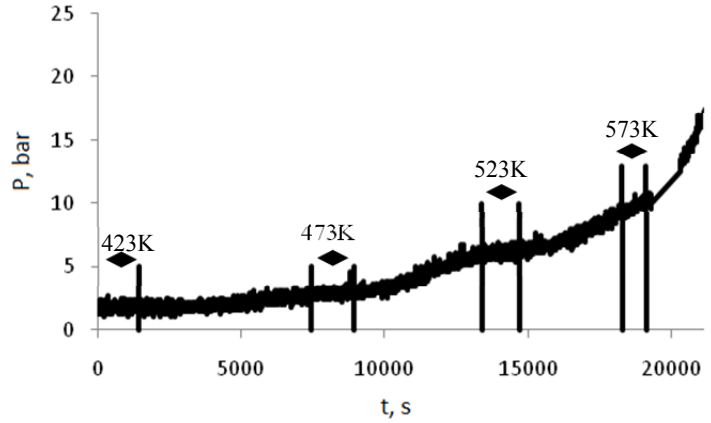

a) Pressure as a function of time at 423, 473, 523 and 573 K

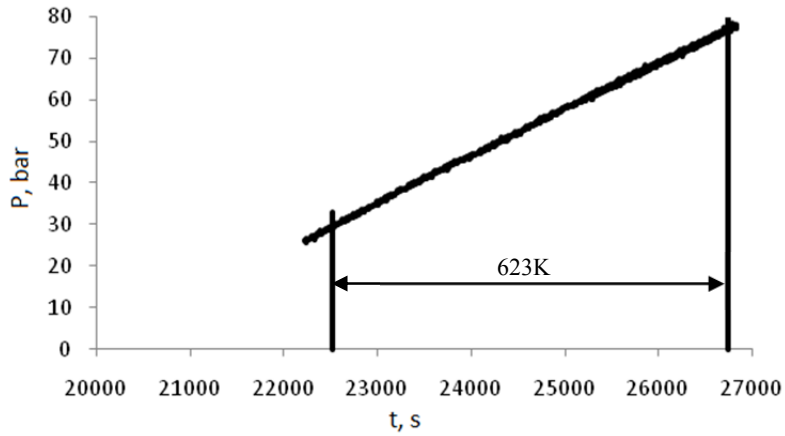

b) Pressure as a function of time at 623 K

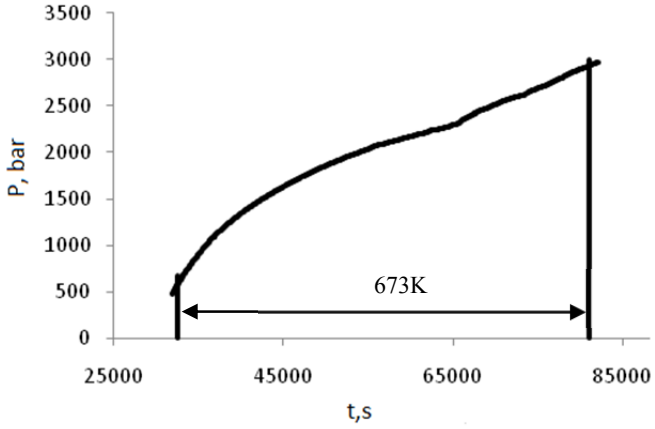

c) Pressure as a function of time at 673 K

Figure 3.8. vacuum residue A vapor pressure as a function of time

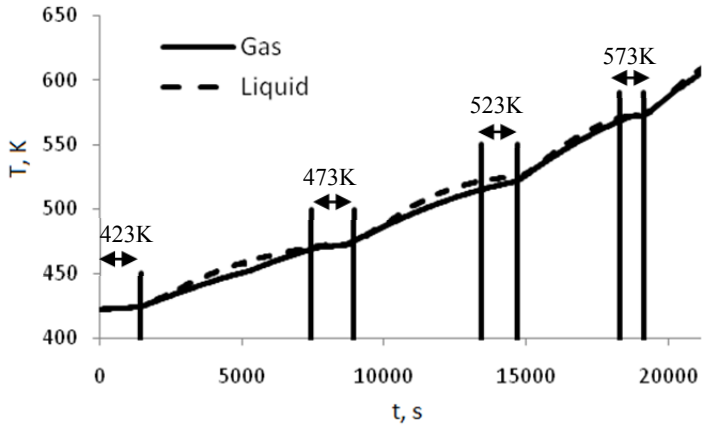

a) Temperature as a function of time at 423, 473, 523 and 573 K

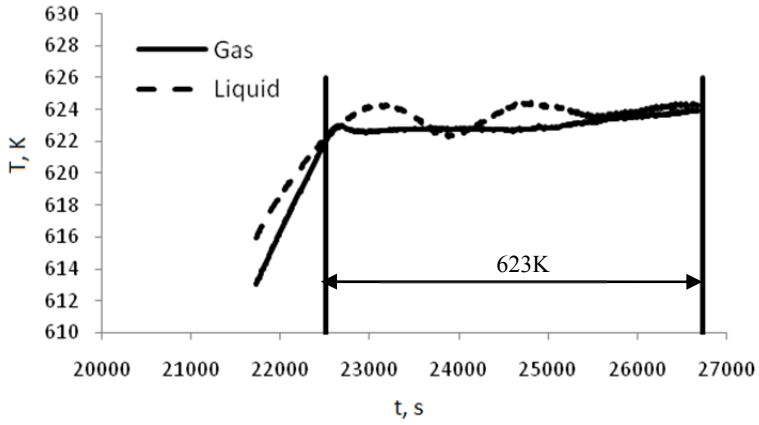

b) Temperature as a function of time at 623 K

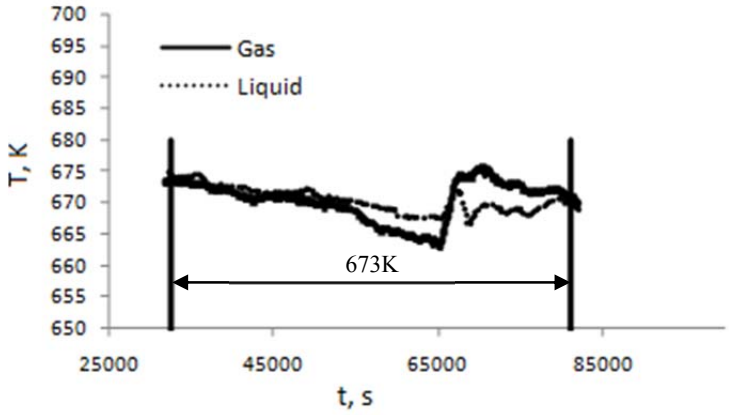

c) Temperature as a function of Time at 673 K

Figure 3.9. vacuum residue A temperature as a function of time

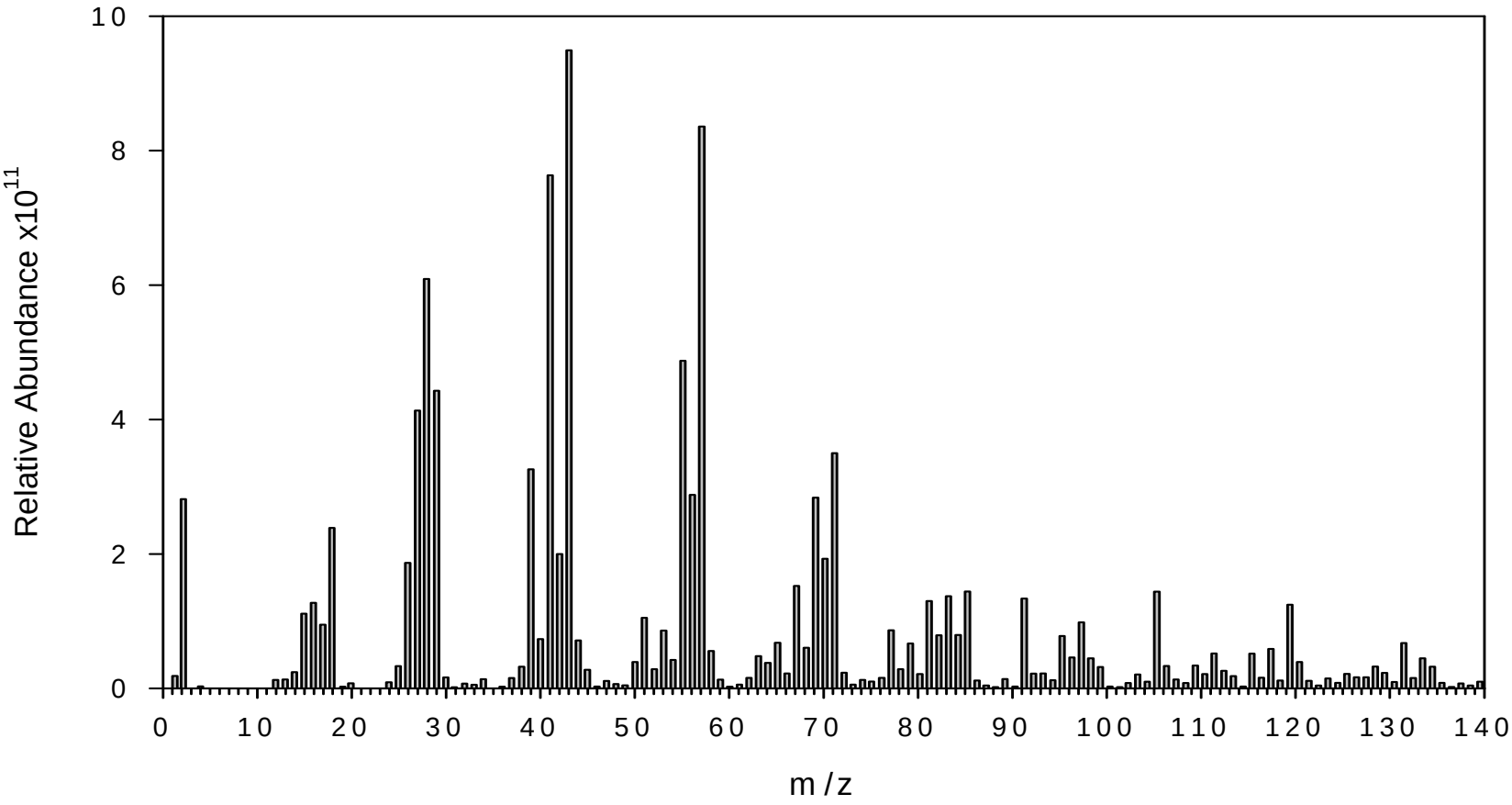

Figure 3.10. Mass spectrum of gas sample taken from vacuum residue A at 673 K

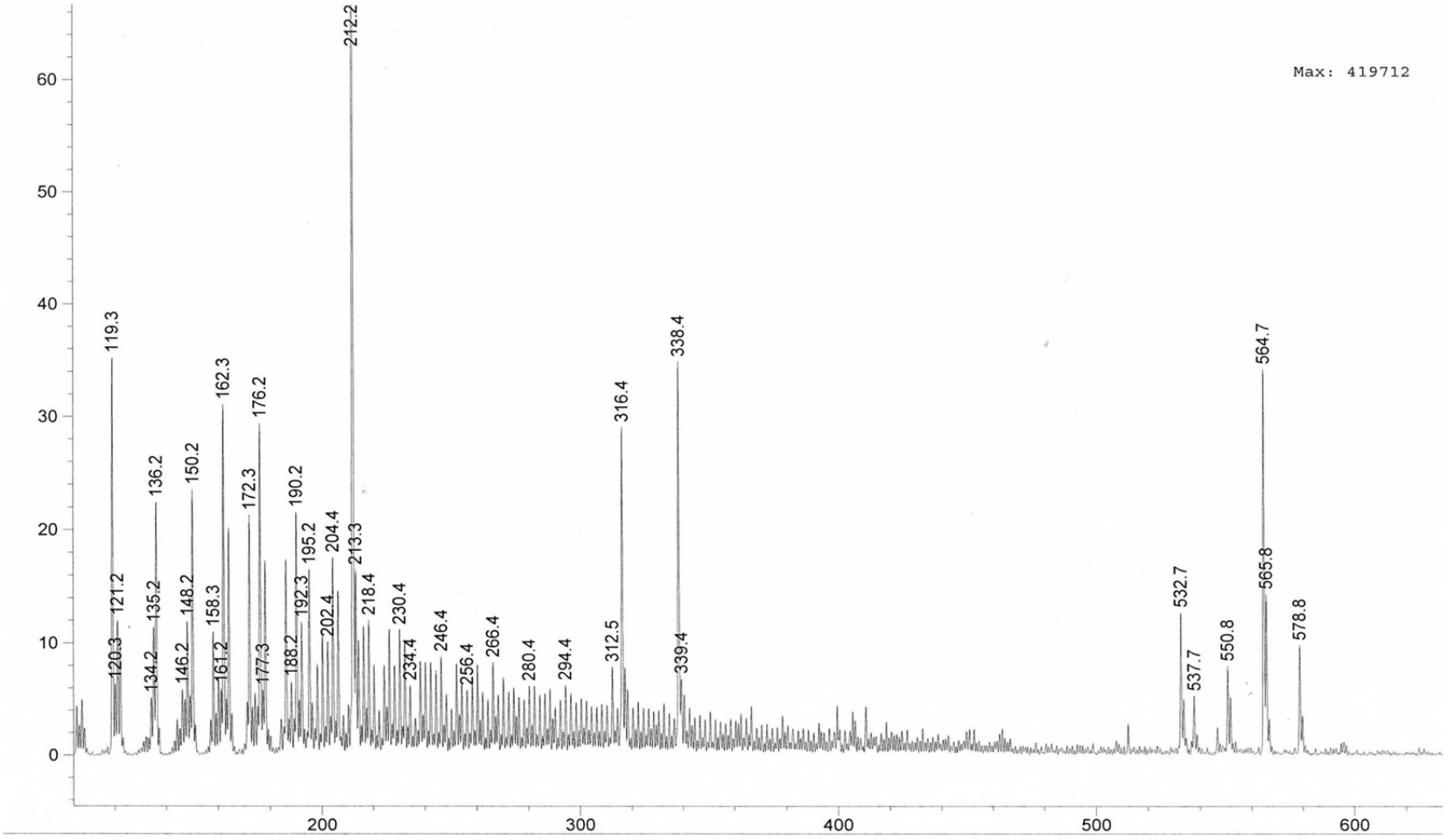

Figure 3.11. Mass spectrum of liquid sample taken at 673 K from vacuum residue A

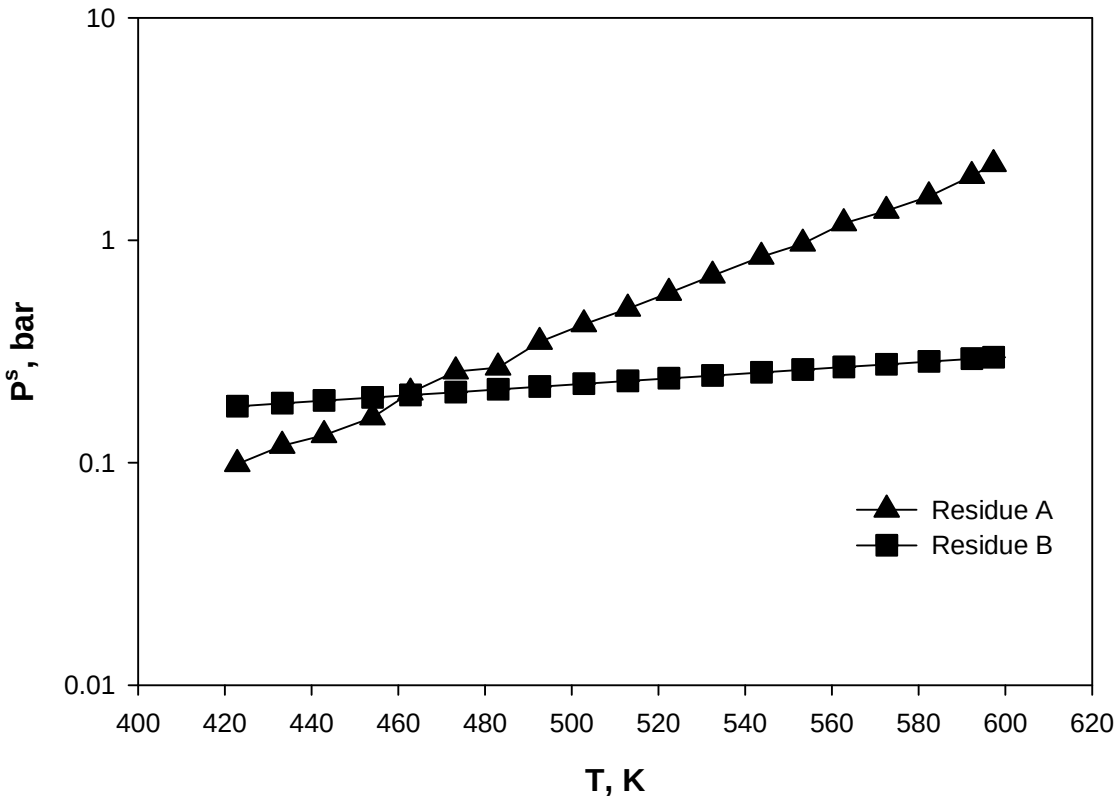

Figure 3.12. Effect of temperature on vapor-phase pressure of vacuum residues A and B

The vapor pressure of the paraffins mixture was predicted using the Asymptotic Behavior Correlations (ABC) developed by Marano and Holder[81, 82]. The vapor pressure was correlated as a function of temperature using the following equation:

$$\log_{10}\left(P^S\right) = -\frac{2.7x10^5}{T^2} - \frac{1439.5}{T} + 3.98 \tag{3-18}$$

The vapor pressure for Sasol Wax was estimated from literature data for C_{17} to C_{79} linear hydrocarbons reported by Kudchadker et al.[83] and using their corresponding molar composition in the Sasol wax, the resulting vapor pressure-temperature relation can be written as:

$$\log_{10}\left(P^S\right) = -\frac{164347.3}{T^2} - \frac{5165.4}{T} + 6.39 \tag{3-19}$$

The vapor pressure of the paraffins mixture and Sasol wax are shown as a function of temperature in Figure 3.13.

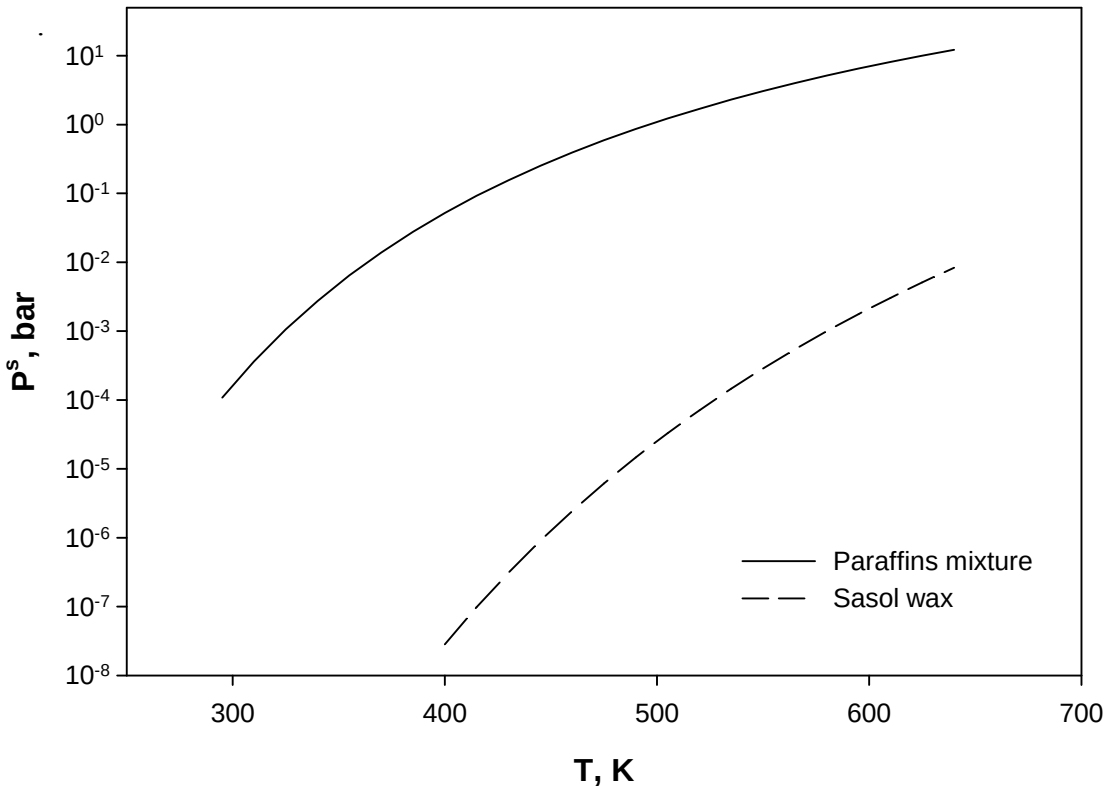

Figure 3.13. Effect of temperature on vapor-phase pressure of paraffins mixture and Sasol wax

The vapor pressures for the liquid mixtures were determined experimentally in our laboratory. the effect of temperature on the vapor pressure for the two liquid mixtures is presented in Figure 3.14.

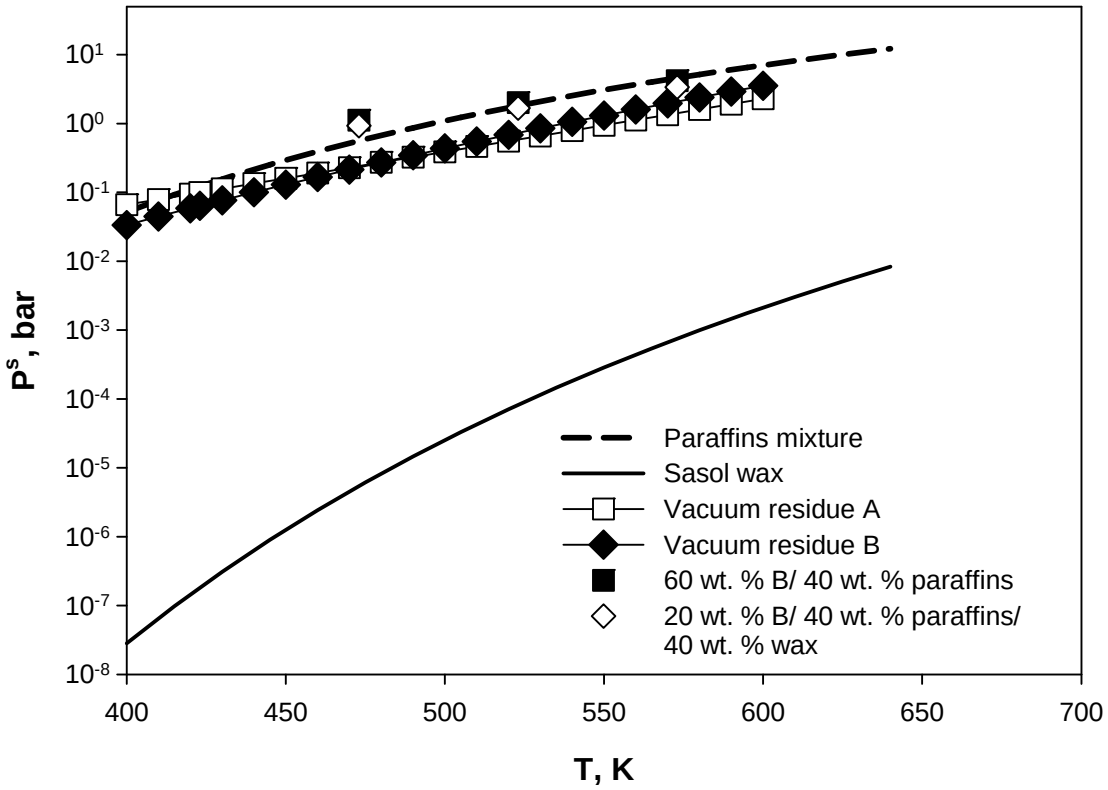

Figure 3.14. Effect of temperature on vapor-phase pressure of liquid mixtures

3.2.6 Surface tension

The surface tension of the vacuum residues A and B were estimated using Equation (3-20)[75]

$$\sigma = 0.03 - 2.48 \times 10^{-5}(T) \tag{3-20}$$

where σ is in N m^{-1} and T is in degrees K.

A plot of the liquid surface tension as a function of temperature for vacuum residues A and B is presented in Figure 3.15.

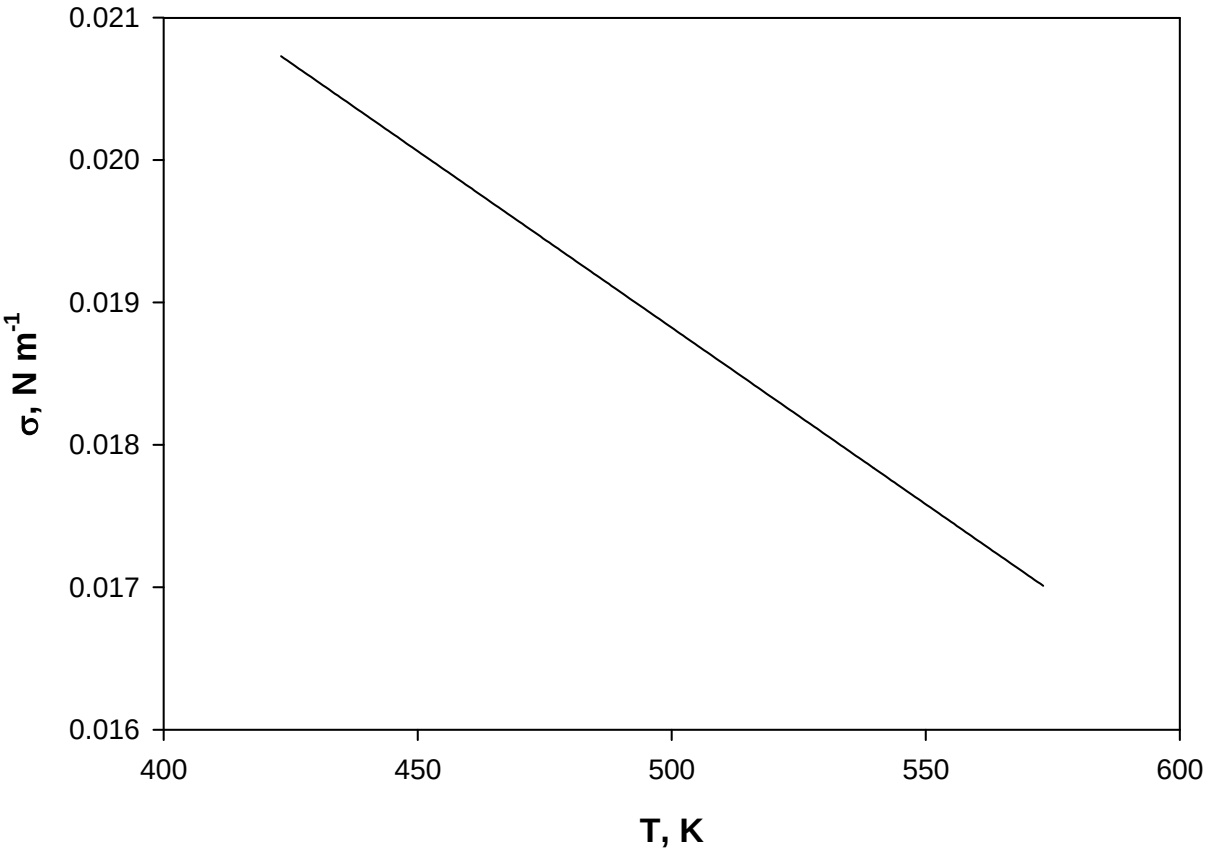

Figure 3.15. Effect of temperature on surface tension of vacuum residues A and B

The surface tension of the paraffins mixture was predicted by Marano and Holder[81, 82] using the Asymptotic Behavior Correlations (ABC) developed. Also, the surface tension of Sasol wax as a function of temperature was obtained using the following equation:

$$\sigma_L = 57.32 - 0.11 \times T + 5.50 \times 10^{-5} \times T^2 \quad (3\text{-}21)$$

The surface tension of the paraffins mixture and Sasol wax are shown as a function of temperature in Figure 3.16.

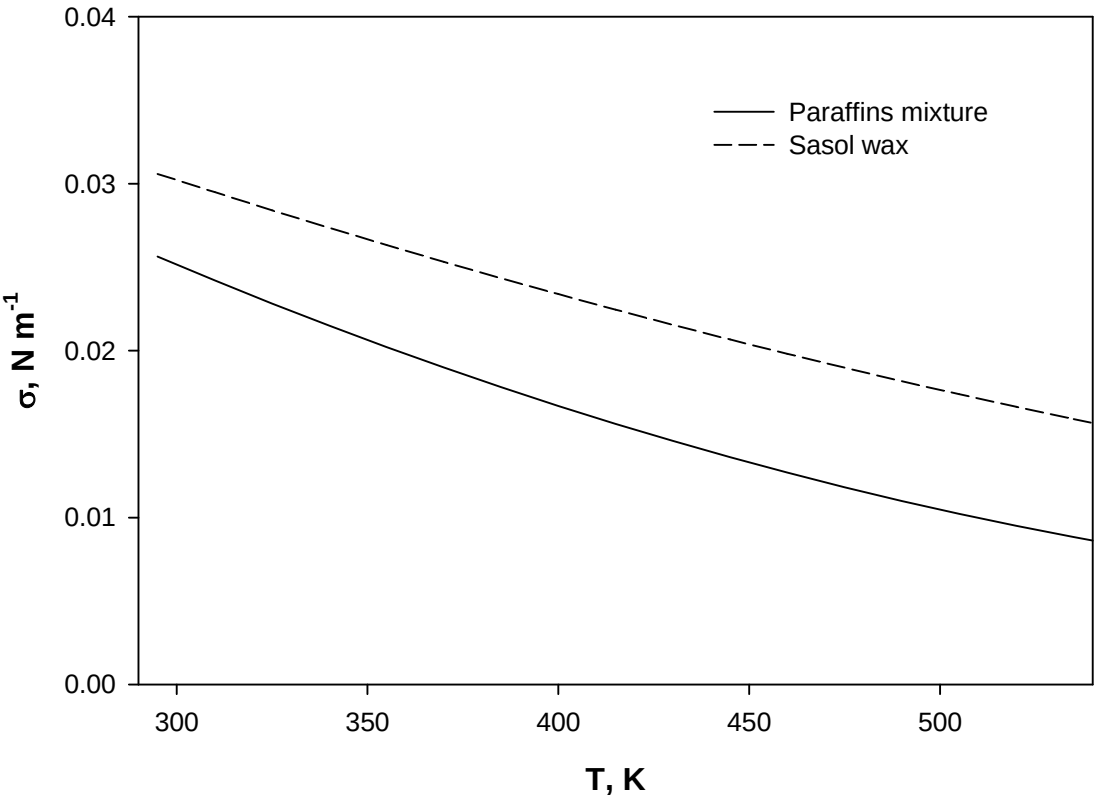

Figure 3.16. Effect of temperature on surface tension of paraffins mixture and Sasol wax

The ideal mixing rule Equation (3-15) was used to predict the surface tension (σ_L) of liquid mixtures. The effect of temperature on the surface tension is presented in Figure 3.17 for paraffins mixture, Sasol wax, vacuum residue B and the liquid mixtures.

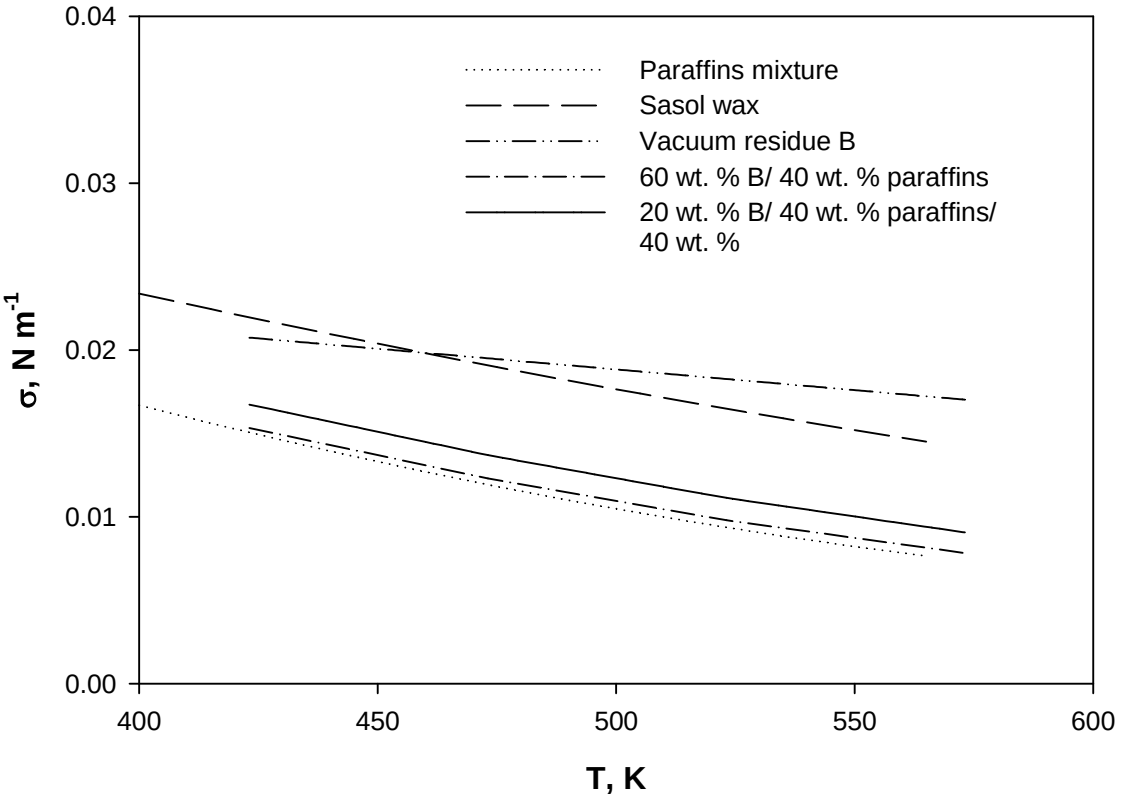

Figure 3.17. Effect of temperature on surface tension of liquid mixtures

3.2.7 Specific heat and heat of combustion

The specific heat, in BTU lb^{-1} $°F^{-1}$ and heat of combustion, in cal g^{-1} were calculated using Equations (3-22) and (3-23) respectively[2].

$$C = \frac{1}{SGat60^{\circ}F(0.39 + 4.5x10^{-4}T)} \tag{3-22}$$

$$Q = 12400 - 2100(SG \quad at \quad 60°F)^2 \tag{3-23}$$

C is the specific heat, T is the temperature in Fahrenheit, and SG is the specific gravity at 60 ºF. The heat of combustion (Q) for vacuum residues A and B were found to be 10,123 cal g^{-1} and 10,016 cal g^{-1}, respectively. Figure 3.18 shows the effect of the temperature on the specific heat of vacuum residues B and A.

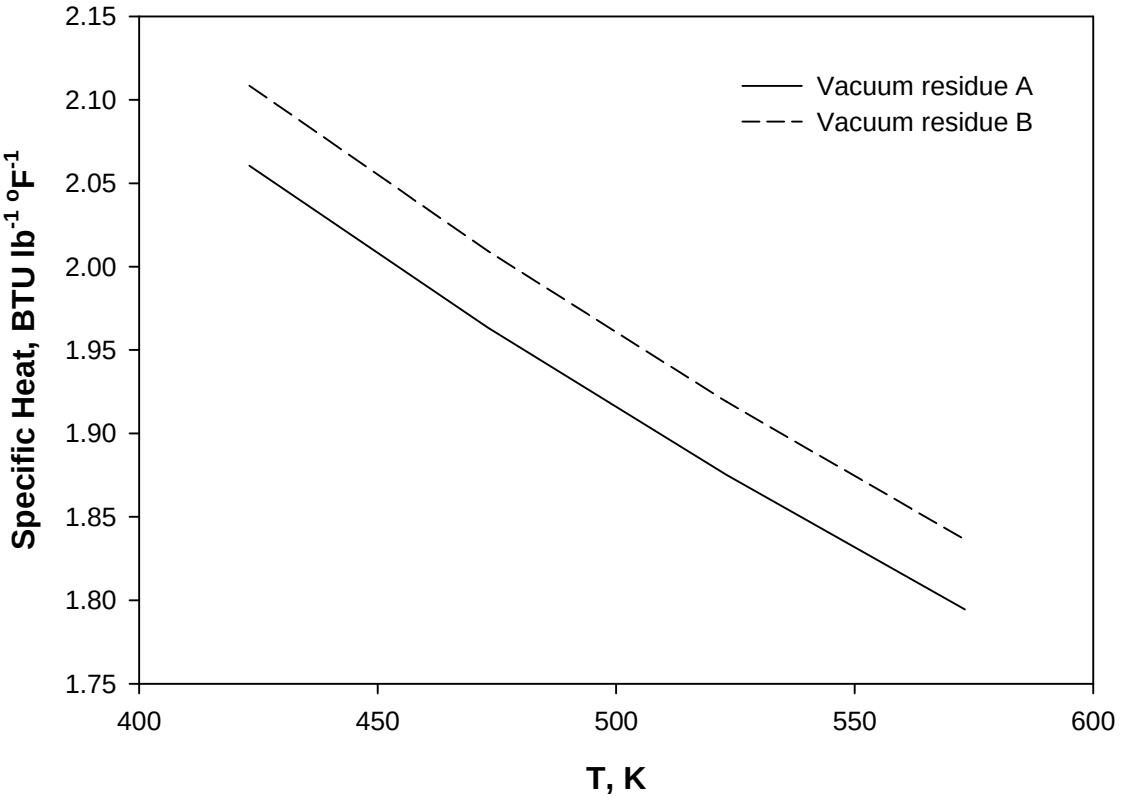

Figure 3.18. Effect of temperature on specific heat of vacuum residues A and B

3.2.8 Heat capacity

The heat capacities of both residues were calculated using Kesler and Lee's Equation[76]:

$$C_p = \left[a + bT + cT^2\right]4184 \tag{3-24}$$

in which:

$$a = 0.32646 + 0.02678K_W - CF(0.084773 - 0.080809SG) \tag{3-25}$$

$$b = -\left[1.3892 - 1.2122K_W + 0.0383K_W^2 - CF(2.1773 - 2.0826SG)\right]x10^{-4} \tag{3-26}$$

$$c = -\left[1.5393 + CF(0.78649 - 0.70423SG)\right]x10^{-7} \tag{3-27}$$

$$CF = \left[(\frac{12.8}{K_W} - 1)(\frac{10.0}{K_W} - 1)100\right]^2 \tag{3-28}$$

$$K_W = \frac{T_b^{1/3}}{SG} \tag{3-29}$$

In these equations, T_b is the mean average boiling point in ºR.

The calculated heat capacity for vacuum residues A and B at T = 573.15 K are 2,241 and 2,343 J kg^{-1} K^{-1}, respectively.

3.3 SOLID-PHASE

The solid-phase used was activated carbon (Carbsorb 20x50 WW) purchased from Calgon Carbon Corporation (Pittsburgh, PA, USA). The specific gravity and particle size, provided by Calgon Carbon, were 0.4-0.7 and 297-841 μm, respectively. The solid skeletal density (ρ_S) for the activated carbon was measured in our laboratory and was found to be 1,539± 5% kg m^{-3}.

3.4 SLURRY PROPERTIES

3.4.1 Slurry density

The slurry density, ρ_{SL}, was estimated using the following equation:

$$\rho_{SL} = \frac{m_{cat} + m_L}{\left(\frac{m_{cat}}{\rho_{cat}}\right) + \left(\frac{m_L}{\rho_L}\right)} \tag{3-30}$$

Where ρ_L was calculated from Equations (**(3-2**) and ((**3-3)** for residues A and B, respectively, and the activated carbon density, ρ_s, was 1,539 kg m^{-3}. Figure 3.19 and 3.20 show different

values for slurry densities as a function of temperature at different solid concentrations for the vacuum residues A and B, respectively

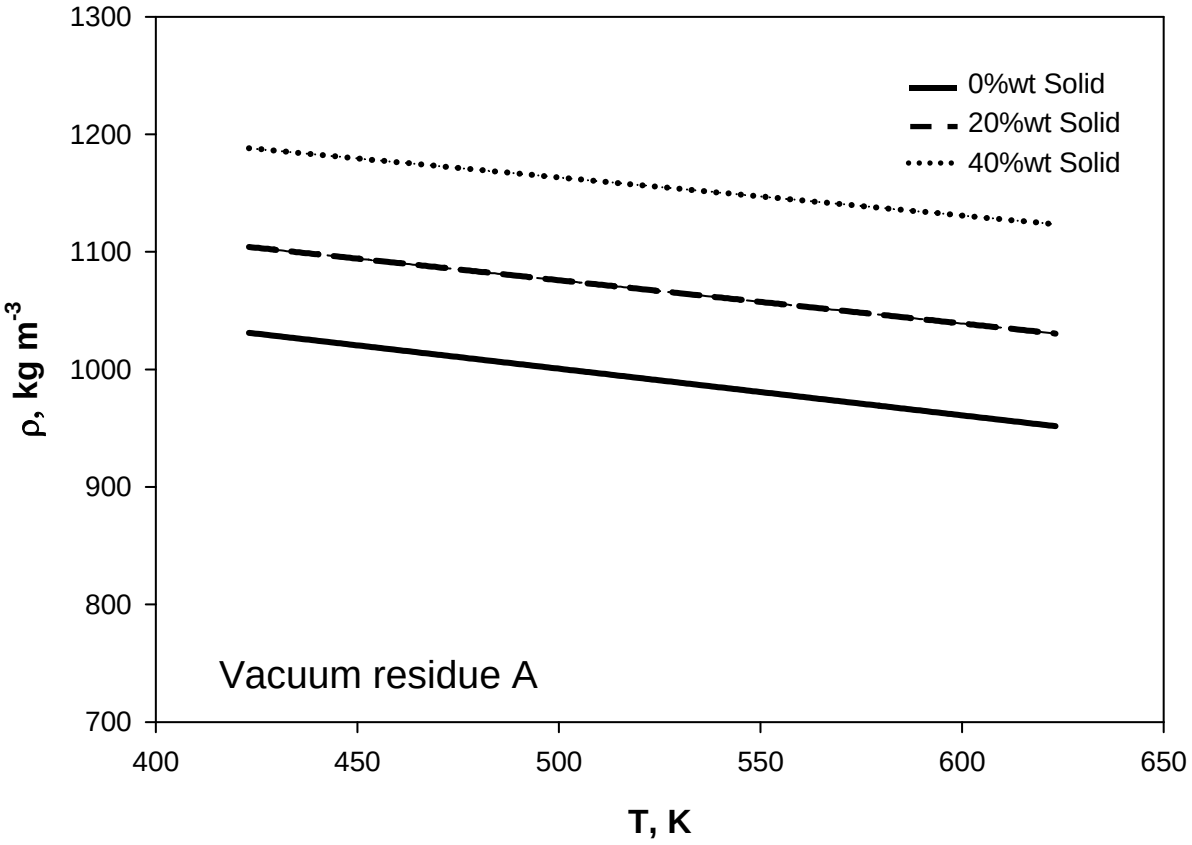

Figure 3.19. Effect of temperature on slurry density of vacuum residue A

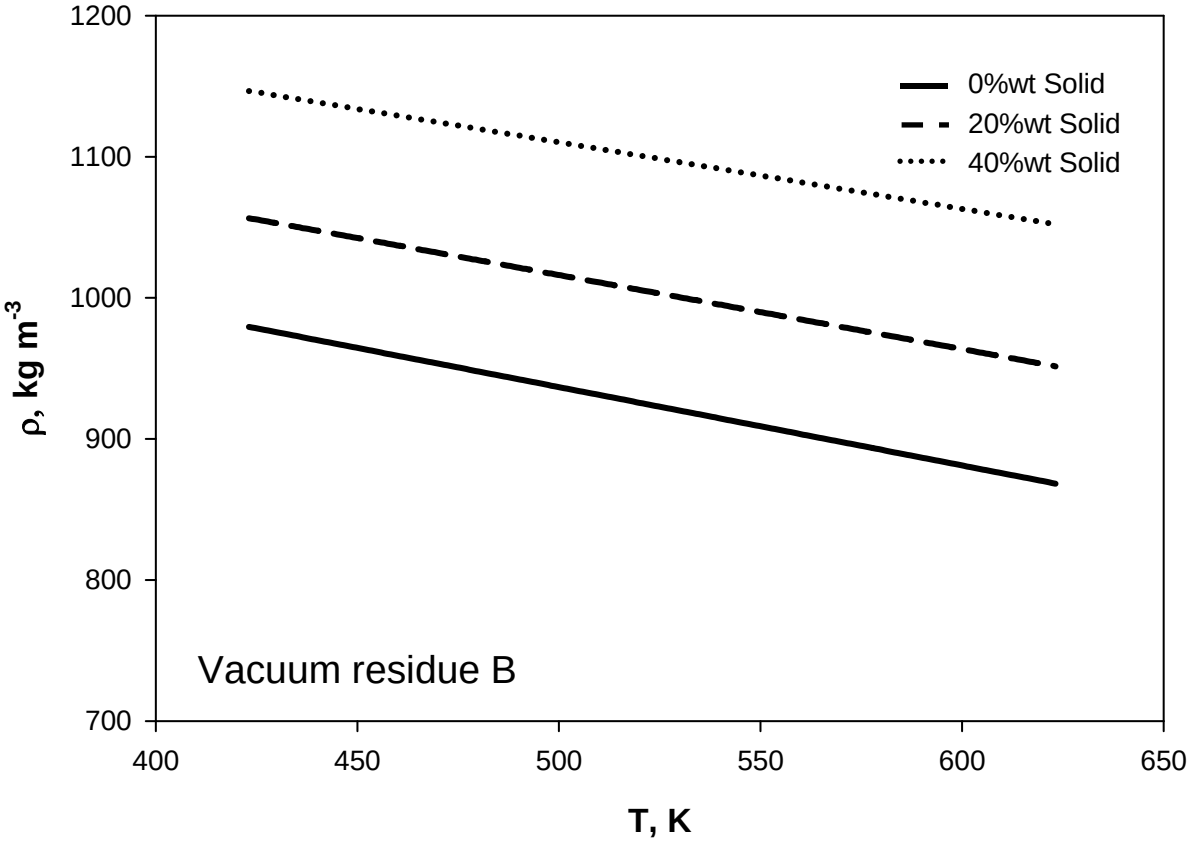

Figure 3.20. Effect of temperature on slurry density of vacuum residue B

3.4.2 Slurry viscosity

The equation proposed by Barnea et at.[84] (Equation (3-31)) was used to calculate the viscosity of the slurry since this equation had been developed using data for several different liquids (with densities from 848 to 1,585 kg m^{-3} and viscosities from 0.628 to 713 mPa.s), and it contains a wide range of solid concentrations and particle types (with densities from 1,603 to 10,792 kg m^{-3} and particle diameters from 0.0136 to 5.2 mm). Figure 3.21 shows the viscosity of residues A and B as a function of temperature with different activated carbon concentrations.

$$\mu_{SL} = \mu_L \exp\left(\frac{\frac{5}{3} C_V}{1 - C_V}\right) \tag{3-31}$$

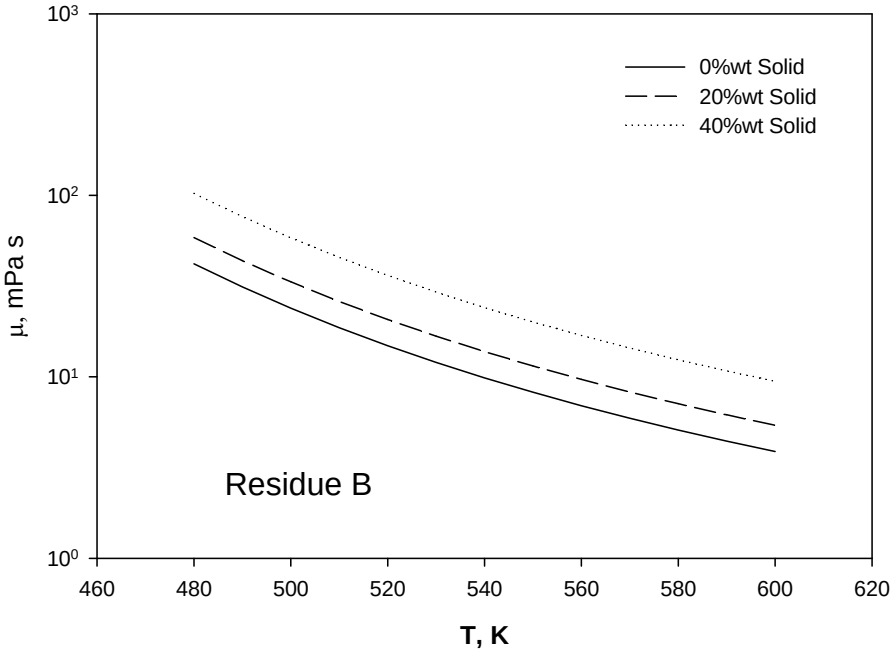

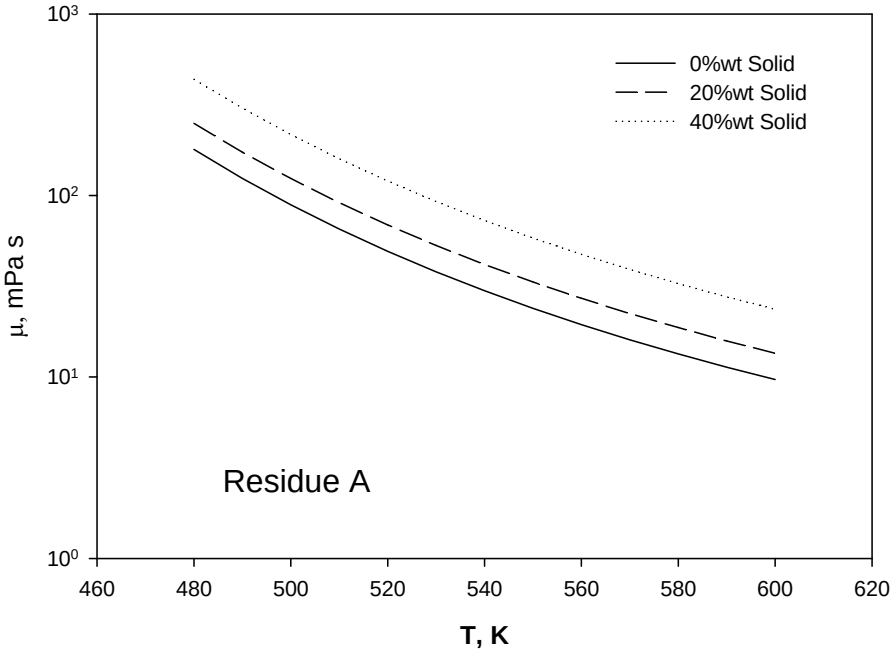

Figure 3.21. Effect of temperature on slurry viscosity of vacuum residues A and B

3.5 EXPERIMENTAL SETUP

The experimental setup used in this study, shown schematically in Figure 3.22, consists of the following main units: reactor, preheater, vacuum system, and data acquisition system. Details of these units are provided below.

Reactor:

The reactor is a 1-liter bolted autoclave manufactured by Autoclave Engineers, Inc. USA with an effective volume of 1.03×10^{-3} m^3 operating in a gas-inducing mode. The reactor is rated for a maximum working pressure of 375.76 bars at a maximum temperature of 728 K. The reactor dimensions are given in Table 3.9 and Figure 3.23. The reactor is equipped with four baffles located symmetrically in order to minimize or eliminate vortex formation. An internal cooling coil and an external heating jacket as well as heating tape and thermal insulation wrapped around the upper part of the reactor are used to achieve good temperature control. A hollow shaft connected to a 6 flat-blade impeller (Rushton Turbine) is used for mixing the liquid phase. Four holes 2.4 mm in diameter and drilled at both ends of the hollow shaft enable the reactor to be operated in a gas-inducing mode. The agitator is driven by a magnetic drive with enough capacity to avoid any eccentricity. Two thermocouples (K-type) and a Setra pressure transducer (model 205-2: 0-1000 psia) were used to measure and record the change of temperature and pressure in both the liquid and gas phases.

Preheater:

The preheater is a high-pressure bomb with an effective volume of 5.47×10^{-4} m^3. It is used to heat the gas to a desired temperature before it is charged into the reactor. It was maintained at the desired temperature by a furnace with an automatic temperature controller manufactured by Lindberg, USA. A radiation shielded K-type thermocouple was used to measure the temperature,

and a pressure transducer (model 205-2: 0-1000 psia) from Setra Inc. was used to record the pressure.

Table 3.9. Reactor dimensions

Reactor's inside diameter, d_T	76(*)
Reactor's outer diameter	111
Impeller diameter	31.75
Baffle width ($1/10^{th}$ of d_T)	7.6
Number of baffles	4
Reactor's construction material	316 SS
Shape	Cylindrical
Lower impeller clearance from the bottom	45
Length of hollow shaft	178
Number of impellers	1
Number of blades	6
Impeller type	Flat blade disk turbine
Diameter of shaft hole"	2.4
Reactor's internal depth	238
Reactor volume	1.03 Liter

(*) *all dimensions are in mm unless stated otherwise*

The Vacuum System:

A HYVAC-14, 2-stage mechanical vacuum pump from CENCO, Chicago, Illinois, USA was used to vacuum the entire system. The vacuum pump was used to degas the reactor and the entire system before the start of the experiment. A Jerguson sight-window liquid trap was placed between the reactor and the vacuum pump to prevent liquid from entering into the vacuum system and to be able to monitor any possible liquid loss. The outlet of the vacuum pump was vented directly into a fume hood.

Data Acquisition System:

Data on the temperatures and pressures from the thermocouples and pressure transducers was acquired online using National Instrument data acquisition modules NI cDAQ-9172 (NI9211 and NI9215) connected to a personal computer (PC). The National Instrument LabView 8.2 software

was also used to monitor the entire process and record the temperatures and pressures within the system. Figure 3.24 shows a photograph of the complete set-up.

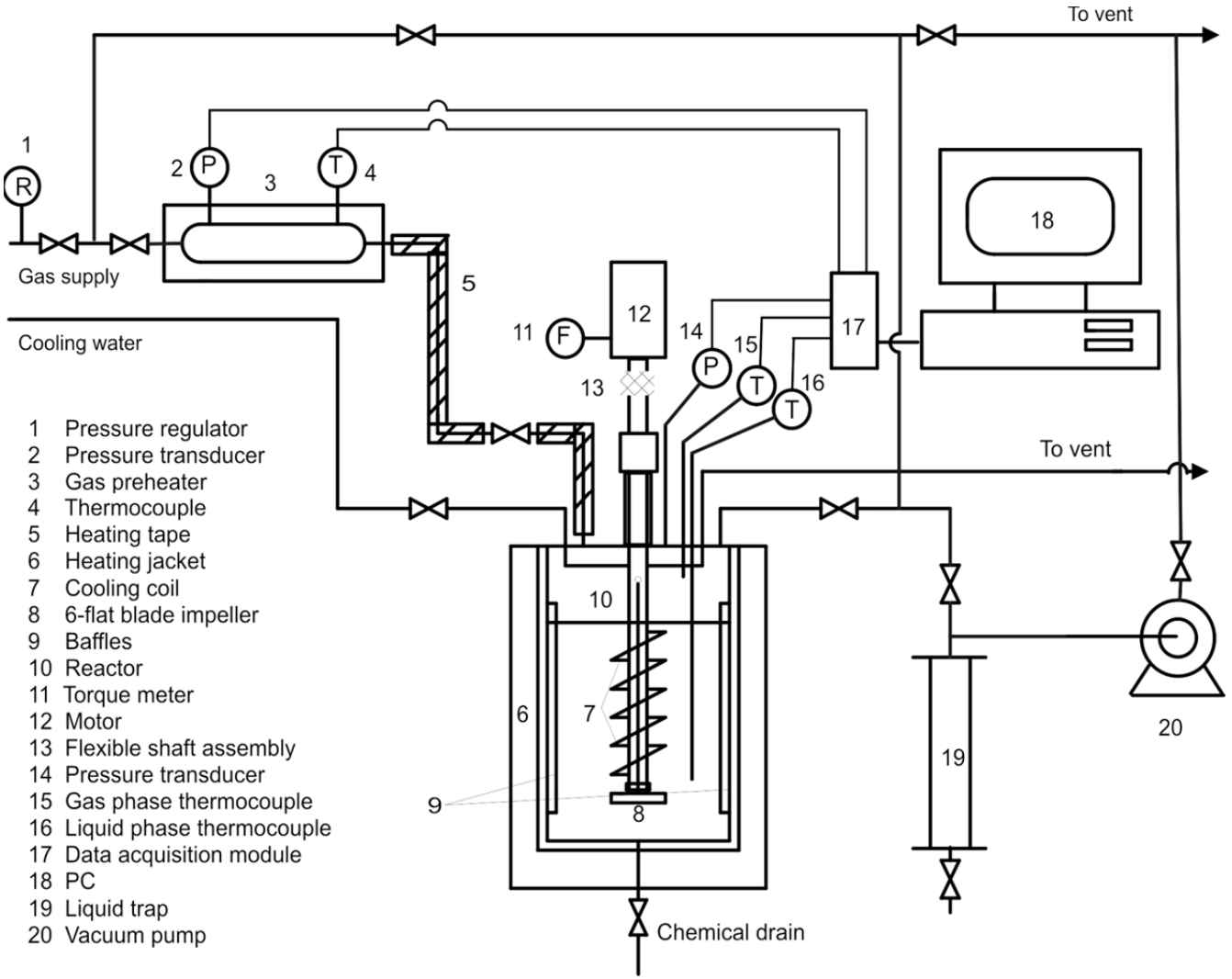

Figure 3.22. Schematic diagram of experimental setup

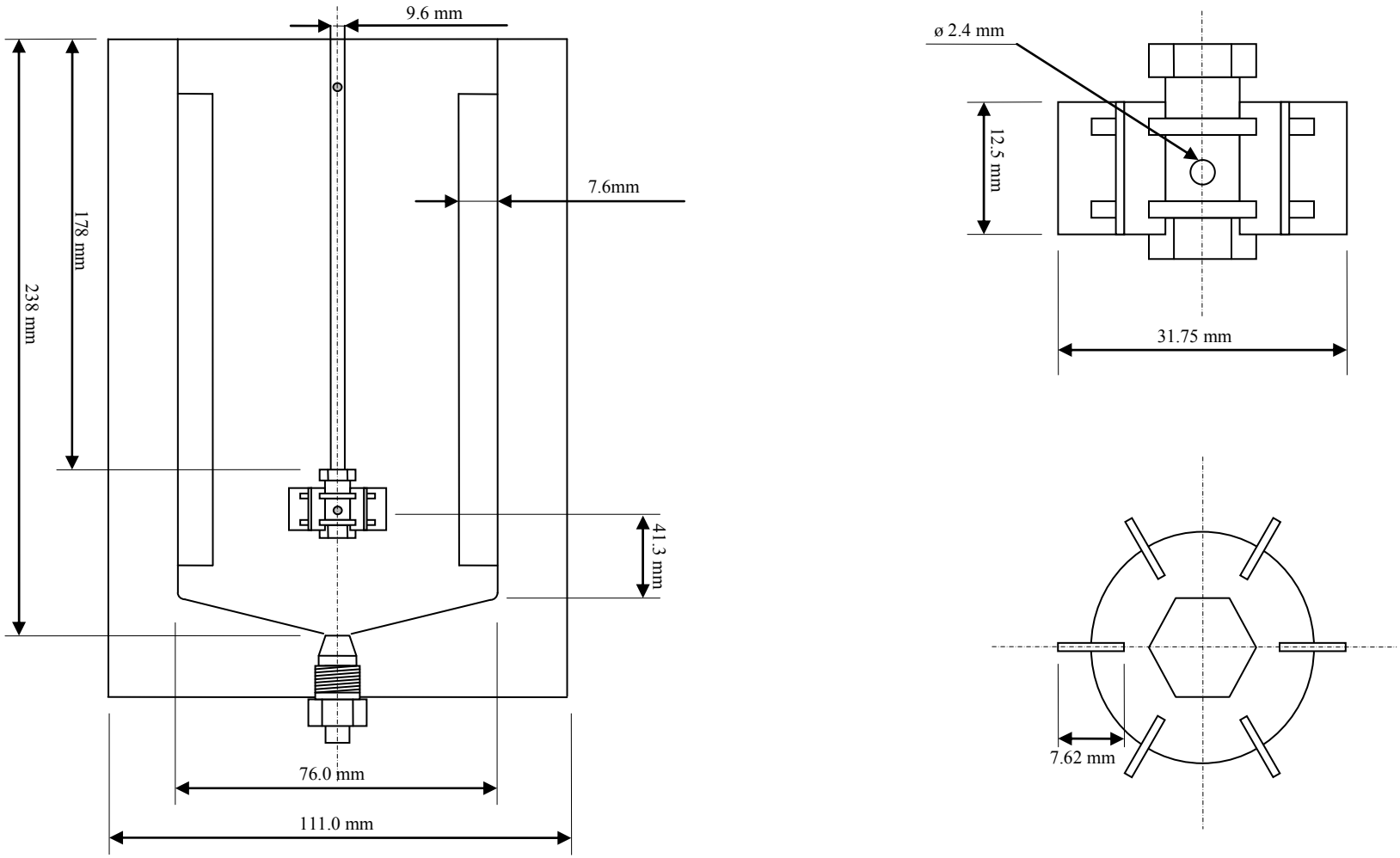

Figure 3.23. Reactor dimensions and details of impeller

Figure 3.24. Photograph of experimental set-up

3.6 OPERATING CONDITIONS

The gas-liquid-solid system and the operating conditions used in this study are tabulated below.

Table 3.10. Range of the operating conditions

Gas	H_2
Liquids	Vacuum residues A and B, paraffins mixture, and Sasol wax
Solid	Activated carbon
Pressure	27.5-55 bar
Temperature	423-623 K
Mixing speed	1200-2000 rpm
Solid concentration	0-40 wt.%
Reactor operating mode	GIR

3.7 OPERATING THE REACTOR IN 3-PHASE SYSTEM GAS- INDUCING MODE

The reactor was operated in the presence of two-phase (gas-liquid) and 3-phase (gas-liquid-solid) systems. As mentioned above, the shaft in the reactor has two holes in both the liquid-phase and the gas-phase, allowing the gas to be induced in the liquid or at certain mixing speeds. Under these conditions, the reactor is operating as a Gas-Inducing Reactor (GIR) as depicted in Figure 3.25.

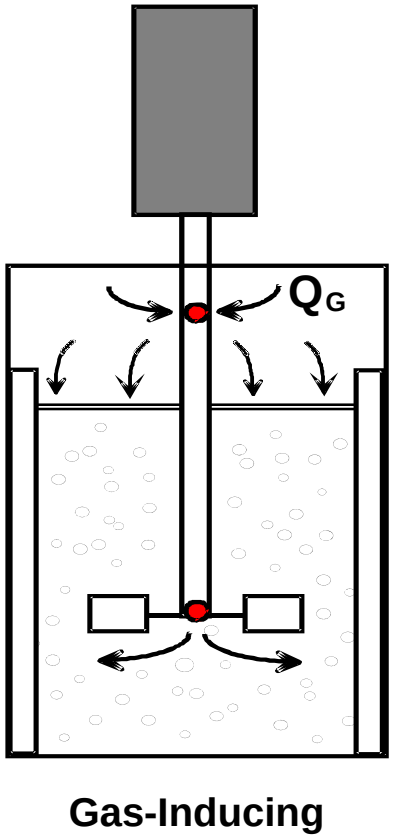

Figure 3.25. Gas-Inducing Reactor (GIR)

When mixing speed is gradually increased, the local pressure created underneath the impeller steadily decreases, eventually reaching the critical mixing speed for gas induction. At this specific mixing speed, the gas bubbles overcome the hydrostatic head of the liquid or slurry and are induced through the holes on the hollow shaft into the slurry. Thus, the knowledge of the critical mixing speed for gas induction, $N_{CRI,}$ is essential to operate the reactor in a gas-inducing mode.

Using 2-phase systems, Lemoine et al.[85] proposed the following correlation to predict the critical mixing speed for gas induction:

$$\frac{N_{CRI}^2 d_{imp.}}{g} = 0.512 \times \left(\frac{\mu_L}{\mu_{Water}}\right)^{0.146} \left(\frac{\sigma_L}{\sigma_{Water}}\right)^{-0.180} \left(\frac{\rho_L}{\rho_{Water}}\right)^{-0.265} \left(\frac{H_L}{d_T}\right) \tag{3-32}$$

The physical properties in this correlation are measured at the actual operating temperature for the liquid, but at the ambient temperature for water. This correlation was developed using various reactor sizes (up to 1.5 m) and for different gas-liquid systems.

In 3-phase systems, Zwietering[86] proposed the following correlation to predict the critical mixing speed necessary for solid suspension. This critical mixing speed is defined as the speed needed for no particles to remain settled at the bottom of the reactor for more than 2 seconds.

$$N_{suspension} = \frac{s\nu^{0.1} d_p^{0.2} \left(g\Delta\rho / \rho_L\right)^{0.45} C_V^{0.13}}{d_{imp.}^{0.85}} \tag{3-33}$$

In this correlation, ν is the kinematic viscosity, $\Delta\rho$ is the density difference between the solid phase and the liquid phase, and s is a dimensionless coefficient that depends on the reactor design ($d_T/d_{imp.}$ ratio).

Zwietering's correlation has been modified by several researchers [87-91] to account for different reactor and impeller geometries, including different liquid-solid systems or for multiple impellers. However, this correlation was developed for liquid-solid systems only and does not account for any effects of the gas phase induced into the liquid. Recent work by Murugesan[92] suggests that gas bubbles might increase the critical mixing speed for solid suspension.

3.8 EXPERIMENTAL PROCEDURE

The multi-step transient physical gas absorption (TPGA) method was used to obtain the equilibrium solubility (C^*) and the volumetric liquid-side mass transfer coefficient (k_La) for H_2

in vacuum residues A and B, as well as in the liquid mixtures within the operating conditions listed earlier. This experimental method was similar to that previously employed by Chang et al.[93-95], Tekie et al. [96, 97], Fillion [98], Martinez [99], Alghamdi [100], Lemoine [101], and Soriano [77]. The experimental procedure is described below:

1. A predetermined amount of vacuum residue or liquid mixture was charged into the reactor at 393 K (the temperature at which the residues became a viscous liquid).
2. The reactor was closed and the system was checked for leaks. Then the entire system was degassed using the vacuum pump.
3. The temperature in the reactor was kept at 393 K, and it was again degassed to remove the gas trapped in the liquid residue.
4. Hydrogen was charged into the preheater.
5. Both the reactor and preheater were heated to the desired temperature to eliminate any thermal gradient between the liquid and gas phases.
6. The data acquisition system recorded and stored the pressure and temperature of the gas and liquid phases in the reactor and the preheater as a function of time.
7. Hydrogen was then charged into the reactor until the desired pressure was reached without any mixing.
8. The reactor content was stirred at a predetermined mixing speed until the thermodynamic equilibrium was reached, indicated by a constant final reactor pressure. The decrease in reactor pressure was recorded as a function of time.
9. The data acquisition for the reactor and preheater was stopped.
10. Steps 5 through 8 were repeated to collect multiple data points at different pressure ranges under the same temperature, as shown in Figure 3.26.

This experimental procedure was followed for each set of operating conditions.

3.9 CENTRAL COMPOSITE STATISTICAL DESIGN OF EXPERIMENTS

A statistical design of experiments similar to that employed earlier by Tekie et al.[102] and Alghamdi[100] was used in this study. The advantage of the current approach is that it allows reliable investigation of the effect of the operating variables on the parameter studied, in this case on the liquid-side mass transfer coefficient (k_La), using a small number of experiments. Also, the statistical correlations produced with this method generally warrant a high degree of confidence. In this study, the effect of 4 variables (temperature, pressure, mixing speed and solid concentration) at three levels on k_La was investigated. In this technique, for k independent variables at 3 levels, the total number of experiments is 2^k factorial points, augmented by $2\times k$ axial points, and with a number of replicates at the central point based on Equation (3-34) in order to create a design with uniform precision.

$$N_{Central} = \gamma \times \left(\sqrt{N_F} + 2\right)^2 - N_F - 2 \times k \tag{3-34}$$

$N_{Central}$ is the number of replicates at the central point, N_F the number of factorial points, and γ is defined by the following equation:

$$\gamma = \frac{(k+3) + \sqrt{9k^2 + 14k - 7}}{4 \times (k+2)} \tag{3-35}$$

The factorial and axial points are equidistant from the central point to offer the property of rotatability to the design.

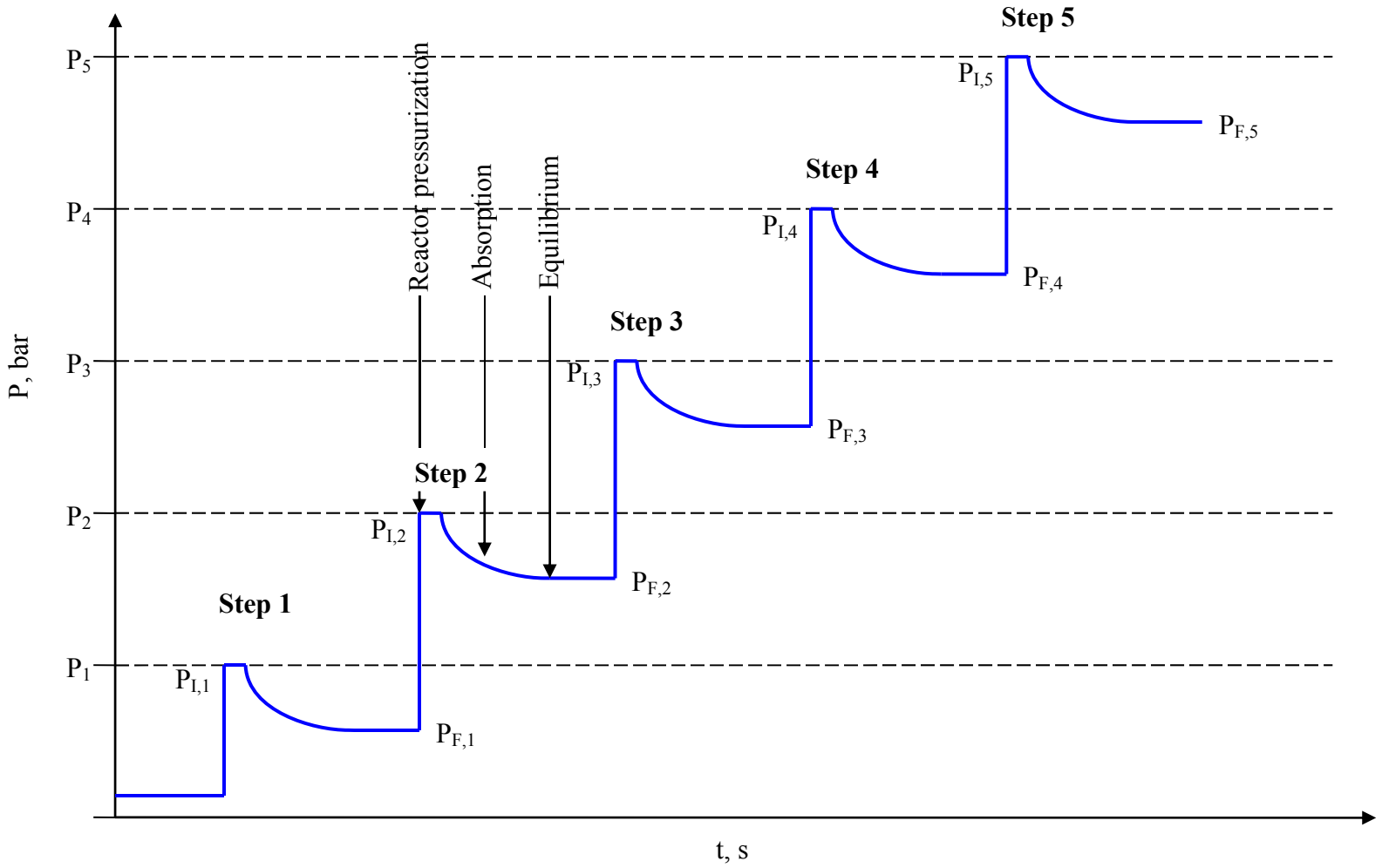

Figure 3.26. Schematic of multi-step procedure at constant temperature

The central composite matrix design is made rotatable by setting the axial point values as follows:

$$\alpha = \sqrt[4]{\left(2^k\right)} \tag{3-36}$$

In which k = 4, $N_{Central} = 7$, $N_F = 16$ and $\alpha = 2$.

The coded variables x_i (i = 1, 2, 3, 4) as defined by Equation (3-37) were used in the distribution and analysis of the experiments.

$$x_i = 2\left[\frac{2X_i - \left(X_{i,L} + X_{i,H}\right)}{X_{i,H} - X_{i,L}}\right] \tag{3-37}$$

where X_i is the value of the i^{-th} variable, $X_{i,L}$, and $X_{i,H}$ are the lowest and highest levels of X_i. The distribution of experiments for $k = 4$ can be mathematically represented by equation:

$$\sum_{i=1}^{4} X_i^2 = \left(\sqrt[4]{N_F}\right)^2 = 2^2 \tag{3-38}$$

Table 3.11 shows the coded values for the variables. The distribution of experiments over the range of the study is shown in Figure 3.27.

Conventionally, experimental data obtained using the 2k central composite design is correlated using the quadratic response surface model given in Equation (3-39):

$$ln(Y_{Pred.}) = \beta_0 + \sum_{i=1}^{n}(\beta_i x_i) + \sum_{i=1}^{n}\sum_{j=1}^{n}(\beta_{ij} x_i x_j) \tag{3-39}$$

where x_i is the coded variable, β_0, β_i and β_{ij} are constants, and n is the number of variables.

Table 3.11. Values and coded variables for statistical composite design

Variable	Coded Variable (x_i)	Value of Coded Variables		
		1	0	1
P, bar	x_1	27	41	55
N, rpm	x_2	1200	1600	2000
T, °C	x_3	200	250	300
C_s, wt.%	x_4	0	20	40

P: Pressure

T: Temperature

N: Mixing speed

C_S: Solid concentration

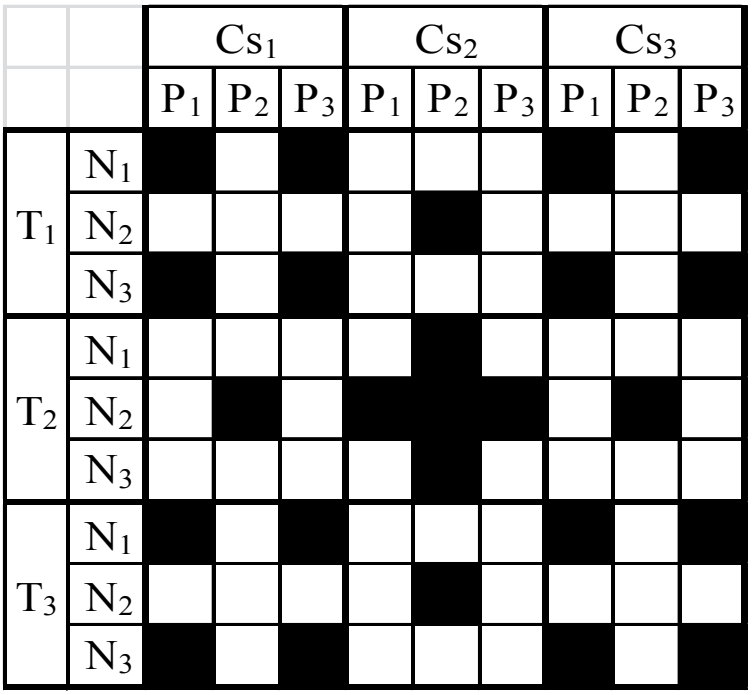

Figure 3.27. Distribution of experiments based on central composite statistical design

3.10 CALCULATION PROCEDURE

The equilibrium solubility (C^*) for hydrogen in the vacuum residues A and B and liquid mixtures were calculated from the steady-state portion of the pressure decline (pressure vs. time) curve, whereas the volumetric liquid-side mass transfer coefficient, k_La, was obtained from the

transient portion of the same curve. The calculations were performed by mass balances on the preheater and the reactor and using the Peng-Robinson Equation of State (PR-EOS).

The following assumptions were made in order to calculate C^* and k_La:

1. The gas-phase (H_2) in the preheater and reactor behaves as a non-ideal gas and the Peng-Robinson Equation of State (PR-EOS) is applicable.
2. The gas and liquid (molten vacuum residues A or B and liquid mixtures) phases are well mixed, resulting in homogeneous concentrations for each phase.
3. No gas absorption occurs prior to mixing.
4. The liquid volume is constant.
5. The vapor-phase pressure exerted by the liquid is negligible when compared with the total pressure in the reactor, and accordingly, the mass transfer resistance in the gas phase (k_G) is negligible.

3.10.1 Peng-Robinson Equation of State

The Peng-Robinson Equation of State was used to calculate the number of moles of gas in the preheater before and after the reactor was charged, and to calculate the number of moles remaining in the reactor after gas absorption. A general form of the PR-EOS is written as:

$$P = \frac{RT}{v - b} - \frac{a(T)}{v(v + b) + b(v - b)} \tag{3-40}$$

This equation can be expressed in terms of the compressibility factor, Z as:

$$Z^3 - (1 - B)Z^2 + (A - 3B^2 - 2B)Z - (AB - B^2 - B^3) = 0 \tag{3-41}$$

where:

$$A = \frac{aP}{R^2T^2} \tag{3-42}$$

$$B = \frac{bP}{RT} \tag{3-43}$$

For a single-component, one-phase system, the solution of Equation (3-41) results in three real roots or one real and two imaginary roots. The real root is represents the gas-phase. At the critical point:

$$a(T_C, P_C) = 0.45724 \frac{R^2 T_C^2}{P_C} \tag{3-44}$$

$$b(T_C, P_C) = 0.07780 \frac{R T_C}{P_C} \tag{3-45}$$

At any temperature:

$$a(T) = a(T_C, P_C)\alpha(T_r, \omega) \tag{3-46}$$

$$b(T) = b(T_C) \tag{3-47}$$

where:

$$\alpha^{1/2} = 1 + \kappa(1 - T_r^{1/2}) \tag{3-48}$$

and $T_r = T / T_c$

$$\kappa = 0.37464 + 1.5422\,\omega - 0.26992\omega^2 \tag{3-49}$$

Equation (3-41) was used to calculate the number of moles of gas before and after absorption in the liquid-phase in order to calculate the gas solubility.

3.10.2 Calculation of equilibrium solubility, C*

The equilibrium gas solubility (C^*) is defined as the number of moles of gas (H_2) absorbed into the liquid (molten vacuum residues B or A), or liquid mixtures at equilibrium, and can be defined as:

$$C_i^* = \frac{n_i}{V_L} \tag{3-50}$$

The solubility of H_2 in the liquid phase was calculated using the initial and final moles of hydrogen in the gas phase as follow:

$$C_i^* = \frac{n_{i,I} - n_{i,F}}{V_L} \tag{3-51}$$

where $n_{i,I}$ is the initial number of moles of the gaseous species (i) in the reactor prior to absorption and $n_{i,F}$ is the number of moles of the gaseous species (i) remaining in the reactor at thermodynamic equilibrium. $n_{i,I}$ and $n_{i,F}$ are calculated as follows:

$$(n_{i,I})_{step1} = \frac{V_G}{Z_{i,I} R T_I} (P_{i,I})_{step1} \tag{3-52}$$

(3-53)

where T_I is the initial temperature before the absorption begins and T_F is the final temperature of the gas phase after thermodynamic equilibrium is reached.

When the multi-step procedure is used, any new step will have to take into account the number of moles of gas already absorbed during the preceding steps. For example for step 2, Equations (3-52) and (3-53) are modified as follows:

$$(n_{i,I})_{step2} = \frac{V_G}{Z_{i,I} R.T_I} (P_{i,I})_{step2} + (n_{i,I} - n_{i,F})_{step1} \tag{3-54}$$

$$(n_{i,F})_{step2} = \frac{V_G}{Z_{i,F} R.T_F}(P_{i,F})_{step2} \tag{3-55}$$

The volume of the gas phase, V_G, is calculated by subtracting the liquid volume from the total reactor volume as follows:

$$V_G = V_R - (\frac{m_L}{\rho_L}) \tag{3-56}$$

In the above equation, m_L and ρ_L are the mass and density of the liquid, respectively. The solubility, C^*, is then obtained by substituting Equations (3-52) or (3-53) and (3-54) into Equation (3-51).

3.10.3 Calculation of the volumetric liquid-side mass transfer coefficient, k_La

The hydrogen volumetric mass-transfer coefficient (k_La) was calculated using the Transient Physical Gas Absorption technique. During the absorption of hydrogen into the liquid (molten residues A, B, or liquid mixtures), the decline of reactor pressure was recorded as a function of time until equilibrium was reached.

The rate of mass transfer of H_2 into the residue can be calculated using the two-film model as:

$$\frac{dn_{i,L}}{dt} = k_L a_i (C^* - C_{i,L}) V_L \tag{3-57}$$

The rate of solute gas uptake by the liquid can be related to the decline in pressure as a function of time using a differential form of the general gas law shown in Equation (3-58) below:

$$\frac{dn_{i,L}}{dt} = -\frac{V_G}{ZRT}\frac{dP_{i,t}}{dt} \tag{3-58}$$

$C_{i,L}$, the bulk concentration of the solute gas in the liquid, can be expressed as follows:

$$C_{i,L} = \frac{V_G}{ZV_L RT}(P_{i,I} - P_{i,t}) \tag{3-59}$$

When the gas solubility at constant temperature is a linear function of pressure, Henry's law can be applied as:

$$He = \frac{P_{i,t}}{C*} \tag{3-60}$$

Substituting Equations (3-58), (3-59), and (3-60) into Equation (3-57) yields the following equation:

$$-\frac{V_G}{ZRT}\frac{dP_{i,t}}{P_{i,t}(\frac{V_L}{He}+\frac{V_G}{ZRT})-\frac{V_G P_{i,I}}{ZRT}} = k_L a dt \tag{3-61}$$

Let $Y = P_{i,t}(\frac{V_L}{He}+\frac{V_G}{ZRT})-\frac{V_G P_{i,I}}{ZRT}$; this gives $dY = dP_{i,t}(\frac{V_L}{He}+\frac{V_G}{ZRT})$

By integrating between the limits of P_I at t = 0 and $P_{i,\,t}$ at any time (t), the following relationship can be obtained:

$$\ln\left[\frac{P_{i,t}(\frac{V_L}{He}+\frac{V_G}{ZRT})-\frac{V_G P_{i,I}}{ZRT}}{\frac{P_{i,I}V_L}{He}}\right] = -[\frac{V_L ZRT}{V_G He}+1]k_L a.t \tag{3-62}$$

By multiplying the numerator and denominator on the left-hand-side of Equation (3-62) by (ZRT/V_G) and then rearranging the equation, the following relationship can be obtained:

$$\ln\left[\frac{P_{i,t}(\psi+1)-P_{i,I}}{\psi P_I}\right] = -[\psi+1]k_L a.t \tag{3-63}$$

The function ψ is defined as $\psi = (V_L\, ZRT/V_G\, He)$.

At equilibrium, the final equilibrium concentration, $C^*_{eq,}$ is defined as follows:

$$C_{eq}^{*} = \frac{V_G}{V_L ZRT}(P_{i,I} - P_{i,F}) \tag{3-64}$$

C^*_{eq} can also be expressed as:

$$C_{eq}^{*} = \frac{P_{i,F}}{He} \tag{3-65}$$

By equating Equations (3-64) and (3-65), one can obtain:

$$\frac{P_{i,I} - P_{i,F}}{P_{i,F}} = \frac{V_L ZRT}{HeV_G} = \psi \tag{3-66}$$

By substituting Equation (3-66) into (3-63) and multiplying the left-hand-side of Equation (3-63) by $(P_{i,F}/P_{i,I})$, the following working equation can be obtained:

$$\frac{P_{i,F}}{P_{i,I}} \ln\left[\frac{P_{i,I} - P_{i,F}}{P_{i,t} - P_{i,F}}\right] = k_L at \tag{3-67}$$

If k_La is a constant, Equation (3-67) becomes a linear function of time and can be written as:

$$F(t) = k_L at \tag{3-68}$$

If the left side of Equation (3-68) is plotted against time, and a linear relationship is obtained, the slope of the line will be k_La.

4.0 RESULTS AND DISCUSSION

The solubility (C^*) and the liquid-side volumetric mass transfer coefficients (k_La) for H_2 were measured in the following four liquids: 1. vacuum residue A; 2. vacuum residue B; 3. mixtures of vacuum residue B + paraffins; and 4. vacuum residue B + paraffins + wax. The measurements were based on Central Composite Statistical Design (CCSD). The experiments were performed under the following operating conditions: temperature (473 K to 573 K), pressure (27.5 bars to 55.0 bar), mixing speed (1200 rpm to 2000 rpm), and solid concentration (0 wt. % to 40 wt. %.). The error analysis of C^* and k_La as well as some numerical examples are provided in Appendix B.

4.1 EQUILIBRIUM SOLUBILITY OF H2 IN A AND B VACUUM RESIDUES AND LIQUID MIXTURES

In this section, the solubilities for H_2 in the four liquids, expressed in mol kg^{-1} are presented as a function of equilibrium H_2 partial pressure ($P_{i,F}$). Figure 4.1 and 4.2 show the reproducibility of C^* for H_2 in the residues A and B; and liquid mixtures, respectively; with an AAER of less than 12%.

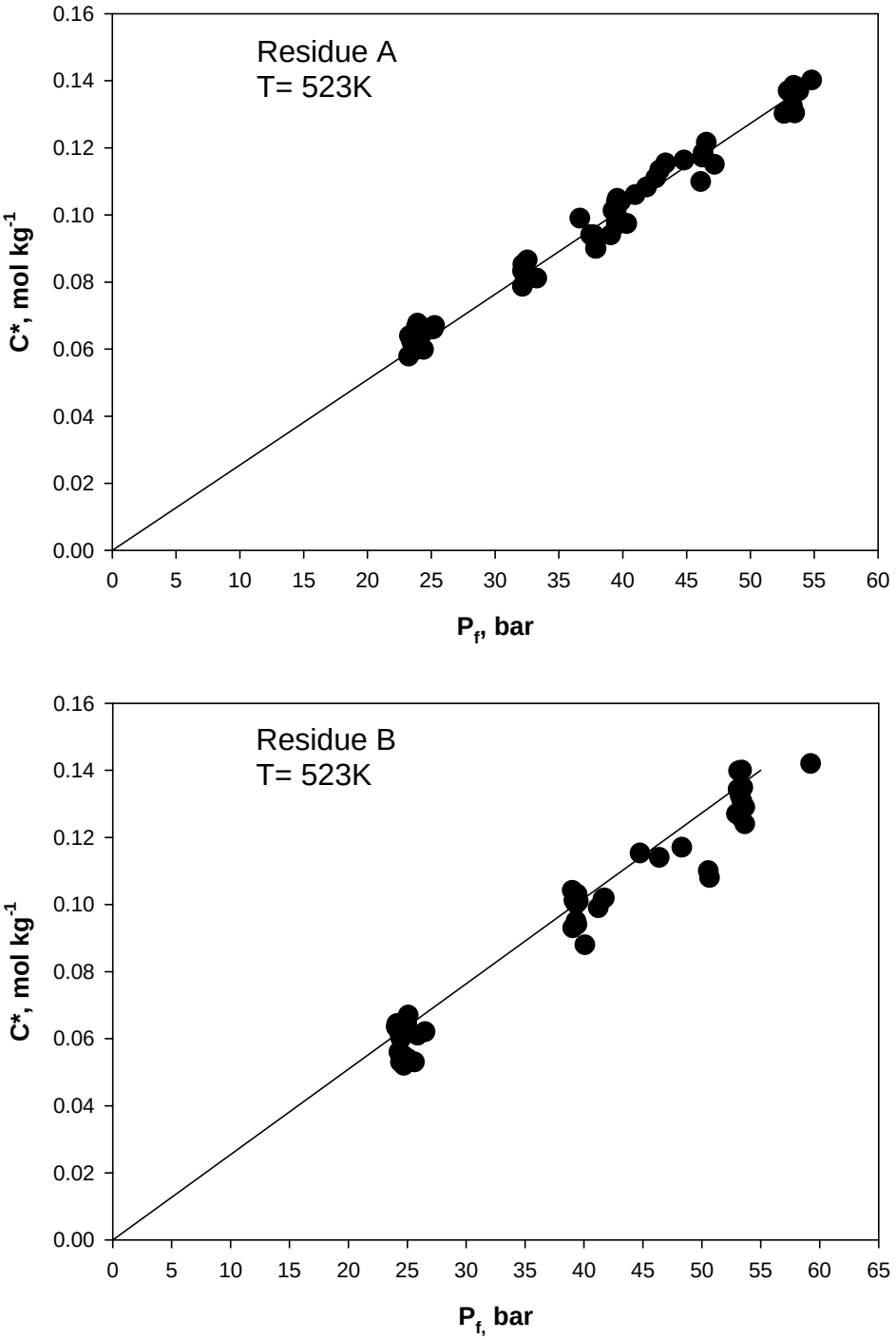

Figure 4.1. Reproducibility of *C** values for residues A and B

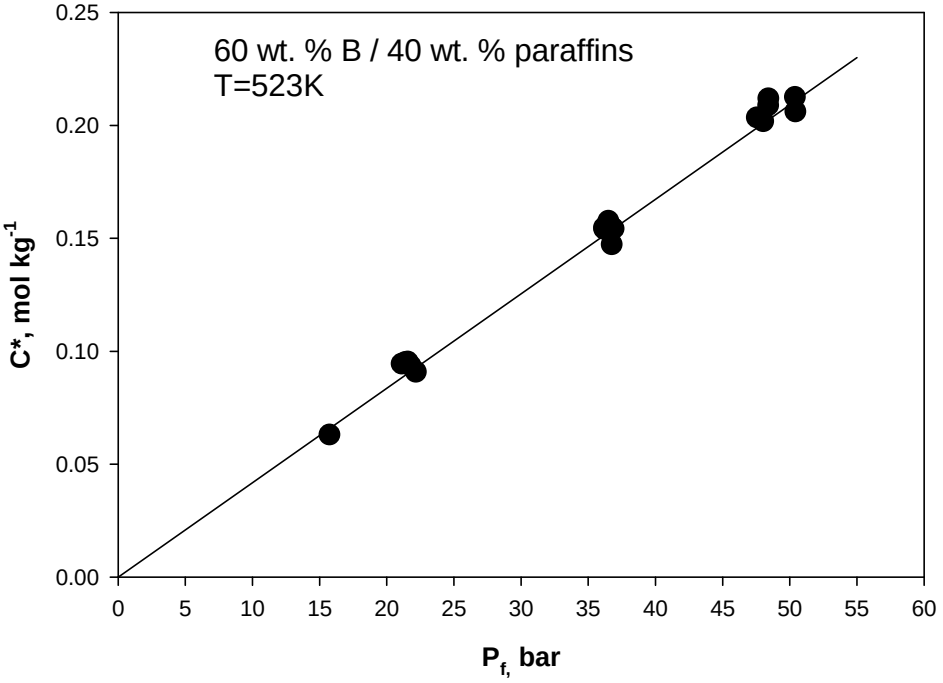

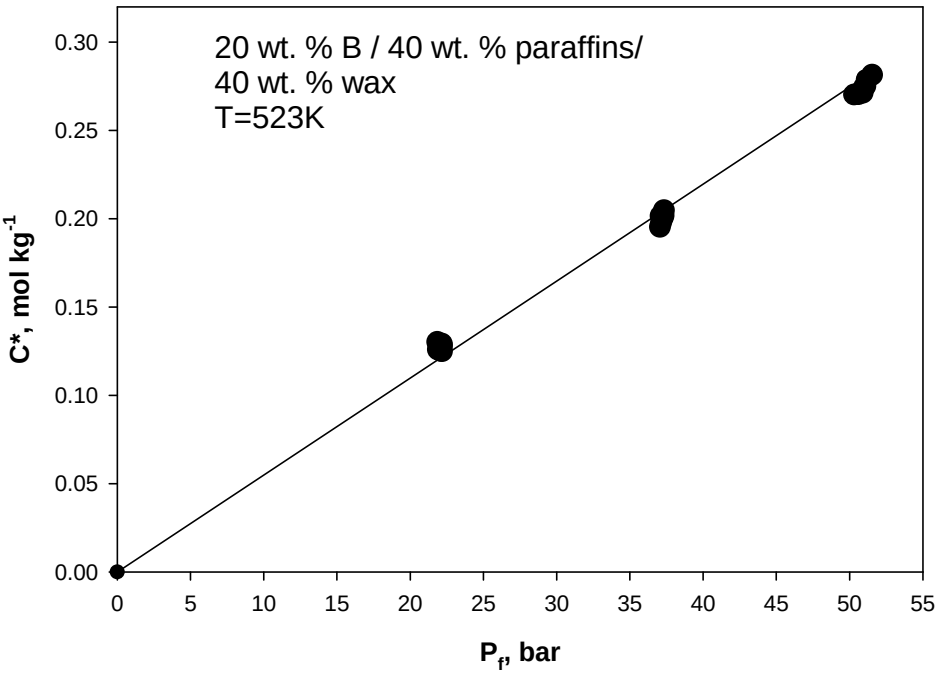

Figure 4.2. Reproducibility of *C** values for liquid mixtures

4.1.1 Effect of pressure and temperature on C*

Within the range of operating conditions used, the H_2 solubilities in the four liquids appear to increase linearly with pressure at a constant temperature; as can be seen in Figure 4.3 and 4.4. Similar result were obtained by both Cai et al.[79] in heavy virgin gas oil, bitumen, vacuum bottoms and atmospheric residue, as well as by Lal et al. [103] in bitumen. The obtained solubility data can be modeled using Henry's law, expressed as:

$$C^* = \frac{P_{i,F}}{He} \tag{4-1}$$

Where He is the Henry's law constant and $P_{i,F}$ is the partial pressure of H_2 in the reactor at thermodynamic equilibrium.

This increase of H_2 solubility with pressure can be related to the increase in the concentration difference (driving force) between the gaseous and the liquid phases when the system pressure increases. This solubility behavior is consistent with a number of earlier findings available in the literature[103, 104]. Also, similar results were reported in the literature[23, 95, 100, 105-107] for different gas-liquid systems. This behavior is not surprising since the mass fraction of hydrogen in the liquid-phase is low even at elevated pressures. Typical reported values range from 0.001 moles of hydrogen/kg of liquid/100 kPa at room temperature to 0.01 moles of hydrogen/kg of liquid/100 kPa under processing conditions [104].

Table 4.1 includes the calculated values of Henry's Law constant, listed as a function of temperature, along with their corresponding regression coefficients (R^2).

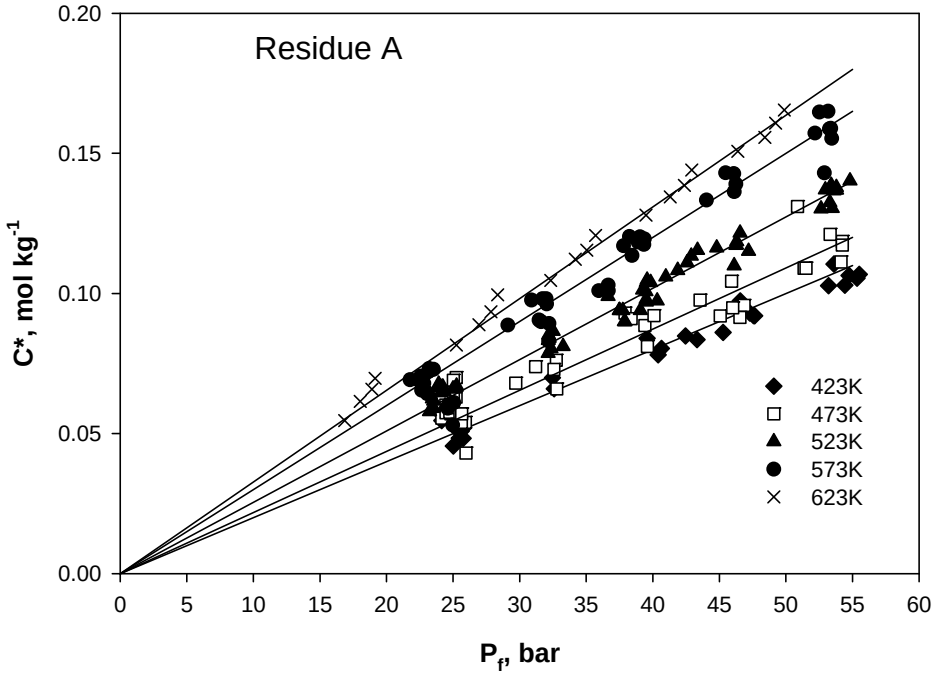

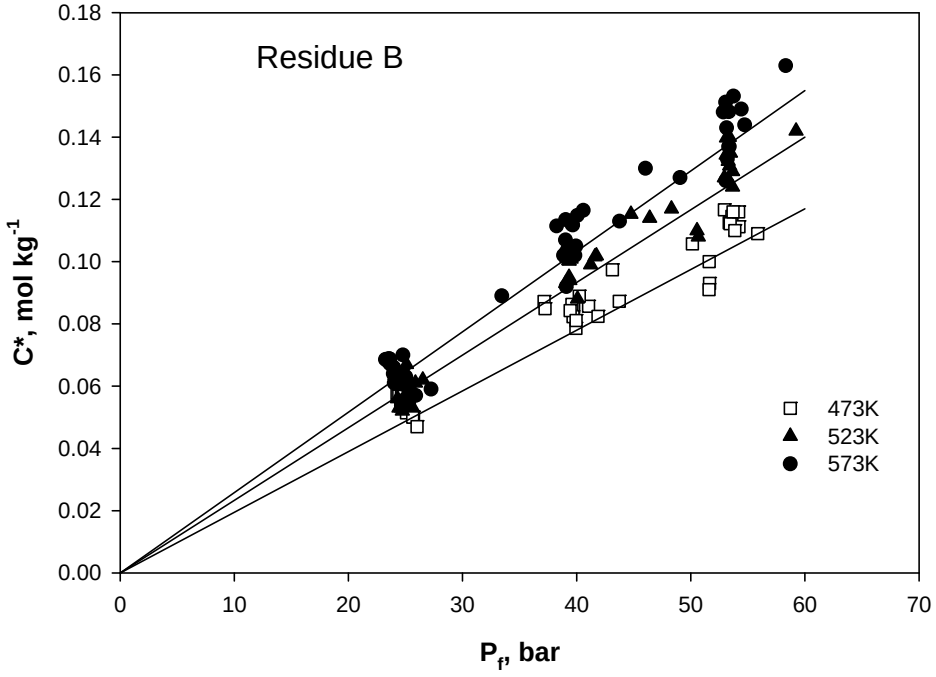

Figure 4.3. Effect of pressure and temperature on solubility of H_2 in vacuum residues A and B

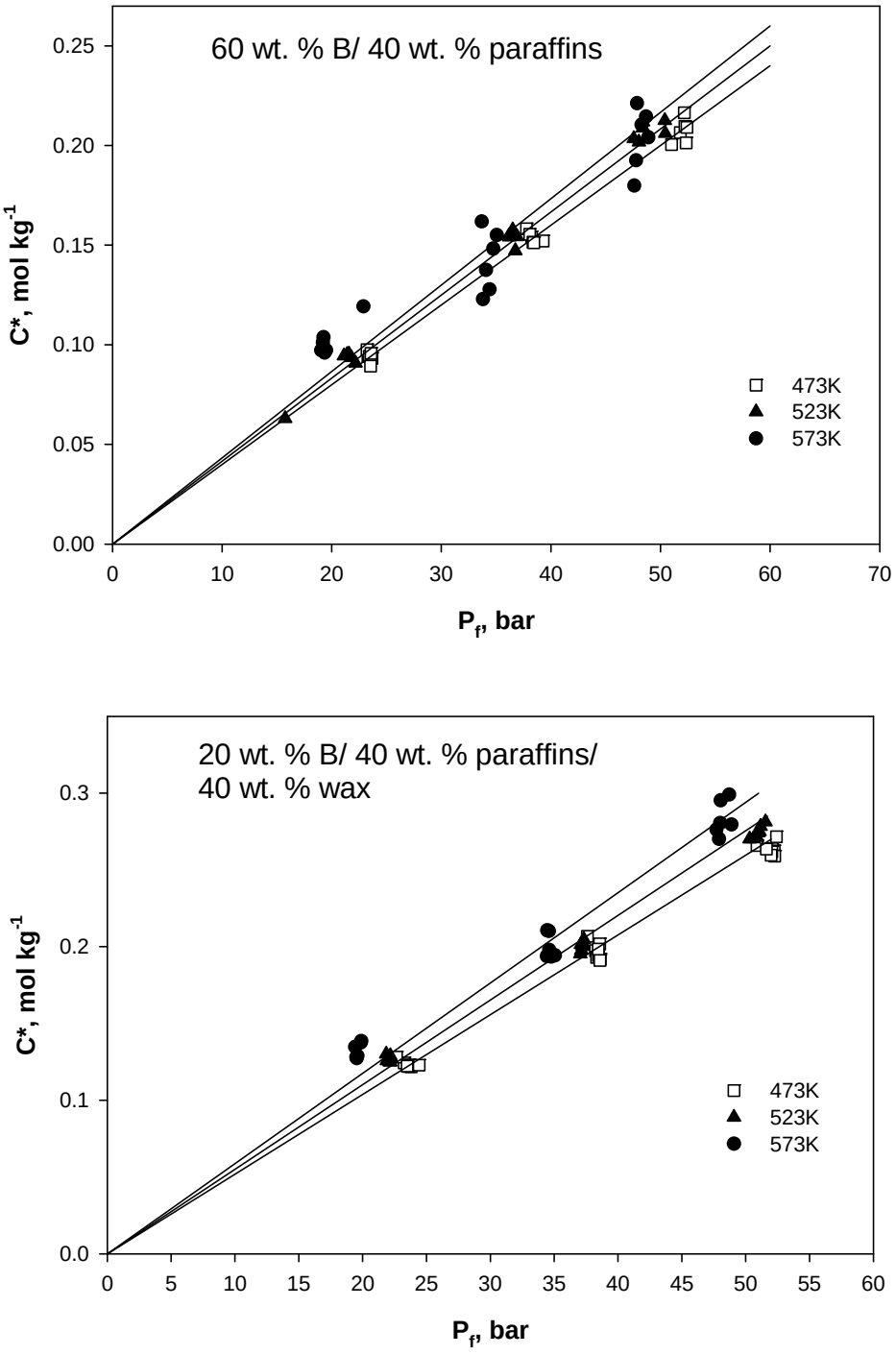

Figure 4.4. Effect of pressure and temperature on solubility of of H_2 in liquid mixtures

Table 4.1. Henry's Law constants of H_2 as a function of temperature

	T, K	*He, bar kg mol^{-1}*	R^2
Residue A	425	500	0.98
	474	455	0.95
	523	385	0.98
	574	333	0.99
	620	303	0.99
Residue B	472	476	0.99
	525	400	0.99
	575	357	0.99
60 wt. % B/ 40 wt. % paraffins	473	250	0.99
	523	238	0.99
	573	238	0.88
20 wt. % B/ 40 wt. % paraffins/ 40 wt. % Sasol wax	473	196	0.99
	523	185	0.99
	573	169	0.96

Figure 4.3 and 4.4 also indicate the effect of temperature on the H_2 solubility in vacuum residues A and B, and the two liquid mixtures, respectively. As can be seen in these figures, the *C** values increase with temperature for the four liquids. Several authors found similar results under different conditions for H_2 solubilities in soybean oil [108], Sasol wax [77], PSS-8, heavy virgin gas oil, bitumen vacuum bottoms, and atmospheric residue [79, 103].

The effect of temperature on *C** values, is generally described using the Henry's Law constant and the heat of solution due to absorption. Within a small temperature range, an

Arrhenius-type equation [29, 95, 96, 100, 102], Equation (4-2), is used to predict the effect of temperature on *He*, assuming that the heat of solution, ΔH^0, is constant [29, 95, 96, 100, 102].

$$He = He_0 e^{\frac{\Delta H^0}{RT}} \tag{4-2}$$

Within a relatively wide temperature range, however, ΔH^0 may become temperature dependent and Equation (4-3) [109, 110] should be used.

$$\frac{\Delta H^0}{R} = \left[\frac{\partial \ln(He)}{\partial\left(\frac{1}{T}\right)} \right] \tag{4-3}$$

Figure 4.5 shows ln(*He*) as a function of 1/*T* for the four liquids studied, paraffins mixture, and Sasol wax from Soriano[77], and as can be observed, Equation (4-2) models the experimental data with a regression coefficient (R^2) > 0.97 for the four liquids studied, indicating that ΔH^0 is constant.

For vacuum residue A, however, when ln(*He*) was correlated as a function of 1/*T* using Equation (4-4) the resulting regression coefficient was (R^2) = 0.99, suggesting that ΔH^0 could be temperature dependent. The coefficients of this equation are listed in Table 4.2 suggesting that ΔH^0 is dependent on the temperature.

$$\ln(He) = A + \frac{B}{T} + \frac{C}{T^2} \tag{4-4}$$

Table 4.2. Coefficients in Equation (4-4)

	A	***B***	***C***
	-	*K*	K^2
Residue A	3.09	2246.6	-3.9×10^5

The calculated heats of solution of H_2 absorption in the vacuum residues B and A and in the two liquid mixtures are listed in Table 4.4. Also, Soriano[77] correlated the effect of temperature on Henry's law constant for paraffins mixture and Sasol wax using the following equation:

$$He = H_0 e^{\left[A\left(\frac{1}{T}\right)^2 + \frac{B}{T}\right]} \tag{4-5}$$

The coefficients for Equation (4-5) are listed in Table 4.3.

Table 4.3. Coefficients in Equation (4-5) from Soriano[77]

	A	***B***	***H_0***
Parafins mixture	-3.56×10^4	607.60	97.71
Sasol wax	-1.93×10^5	1345	42.18

It should be noted that a similar behavior of Henry's Law as a function of temperature was reported by Himmelblau [109] for six different gases (O_2, N_2, H_2, He, Xe and CH_4) in water from 273 to 647 K. Table 4.5 shows Henry's Law constant of H_2 as a function of temperature for the four liquid studied calculated using Equation (4-2).

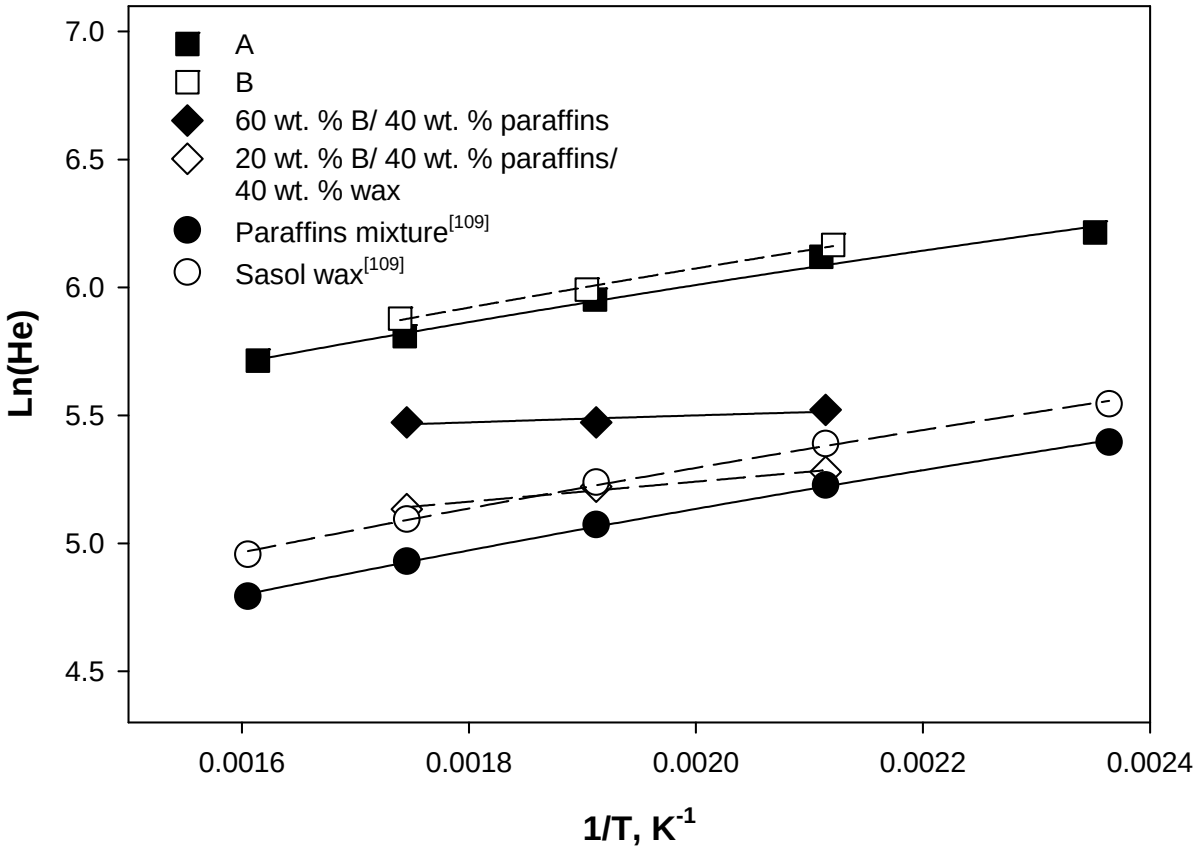

Figure 4.5. Effect of temperature on Henry's Law constants for residues A and B and liquid mixtures

Table 4.4. Apparent standard enthalpy of solution for H_2 in vacuum residues A and B and liquid mixtures from 425 K to 620 K

Liquid	ΔH^0, kJ mol^{-1}
Residue A	5,849
Residue B	6,291
60 wt. % B/40 wt. % paraffins	1,644
20 wt. % B/40 wt. % paraffins/40 wt. % Sasol wax	3,551

Table 4.5. Henry's Law constants of H_2 as a function of temperature

	T, K	*He, bar kg mol^{-1}*
Residue A	653	290
	673	281
	693	274
Residue B	653	304
	673	294
	693	284
60 wt. % B/ 40 wt. % paraffins	653	229
	673	228
	693	227
20 wt. % B/ 40 wt. % paraffins/ 40 wt. % Sasol wax	653	157
	673	154
	693	152

4.1.2 Effect of solid concentration on C*

Even though the gas solubility, as a thermodynamic parameter, depends on the temperature and pressure, Cai et al.[111] found an effect of solids addition on the apparent solubility of hydrogen in hydrocarbon liquids. Figure 4.6 and 4.7 show the effect of activated carbon concentration on the solubility of hydrogen in vacuum residues A and B; and as can be seen, the presence of the activated carbon did not affect *C** values for hydrogen in both residues within the operating conditions used.

4.1.3 Effect of liquid nature on C*

Figure 4.5, 4.8 and 4.9 show the effect of liquid nature on H_2 solubility and Henry's Law constant in the four liquids used. As can be observed, the H_2 solubilities are almost the same in the two residues under similar operating conditions. This is because the vacuum residues A and B have almost similar molecular weights. The addition of paraffins and wax to the vacuum residue B, however, changed the H_2 solubility in the following order: C* in vacuum residue B + paraffins + wax > C* in vacuum residue B + paraffins > C* in the vacuum residue B. This behavior could be due to the fact the three different liquids have different molecular weights compositions, and viscosity since the addition of paraffins to the vacuum residue decreased its viscosity.

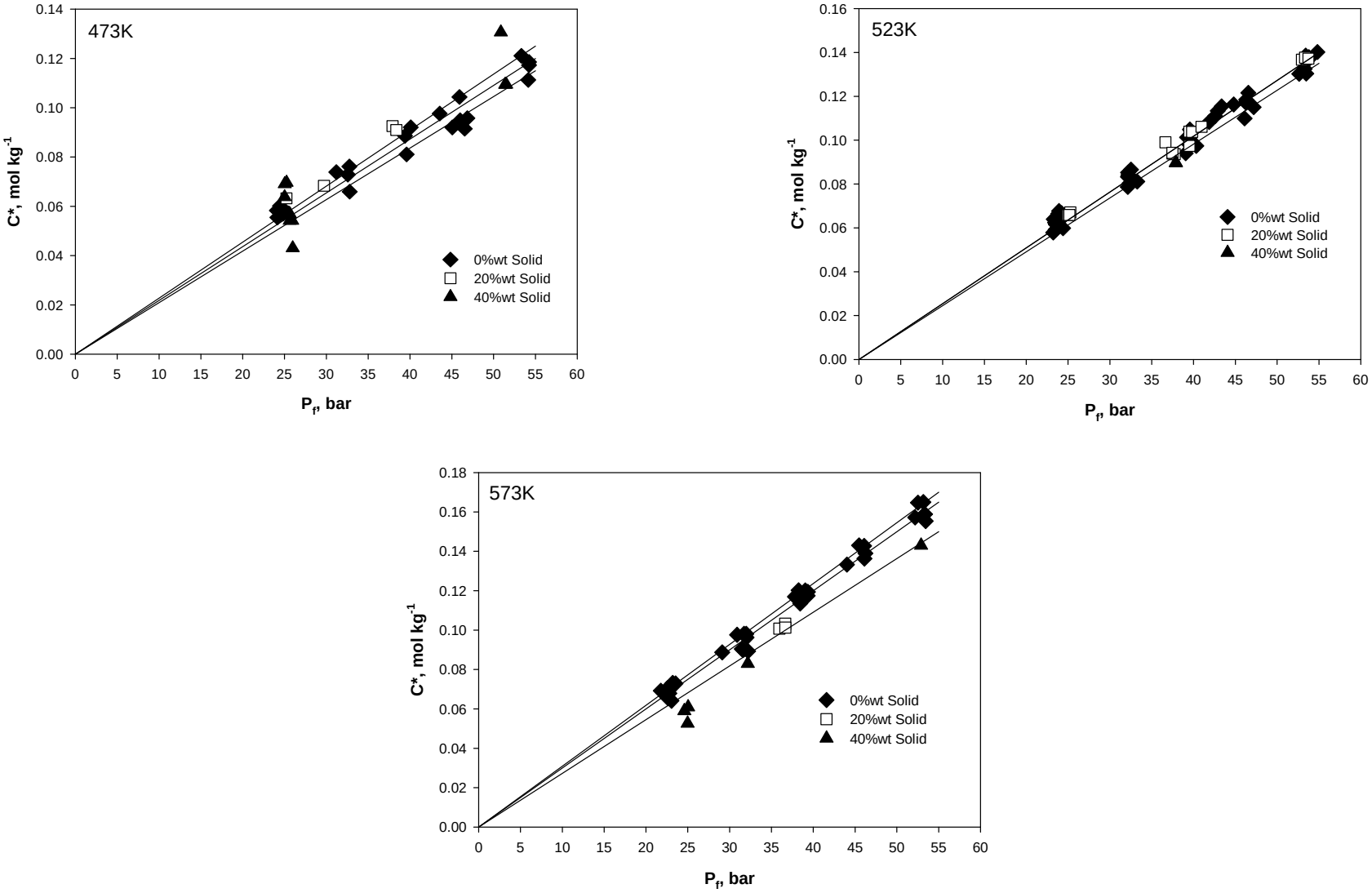

Figure 4.6. Effect of solid concentration on *C** for H_2 in vacuum residue A at 473, 523 & 573 K

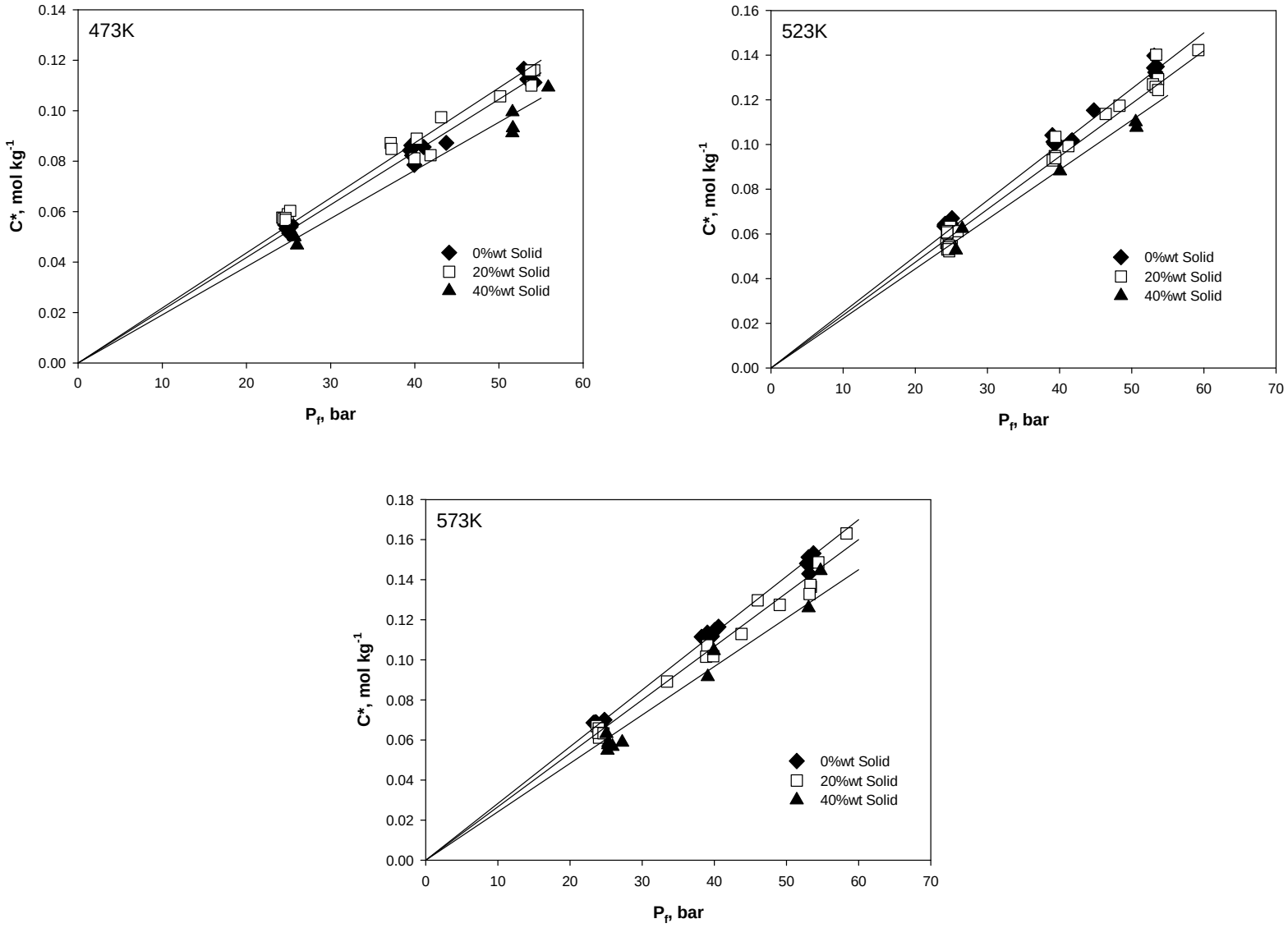

Figure 4.7. Effect of solid concentration on *C** for H_2 in vacuum residue B at 473, 523 & 573K

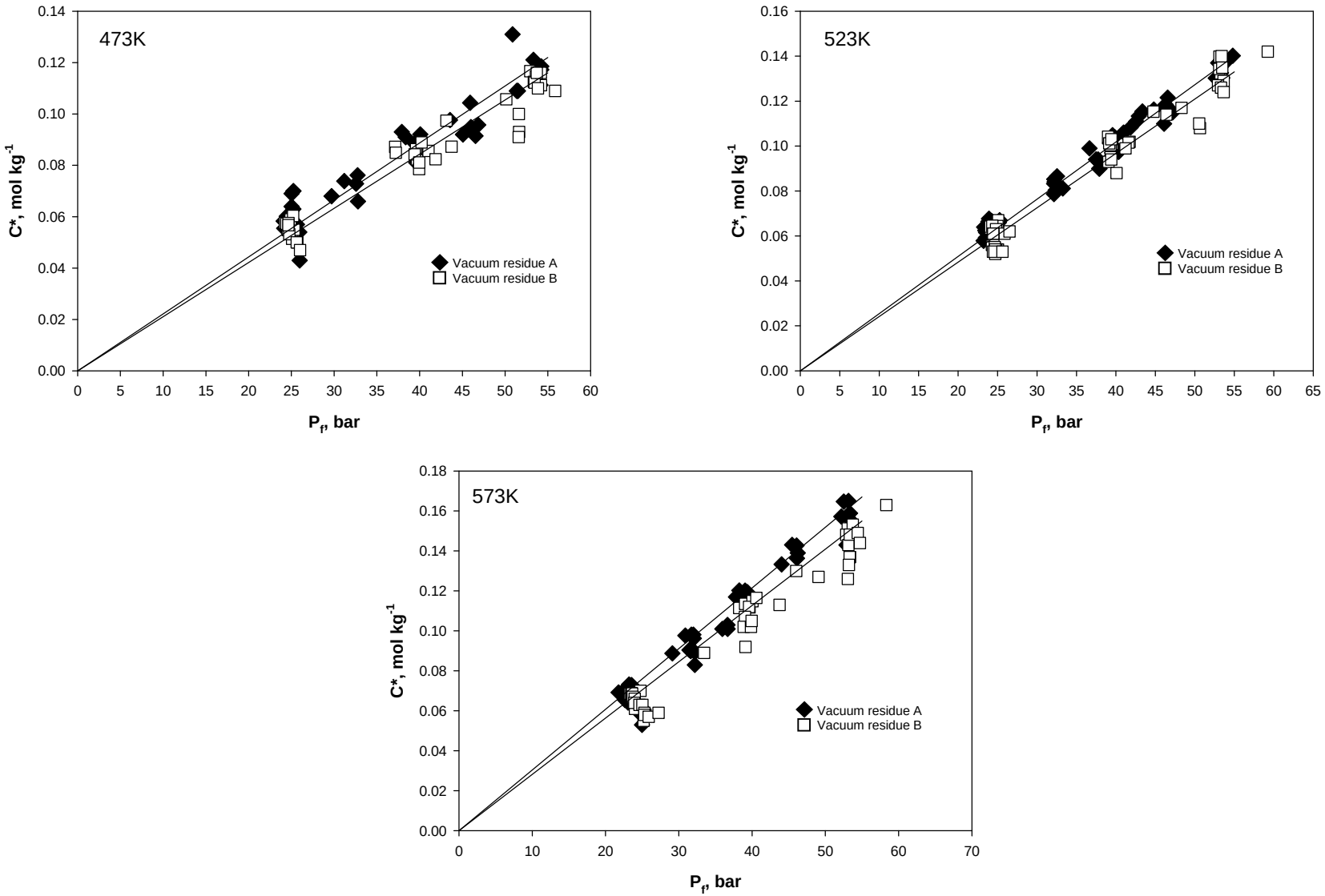

Figure 4.8. Effect of liquid nature on *C**, vacuum residuesA and B

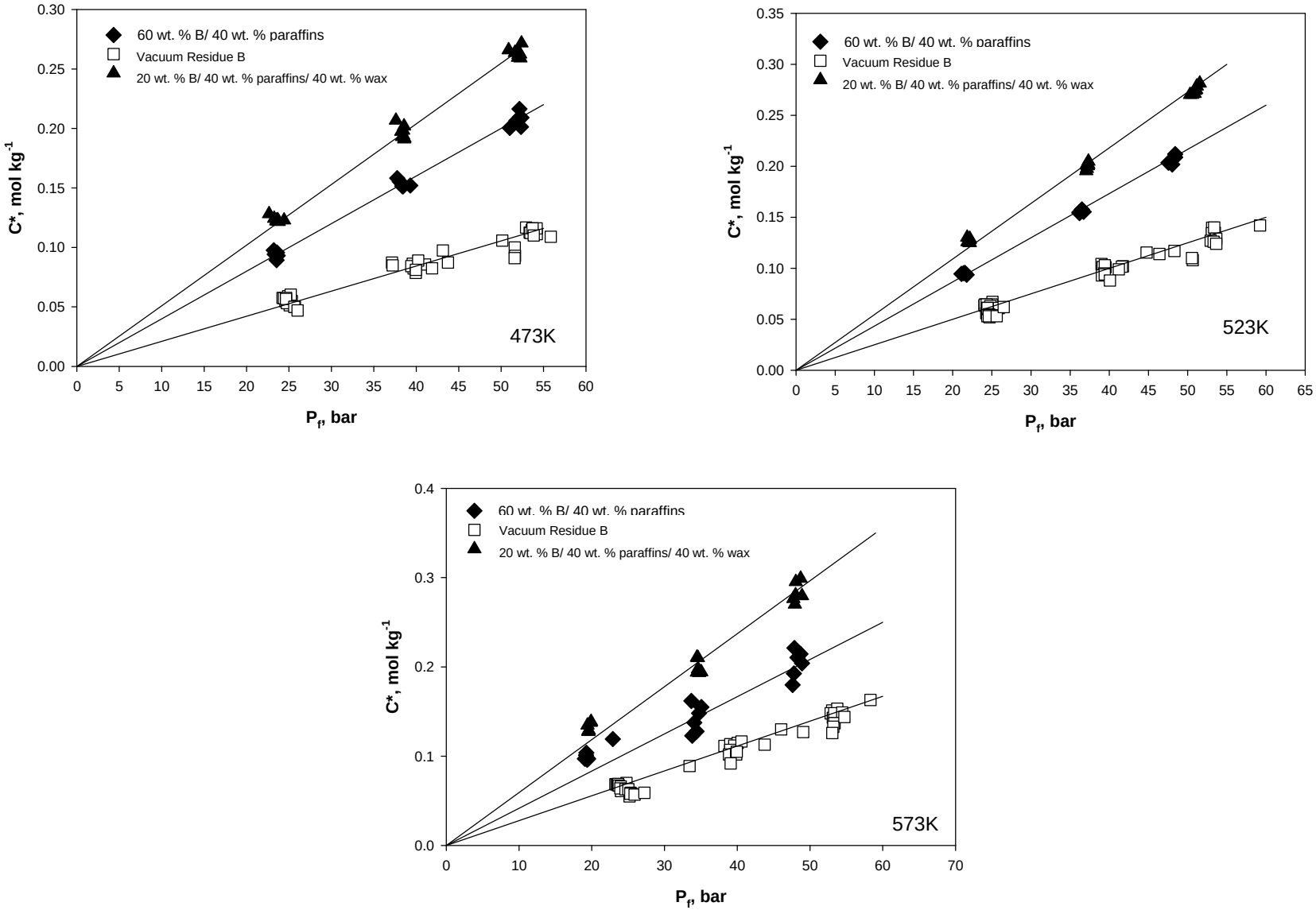

Figure 4.9. Effect of liquid nature on *C** , vacuum residue B and liquid mixtures

4.2 VOLUMETRIC MASS TRANSFER COEFFICIENTS OF H_2 IN VACUUM RESIDUES A AND B AND LIQUID MIXTURES

Literature search revealed the lack of data on the volumetric liquid-side mass transfer coefficients of H_2 in vacuum residues and heavy oils using gas-inducing reactors. In the following section, the effects of pressure, temperature, mixing speed, and solid concentration as well as the liquid nature on H_2 mass transfer coefficients in the vacuum residues A and B, and liquid mixtures is discussed.

Figure 4.10 shows the reproducibility of H_2 k_La data in vacuum residues A and B, and Figure 4.11 shows the reproducibility for H_2 k_La data in the liquid mixtures; and as can be reported the k_La data were obtained with an AAER < 15%.

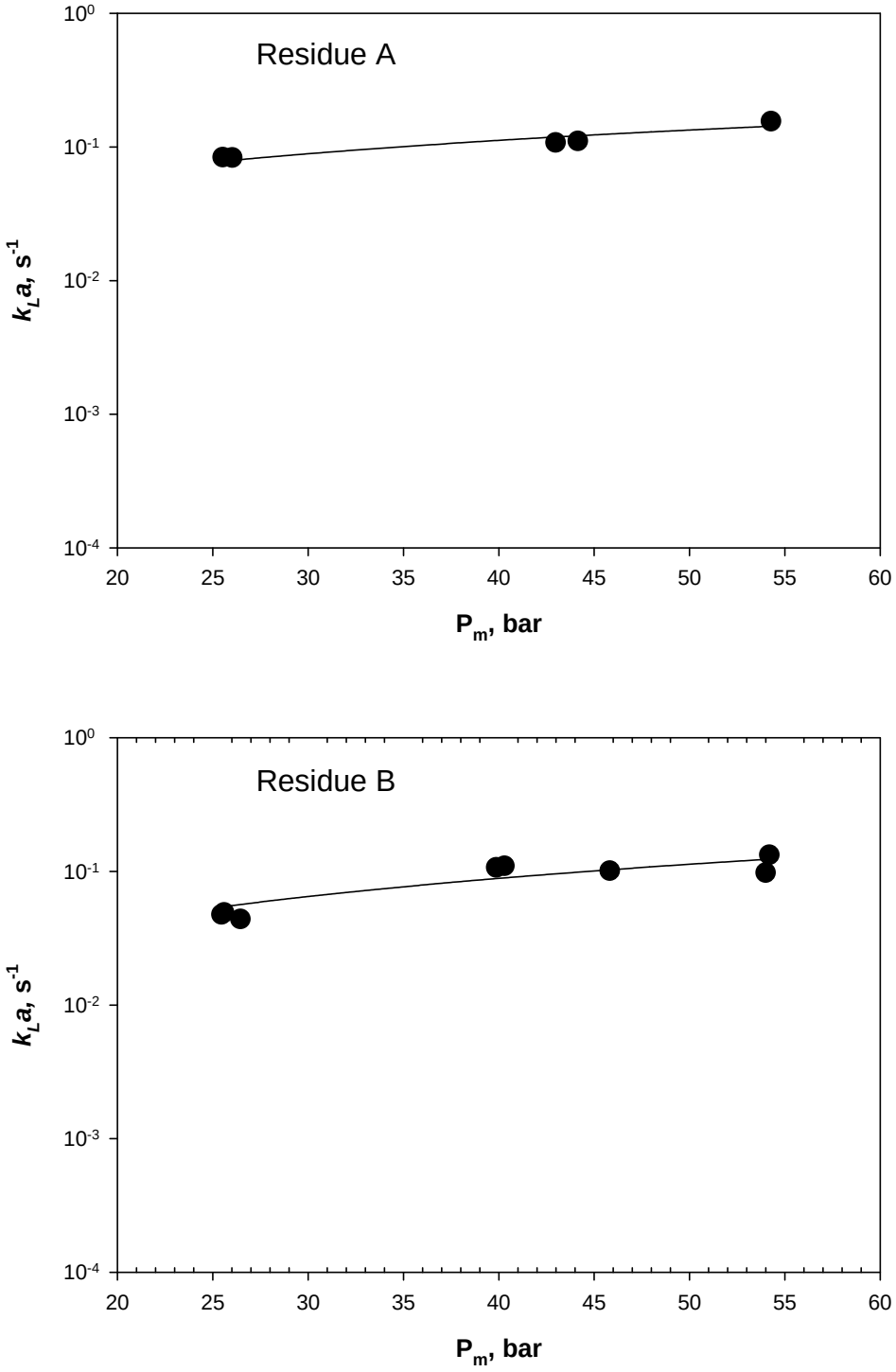

Figure 4.10. Reproducibility of k_La values at 1600RPM with 0 wt. % of solid at 523K vacuum residues

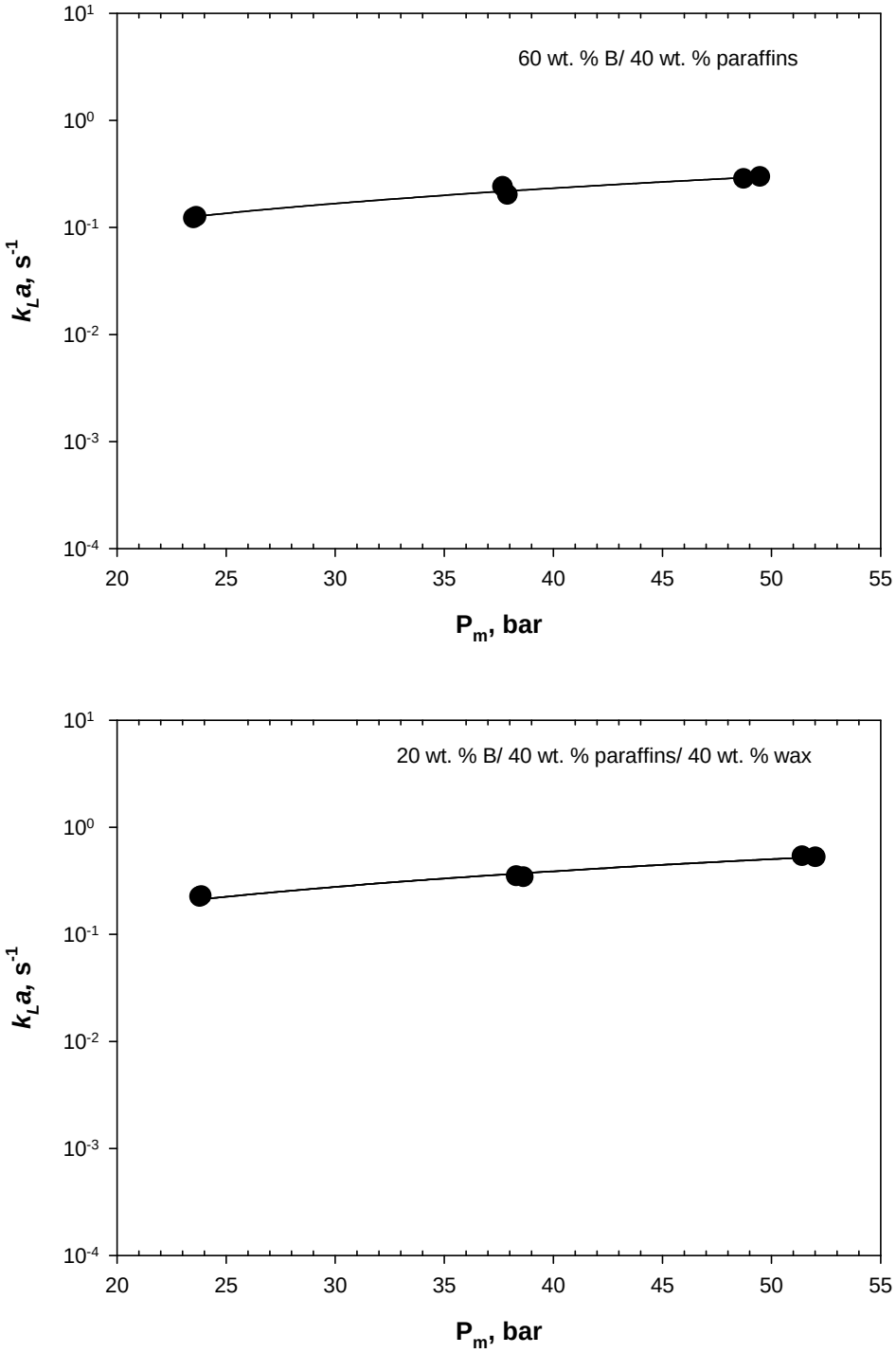

Figure 4.11. Reproducibility of $k_L a$ values at 1600RPM with 0 wt.% of solid at 523K liquid mixtures

4.2.1 Effect of mixing speed on k_La

Figure 4.12 through 4.19 show the effect of mixing speed on the volumetric liquid-side mass transfer coefficients of H_2 in the two vacuum residues and the two liquid mixtures. As can be observed, increasing the mixing speed from 1200 rpm to 2000 rpm leads to an increase of k_La values, which is consistent with various earlier studies for comparable gas-liquid systems [16, 97, 102]. This increase of H_2 mass transfer coefficients with mixing speed can be attributed to the increase in the pumping capacity of the impeller, which induces more gas bubbles into the liquid phase through the hollow shaft, resulting in increasing the gas-liquid interfacial area, a. Also, increasing the mixing speed increased the turbulence and shear rate, which decreases the liquid film thickness (δ) and increases the mass transfer coefficient (k_L), since $k_L = D_{AB}/\delta$. Thus, the combined effects of mixing speed on the gas-liquid interfacial area (a) and the mass transfer coefficient (k_L) led to the increase of k_La.

Figure 4.12 through 4.19 also show that when increasing mixing speed from 1200 rpm to 2000 rpm, k_La values increase by 60% to 500%. On the other hand, in some case, increasing mixing speed from 1600 to 2000 rpm, a small increase in k_La was observed. This small increase in k_La values at such mixing speeds can be related to the effect of mixing speed on the induced gas flow rate through the hollow shaft, Q_{GI}. As reported by Lemoine et al.[85], at mixing speeds greater than the critical mixing speed for gas induction, Q_{GI} increases with mixing speed until a fully developed hydrodynamic regime is reached, and after that Q_{GI} is not affected by mixing speed any longer. Thus, increasing the mixing speed after reaching the fully developed hydrodynamic regime did not significantly increase Q_{GI} and subsequently k_La.

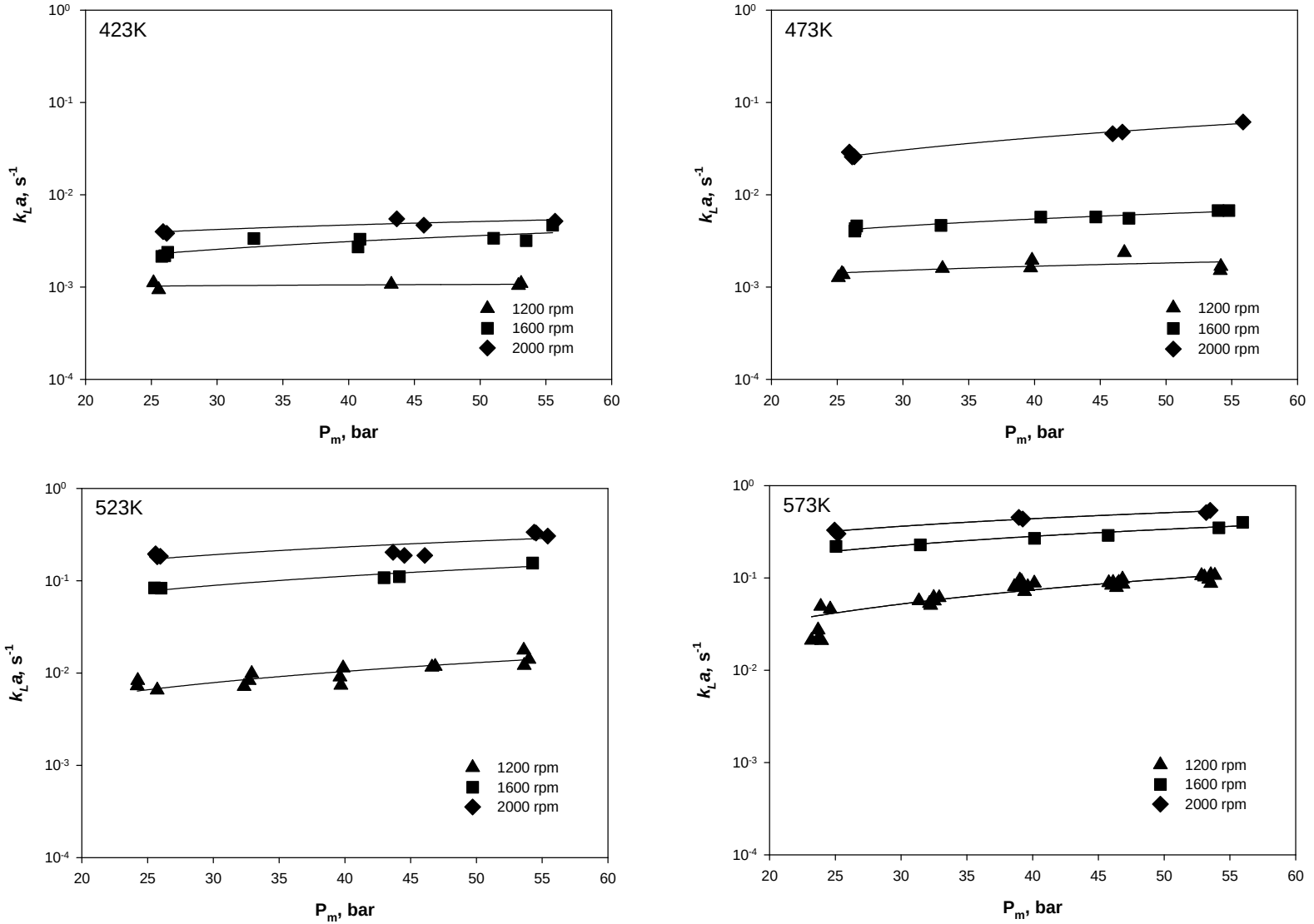

Figure 4.12. Effect of mixing speed on k_La, 0 wt. % solid, residue A

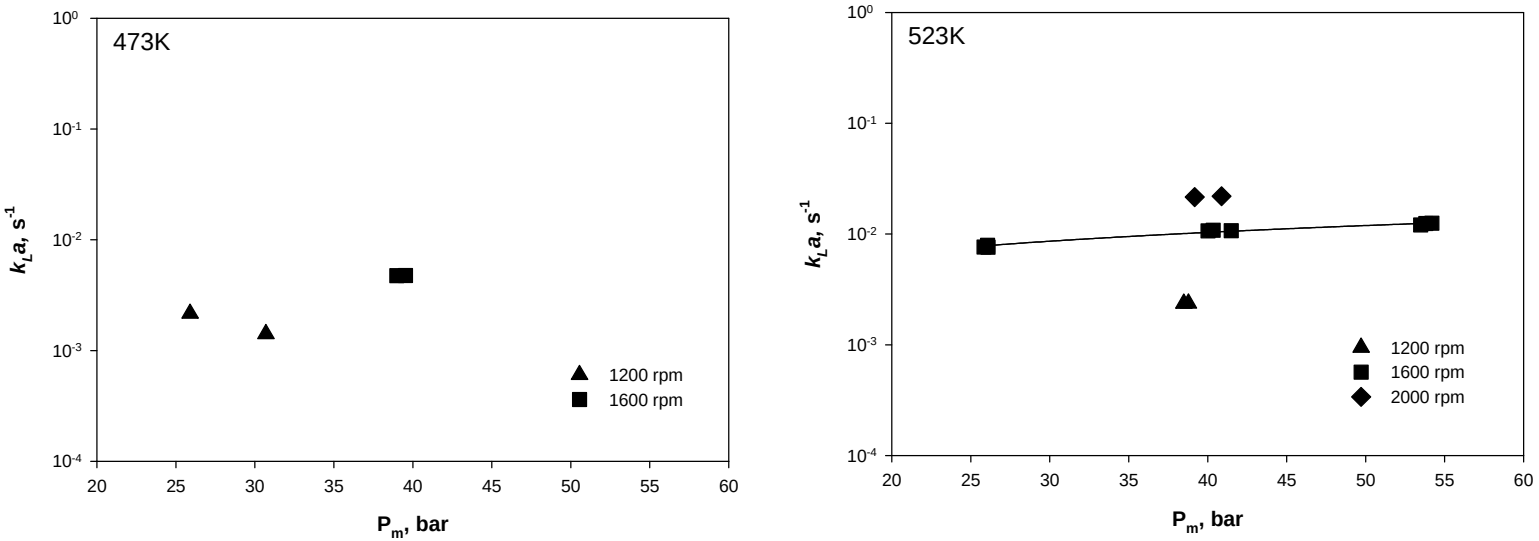

Figure 4.13. Effect of mixing speed on k_La, 20 wt. % solid, residue A

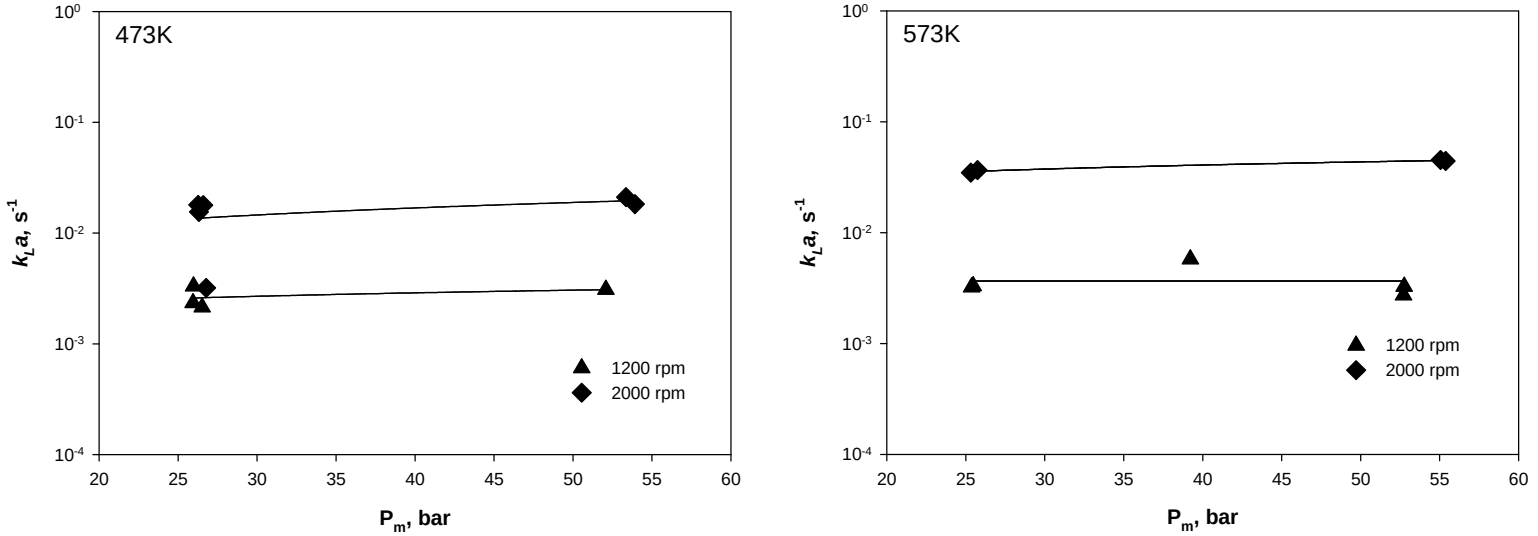

Figure 4.14. Effect of mixing speed on k_La, 40 wt. % solid, residue A

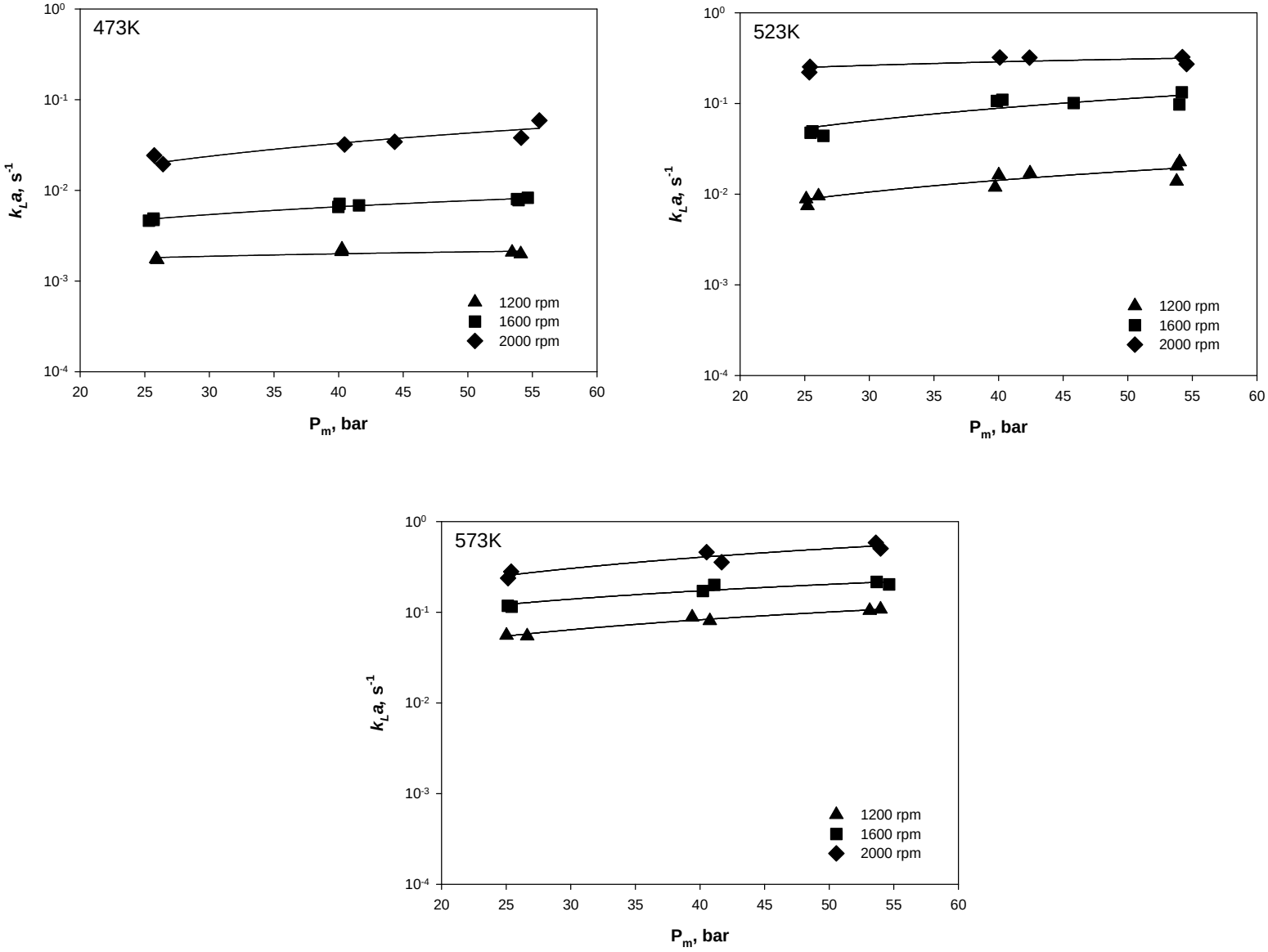

Figure 4.15. Effect of mixing speed on k_La, 0 wt. % solid, residue B

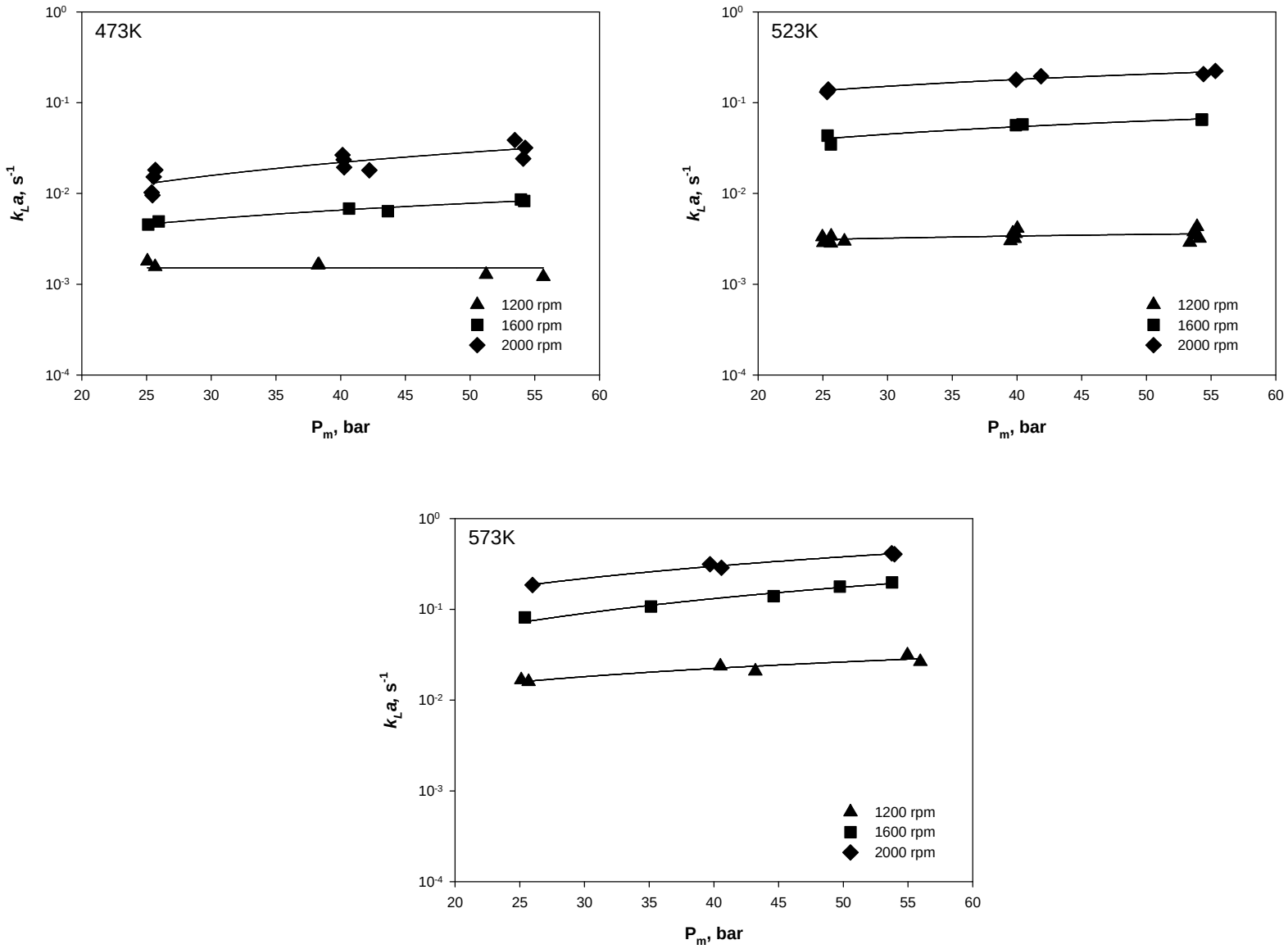

Figure 4.16. Effect of mixing speed on $k_L a$, 20 wt. % solid, residue B

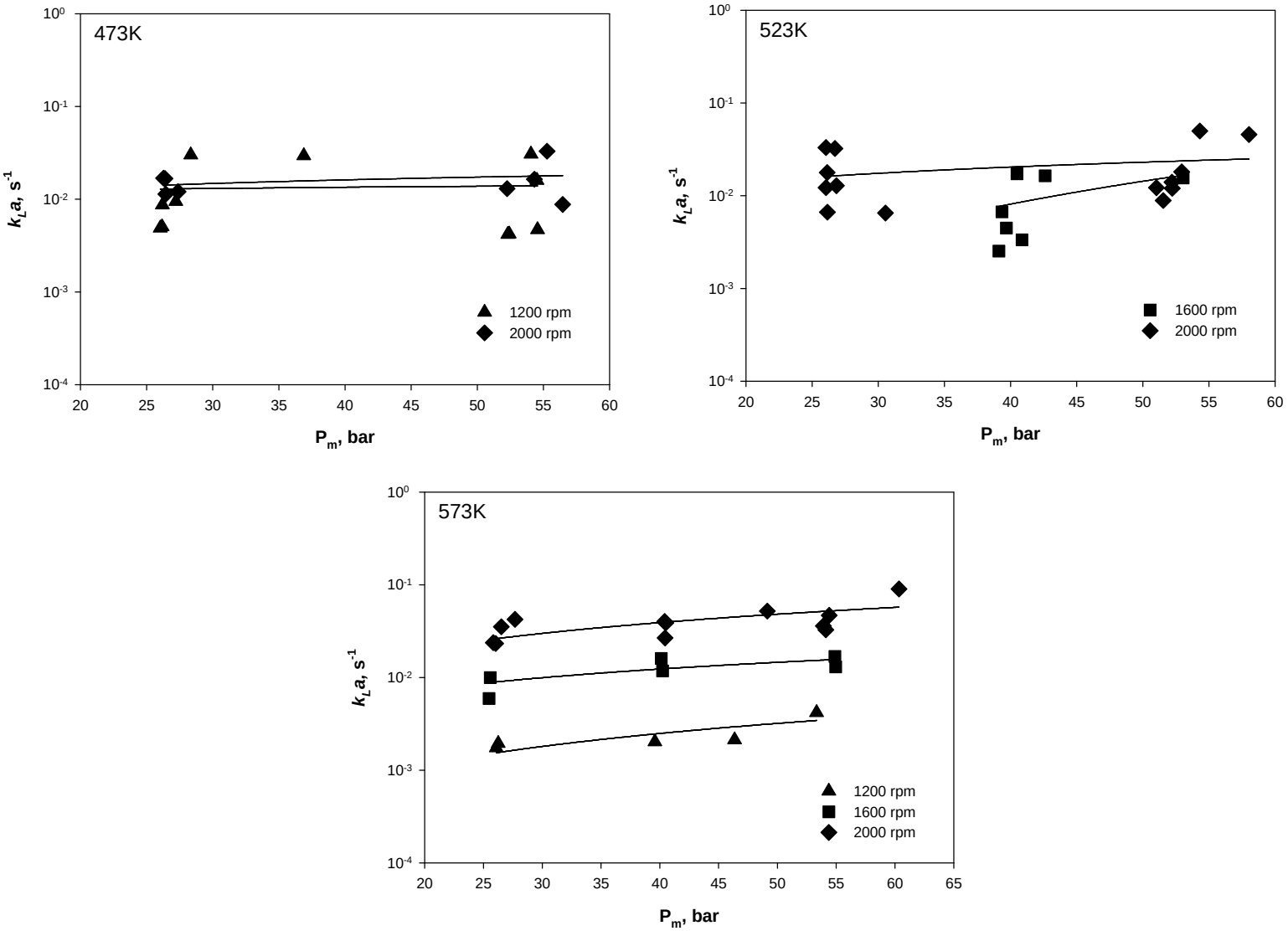

Figure 4.17. Effect of mixing speed on k_La, 40 wt. % solid, residue B

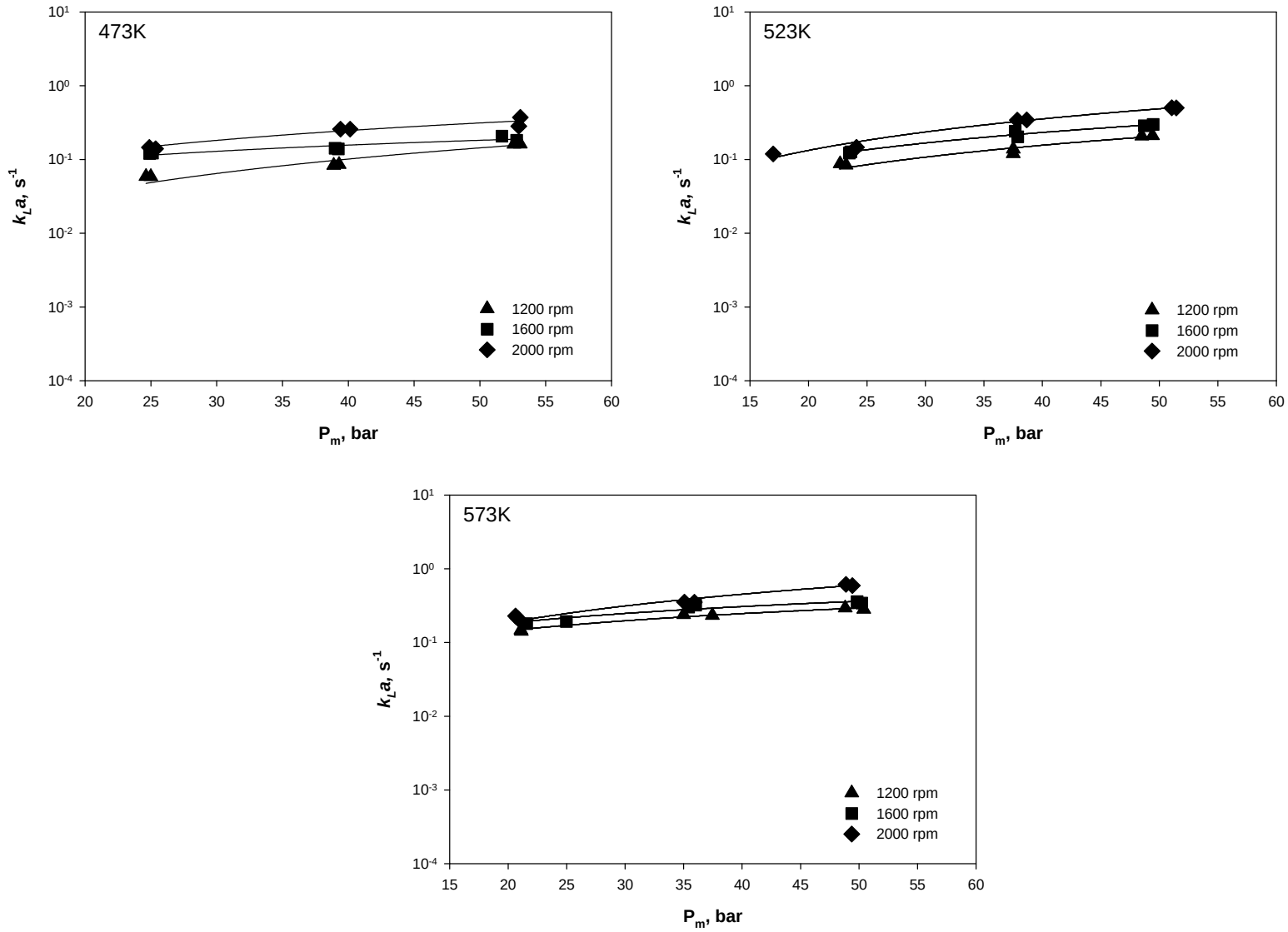

Figure 4.18. Effect of mixing speed on k_La, 0 wt. % solid, 60 wt. % vacuum residue B + 40 wt. % paraffins mixture

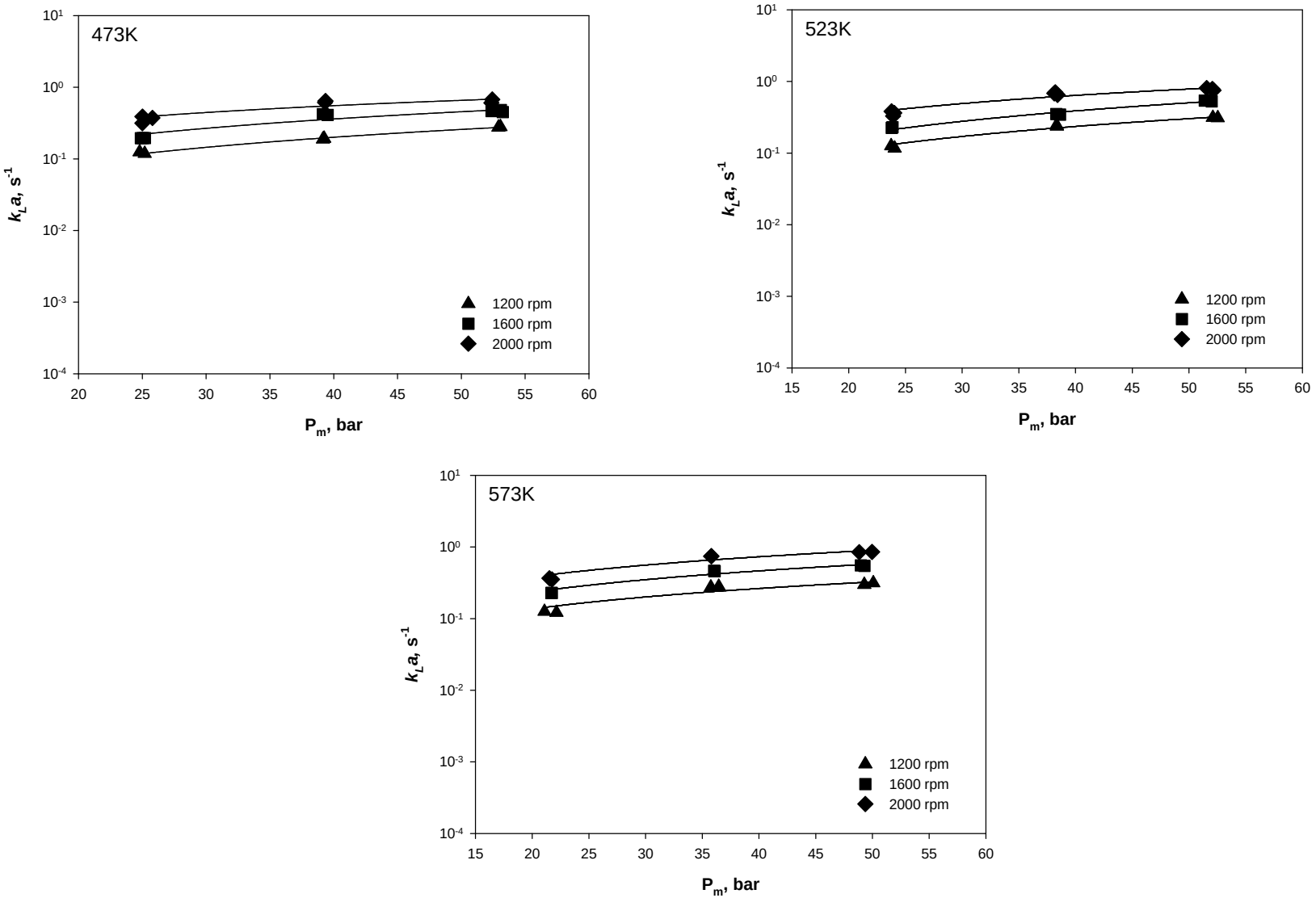

Figure 4.19. Effect of mixing speed on $k_L a$, 0 wt. % solid, 20 wt. % vacuum residue B + 40 wt. % paraffins mixture + 40 wt. % Sasol wax

4.2.2 Effect of temperature on k_La

The effect of temperature on the volumetric liquid side mass transfer coefficient for H_2 in the vacuum residues A and B, and the two liquid mixtures are presented in Figure 4.20 through 4.27. As can be observed, increasing the temperature increase k_La for H_2 in the four liquids used. This k_La behavior is consistent with that reported earlier by other investigators [28, 48, 49, 100, 112]. This increase of k_La with temperatutre could be attributed to the resultant its effect on both k_L and a, which is usually related to the alteration of the liquid physico-chemical properties with increasing temperature.

Increasing temperature decreases the liquid viscosity and increases the gas diffusivity in the liquid according to the Wilke-Chang, [9] Equation (4-6). This increase of diffusivity leads to the inctesae of k_L; since the latter is directly related to diffusivity to the power 0.5 to 1 according to the Penetration Theory and the Two-film Model, respectively, as can be seen in Equation (4-7). Also, inceasing temepratyure decrease liquid surface tension which decreases the gas bubble Sauter mean diameter (d_S) and increases the gas holdup [101, 113]. As a result, the gas-iquid interfacial area, a, increases according to Equation (4-8). Thus, increasing temeprtaure should increase k_L and a and consequently k_La.

$$D_{AB} = \frac{1.1728\times10^{-16}\left(\lambda\, MW_L\right)^{0.5} T}{\mu_L \upsilon_G^{\,0.6}} \tag{4-6}$$

$$k_L \propto D_{AB}^{\,n} \tag{4-7}$$

$$a = \frac{6\varepsilon_G}{d_s(1-\varepsilon_G)} \tag{4-8}$$

Figure 4.20 through 4.27 show that increasing temperature from 423 to 623 K results in up to two orders of magnitude increase of k_La values.

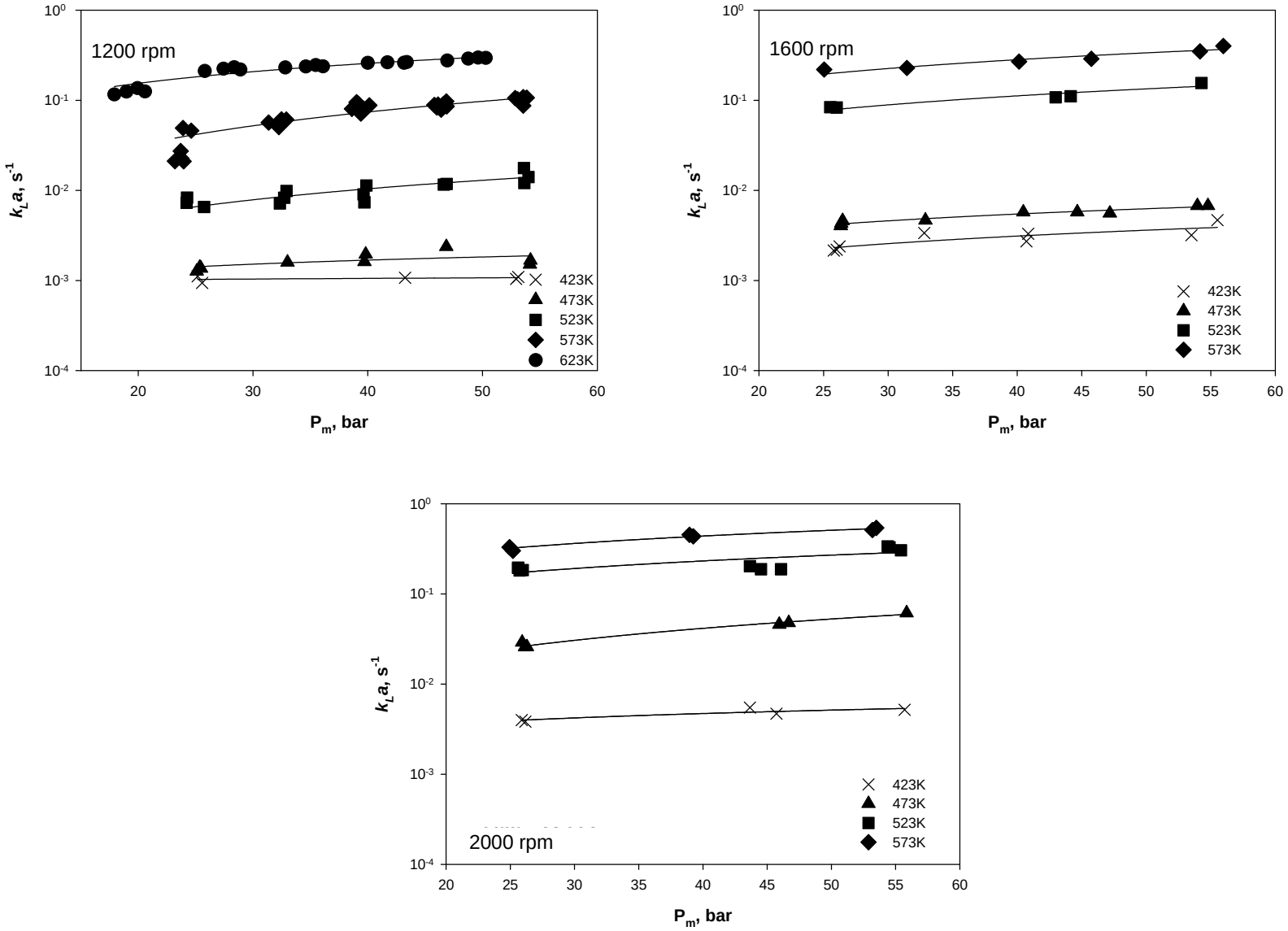

Figure 4.20. Effect of temperature on $k_L a$ for H_2 in vacuum residue A at 0 wt.%

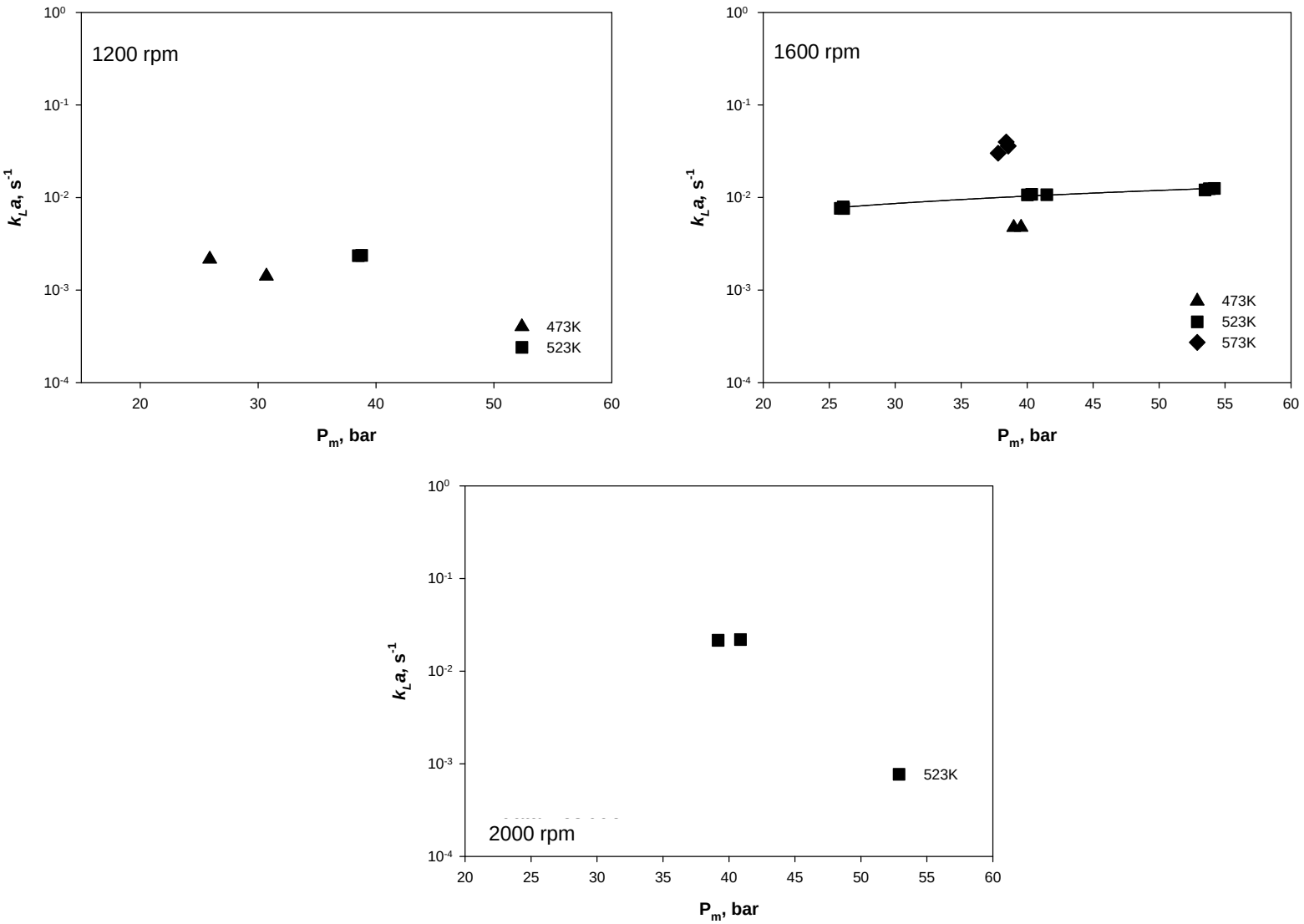

Figure 4.21. Effect of temperature on k_La for H_2 in vacuum residue A at 20 wt.%

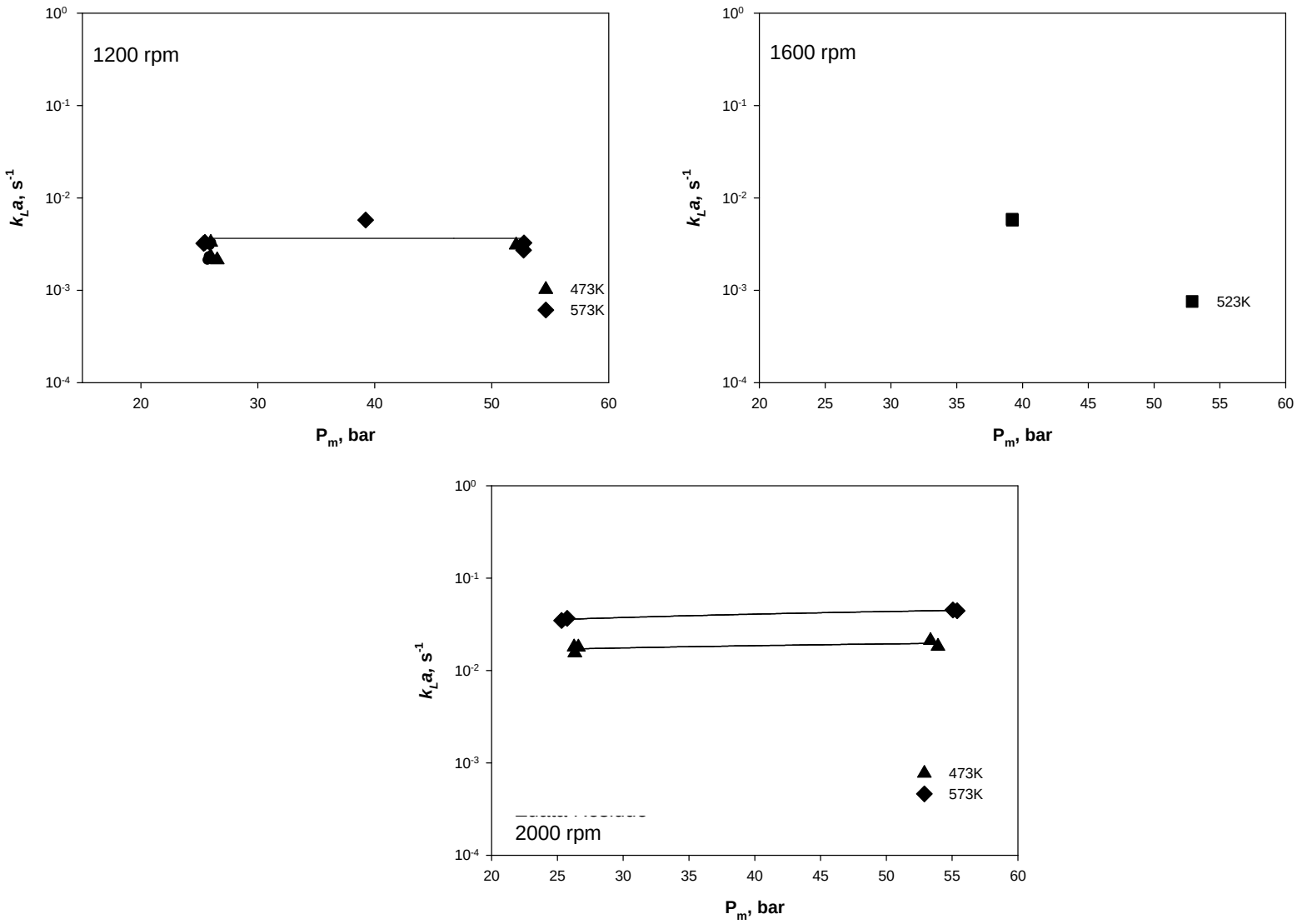

Figure 4.22. Effect of temperature on k_La for H_2 in vacuum residue A at 40 wt.%

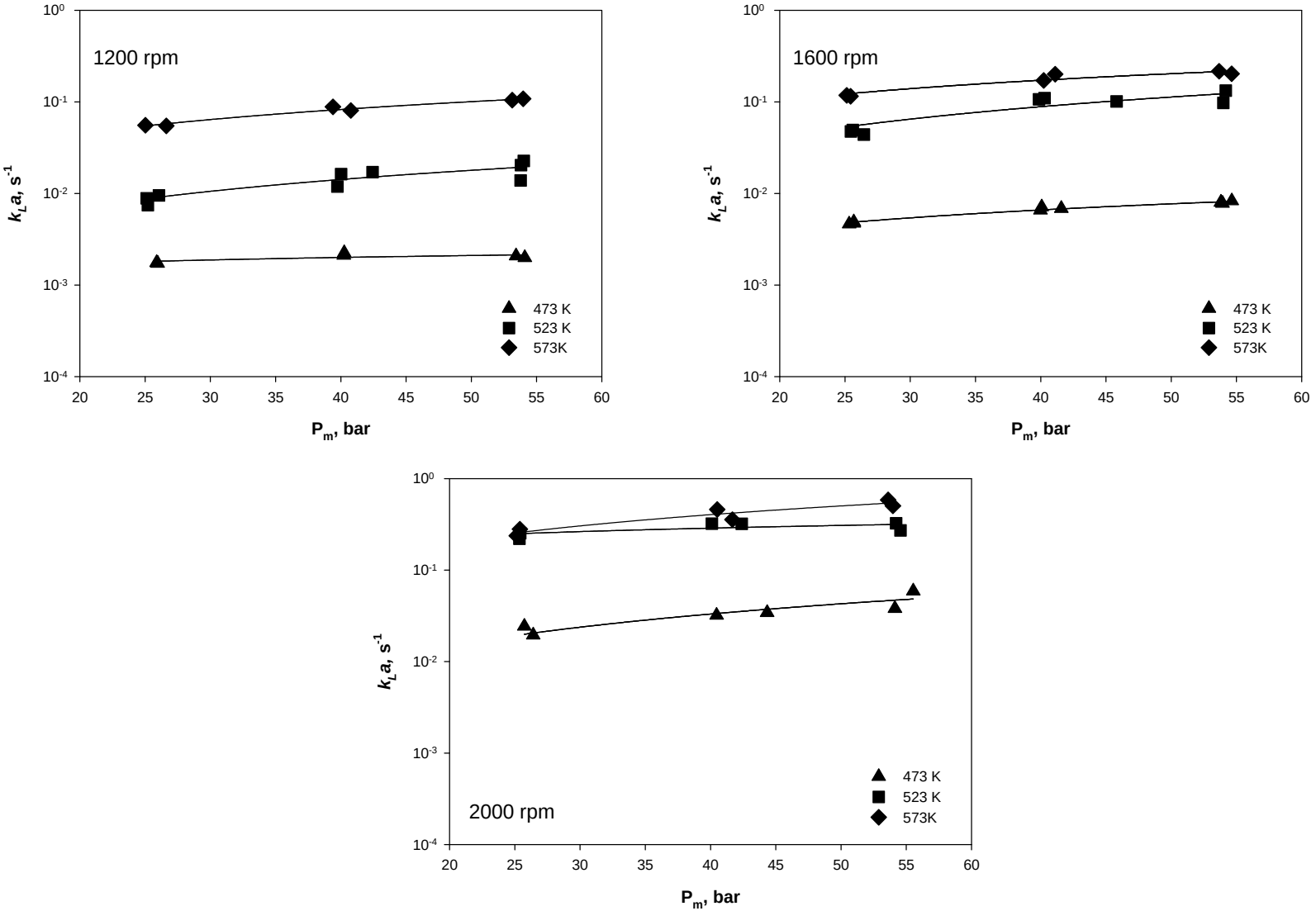

Figure 4.23. Effect of temperature on k_La for H_2 in vacuum residue B at 0 wt.%

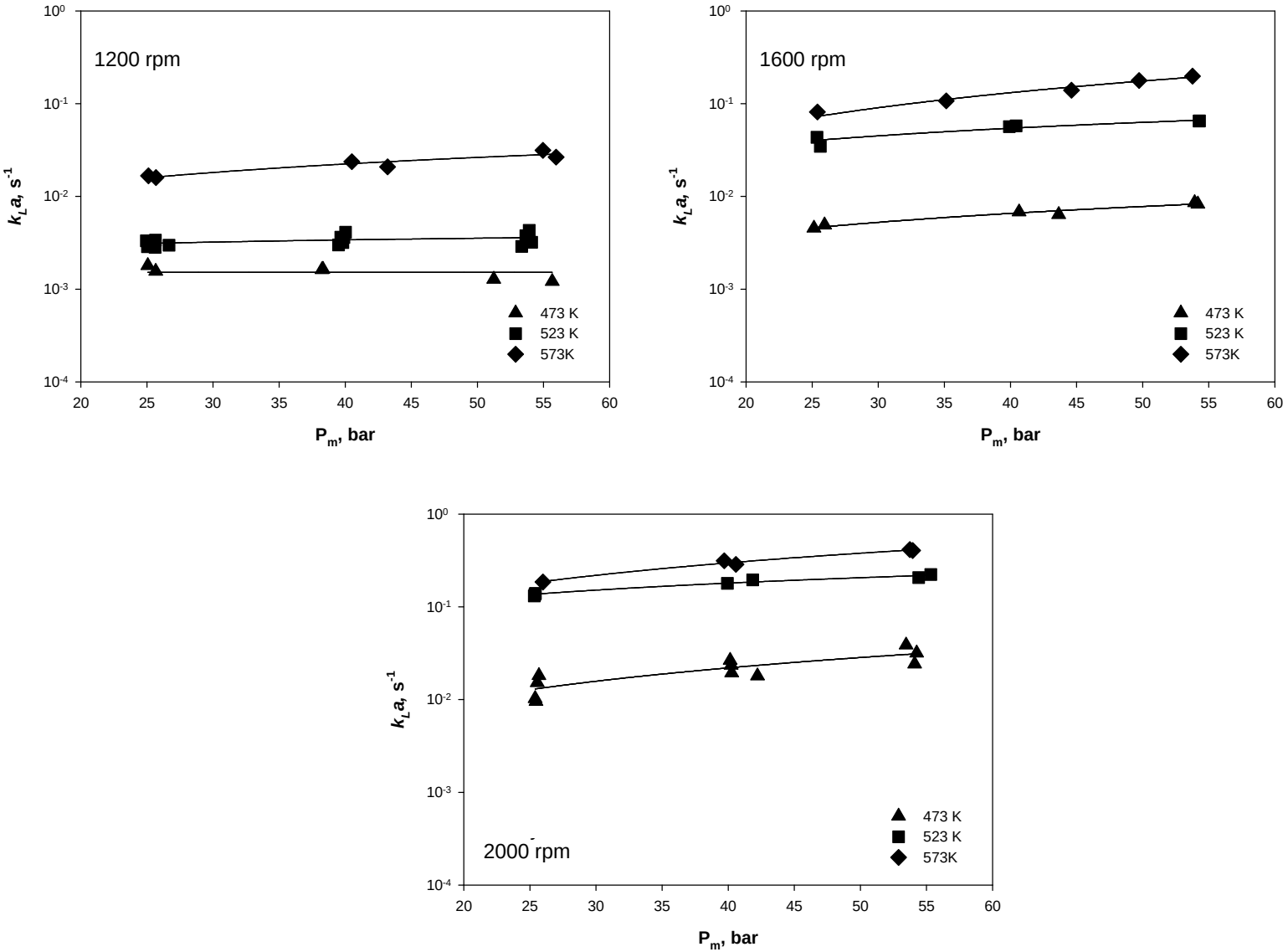

Figure 4.24. Effect of temperature on k_La for H_2 in vacuum residue B at 20 wt.%

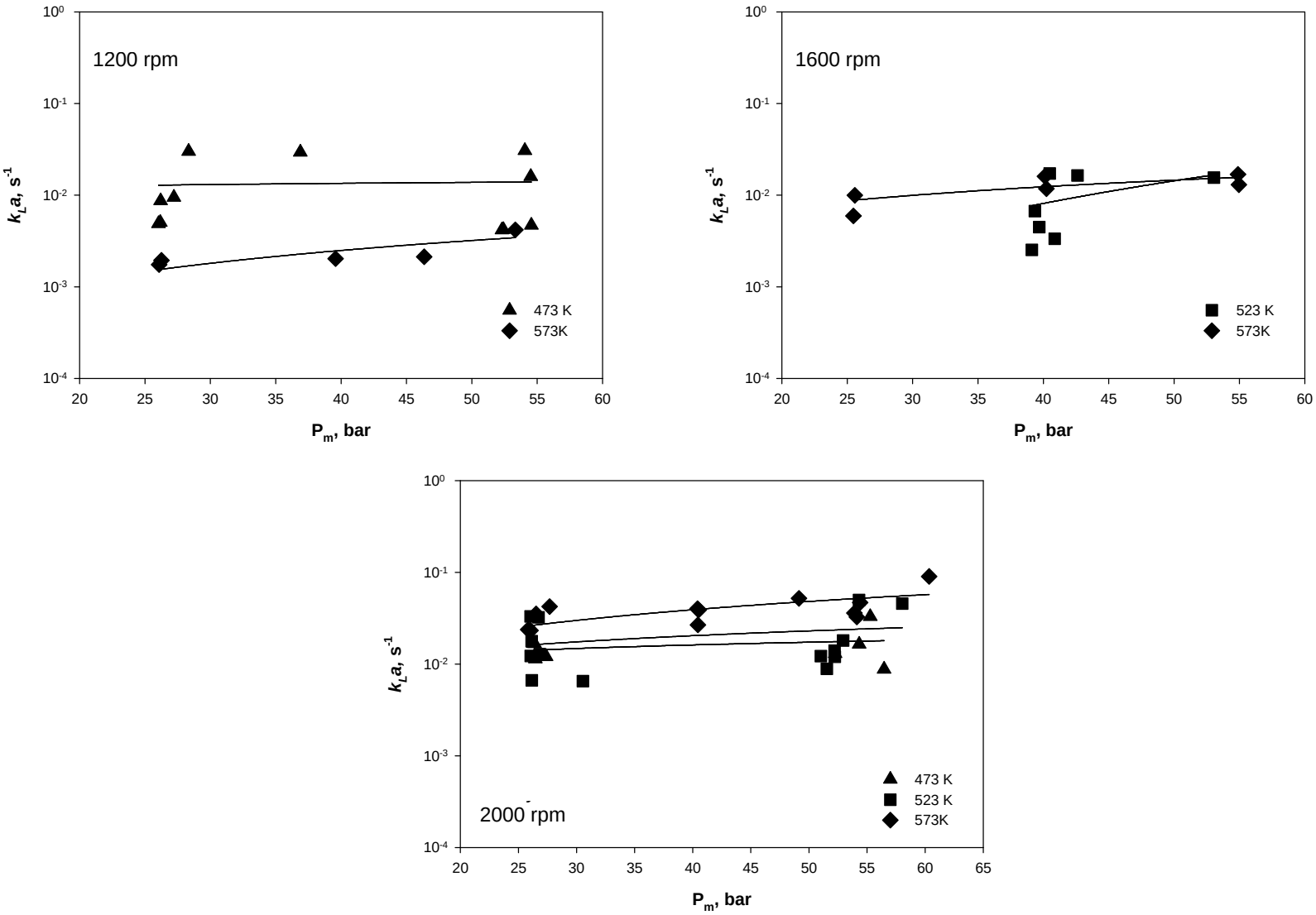

Figure 4.25. Effect of temperature on k_La for H_2 in vacuum residue B at 40 wt.%

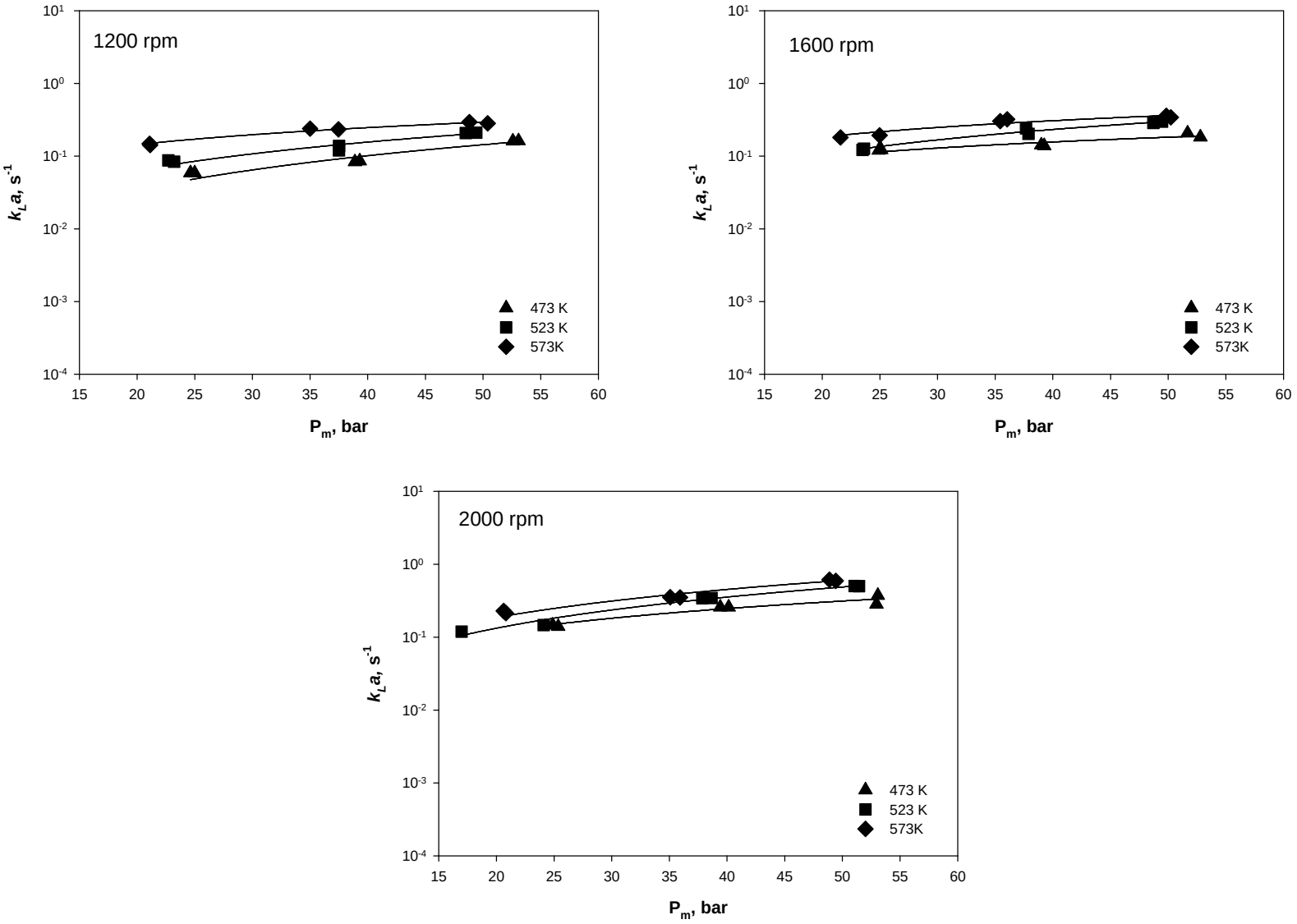

Figure 4.26. Effect of temperature on k_La for H_2 in 60 wt. % vacuum residue B + 40 wt.% paraffins

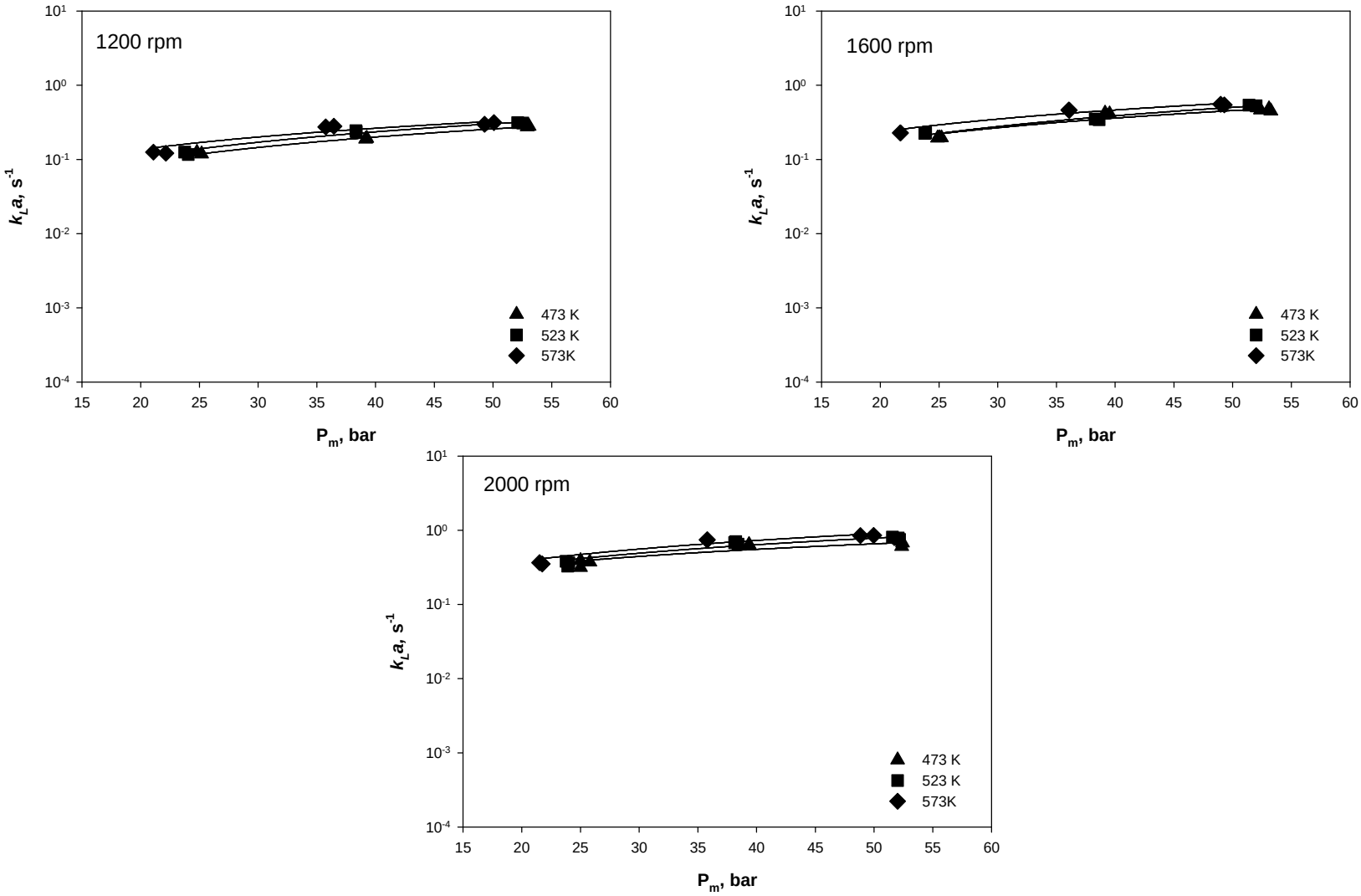

Figure 4.27. Effect of temperature on k_La for H_2 in 20 wt. % vacuum residue B + 40 wt. % paraffins + 40 wt. % Sasol wax

4.2.3 Effect of pressure on k_La

The effect of pressure on k_La is strongly system-dependent since increasing pressure may result in an increase[47-49, 95, 100, 102, 112, 114], a decrease[115], or no change[28, 63, 64, 106, 116, 117] in k_La values. Figure 4.10 through 4.27 show the effect of the mean pressure on H_2 k_La in vacuum residues A and B; and in the two liquid mixtures. As as can be seen in these figures, k_La values increase slightly with increasing the H_2 mean pressure. This effect can be realted to the alteration of the physico-chemical properties of the gas-liquid system with increasing pressure. Increasing pressure increases the gas solubility, which decreases the liquid surface tension and viscosity. Decreasing liquid viscosity increases the diffusivity of H_2 in the four liquids since D_{AB} is inversely proportional to the liquid viscosity, as shown in the Wilke-Chang correlation (Equation (4-6)). The increase of pressure can also influence the interfacial area (a) by affecting the gas holdup and the gas bubble Sauter mean bubble diameter (d_S), as can be deduced from Equation (4-8).

The decrease of the liquid surface tension and viscosity, reportd to decrease the size of gas bubbles and increase the gas holdup[101, 118], should increase the gas-liquid interfacial area (a). Thus, the increase of both k_L and a with increasing pressure led to the increase of k_La for H_2 in the four liquids used.

4.2.4 Effect of solid concentration on k_La

The addition of solid particles to the liquid can lead to different effects on k_La. Several studies showed that when a small amount of solid particles are added to the liquid, there is either little effect [117, 119] or even an increase [63, 64, 100, 112, 120-123] of k_La values, whereas when large amount

of solids (high solid concentrations) is used, k_La values appeared to dramatically decrease [49, 63, 64, 100, 112, 120].

Figure 4.28 through 4.33 show the effect of the solid concentration on k_La for H_2 in vacuum residues A and B. The addition of solid particles decreased k_La values under most of the operating conditions studied; however, at 473 K for 1200 and 1600 rpm, k_La did not change, probably due to the high viscosity of the vacuum residues. Kluytmans [121] reported that the addition of small solid particles adsorb gas from the gas-liquid diffusion layer and desorb it into the liquid bulk, which is referred to as the shuttle or grazing effect, thereby increasing the mass transfer rate. Also, small solid concentrations were found to create turbulence at the gas-liquid interface, which decreases the effective diffusion layer and increases the mass transfer coefficient k_L, and subsequently k_La. On the other hand, high concentrations of small particles were found to greatly increase the slurry viscosity, as can be seen in Figure 3.21, where increasing solid loadings from 0 to 20 wt.% and from 20 to 40 wt.% increases the slurry viscosity by 39% and 75%, respectively. This increase in slurry viscosity decreases the gas diffusivity and therefore k_L, which is related to the diffusivity as stated previusly. Also, the increase of slurry viscosity promotes gas-bubble coalescence, which decreases the gas-liquid interfacial area a. Thus, increasing solid concentration to high values decreases both k_L and a, and consequently, k_La.

4.2.5 Effect of liquid nature on k_La

Figure 4.34 through 4.42 show that under similar operating conditions, the volumetric mass-transfer coefficients for H_2 in the vacuum residues A and B are almost the same. On the other hand, Figure 4.43 through 4.45 show that when vacuum residue B is compared to the two liquid

mixtures, the mass transfer coefficient change in the following order: k_La in vacuum residue B + paraffins + wax > k_La in vacuum residue B + paraffins > k_La in vacuum residue B. It can also be seen that, as the temperature increases at constant mixing speed, the difference in the mass-transfer coefficient for the three liquids at constant pressure decreases. This behavior can be related to the fact that at higher temperatures, the viscosity difference among the three liquids decreases.

Figure 4.46 compares the mass transfer coefficient for vacuum residues A and B with those in the tow liquid mixtures at different viscosities, and as can be seen, as the liquid viscosity increases, the mass transfer coefficient decreases. When comparing k_La values in the four liquids, there is no clear trend. This is because for vacuum residues A and B at similar viscosities, the mass transfer coefficient for vacuum residue A is greater than that in the vacuum residue B, whereas for the liquid mixtures, at similar visosities, the mass transfer coefficient for vacuum residue B + paraffins is lower than that in the vacuum residue B + paraffins + wax.

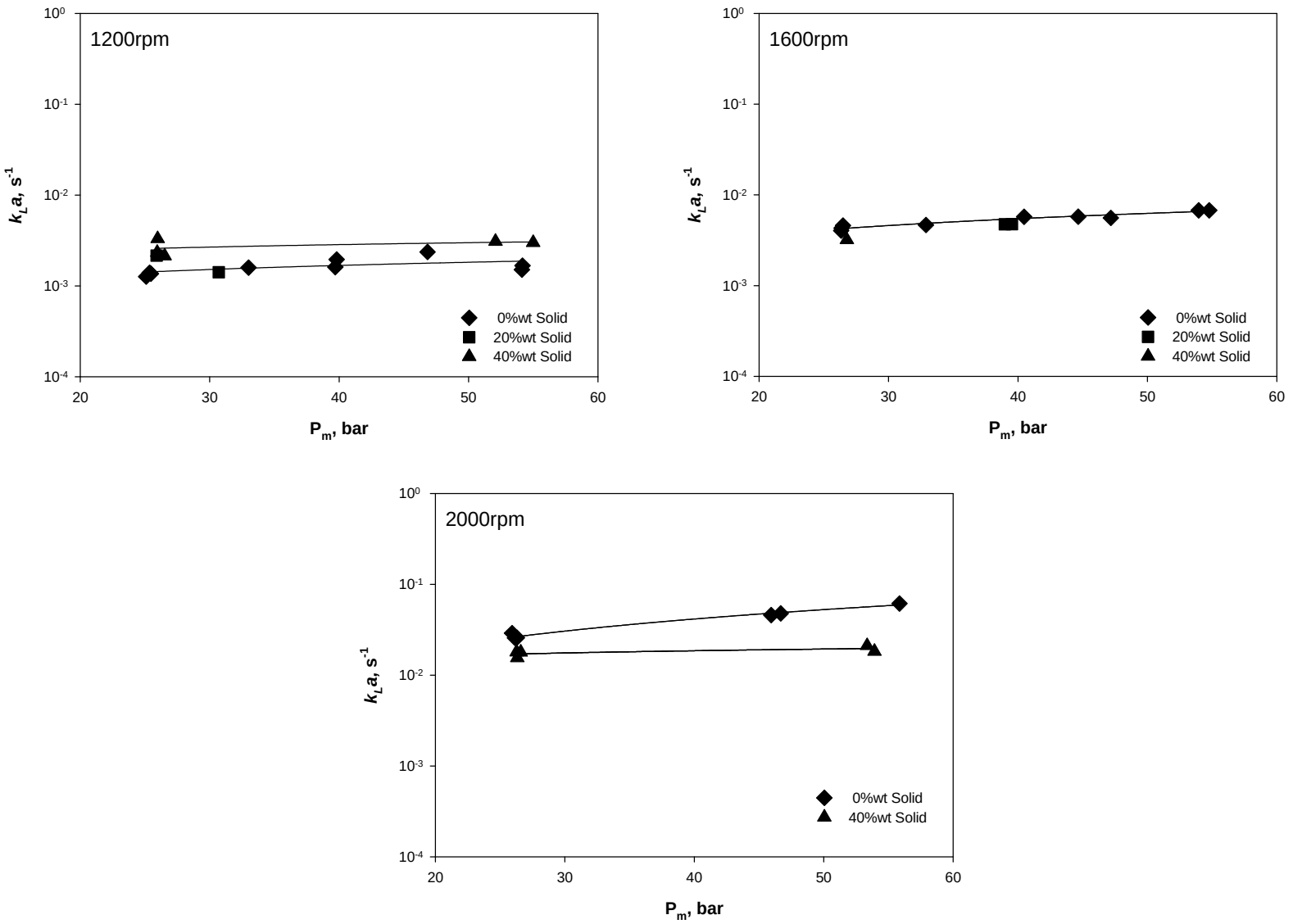

Figure 4.28. Effect of solid concentrations on k_La at 473K in residue A

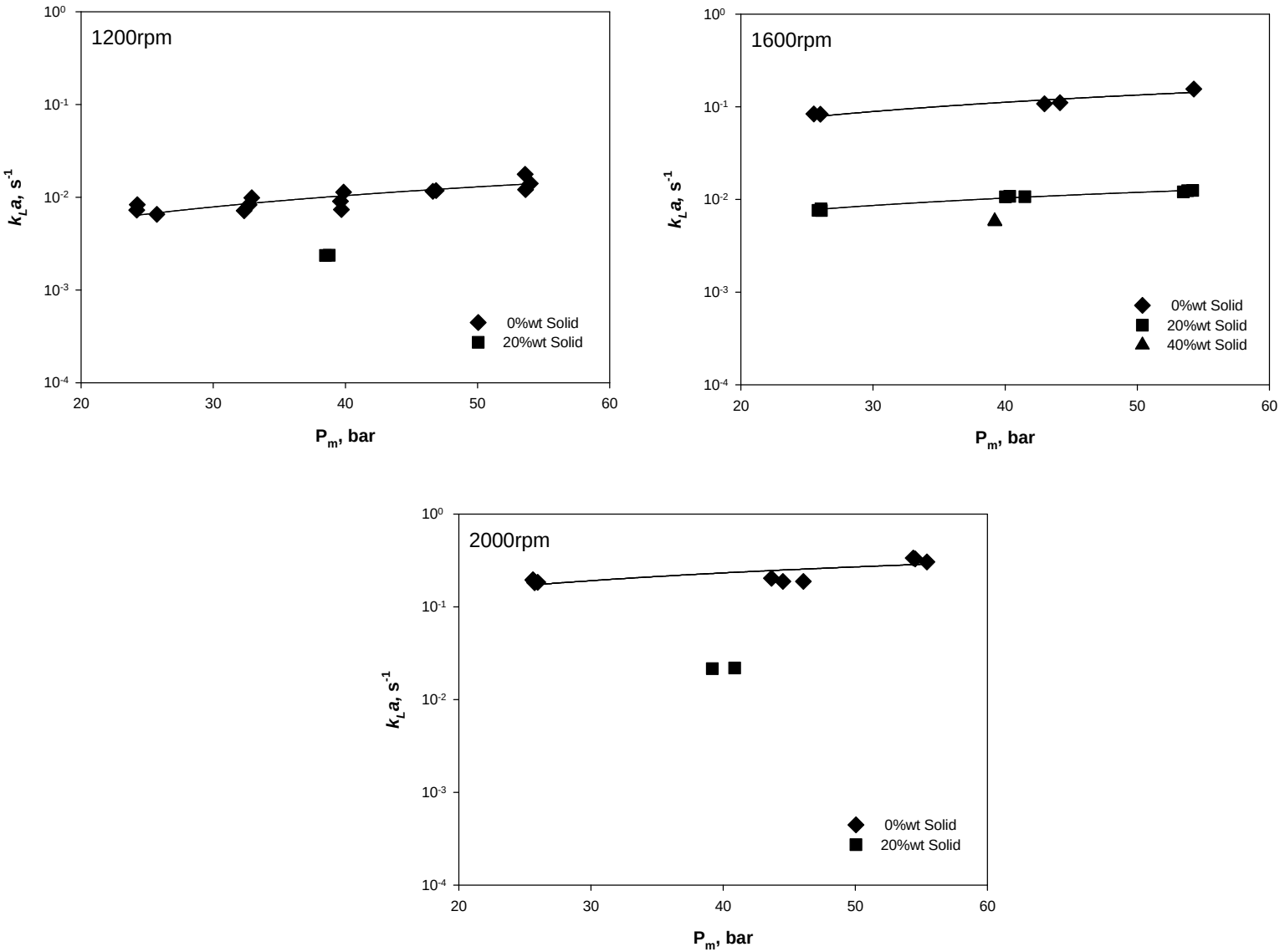

Figure 4.29. Effect of solid concentrations on k_La at 523K in residue A

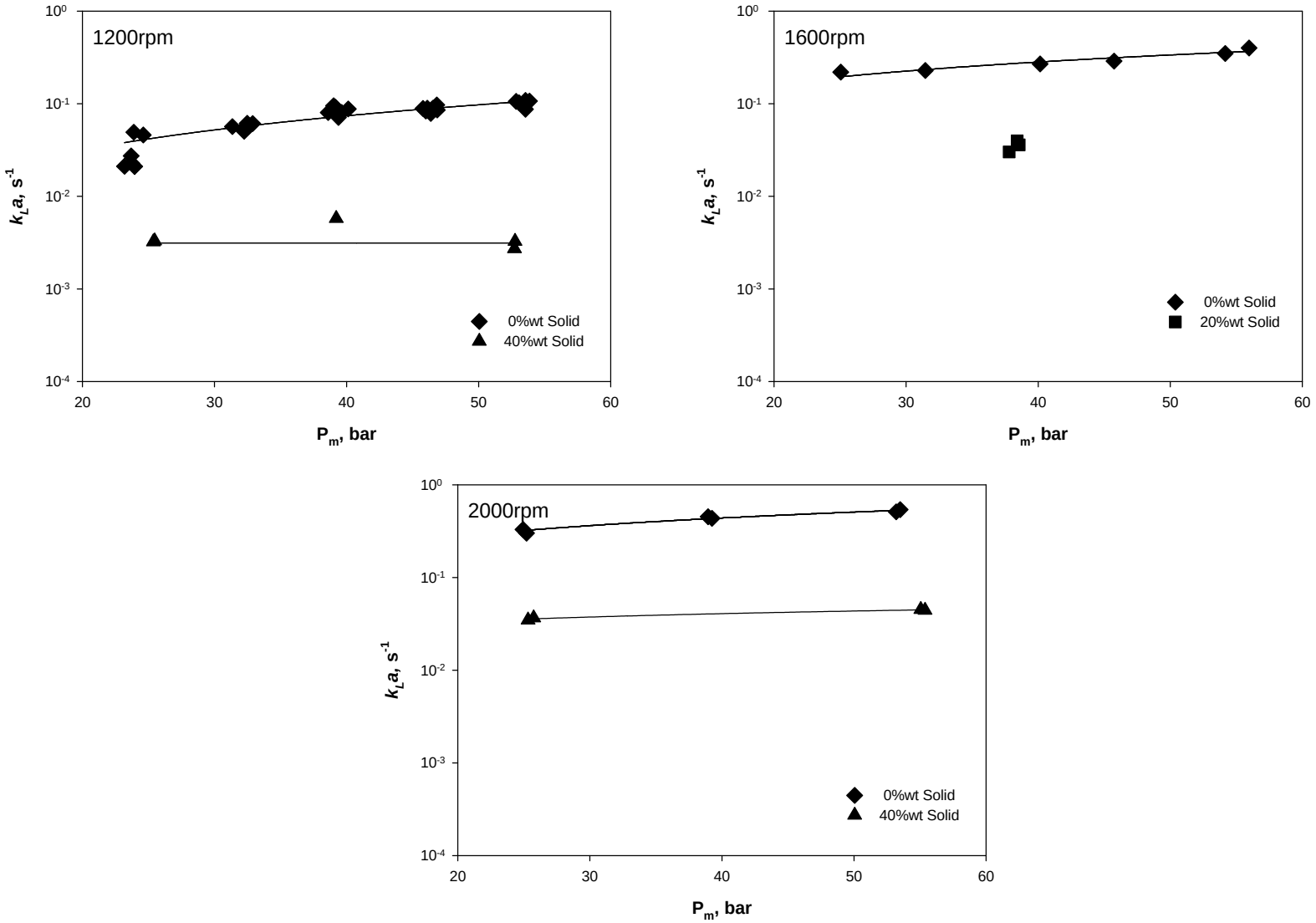

Figure 4.30. Effect of solid concentrations on k_La at 573K in residue A

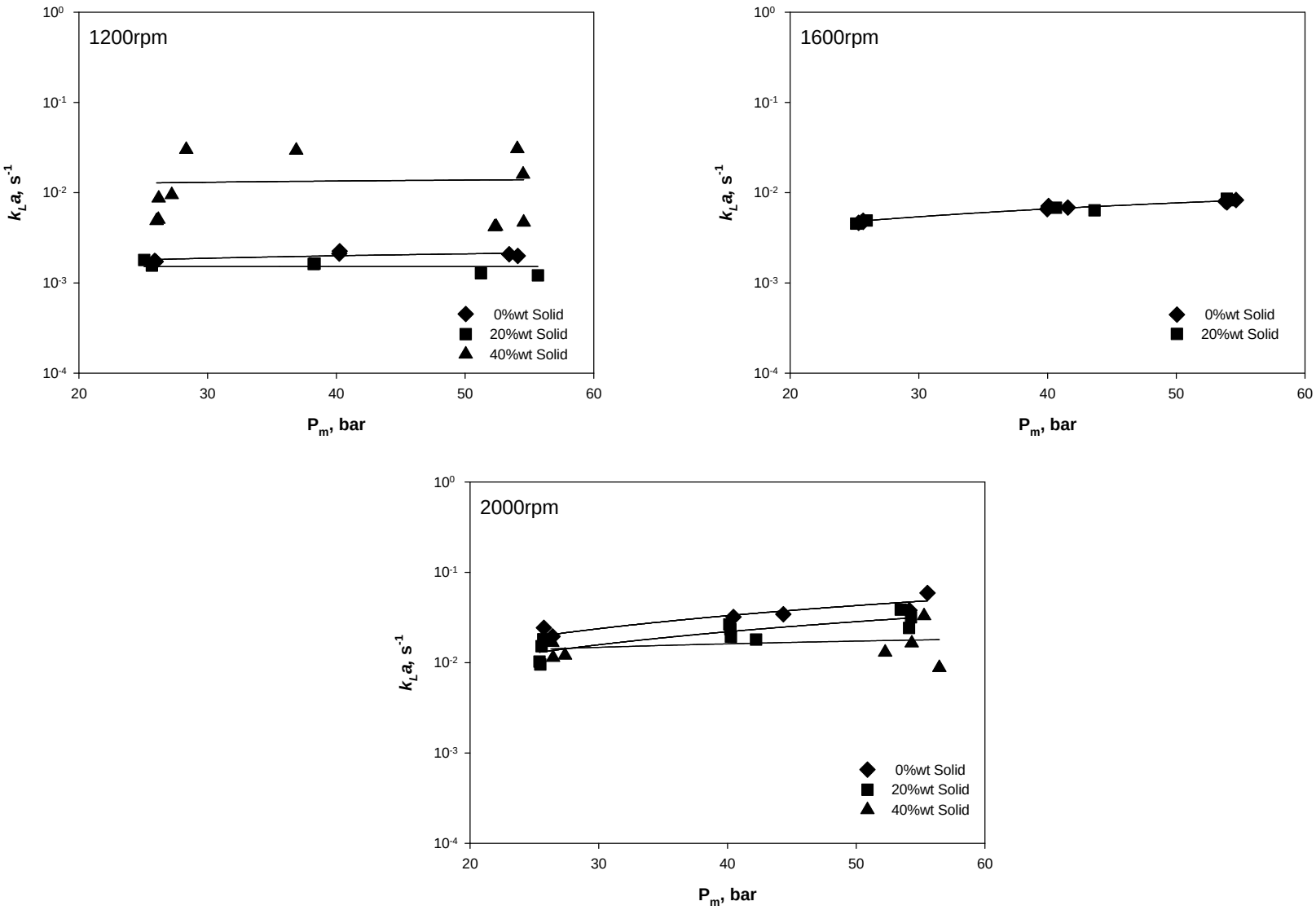

Figure 4.31. Effect of solid concentrations on k_La at 473K in residue B

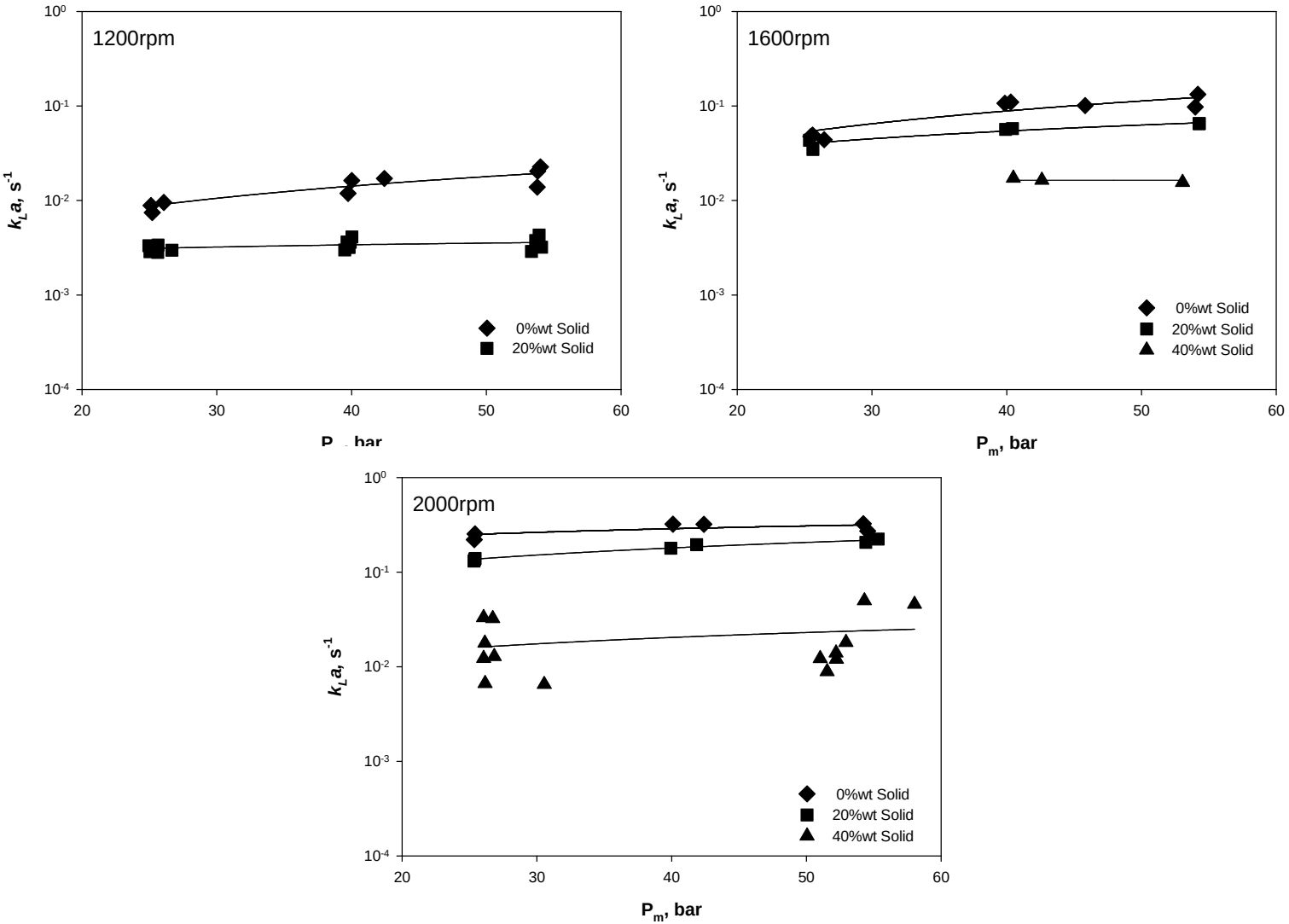

Figure 4.32. Effect of solid concentrations on k_La at 523K in residue B

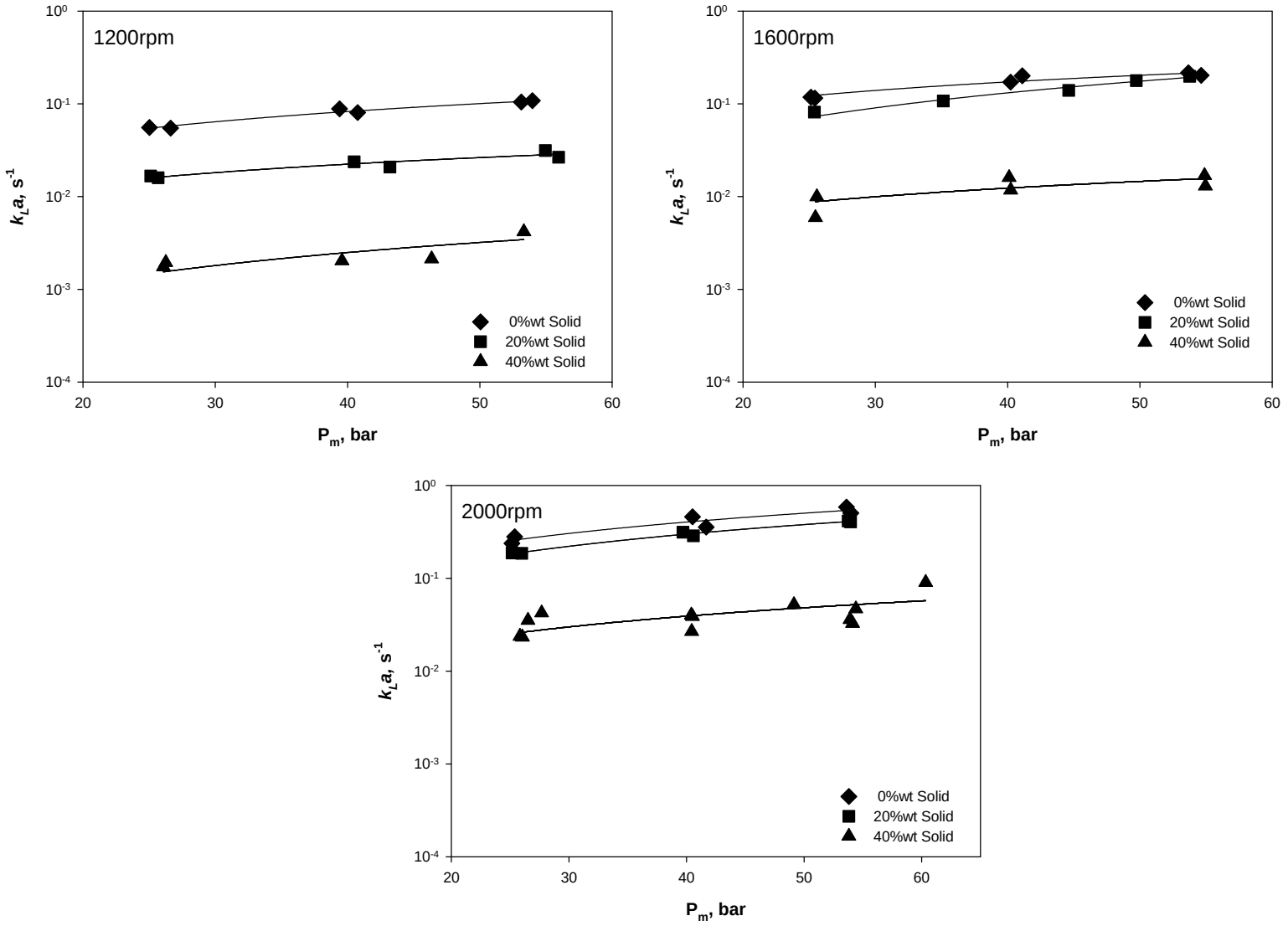

Figure 4.33. Effect of solid concentrations on k_La at 573K in residue B

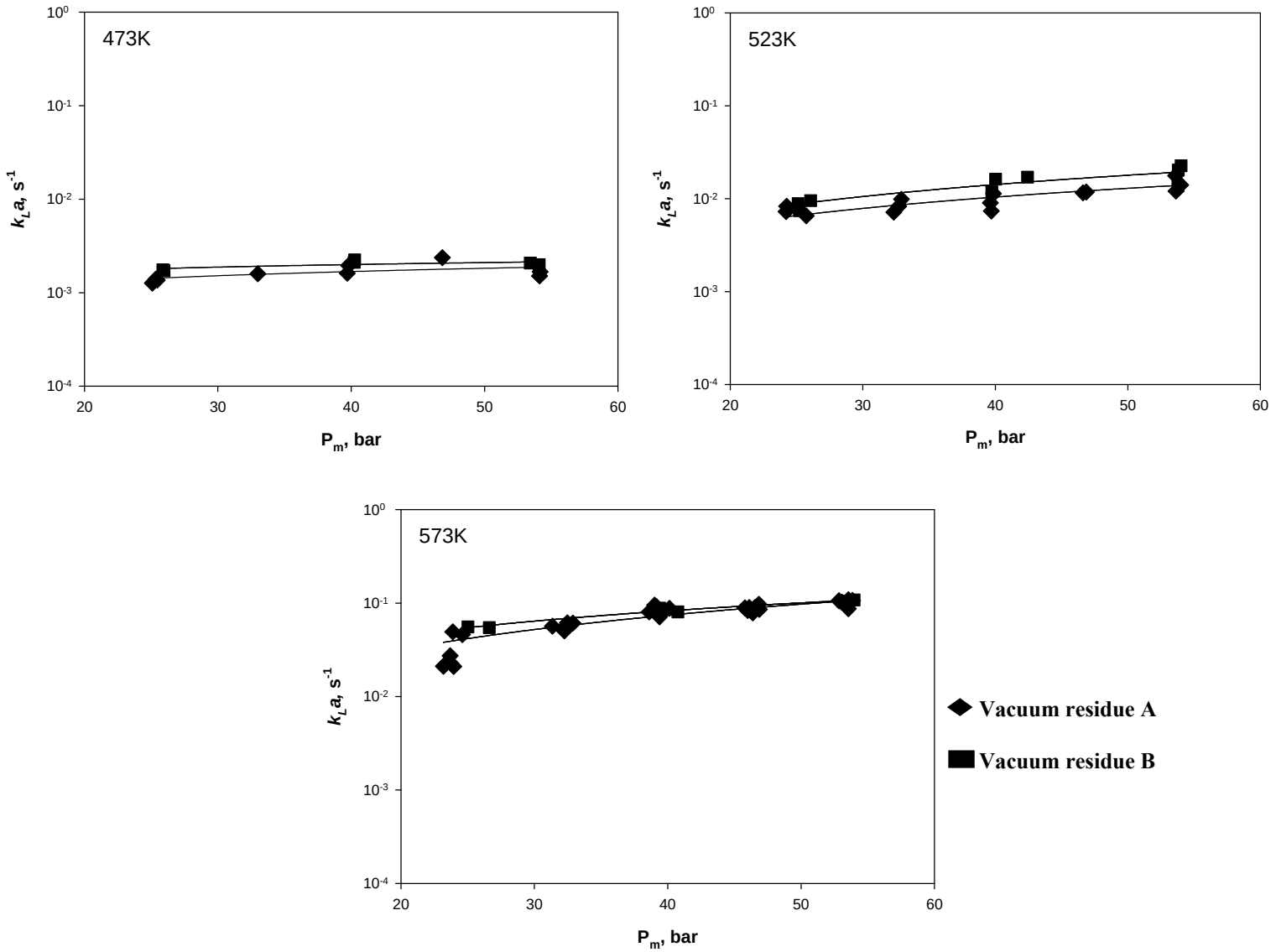

Figure 4.34. Effect of liquid nature on k_La at 0 wt% solid and 1200 rpm

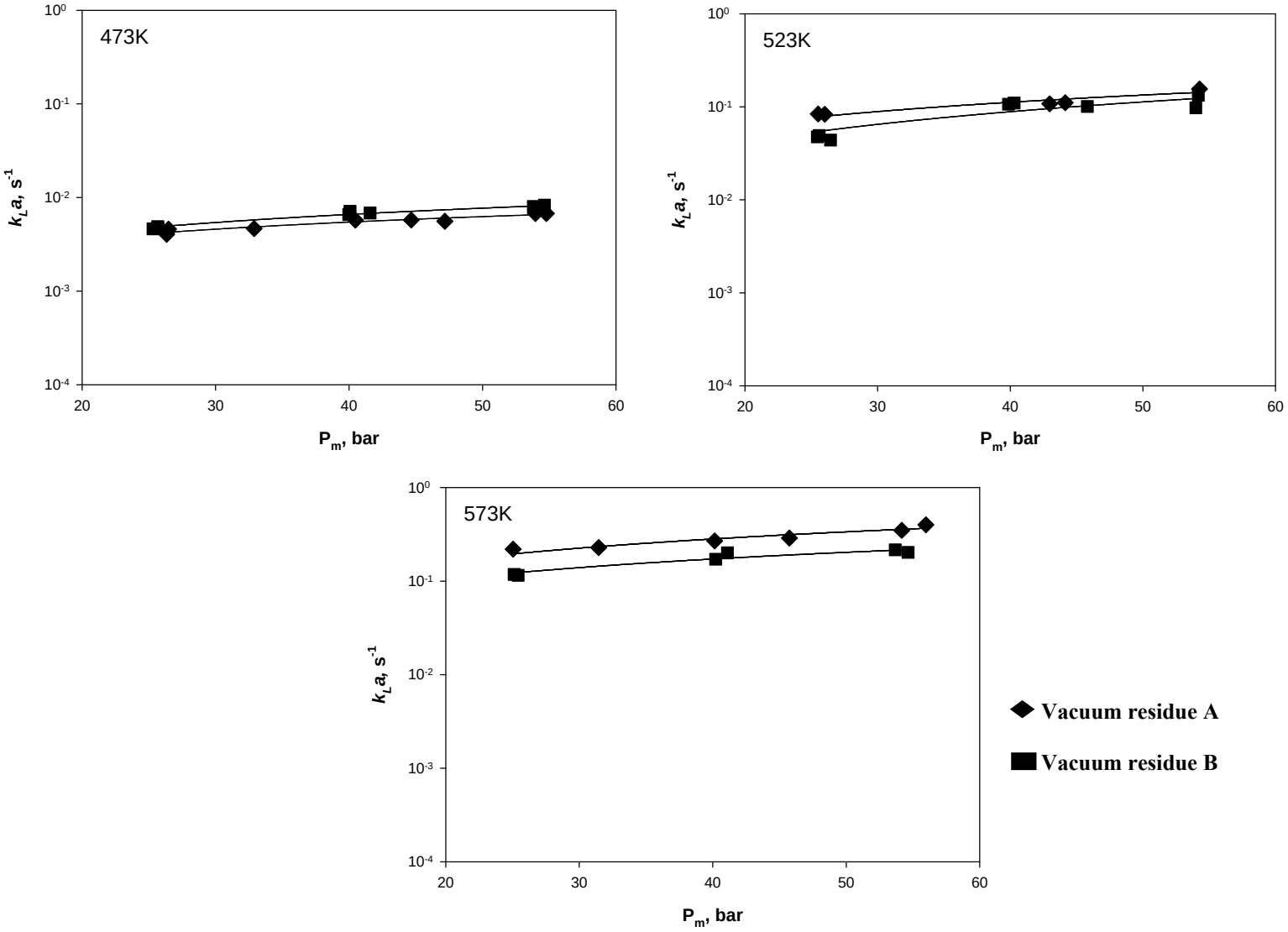

Figure 4.35. Effect of liquid nature on k_La at 0 wt% solid and 1600 rpm

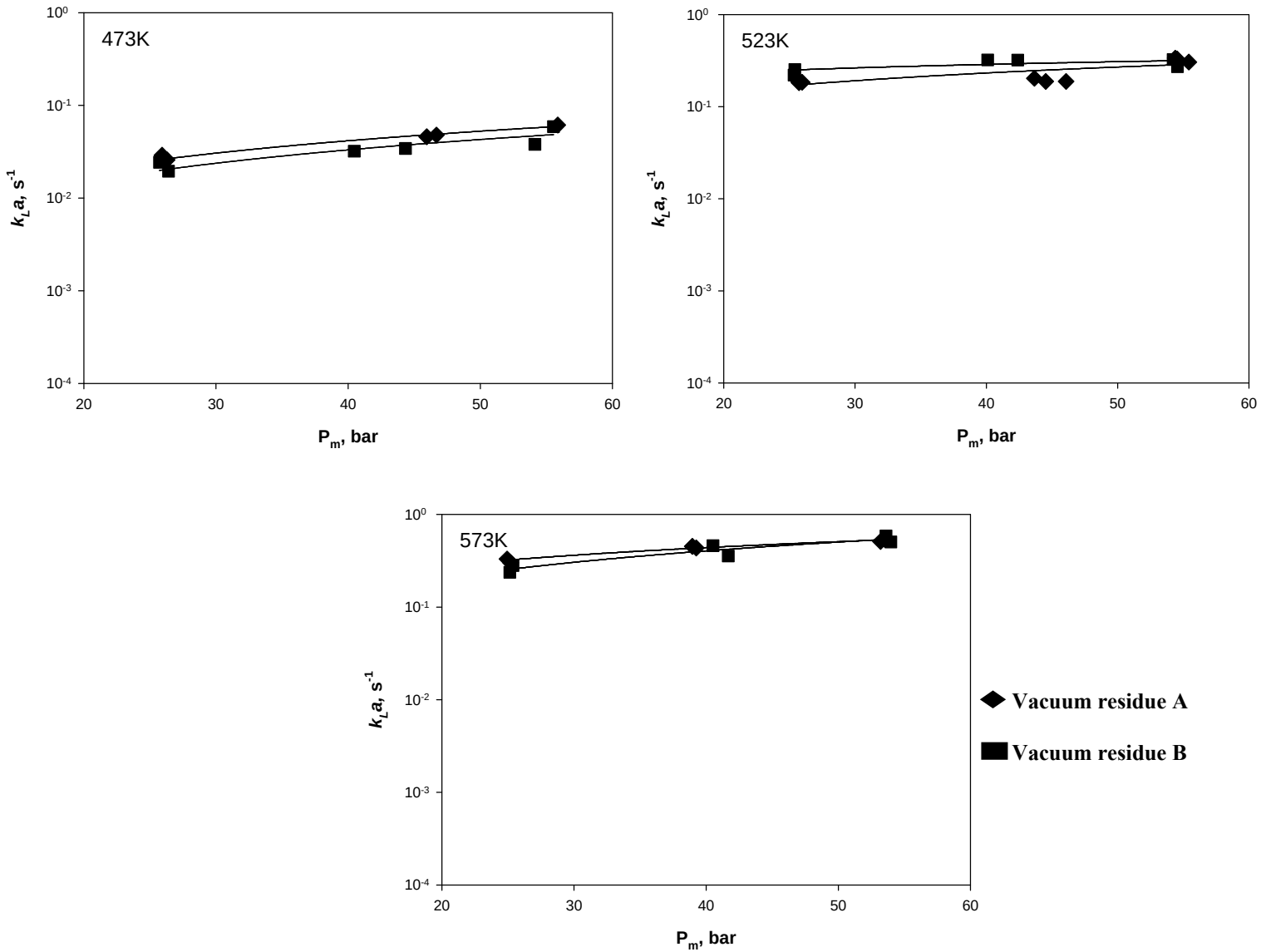

Figure 4.36. Effect of liquid nature on k_La at 0 wt% solid and 2000 rpm

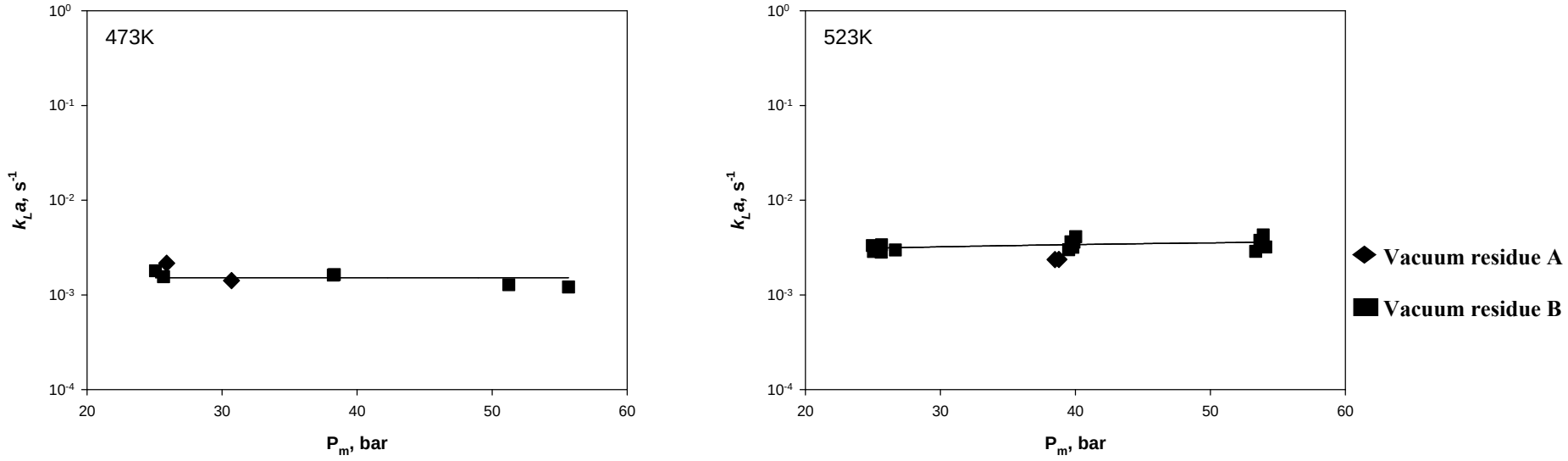

Figure 4.37. Effect of liquid nature on k_La at 20 wt% solid and 1200 rpm

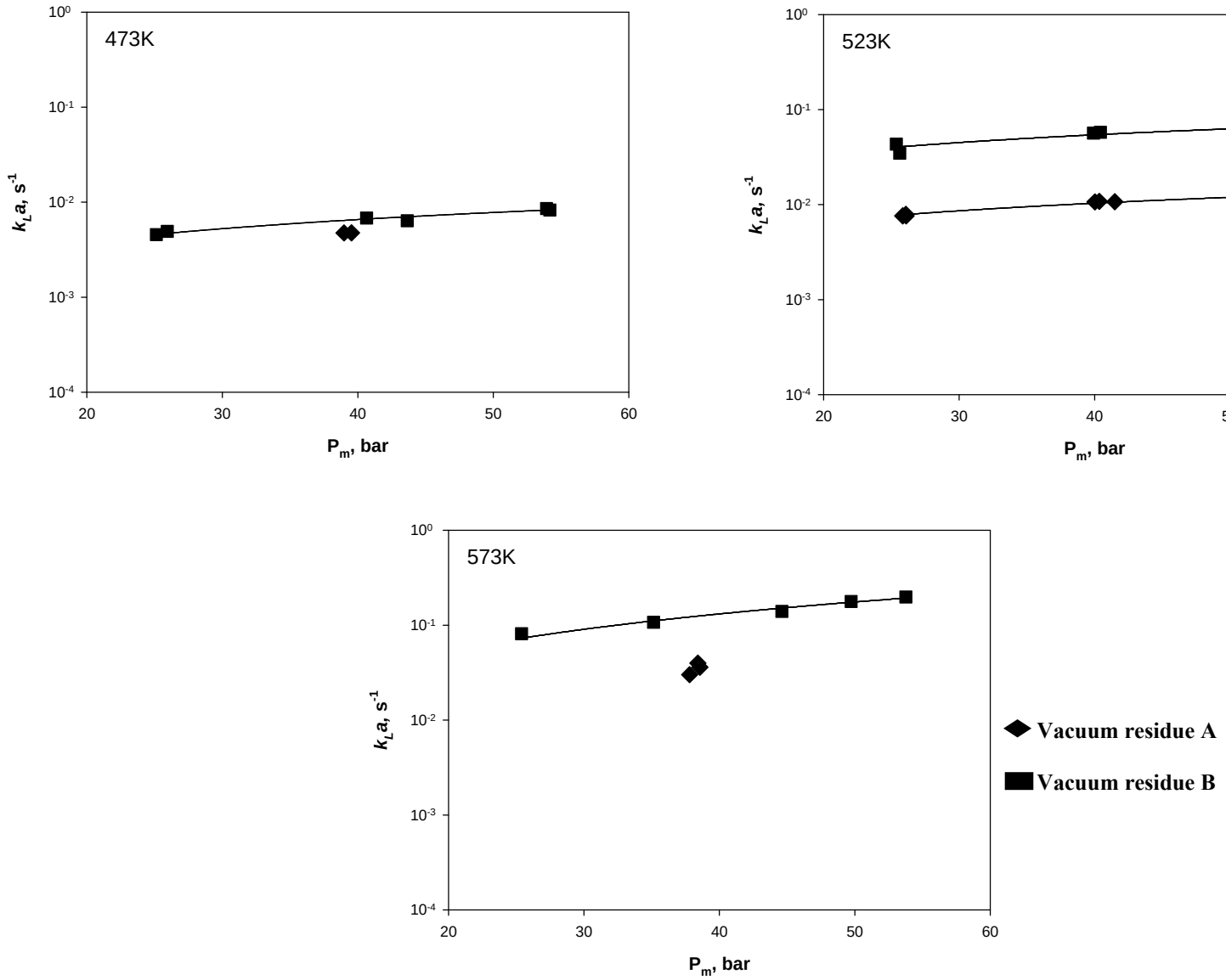

Figure 4.38. Effect of liquid nature on k_La at 20 wt% solid and 1600 rpm

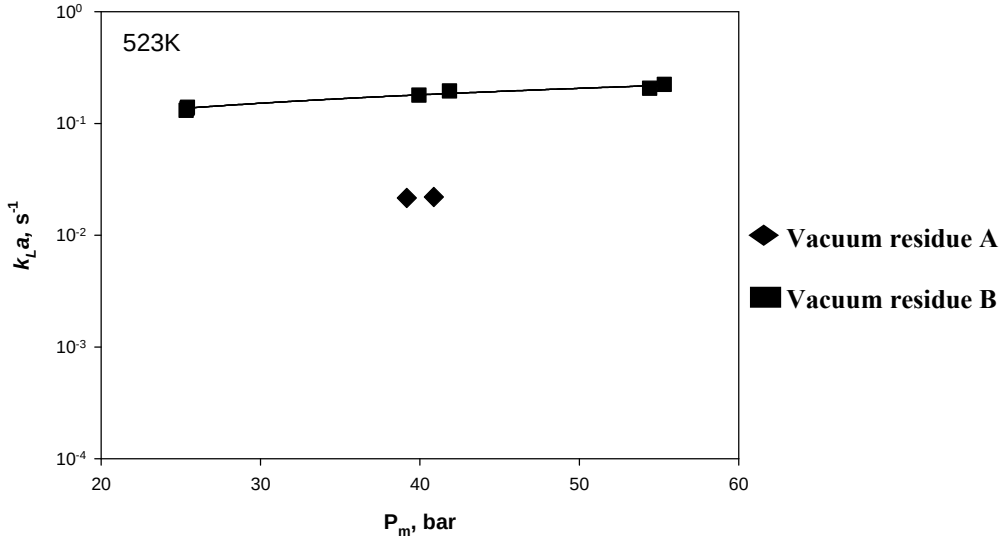

Figure 4.39. Effect of liquid nature on k_La at 20 wt% solid and 2000 rpm

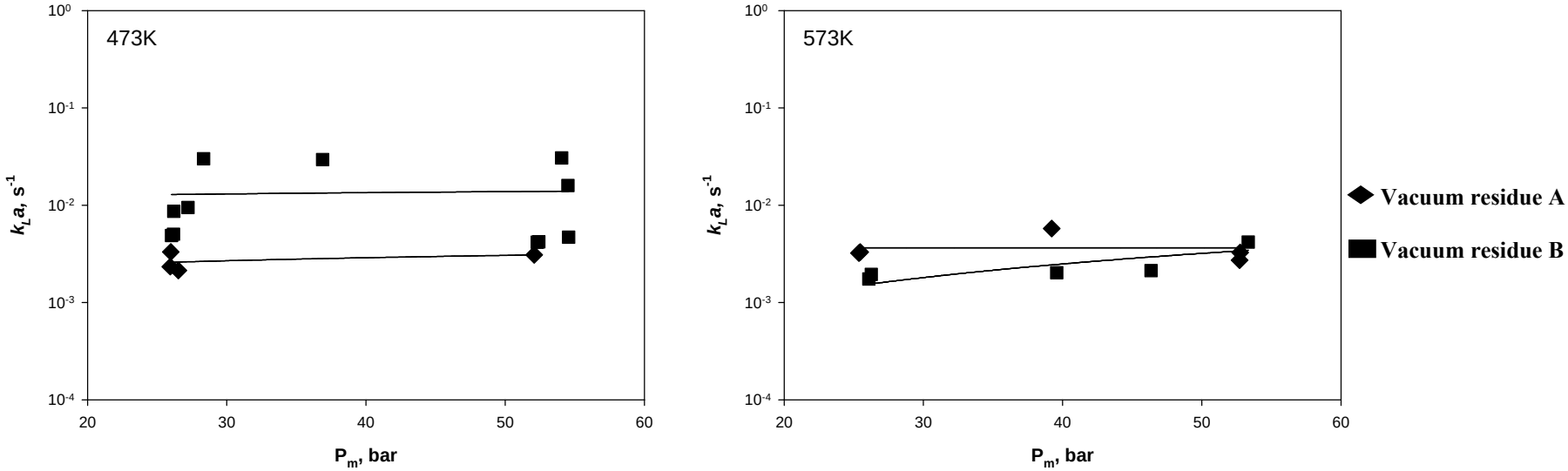

Figure 4.40. Effect of liquid nature on k_La at 40 wt% solid and 1200 rpm

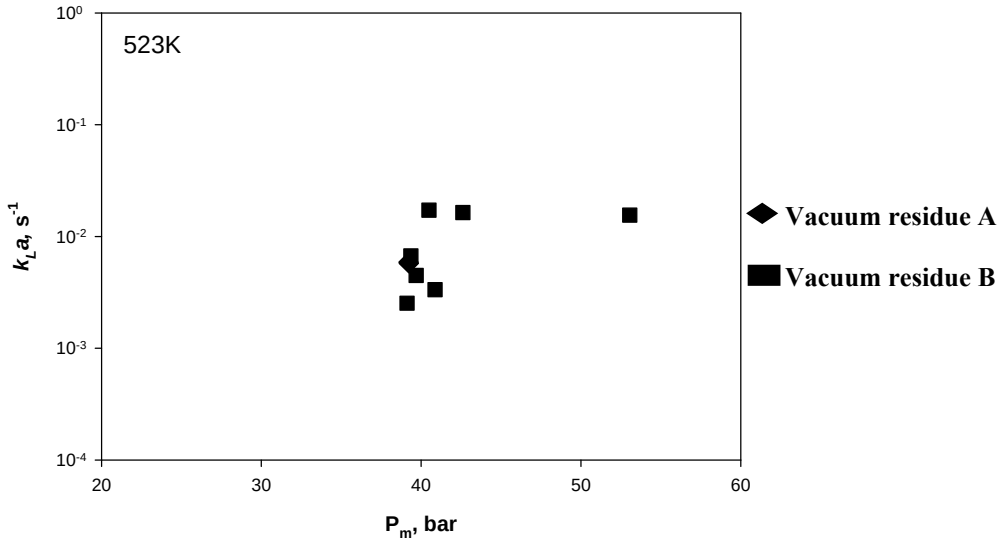

Figure 4.41. Effect of liquid nature on $k_L a$ at 40 wt% solid and 1600 rpm

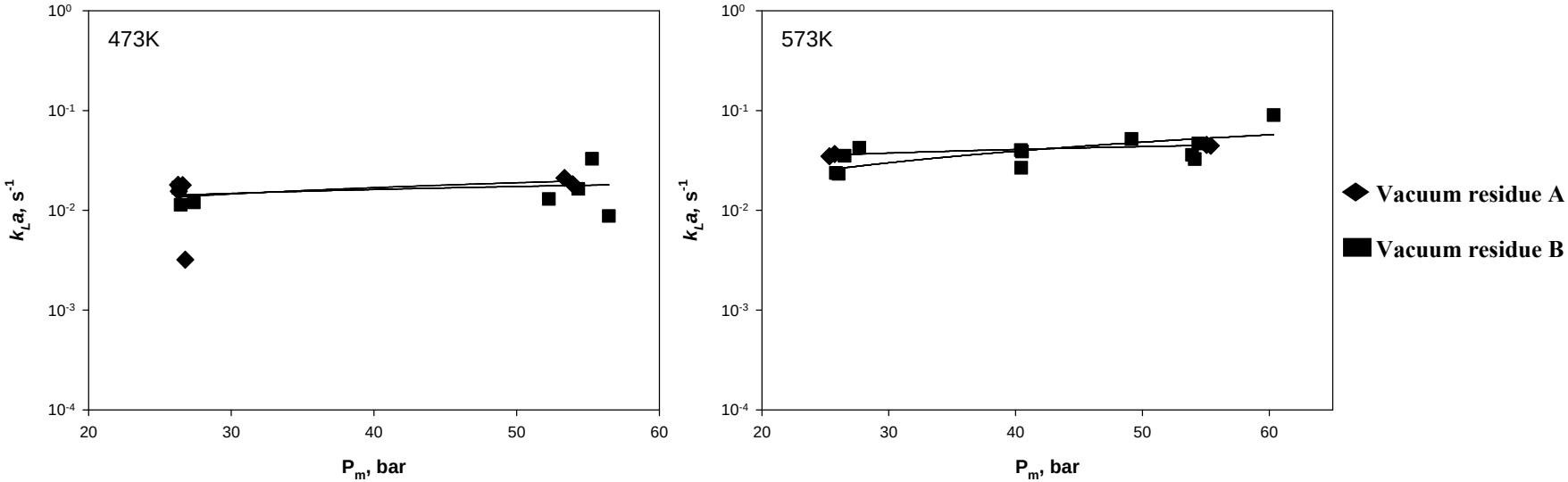

Figure 4.42. Effect of liquid nature on $k_L a$ at 40 wt% solid and 2000 rpm

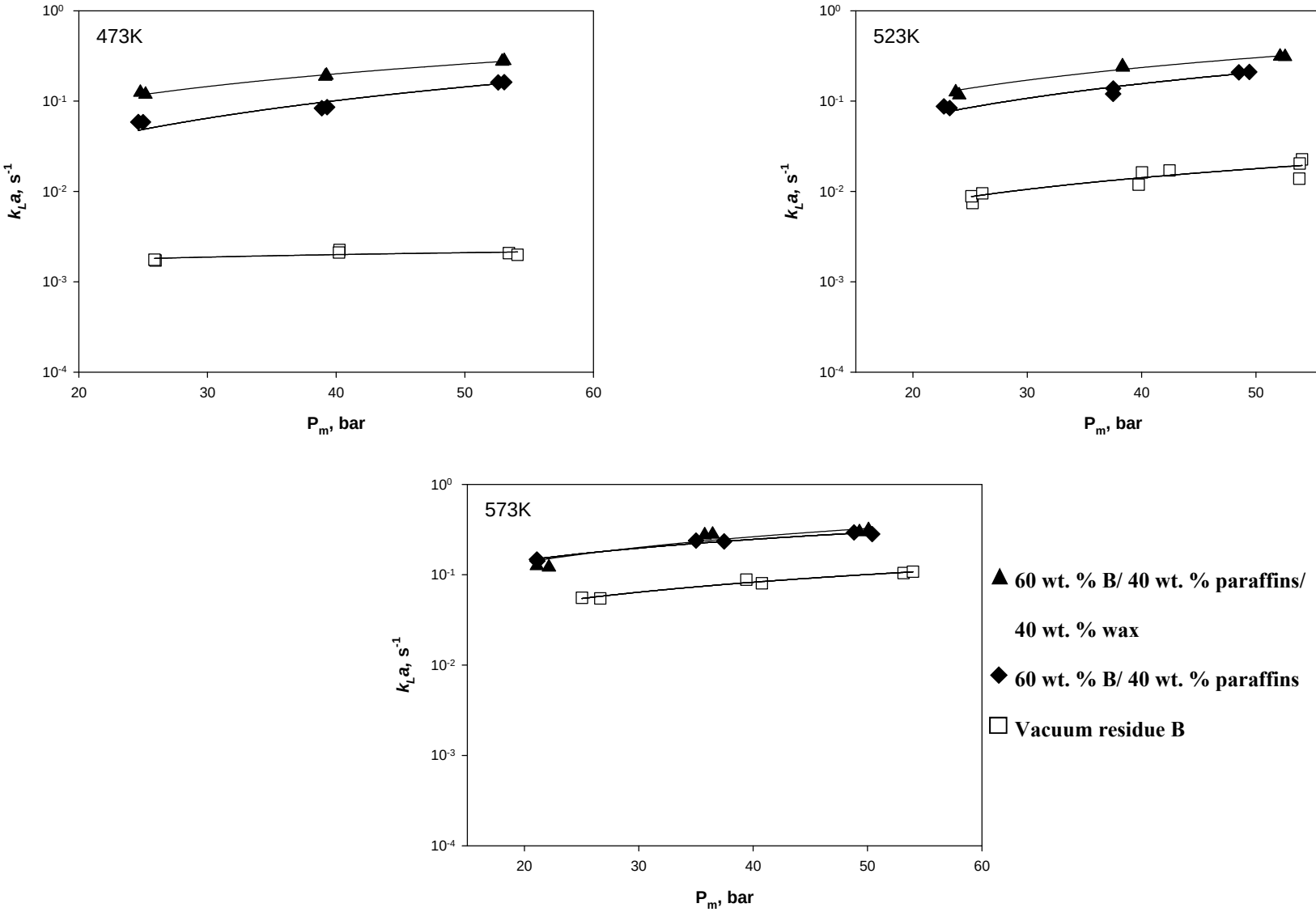

Figure 4.43. Effect of liquid nature on k_La , liquid mixtures 1200 rpm

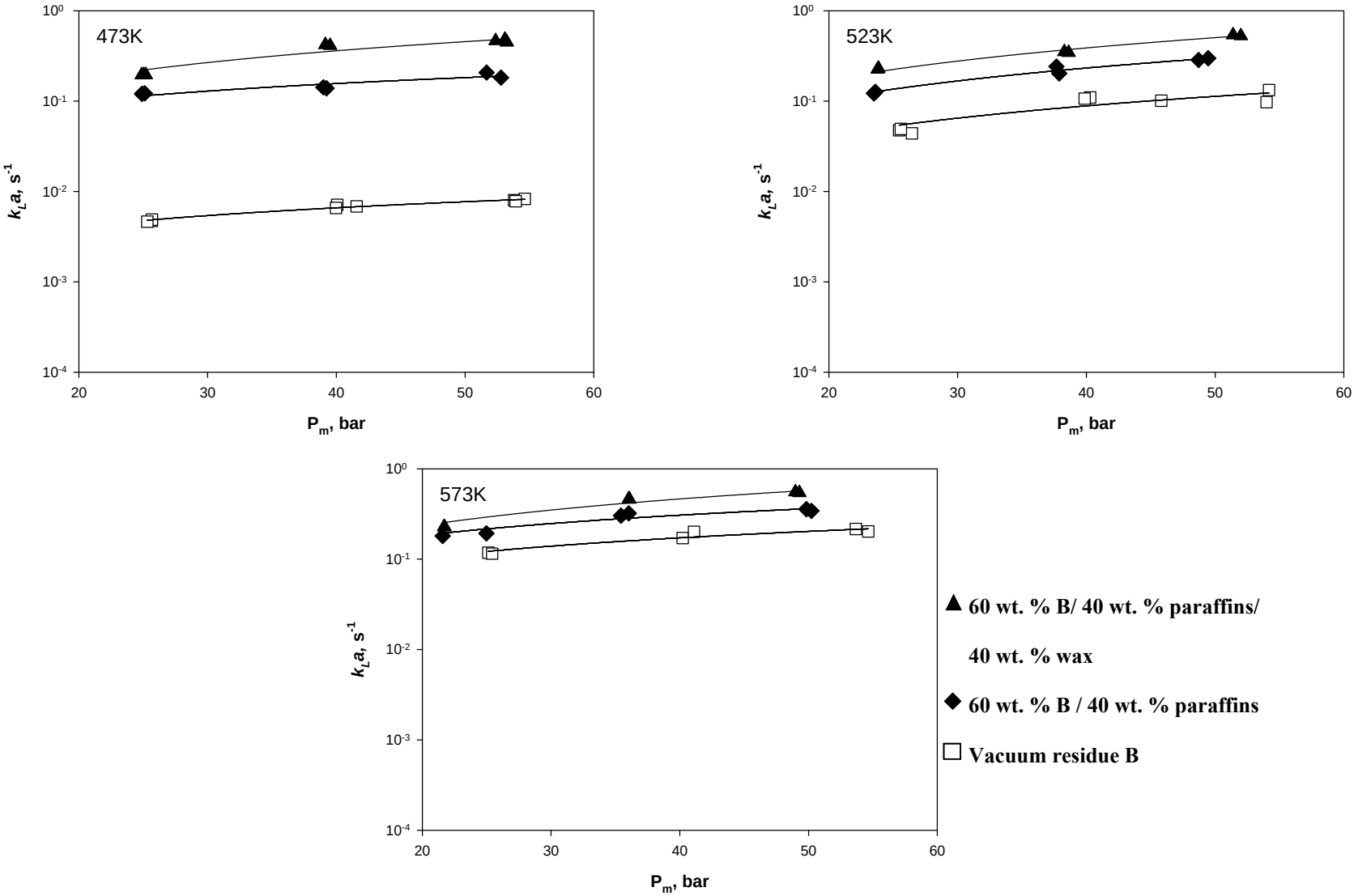

Figure 4.44. Effect of liquid nature on k_La , liquid mixtures 1600 rpm

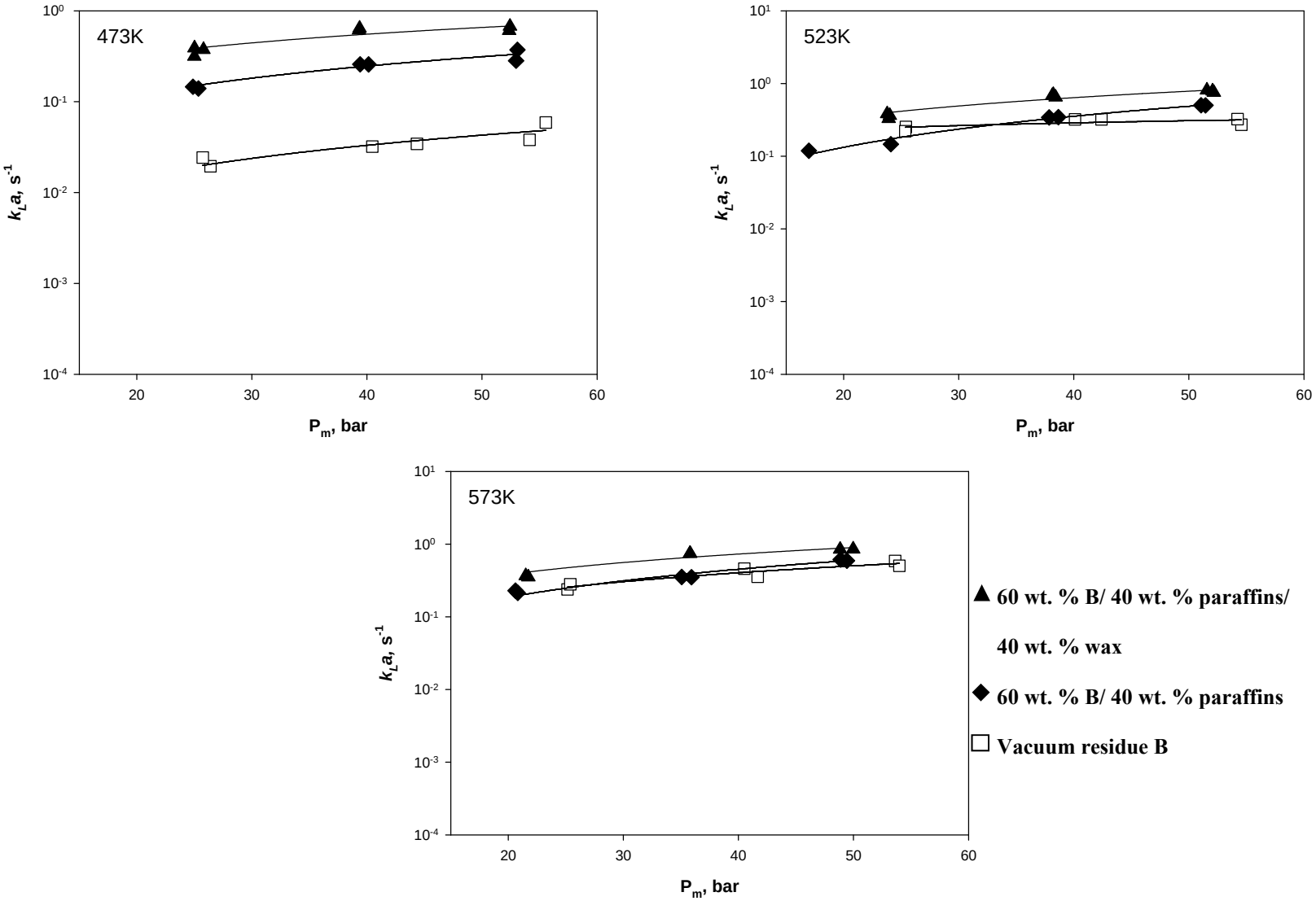

Figure 4.45. Effect of liquid nature on k_La, liquid mixtures 2000 rp

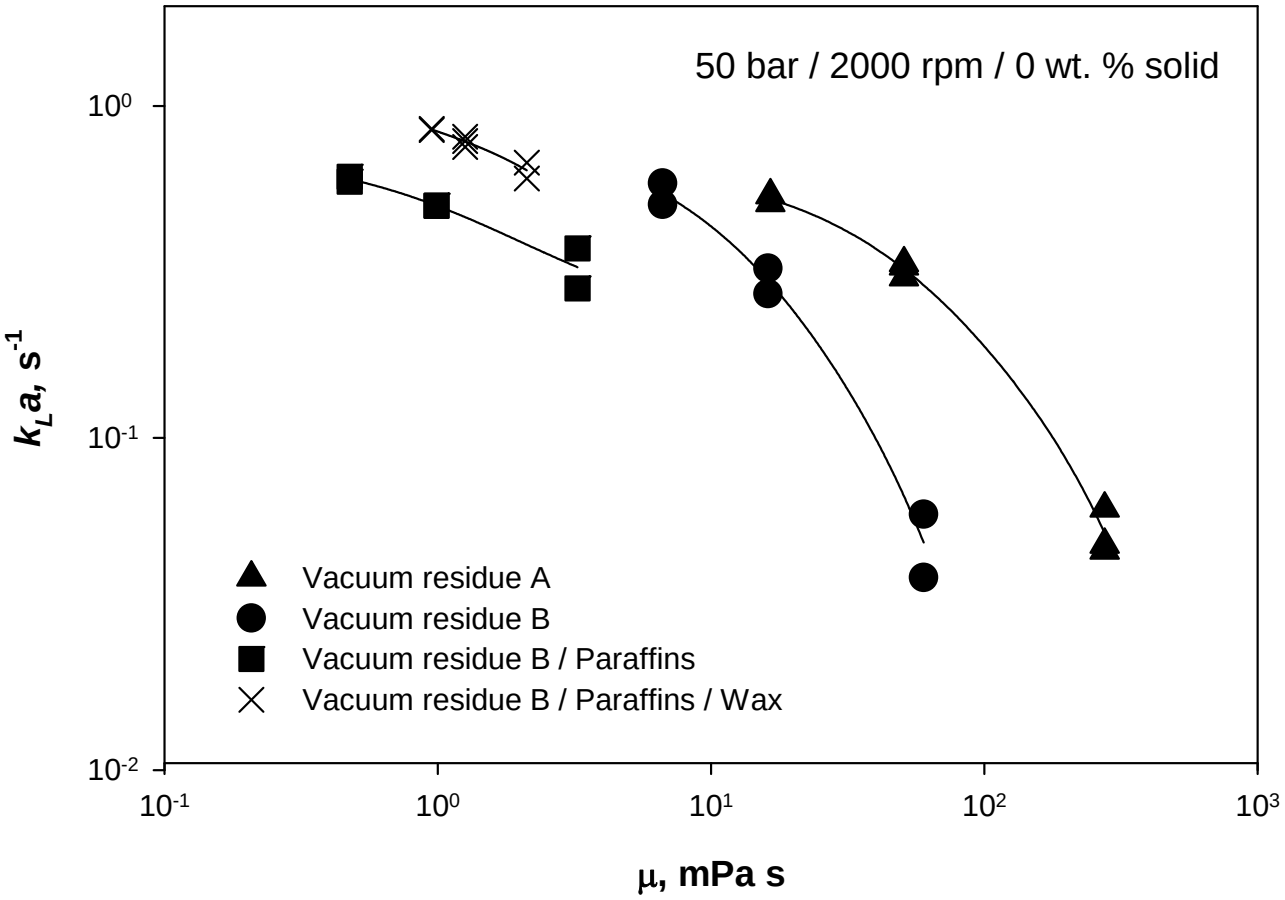

Figure 4.46. Effect of liquid viscosity on k_La

4.3 STATISTICAL CORRELATIONS OF THE H_2 VOLUMETRIC LIQUID-SIDE MASS TRANSFER COEFFICIENTS

The k_La values of H_2 in the four liquid used, obtained using the Central Composite Statistical Design, were correlated using the following empirical statistical correlation:

$$\ln(k_L a) = \beta_0 + \sum_{i=1}^{4} \beta_i x_i + \sum_{i=1}^{4} \sum_{j \geq i}^{4} \beta_{ij} x_i x_j \qquad (4\text{-}9)$$

Where x_i and x_j are the coded variables (Table **3**.**11**); and β_0, β_j, β_{ij} are constants.

The constants in Equation (4-9), listed in Table 4.6, were calculated, with an $R^2 > 90\%$ using the least square method. A comparison between the experimental and predicted k_La values for H_2, in vacuum residues A and B is given in Figure 4.47. As can be observed in this figure, these correlations fit the experimental data with an average deviation of ±45%. It should be mentioned that this statistical correlation is restricted to the gas-liquid system and valid only within the operating conditions used in this study and therefore it should not be used for other systems under different operating conditions.

Table 4.6. Coefficients in Equation (4-9)

	Vacuum residue A	**Vacuum residue B**
β_0	-4.4369	-3.544
β_1	0.9857	1.1331
β_2	-0.7738	-1.0013
β_3	1.1549	1.3412
β_4	0.1711	0.2861
β_{11}	-0.1585	-0.1049
β_{22}	0.6839	-0.3765
β_{33}	-0.0757	-0.2198
β_{44}	-0.0104	0.0362
β_{12}	-0.769	-0.5811
β_{13}	-0.1139	-0.0282
β_{14}	9.74×10^{-2}	1.05×10^{-4}
β_{23}	-0.1663	-0.0354
β_{24}	-0.0988	0.0108
B_{34}	-0.0143	-0.0302

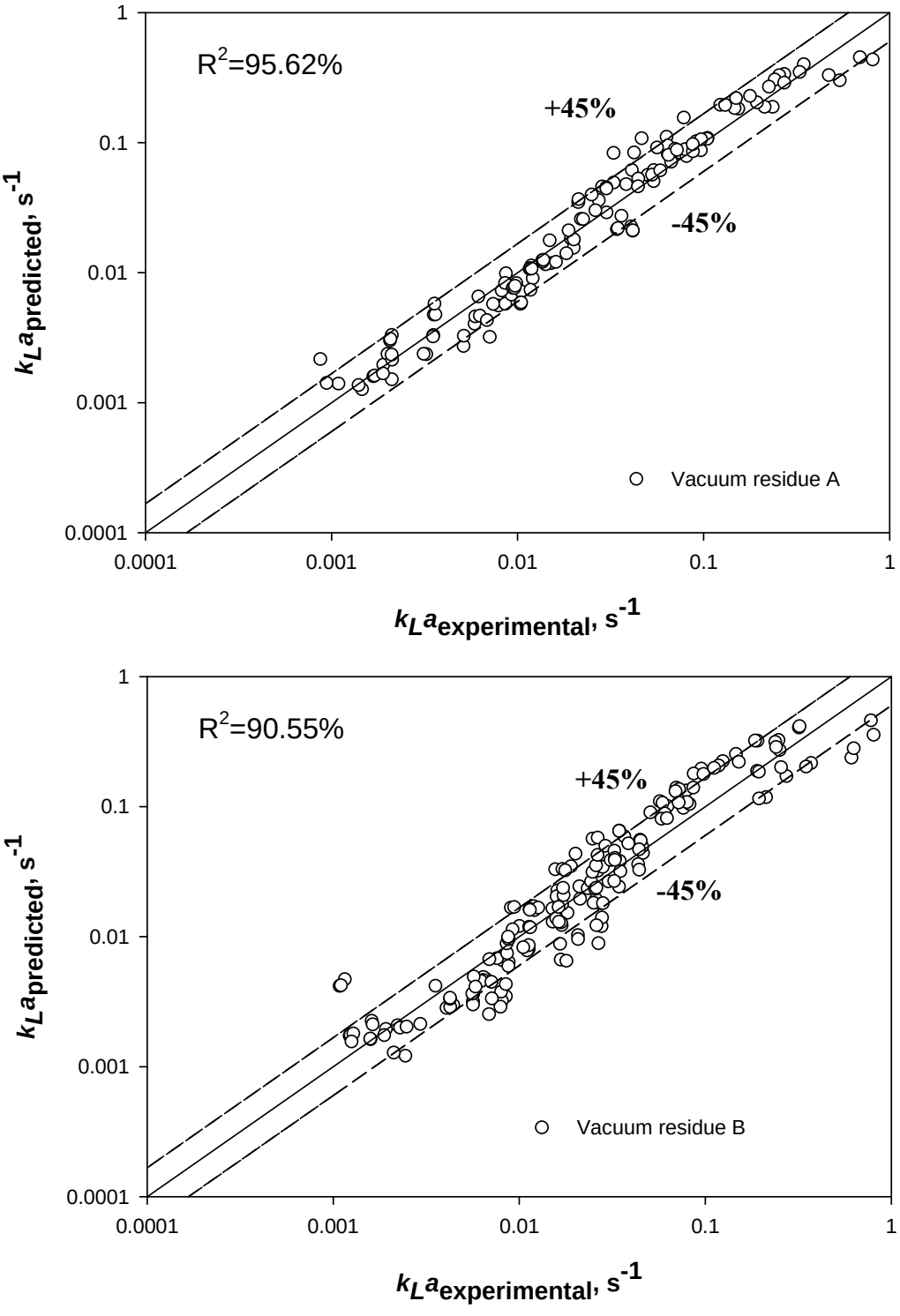

Figure 4.47. Comparison of experimental and predicted k_La values for vacuum residues A and B using statistical correlation

4.4 EMPIRICAL CORRELATIONS OF H_2 VOLUMETRIC LIQUID-SIDE MASS TRANSFER COEFFICIENTS

The k_La values obtained for H_2 in vacuum residues A and B and for the two liquid mixtures were also correlated using dimensionless numbers following Soriano's empirical correlation[77] as follows:

$$Sh = 1.24\times10^{-8}\, Sc^{0.5} Eu^{0.55} We^{2.21} Re^{0.51} e^{(11.77 C_s^{\,2} - 8.36 C_s)} \tag{4-10}$$

With this correlation, it is possible to predict the experimental Sherwood Number (Sh) with a regression coefficient, $R^2 > 57\%$ which seems to be a poor correlation, as can be seen in Figure 4.48. Again, the above correlation is only valid within the ranges of dimensionless numbers given in Table 4.7.

Table 4.7. Lower and upper limits of the dimensionless numbers in Equation (4-10)

Variable	Minimum	Maximum
Sc	24	5,129,279
Eu	1986	19,368
We	648	3,248
Re	47	50,504
Cs	0	0.4

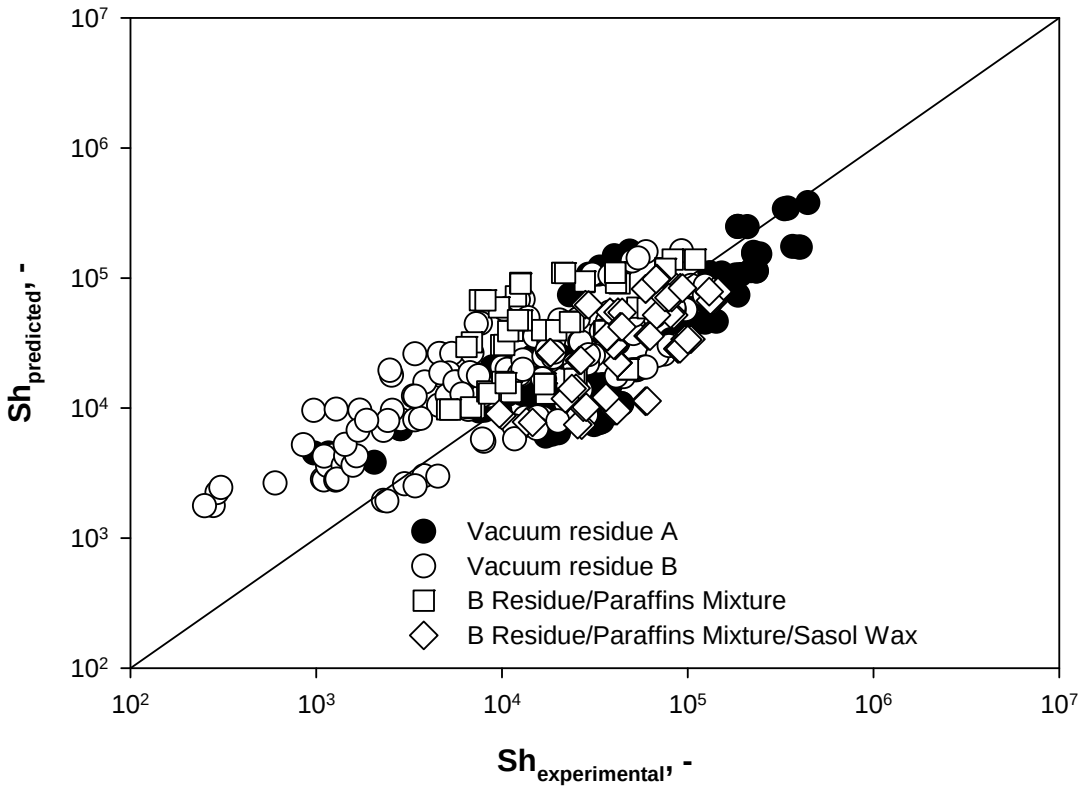

Figure 4.48. Comparison between predicted and experimental *Sh* values

4.5 MODELING OF HYDROCRACKING OF VACUUM RESIDUE IN A SERIES OF CSTRs

Sanchez et al.[1] proposed the following scheme (Figure 4.49) to describe hydrocracking of vacuum residue at three different temperatures 380, 400 and 420 ^{o}C with the corresponding kinetic rate constants shown in Table 4.8.

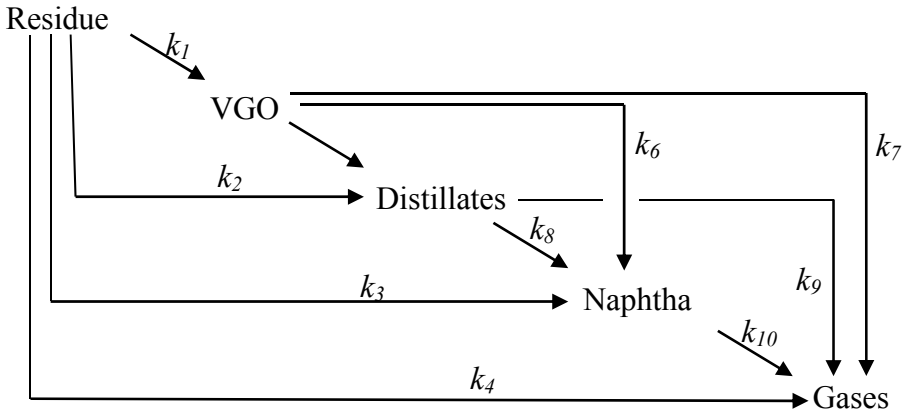

Figure 4.49. Proposed kinetic models by Sanchez[1]

Table 4.8. Kinetic parameters of Sanchez's model[1]

Kinetic constant (h^{-1})	Temperature			Activation energy E_A(kcal/mol)
	380°C	400°C	420°C	
Residue				
k_1	0.042	0.147	0.362	48.5
k_2	0.008	0.022	0.057	44.2
k_3	0.008	0.020	0.043	38.0
k_4	0.041	0.098	0.137	27.3
VGO				
k_5	0.018	0.057	0.104	39.5
k_6	0	0.007	0.016	37.1
k_7	0	0	0	-
Distillate				
k_8	0	0.003	0.010	53.7
k_9	0	0	0	-
Naphta				
k_{10}	0	0	0	-

In our study, a series of CSTRs was used to model the hydrocracking of vacuum residue in a slurry process as depicted in Figure 4.50 using the reaction rate constants given by Sanchez at al. [1]. Each CSTR is equipped with one impeller, a gas distributor, baffles, and gas as well as liquid

inlets and outlets. The gas is sparged at the bottom of the reactor into the liquid through a multi-orifices gas distributor. The gas/liquid mixing is insured using the impeller. The gas and liquid phases are fed continuously to the CSTRs in a co-current scheme. The gas and liquid exiting the n^{th} reactor represent the feed for the $(n+1)^{th}$ reactor. The "standard" geometrical ratios accepted in the literature [124] for CSTRs are given in Table 4.9.

Table 4.9. Geometrical ratios of agitated reactors

Ratios	Ranges
H/d_T	1
d_{imp}/d_T	1/4 - 1/2
H_L/d_T	1/2 - 5/6
d_w/d_{imp}	1/4 - 1/6
W/d_T	1/10 – 1/12

In order to formulate the model, the following assumptions were made: (1) hydrogen in excess is flown through the reactors and consequently the kinetics of the reaction is independent of hydrogen concentration and the resistance to gas-liquid mass transfer for hydrogen is negligible, (2) the mass transfer resistance for the gaseous products is negligible, (3) the gas-phase is in thermal equilibrium with the liquid phase and the process occurs isothermally, (4) the liquid and gas superficial velocities are constants, (5) all the hydrocracking reactions take place in the liquid-phase, and (6) the CSTRs operate under steady state conditions. The mass balance equations for the residue and the reaction products are given in the following:

The residue mass balance is:

$$-\frac{(U_{L,R_i}C_{R,L,R_{i-out}} - U_{L,R_i}C_{R,L,R_{i-in}})}{H} + r_R = 0 \quad (4\text{-}11)$$

where $r_R = -(k_1 + k_2 + k_3 + k_4)C_R$ [1]

The VGO mass balance is:

$$-\frac{(U_{L,R_i}C_{VGO,L,R_{i-out}} - U_{L,R_i}C_{VGO,L,R_{i-in}})}{H} + r_{VGO} = 0 \quad (4\text{-}12)$$

where $r_{VGO} = k_1 C_R - (k_5 + k_6)C_{VGO}$ [1]

The distillate mass balance is:

$$-\frac{(U_{L,R_{i-out}}C_{D,L,R_{i-out}} - U_{L,R_i}C_{D,L,R_{i-in}})}{H} + r_D = 0 \quad (4\text{-}13)$$

where $r_D = k_2 C_R + k_5 C_{VGO} - (k_8)C_D$ [1]

The naphtha mass balance is:

$$-\frac{(U_{L,R_i}C_{N,L,R_{i-out}} - U_{L,R_i}C_{N,L,R_{i-in}})}{H} + r_N = 0 \quad (4\text{-}14)$$

where $r_N = k_3 C_R + k_6 C_{VGO} + k_8 C_D$ [1]

The gaseous products mass balance is:

$$-\frac{(U_{L,R_i}C_{GP,L,R_{i-out}} - U_{L,R_i}C_{GP,L,R_{i-in}})}{H} + r_{GP} = 0 \quad (4\text{-}15)$$

where $r_{GP} = k_4 C_R$ [1]

These equations were solved numerically using Excel and the results are discussed below.

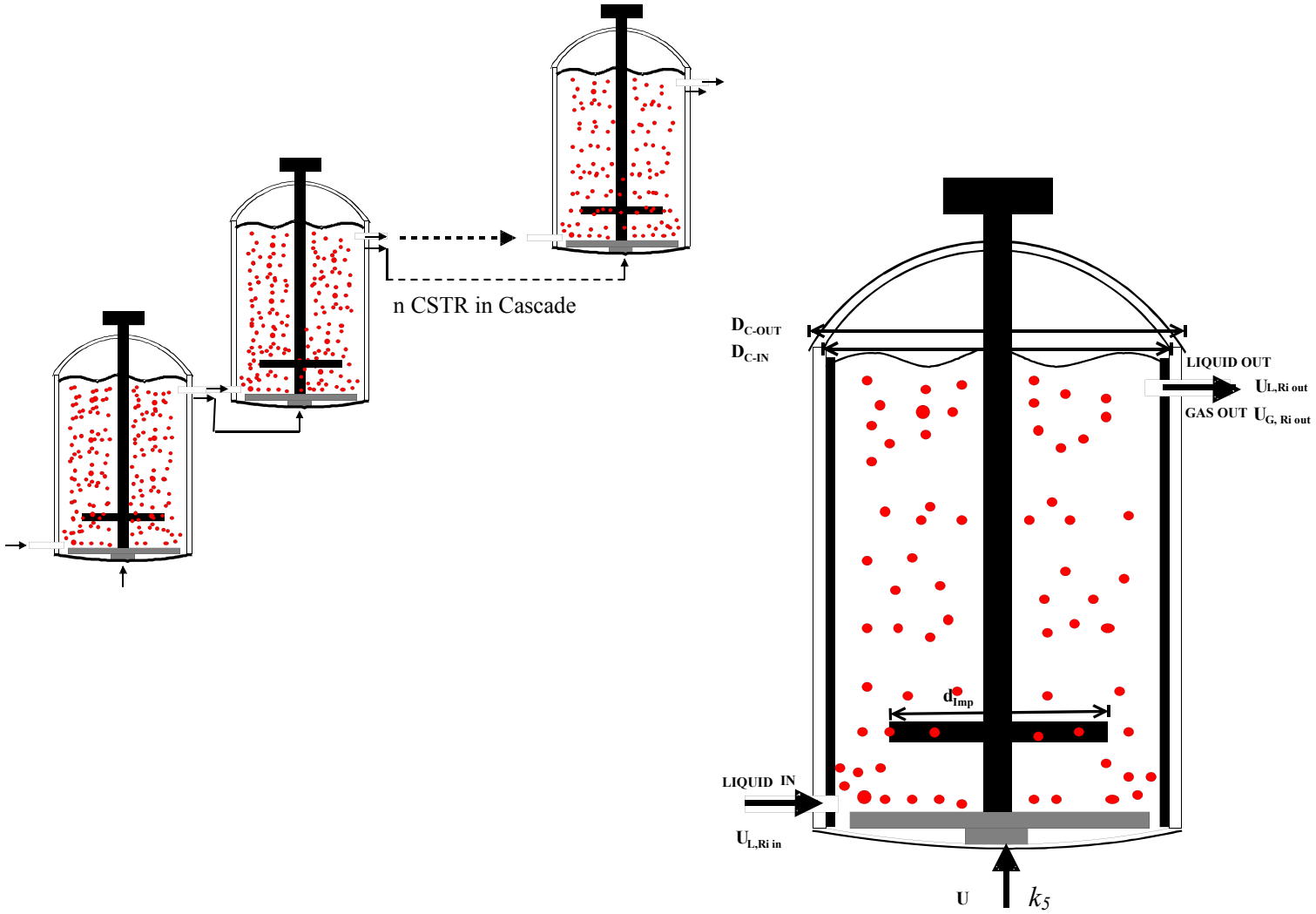

Figure 4.50. Arrangement of n-GSRs in series.

In order to calculate the residue conversion in the series of CSTRs considering a first order reaction according to Sanchez et al. [1], the following analysis was made.

For a first order reaction: A → B, the reaction rate in a CSTR can be expressed as:

$$F_{A0}\left(\frac{x}{V_R}\right) = -r_A = kC_A \tag{4-16}$$

In this equation, F_{Ao} is the molar flow rate (mol/h), x is the conversion and V_R is the reactor volume (m^3), k is the reaction rate constant (h^{-1}), and r_A is the reaction rate (mol/m^3.h).

The conversion for reactant (A) is defines as:

$$x = 1 - \frac{C_A}{C_{A0}} \tag{4-17}$$

The reaction rate in each reactor can be written as:

$$F_{A0} = Q_L C_{A0} \tag{4-18}$$

Combining Equations (4-16) through (4-18) gives:

$$k(1-x) = x(LHSV) \tag{4-19}$$

The above equation can be rearranged as:

$$x = \frac{k}{k + LHSV} \tag{4-20}$$

In the above equation, LHSV is the liquid hourly space velocity (h^{-1}) which can be expressed as:

$$LHSV = \frac{Q_L}{V_R} = \frac{U_L}{H_L} \tag{4-21}$$

Note that the reactor volume (V_R) is actually the liquid volume (V_L), Q_L is the liquid volumetric rate fed to the reactor, U_L is the liquid superficial velocity, and H_L is the liquid height in the reactor.

4.5.1 MODEL RESULTS

The operating conditions used in the model are shown in Table 4.10. For a series of CSTRs, different conversions can be reached as the numbers of reactors increases. Table 4.11 and 4.12 show the residue conversion (x) as well as the residue, liquid and gaseous products concentrations, for four CSTRs in series at 0.99 m h^{-1}, and 4.5 m h^{-1} superficial liquid velocity, respectively. These LHSVs were selected because they were specified in the work by Sanchez et al. [1]. As can be seen in Figure 4.51, as the number of reactors increases, the conversion increases for the two liquid velocities, however, for the same reactor number, the conversion is higher at 0.99 m h^{-1} which is the lowest liquid velocity due to the longer residence time of the residue in the reactor at this small velocity.

Table 4.10. Operating conditions used for scaling up the hydrocracking reactor

Conditions	Values
Reactor diameter, m	3.0
Liquid height, m	3.0
Temperature, K	673.15
LHSV, h^{-1}	0.33 and 1.5
Liquid velocity, m h^{-1}	0.99 and 4.5

Table 4.11. Residue conversion, and residue, liquid products, and gas final concentrations, at 0.99 m h^{-1} liquid velocity for a series of CSTRs

n	1	2	3	4
Residue conversion, %	46.52	71.39	84.70	91.82
$C_{R,f}$, mol m^{-3}	90.92	48.63	26.00	13.91
$C_{VGO,f}$, mol m^{-3}	33.92	18.14	9.70	5.19
$C_{D,f}$, mol m^{-3}	11.81	6.32	3.38	1.81
$C_{N,f}$, mol m^{-3}	6.34	3.39	1.81	0.97
$C_{GP,f}$, mol m^{-3}	27.00	14.44	7.72	4.13

Table 4.12. Residue conversion, and residue, liquid products, and gas final concentrations, at 4.5 m h^{-1} liquid velocity for a series of CSTRs

n	1	2	3	4
Residue conversion, %	16.06	29.54	40.86	50.36
$C_{R,f}$, mol m^{-3}	142.70	119.80	100.54	84.39
$C_{VGO,f}$, mol m^{-3}	13.41	11.26	9.45	7.93
$C_{D,f}$, mol m^{-3}	2.60	2.18	1.83	1.54
$C_{N,f}$, mol m^{-3}	1.97	1.65	1.39	1.17
$C_{GP,f}$, mol m^{-3}	9.32	7.83	6.57	5.51

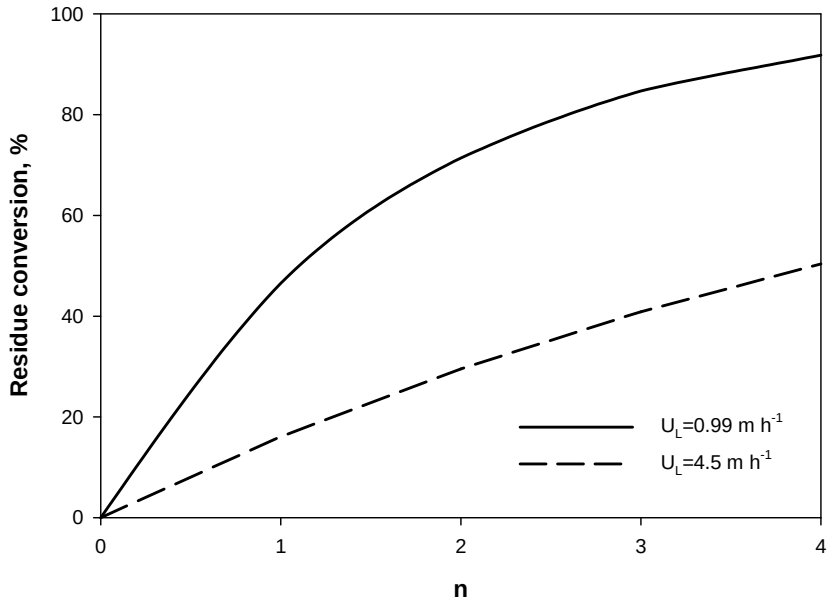

Figure 4.51. Residue conversion vs. number of reactors.

Figure 4.52 and 4.53 show the molar flow rate of the residue, liquid and gas products at 0.99 m h^{-1} and 4.5 m h^{-1} liquid velocity, respectively, and as can be seen, the residue molar flow rate decreases in the reactor as the number of reactors increases, while the molar flow rates of the VGO, distillate, naphtha, and gaseous products appears to increase.

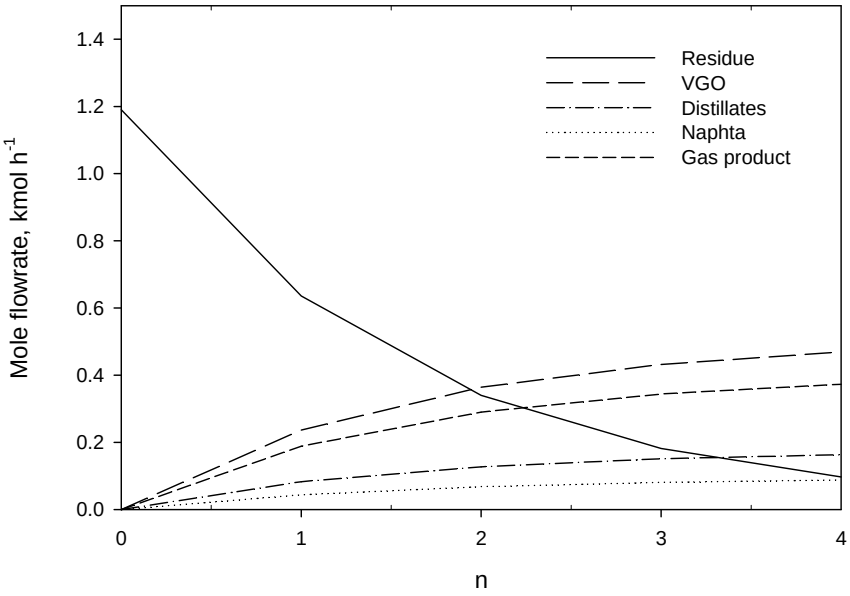

Figure 4.52. Residue, liquids, and gas product mole flowrate vs. number of reactors at 0.99 m h^{-1}liquid velocity

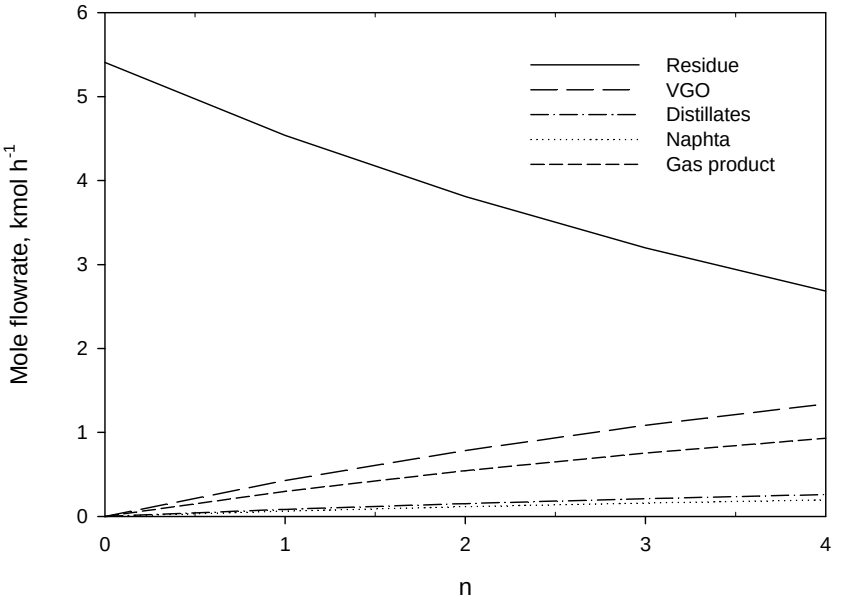

Figure 4.53. Residue, liquids, and gas product mole flowrate vs. number of reactors at 4.5 m h^{-1}liquid velocity.

5.0 CONCLUSIONS

The equilibrium solubility (C^*) and liquid-side mass transfer coefficient (k_La) for H_2 were measured in four liquids, two vacuum residues (A and B) and two mixtures (vacuum residue B + liquid paraffins and vacuum residue B + liquid paraffins + molten wax). The data were measured in the presence and absence of solid particles (activated carbon) in one-liter agitated reactor operating in a gas-inducing mode. The effect of operating variables, including pressure (27.5–55 bar), temperature (423–623 K), mixing speed (20–33 Hz), and activated carbon concentration (0 – 40 wt %) on k_La and C^* values were statistically investigated using the Central Composite Statistical Design technique. The Transient Physical Gas Absorption technique was employed to obtain k_La; and C^* was calculated at the thermodynamic equilibrium. A simple model to predict the performance of a vacuum residue hydrocracker operating at 400 ^oC was also introduced. From this study, the following concluding remarks can be made:

1. The C^* values for H_2 in the four liquids increased linearly with pressure at constant temperature, and the values were modeled using Henry's Law over the pressure and temperature ranges studied.
2. The C^* values for H_2 in the vacuum residues A and B were nearly identical. The C* values for H_2 in the four liquids followed the order: C* in the vacuum residue B < C* in the vacuum residue B + paraffins liquid < C* in the vacuum residue B + paraffins + wax.

3. The C* values for H_2 in the four liquids were found to increase with the temperature at constant pressure; and the effect of temperature was modeled using an Arrhenius-type equation, where the heat of solution appeared to be constant.
4. The k_La values of H_2 in the four liquids were found to strongly increase with increasing temperature and mixing speed, and to slightly increase with increasing H_2 partial pressure. The k_La values of H_2, however, decreased in the vacuum residues A and B with increasing the solid concentrations (activated carbon). Under similar operating conditions, k_La values of H_2 in the vacuum residues A and B were nearly identical. The k_La values for H_2 in the four liquids followed the order: k_La in the vacuum residue B < k_La in the vacuum residue B + paraffins liquid < k_La in the vacuum residue B + paraffins + wax.
4. Statistical correlations were developed to predict the k_La values of H_2 in the vacuum residues A and B. Also, empirical correlations using dimensionless numbers were developed to predict k_La values of H_2 in the four liquids used in the presence and absence of solid particles in the gas-inducing slurry agitated reactor.
5. The kinetic rate constants proposed by Sanchez at al. [1] for hydrocracking of vacuum residue at 380, 400 and 420 ^oC were employed in a simple kinetic model using a series of CSTRs to calculate the residue conversion and the VGO, distillate, naphtha and gaseous products concentrations molar flow rates.
6. For a series arrangements of 4-CSTRs (3-m inside diameter and 3-m height), operating at 400 ^oC with an LHSV of 0.33 h^{-1} corresponding to an inlet liquid superficial velocity of 0.99 m s^{-1}, the residue conversion reached 91.8%. However, for the same arrangement at 400 ^oC with an LHSV of 1.5 h^{-1} corresponding to an inlet liquid superficial velocity of 4.5 m s^{-1}, the residue conversion was only 50.36%.

APPENDIX A

STUDIES OF MASS TRANSFER IN GAS-INDUCING REACTORS

Table A.1. Studies of mass transfer in gas-inducing reactors

Reference	Gas	Liquid	Operating Conditions	Findings
Pawlowski and Kricsfalussy[53]	H_2	DNT	41 bar 393-433 K	k_La was found to be a function of P^*/V_L.
Kara et al.[125]	H_2	tetralin, coal liquid	70-135 bar 606-684 K	k_La increased with N and decreased with H/d_T. Coal particles decreased $(k_La)_{Tetralin}$.
Karandikar[40]	CO, CH_4	F-T liquids	10-50 bar	k_La increased with P, N, P^*/V_L, decreased with H/d_T.
Karandikar et al.[47, 48]	CO_2, H_2	contained water	373-573 K	Effect of T on k_La was unclear; k_La: H_2>CO>CH_4>CO_2.

Table A.1 (cont.)

Eiras [36]	H_2, C_2H_4, C_3H_6	n-Hexane	1-40 bar 313-353 K	k_La: H_2>C_2H_4>C_3H_6 , k_La increased with N. Effect of T was not clear. Effect of P on k_La depended on system and operation conditions.
Lee and Foster[126]	O_2, CH_4	silicon fluid perfluoroalkyl polyether	10-70 bar 293-573 K	k_La increased with N, P and T, $(k_La)_{O2} > (k_La)_{CH4}$.
Zlokamik[127]	O_2,N_2	water, Na_2SO_4, NaCl	2 bar 293 K	k_La increased with $(P^*/V_L)^{0.8}$.
Topiwala and Hamer [128]	air	K_2SO_4 (aq)	303 K	k_La increased with N.
Chang et al.[38, 129-131]	H_2, N_2, H_2O, CO, CH_4	n-C_6H_{14}, n-$C_{10}H_{22}$, n-$C_{14}H_{30}$, c-C_6H_{12}	1-60 bar 328-528 K	k_La increased with N, decreased with H. Effect of P on k_La, was system dependent. Effect of T was not clear k_La: H_2>N_2>CO>CH_4, k_La decreased with Cv.

TableA.2. Mass transfer correlations for gas-inducing reactors

Reference	Gas	Liquid	Operating Conditions	Remarks
Kara et al.[125]	H_2	tetralin	70-135 bar, 606-684 K	k_La=C(P*/V_L)^{C1}(H_L/D_t)^{C2}.
		SRCII	0.8-6.7 Hz,	C=(3.42±1.13)10^{-4}.
			P*/V_L<119 W/m^3	C1=0.8±0.009, C2=-1.9±0.66.
Karandikar et al.[47]	CO, H_2	F-T wax	7-45 bar, 423-498 K	k_La=0.1607 (N/1000)$^{3.42}$ exp (0.108P_m)-0.046.
		F-T wax+ H_2O	11.7-16.7 Hz	
	CO_2, CH_4	F-T wax	7-45 bar, 423-498 K	k_La=0.0171(N/1000)$^{6.05}$ exp(0.380 P_m)+0.00525.
		F-T wax+ H_2O	11.7-16.7 Hz	
Chang[38]	N_2,	n-C_6, n-C_{10}	546<Eu<11320	Sh=5.114 x 10^{-12} $Eu^{0.28}$ $Sc^{1.63}$ $Re^{2.18}$ $Fr^{1.73}$.
	CO	n-C_{14}	8<Sc<491	
	CH_4		31101<Re<338409	
			1.2<Fr<2.6	
	H_2	n-C_6, n-C_{10}	569<Eu<10468	Sh = 2.74 x 10^{-18} $Eu^{-0.42}$ $We^{1.29}$ $Sc^{2.21}$ $Re^{3.00}$.
		n-C_{14}	1676<We<7721	
			10<Sc<151	
			68926<Re<264882	

APPENDIX B

ERROR ANALYSIS, CRITICAL MIXING SPEED FOR GAS INDUCING AND SOLID SUSPENSION, AND EXAMPLE CALCULATION

Error Analysis:

The error (ΔF) in a function (F) can be calculated as follows:

Let x_i be the i-th independent variable to be considered and Δx_i the error in x_i.

Let F be a function of those independent variables: $F = f(x_1, x_2, \ldots, x_i \ldots x_n)$

The differential of this function can be obtained as follows:

$$dF = \sum_{i=1}^{n} \left. \frac{\partial F}{\partial x_i} \right|_{x_{j \neq i}} dx_i \qquad \text{(A-1)}$$

The error in this function can be estimated as:

$$\Delta F = \sum_{i=1}^{n} \left| \left. \frac{\partial F}{\partial x_i} \right|_{x_{j \neq i}} \right| \Delta x_i \qquad \text{(A-2)}$$

Also, the relative error (RE) can be calculated as:

$$RE = (\Delta F / F) \qquad \text{(A-3)}$$

Similarly, the expressions of the errors for equilibrium gas solubility (C^*) can be derived as follows:

The solubility is calculated using the following equation:

$$C_i^* = \frac{n_{i,I} - n_{i,F}}{m_L} \tag{A-4}$$

$n_{i,I}$ and $n_{i,F}$ can be calculated from:

$$n_{i,I} = \frac{P_{pre,I} V_{pre}}{Z_{pre,I} RT_{pre,I}} - \frac{P_{pre,F} V_{pre}}{Z_{pre,F} RT_{pre,F}} \tag{A-5}$$

$$n_{i,F} = \frac{P_{R,F} V_G}{Z_{R,F} RT_{R,F}} \tag{A-6}$$

Z is the root of the cubic equation (modified PR-EOS); V_{pre} and V_G are the pre-heater and gas-phase volumes, respectively; and the subscripts I and F represent the initial and final conditions.

Gas-phase volume is determined from the reactor and liquid volumes:

$$V_G = V_R - V_L - V_{cat} \tag{A-7}$$

Thus, independent variables in the solubility equation, *C**, are:

$$C^* = f\left(m_L; P_{pre,I}; T_{pre,I}; Z_{pre,I}; P_{pre,F}; T_{pre,F}; Z_{pre,F}; P_{R,F}; T_{R,F}; Z_{R,F}; V_R; V_L; V_{cat}; V_{pre}\right) \tag{A-8}$$

The error in the experimental solubility value can then be estimated from:

$$\begin{aligned} \Delta C^* = & \left|\frac{\partial C^*}{\partial P_{pre,I}}\right| \Delta P_{pre,I} + \left|\frac{\partial C^*}{\partial T_{pre,I}}\right| \Delta T_{pre,I} + \left|\frac{\partial C^*}{\partial Z_{pre,I}}\right| \Delta Z_{pre,I} + \left|\frac{\partial C^*}{\partial P_{pre,F}}\right| \Delta P_{pre,F} + \left|\frac{\partial C^*}{\partial T_{pre,F}}\right| \Delta T_{pre,F} \\ & + \left|\frac{\partial C^*}{\partial Z_{pre,F}}\right| \Delta Z_{pre,F} + \left|\frac{\partial C^*}{\partial P_{R,F}}\right| \Delta P_{R,F} + \left|\frac{\partial C^*}{\partial T_{R,F}}\right| \Delta T_{R,F} + \left|\frac{\partial C^*}{\partial Z_{R,F}}\right| \Delta Z_{R,F} + \left|\frac{\partial C^*}{\partial V_{cat}}\right| \Delta V_{cat} + \left|\frac{\partial C^*}{\partial V_R}\right| \Delta V_R \\ & + \left|\frac{\partial C^*}{\partial V_{pre}}\right| \Delta V_{pre} + \left|\frac{\partial C^*}{\partial V_L}\right| \Delta V_L + \left|\frac{\partial C^*}{\partial m_L}\right| \Delta m_L \end{aligned} \tag{A-9}$$

The relative error in *C** can be also calculated as:

$$RE = (\Delta C^* / C^*) \tag{A-10}$$

The needed partial derivatives in Equation (A-9) can be obtained as:

$$\frac{\partial C^*}{\partial P_{pre,I}} = \frac{V_{pre}}{Z_{pre,I} R T_{pre,I} m_L} \tag{A-11}$$

$$\frac{\partial C^*}{\partial P_{pre,F}} = -\frac{V_{pre}}{Z_{pre,F} R T_{pre,F} m_L} \tag{A-12}$$

$$\frac{\partial C^*}{\partial T_{pre,I}} = -\frac{P_{pre,I} V_{pre}}{Z_{pre,I} R (T_{pre,I})^2 m_L} \tag{A-13}$$

$$\frac{\partial C^*}{\partial T_{pre,F}} = \frac{P_{pre,F} V_{pre}}{Z_{pre,F} R (T_{pre,F})^2 m_L} \tag{A-14}$$

$$\frac{\partial C^*}{\partial P_{R,F}} = -\frac{V_G}{Z R T_{R,F} m_L} \tag{A-15}$$

$$\frac{\partial C^*}{\partial T_{R,F}} = \frac{P_{R,F} V_G}{Z R T_{R,F}^2} \cdot \frac{1}{m_L} \tag{A-16}$$

$$\frac{\partial C^*}{\partial m_L} = -\left[\left(\frac{P_{pre,I}}{Z_{pre,I} R T_{pre,I}} - \frac{P_{pre,F}}{Z_{pre,F} R T_{pre,F}} \right) V_{pre} - \frac{P_{R,F} V_G}{Z R T_{R,F}} \right] \cdot \frac{1}{m_L^2} \tag{A-17}$$

$$\frac{\partial C^*}{\partial V_{cat}} = \frac{P_{R,F}}{Z R T_{R,F} m_L} \tag{A-18}$$

$$\frac{\partial C^*}{\partial V_L} = \frac{P_{R,F}}{Z R T_{R,F} m_L} \tag{A-19}$$

The volume of the liquid and catalyst phase in the reactor is given by:

$$V_L = \frac{m_L}{\rho_L} \tag{A-20}$$

$$V_{cat} = \frac{m_{cat}}{\rho_{cat}} \tag{A-21}$$

The errors in the liquid and solid volumes are:

$$\Delta V_L = \left|\frac{\partial V_L}{\partial m_L}\right| \Delta m_L + \left|\frac{\partial V_L}{\partial \rho_L}\right| \Delta \rho_L \tag{A-22}$$

$$\Delta V_{cat.} = \left|\frac{\partial V_{cat}}{\partial m_{cat}}\right| \Delta m_{cat} + \left|\frac{\partial V_{cat}}{\partial \rho_{cat}}\right| \Delta \rho_{cat} \tag{A-23}$$

The partial derivatives are:

$$\frac{\partial V_L}{\partial m_L} = \frac{1}{\rho_L} \Delta m_L \tag{A-24}$$

$$\frac{\partial V_L}{\partial \rho_L} = -\frac{m_L}{{\rho_L}^2} \Delta \rho_L \tag{A-25}$$

$$\frac{\partial V_{cat.}}{\partial m_{cat.}} = \frac{1}{\rho_{cat.}} \Delta m_{cat.} \tag{A-26}$$

$$\frac{\partial V_{cat}}{\partial \rho_{cat}} = -\frac{m_{cat}}{{\rho_{cat}}^2} \Delta \rho_{cat} \tag{A-27}$$

Volumetric Mass-Transfer Coefficients; $k_L a$ values are calculated using Equation (3-67):

$$\frac{P_{i,F}}{P_{i,I}} \ln\left[\frac{P_{i,I} - P_{i,F}}{P_{i,t} - P_{i,F}}\right] = k_L a t \tag{A-28}$$

The independent variables used in this expression are:

$$k_L a = f(P_{R,F},\ P_{R,I},\ P_{R,t},\ t) \tag{A-29}$$

Therefore, the error for the volumetric mass-transfer coefficient is calculated from Equation (3-67) as follows:

$$\Delta k_L a = \left|\frac{\partial k_L a}{\partial t}\right| \Delta t + \left|\frac{\partial k_L a}{\partial P_{R,F}}\right| \Delta P_{R,F} + \left|\frac{\partial k_L a}{\partial P_{R,I}}\right| \Delta P_{R,I} + \left|\frac{\partial k_L a}{\partial P_{R,t}}\right| \Delta P_{R,t} \tag{A-30}$$

The needed partial derivatives are:

$$\frac{\partial k_L a}{\partial t} = \frac{-1}{t^2}\frac{P_{R,F}}{P_{R,I}}\ln\left(\frac{P_{R,I}-P_{R,F}}{P_{R,t}-P_{R,F}}\right) \tag{A-31}$$

$$\frac{\partial k_L a}{\partial P_{R,F}} = \frac{1}{tP_{R,I}}\left[\ln\left(\frac{P_{R,I}-P_{R,F}}{P_{R,t}-P_{R,F}}\right)+\frac{P_{R,F}\left(P_{R,I}-P_{R,t}\right)}{\left(P_{R,I}-P_{R,F}\right)\left(P_{R,t}-P_{R,F}\right)}\right] \tag{A-32}$$

$$\frac{\partial k_L a}{\partial P_{R,I}} = \frac{1}{t}\left[\frac{P_{R,F}}{P_{R,I}}\frac{1}{\left(P_{R,I}-P_{R,F}\right)}-\frac{P_{R,F}}{(P_{R,I})^2}\ln\left(\frac{P_{R,I}-P_{R,F}}{P_{R,t}-P_{R,F}}\right)\right] \tag{A-33}$$

$$\frac{\partial k_L a}{\partial P_{R,t}} = \frac{P_{R,F}}{tP_{R,I}}\frac{-1}{\left(P_{R,t}-P_{R,F}\right)} \tag{A-34}$$

In calculating the error (ΔC^*) and relative error ($\Delta C^*/C^*$) in the solubility (C^*), and the (Δk_La) and relative error ($\Delta k_La/k_La$) in the solubility (k_La), the following values of the parameters from the equations given above were used:

$\Delta P_{pre,}$ = 0.075 bar	Δm_L = 0.0001 kg	$\Delta\rho_L$ = 0 kg m^{-3}
$\Delta P_{R,}$ = 0.075 bar	Δm_{cat} = 0.0001 kg	$\Delta\rho_{cat}$ = 0 kg m^{-3}
ΔT_{pre} = 0.1 K	ΔV_{pre} = 0 m^3	ΔZ = 0
ΔT_R = 0.1 K	ΔV_R = 0 m^3	Δt = 0 s

An example of error calculation for C^* and k_La is provided in Table B..

System: Gas: H_2

Liquid: vacuum residue A

Solid: activated carbon

Operating conditions:

C_S = 0 wt%	V_L = 0.000531 m^3	ρ_{cat} = 1539 kg/m^3
N = 2000 rpm	$V_{cat.}$ = 0 m^3	m_L = 0.5262 kg
V_R = 0.00103 m^3	ρ_L = 1011.86 kg/m^3	m_{cat} = 0 kg

Table B.1. Sample error calculation

$P_{R,I}$ bar	$T_{R,I}$ K	$P_{R,F}$ bar	$T_{R,F}$ K	$P_{R,mean}$ bar	t s	C^* kmol/m^{-3}	$\Delta C^*/C^*$ %	k_La s^{-1}	$\Delta k_La/k_La$ %
27.64	527	24.54	30	25.73	13.2	0.07	5.09	0.18	24.98
47.60	527	45.27	30	46.08	9.0	0.12	3.06	0.19	17.69
55.00	527	54.67	31	54.39	0.0	0.12	2.92	0.34	7.00

Critical Mixing Speed for Gas Inducing and Solid Suspension:

The critical mixing speeds for gas induction and for solid suspension were calculated using Equation (3-32), proposed by Lemoine et al.[85], and Equation (3-33), proposed by Zwietering[86].

$$\frac{N_{CRI}^2 d_{imp.}}{g} = 0.512 \times \left(\frac{\mu_L}{\mu_{Water}}\right)^{0.146} \left(\frac{\sigma_L}{\sigma_{Water}}\right)^{-0.180} \left(\frac{\rho_L}{\rho_{Water}}\right)^{-0.265} \left(\frac{H_L}{d_T}\right) \quad \text{(B-5-35)}$$

$$N_{suspension} = \frac{s\nu^{0.1} d_p^{0.2} \left(g\Delta\rho/\rho_L\right)^{0.45} C_V^{0.13}}{d_{imp.}^{0.85}} \quad \text{(B-5-36)}$$

It should be mentioned that Equation (3-32) was proposed for gas-liquid systems in gas-inducing reactors, whereas Equation (3-33) was proposed for gas-slurry systems in surface aeration reactors rather than gas-inducing reactors. Table B**.** compares the calculated critical mixing speeds for gas induction at Cs = 0 wt. %, and the minimum mixing speeds used in the experiments at various temperatures. As can be seen from this table, all the experiments with vacuum residue A were conducted above the critical mixing speed for gas induction, and all the experiments with vacuum residue B, with the exception of the one conducted at 473 K, were carried out above the critical mixing speed for gas induction.

Table B.2. Critical mixing speed for gas induction

	Vacuum residue A		***Vacuum residue B***	
T, K	N_{CRI}, ***rpm***	$N_{experiment}$ ***rpm***	N_{CRI}, ***rpm***	$N_{experiment}$ ***rpm***
473	1157	1200	1242	1200
523	1084	1200	1151	1200
573	1033	1200	1110	1200

Equation (3-33) was applied to predict the critical mixing speed for solid suspension using a worst-case scenario included in the statistical design of the experiments (C_S = 40 wt. % and T = 473K) with a shape factor value equal to 5.4. The critical mixing speeds for solid suspension for vacuum residues A and B were 1868 rpm and 1998 rpm, respectively; whereas the minimum mixing speed used for vacuum residues A and B under this temperature was 1200 rpm. These predicted and actual mixing speeds indicate that under these specific conditions, some particles were not suspended in vacuum residues A and B. It should be mentioned, however, that Equation (3-33) does not account for the presence of induced gas bubbles, which were reported by Murugesan[92] to increase the suspension of the solid particles, and accordingly, the solid particles were suspended under the experimental conditions employed, as shown in Figure 3.27.

Example Calculation:

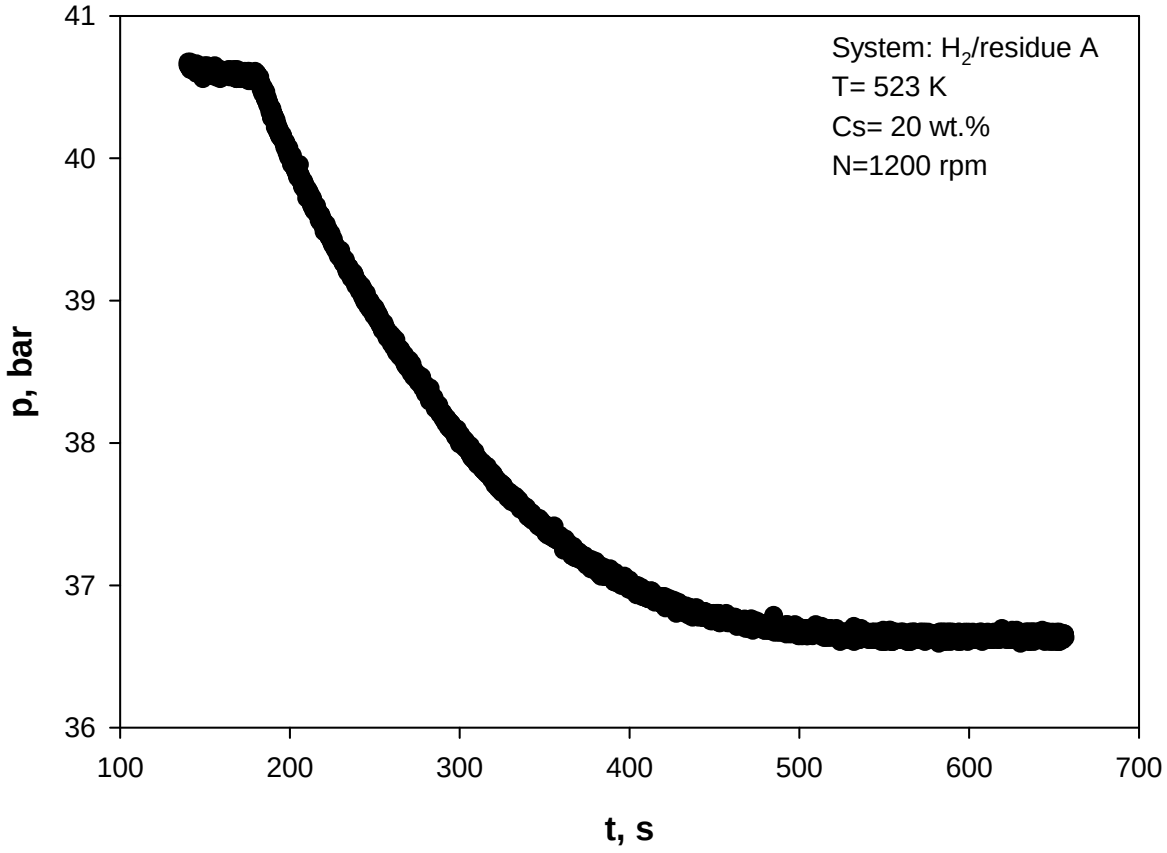

Figure B.1. Experimental P(t) curve showing Transient Gas-Absorption behavior

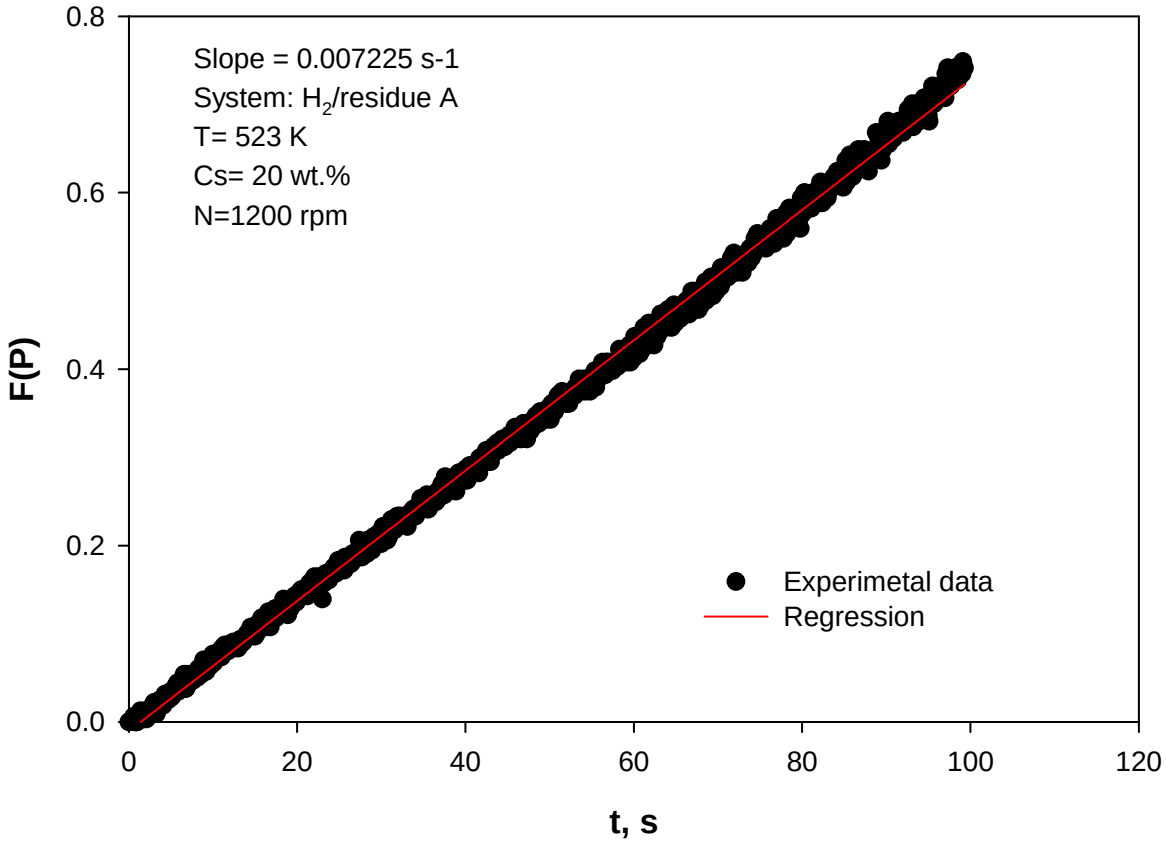

Figure B.2. F(P) vs. time (3-67)

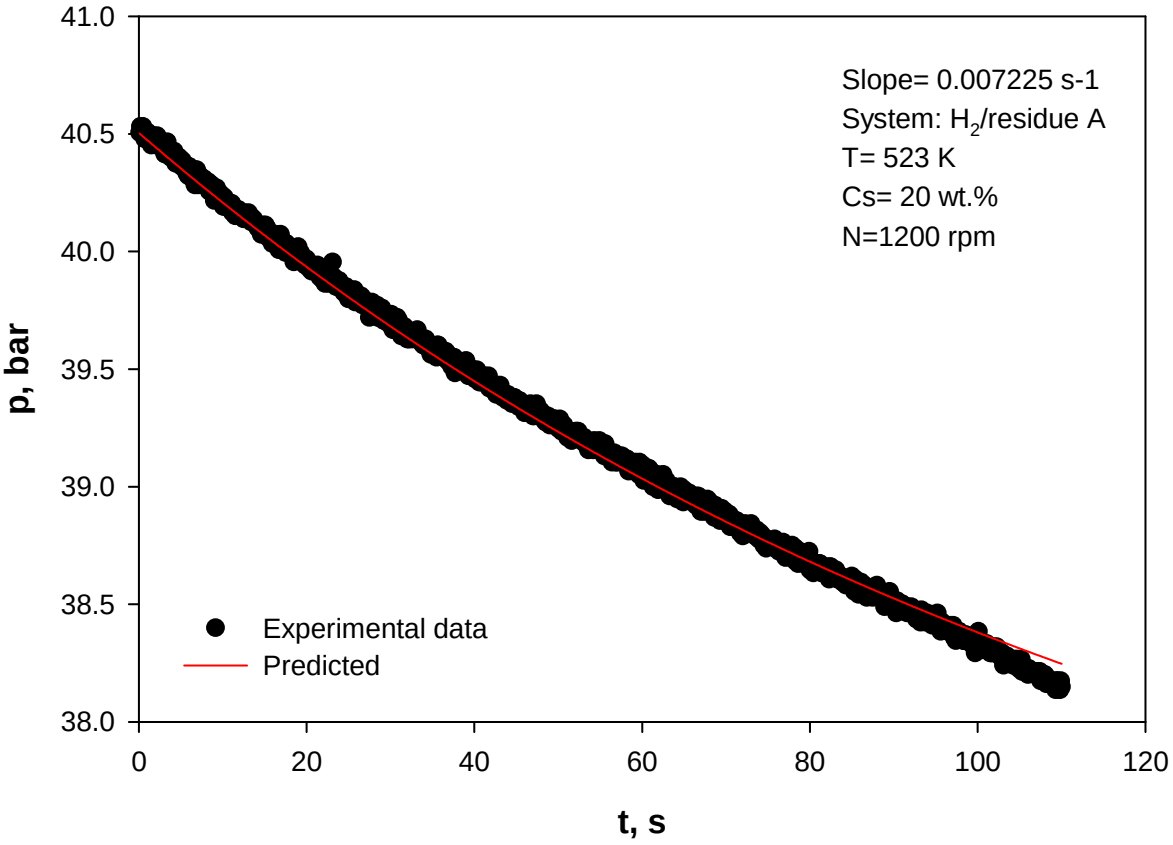

Figure B.3. Comparison of calculated and experimental P vs. t curves

BIBLIOGRAPHY

1. Sergio, S., R.M. A., and J. Ancheyta, *Kinetic Model for Moderate Hydrocracking of Heavy Oils.* Industrial & Engineering Chemistry Research, 2005. **44**: p. 9409-9413.

2. Ancheyta, J. and J.G. Speight, *Hydroprocessing of heavy oil and residue*. 2007.

3. https://www.cia.gov/library/publications/the-world-factbook/rankorder/2178rank.html (2011).

4. Deffeyes, K., *Whe oil peaked*, New York.

5. Alboudwarej, *Highlighting Heavy Oil.* Oilfield Review, 2008.

6. Ancheyta, J., *Modeling and Simulation of Catalytic Reactors for Petroleum Refining*. 2011: John Wiley & Sons, Inc. .

7. *Annual Energy Review 2008*. 2009; Available from: www.eia.doe.gov/aer.

8. Citizendium. *Hydrocracking*. May 2010; Available from: http://en.citizendium.org/wiki/Hydrocracking.

9. Zhang, S., et al., *A review of slurry-phase hydrocracking heavy oil technology.* Energy & Fuels, 2007. **21**(6): p. 3057-3062.

10. Rana, M.S., et al., *A review of recent advances on process technologies for upgrading of heavy oils and residua.* Fuel, 2007. **86**: p. 1216-1231.

11. Solomon, J., G. Benjamin, and V. Sterling, *A lumping and reaction scheme for catalytic cracking.* AIChE Journal, 1976. **22**(4): p. 702-713.

12. Schweitzer, J.-M. and S. Kressman, *Ebullated bed reactor modeling for residue conversion.* Chemical Engineering Science, 2004. **59**: p. 5637-5645.

13. Schweitzer, J.-M. and S. Kressmann, *Ebullated bed reactor modeling for residue conversion.* Chemical Engineering Science, 2004. **59**: p. 5637-5645.

14. Hebert, L., et al., *Kinetic modeling of bitumen hydroprocessing at in-reservoir conditions employing ultadispersed catalyst.* Energy and Fuels, 2011. **25**: p. 1364-1372.

15. Martinez, J., et al., *A Review of Process Aspects and Modeling of Ebullated Bed Reactors for Hydrocracking of Heavy Oils.* Catalysis Reviews, 2010. **52**: p. 60-105.

16. Fillion, B. and B.I. Morsi, *Gas-Liquid Mass Transfer and Hydrodynamic Parameters in a Soybean Oil Hydrogenation Process under Industrial Conditions.* Industrial & Engineering Chemistry Research, 2001. **39**: p. 2157-2169.

17. Fogler, H.S., *Elements of Chemical Reaction Engineering*. 4 ed. 2005.

18. Inga, J., *Scaleup and Scaledown of slurry reactors: a new methodology*, in *Chemical Engineering*. 1997, Pittsburgh: 1997.

19. Whitaker, S. and A. Cassano, *Concepts and Design of Chemical Reactors*. 1986, New York: Gordon and Breach Science Publishers

20. Chang, M.Y. and B.I. Morsi, *Solubilities and mass transfer coefficients of carbon monoxide in a gas-inducing reactor operating with organic liquids under high pressures and temperatures.* Chemical Engineering Science, 1992. **47**(13-14): p. 3541-8.

21. Tsai, F.N., et al., *Solubility of methane, ethane, and carbon dioxide in a Mobil Fischer-Tropsch wax and in n-paraffins.* Chemical Engineering Journal (Amsterdam, Netherlands), 1988. **38**(1): p. 41-6.

22. Ghosh, A., W.G. Chapman, and R.N. French, *Gas solubility in hydrocarbons-a SAFT-based approach.* Fluid Phase Equilibria, 2003. **209**(2): p. 229-243.

23. Ronze, D., et al., *Hydrogen solubility in straight run gas oil.* Chemical Engineering Science, 2002. **57**(4): p. 547-553.

24. Tong, J., et al., *Solubilities of Nitrogen in Heavy Normal Paraffins from 323 to 423 K at Pressures to 18.0 MPa.* Journal of Chemical and Engineering Data, 1999. **44**(4): p. 784-787.

25. Park, J., et al., *Solubilities of Carbon Monoxide in Aromatic Hydrocarbons at Temperatures from 323 to 433 K and Pressures to 23.3 MPa.* Journal of Chemical and Engineering Data, 1995. **40**(1): p. 245-7.

26. Park, J., R.L. Robinson, Jr., and K.A.M. Gasem, *Solubilities of Hydrogen in Heavy Normal Paraffins at Temperatures from 323.2 to 423.2 K and Pressures to 17.4 MPa.* Journal of Chemical and Engineering Data, 1995. **40**(1): p. 241-4.

27. Chou, J.S. and K.C. Chao, *Solubility of synthesis and product gases in a Fischer-Tropsch SASOL wax.* Industrial & Engineering Chemistry Research, 1992. **31**(2): p. 621-3.

28. Albal, R.S., et al., *Mass transfer coefficients and solubilities for hydrogen and carbon monoxide under Fischer-Tropsch conditions.* Chemical Engineering Science, 1984. **39**(5): p. 905-7.

29. Van Vuuren, D.S., J.R. Hunter, and M.D. Heydenrych, *The solubility of various gases in Fischer-Tropsch reactor wax.* Chemical Engineering Science, 1988. **43**(6): p. 1291-1296.

30. Huang, S.H., et al., *Solubility of synthesis gases in heavy n-paraffins and Fischer-Tropsch wax.* Industrial & Engineering Chemistry Research, 1988. **27**(1): p. 162-9.

31. Chou, J.S. and K.C. Chao, *Correlation of synthesis gas solubility in n-paraffin solvents and Fischer-Tropsch waxes.* Fluid Phase Equilibria, 1989. **46**(2-3): p. 179-95.

32. Wang, Y.N., et al., *Correlation for gas-liquid equilibrium prediction in Fischer-Tropsch synthesis.* Fuel, 1999. **78**(8): p. 911-917.

33. Campanella, E.A., *Correlation and prediction of synthesis gas solubility in n-paraffin systems.* Chemical Engineering & Technology, 1997. **20**(6): p. 371-377.

34. Mandagaran, B.A. and E.A. Campanella, *Correlation and prediction of gas solubility in heavy complex liquids.* Chemical Engineering & Technology, 1993. **16**(6): p. 399-404.

35. Alghamdi, A.K.A., *Mass transfer characteristics in a slurry agitated reactor with organic liquid mixtures under high pressures and temperatures*, in *Chemical and Petroleum Engineering Department*. 2001, University of Pittsburgh: Pittsburgh. p. 210.

36. Eiras, J.G., *Mass Transfer in Polymerization Processes*, in *School of Engineering*. 1990, University of Pittsburgh.

37. Mehta, V.D. and M.M. Sharma, *Mass Transfer in Mechanically Agitated Gas-liquid Contactors* Chemical Engineering Science, 1971. **26**: p. 461-479.

38. Chang, M.-Y., *Mass Transfer Characteristics of Gases in Aqueous and Organic Liquids at Elevated Pressures and Temperatures in Agitated Reactors*, in *Chemical and Petroleum Engineering Department*. 1991, University of Pittsburgh: Pittsburgh. p. 2 v. (xxvi, 391 leaves).

39. Marangozis, J., O.B. Keramidas, and G. Paparisvas, *Rate and Mechanism of Hydrogenation of Cottonseed Oil in Slurry Reactors.* Industrial Engineering Chemistry Process Design and Development, 1977. **16**: p. 361-369.

40. Karandikar, B.M., *An Experimental Study of Gas Liquid Mass Transfer at Fischer-Tropsch Reaction Conditions*, in *School of Engineering*. 1986, University of Pittsburgh,.

41. Van't Riet, K., *Review of Measuring Methods and Results in Nonviscous Gas-Liquid Mass-Transfer in Stirred Vessels.* Industrial Engineering Chemistry Process Design and Development, 1979. **19**: p. 357-364.

42. Davies, J.T., A.A. Kilner, and E.A. Ratcliff, *Effect of diffusivity and surface films on rates of gas absorption.* Chemical Engineering Science, 1964. **19**: p. 583-590.

43. Kuthan, K. and Z. Broz, *Mass Transfer In Liquid Films During Absorption Part III: Depedence Of The Liquid Side Mass Transfer Coefficient On The Molecular Diffusivity Of Gases At High Values Of Schmidt Number.* Chemical Engineering Processing, 1989. **25**: p. 75-84.

44. Kozinski, A.A. and C.J. King, *The Influence Of Diffusivity On Liquid Phase Mass Transfer To The Free Interface In A Stirred Vessel* American Institute of Chemical Engineers Journal, 1966. **12**: p. 109-116.

45. Linek, V., J. Mayrhoferova, and J. Mosnerova, *The Influence Of Diffusivity On Liquid Phase Mass Transfer In Solutions Of Electrolytes.* Chemical Engineering Science, 1970. **25**: p. 1033-1045.

46. Albal, R.S., *Mass Transfer, Power Consumption and Suspension Characteristics of Surface Aerated Two and Three Phase Agitated Contactors* in *School of Engineering*. 1983, University of Pittsburgh.

47. Karandikar, B.M., et al., *Effect of water on the solubilities and mass transfer coefficients of gases in a heavy fraction of Fischer-Tropsch products.* Canadian Journal of Chemical Engineering, 1987. **65**(6): p. 973-981.

48. Karandikar, B.M., et al., *Effect of water on the solubility and mass transfer coefficients of CO and H_2 in a Fischer-Tropsch liquid.* Chemical Engineering Journal, 1986. **33**(3): p. 157-168.

49. Deimling, A., et al., *Solubility and mass transfer of carbon monoxide and hydrogen in Fischer-Tropsch liquids and slurries.* Chemical Engineering Journal, 1984. **29**(3): p. 127-140.

50. Yoshida, F. and S.-I. Arakawa, *Pressure Dependence of Liquid Phase Mass Transfer Coefficients* American Institute of Chemical Engineers Journal, 1968. **14**: p. 962-963.

51. Li, J., *Mass Transfer and Mathematical Modeling for Propylene Polymerization Process*, in *School of Engineering*. 1995, University of Pittsburgh.

52. Vinke, H., P.J. Hamersma, and J.M.H. Fortuin, *Enhancement of the Gas-absorption Rate in Agitated Slurry Reactors by Gas-Adsorbing Particles Adhering to Gas Bubbles.* Chemical Engineering Science, 1993. **48**(12): p. 2197-2210.

53. Pawlowski, J. and Z. Kricsfalussy, *Reaktionskinetische Untersuchungen in Drei-phasen-systemen, Dargestellt Am Deispiel Der Dinitrotoluol-hydrierung* Chemich. Ingeniur Technich, 1981. **53**: p. 652-654.

54. Teramoto, M., et al., *Effects of Pressure on Liquid-phase Mass Transfer Coefficients* Chemical Engineering Journal, 1974. **8**: p. 223-226.

55. Versteeg, G.F., P.M.M. Blauwhoff, and W.P.M. Van Swaaij, *The Effect of Diffusivity on Gas-Liquid Mass Transfer in Stirred Vessels. Experiments at Atmospheric and Elevated Pressures* Chemical Engineering Science, 1987. **42**: p. 1103-1119.

56. Iwanaka, H., K. Tojo, and K. Miyanami, *Mass Transfer Characteristics in a Slurry Reactor* Chemical Engineering Communication, 1985. **34**: p. 205-212.

57. Beenackers, A.A.C.M. and W.P.M. Van Swaaij, *Mass Transfer In Gas-Liquid Slurry Reactors," Chemical Engineering Science, Vol. 48, Number 18 (1993), pp. 3109-3139.*

58. Py, X., et al., *Physical And Chemical Mass Transfer Enhacement At Gas-Liquid Interface Due To Fine Catalyst Particles* Transaction of the Institute of Chemical Engineers, 1995. **73**(Part A): p. 253-257.

59. Hsu, Y.-C., et al., *Ozone Transfer into Water in a Gas-Inducing Reactor.* Industrial & Engineering Chemistry Research, 2002. **41**(1): p. 120-127.

60. Hsu, Y.-C., R.Y. Peng, and C.-J. Huang, *Onset of gas induction, power consumption, gas holdup and mass transfer in a new gas-induced reactor.* Chemical Engineering Science, 1997. **52**(21/22): p. 3883-3891.

61. Hichri, H., et al., *Gas-liquid mass-transfer coefficients in a slurry batch reactor equipped with a self-gas-inducing agitator.* Industrial & Engineering Chemistry Research, 1992. **31**(8): p. 1864-7.

62. Sridhar, T. and O.E. Potter, *Interfacial areas in gas-liquid stirred vessels.* Chemical Engineering Science, 1980. **35**(3): p. 683-95.

63. Albal, R.S., et al., *Mass transfer in multiphase agitated contactors.* Chemical Engineering Journal (Amsterdam, Netherlands), 1983. **27**(2): p. 61-80.

64. Dietrich, E., et al., *Raney-nickel catalyzed hydrogenations: gas-liquid mass transfer in gas-induced stirred slurry reactors.* Chemical Engineering Science, 1992. **47**(13-14): p. 3597-604.

65. Tekie, Z., J. Li, and B.I. Morsi, *Mass Transfer Parameters of O2 and N2 in Cyclohexane under Elevated Pressures and Temperatures: A Statistical Approach.* Industrial & Engineering Chemistry Research, 1997. **36**(9): p. 3879-3888.

66. Inga, J.R. and B.I. Morsi, *Effect of catalyst loading on gas/liquid mass transfer in a slurry reactor: a statistical experimental approach.* Canadian Journal of Chemical Engineering, 1997. **75**(5): p. 872-881.

67. Ledakowicz, S., H. Nettelhoff, and W.D. Deckwer, *Gas-liquid mass transfer data in a stirred autoclave reactor.* Industrial & Engineering Chemistry Fundamentals, 1984. **23**(4): p. 510-12.

68. Lekhal, A., et al., *Gas-liquid mass transfer in gas-liquid-liquid dispersions.* Chemical Engineering Science, 1997. **52**(21/22): p. 4069-4077.

69. Karandikar, B.M., et al., *Effect of water on the solubility and mass transfer coefficients of CO and H2 in a Fischer-Tropsch liquid.* Chemical Engineering Journal (Amsterdam, Netherlands), 1986. **33**(3): p. 157-68.

70. Deimling, A., et al., *Solubility and mass transfer of carbon monoxide and hydrogen in Fischer-Tropsch liquids and slurries.* Chemical Engineering Journal (Amsterdam, Netherlands), 1984. **29**(3): p. 127-40.

71. Chen, J.-H., et al., *Application of gas-inducing reactor to obtain high oxygen dissolution in aeration process.* Water Research, 2003. **37**(12): p. 2919-2928.

72. Linek, V., et al., *Gas-liquid mass transfer coefficient in stirred tanks interpreted through models of idealized eddy structure of turbulence in the bubble vicinity.* Chemical Engineering and Processing, 2004. **43**(12): p. 1511-1517.

73. Yaws, C.L., *Chemical Properties Handbook*. 1999: McGraw-Hill.

74. Gao, W., et al., *Improved correlations for heavy n-paraffin physical properties.* Fluid Phase Equilibria, 2001. **179**(1-2): p. 207-216.

75. Li, X.-S., et al., *Dynamic surface tensions of Athabasca bitumen vacuum residue including the effect of dissolved air.* Journal of Colloid and Interface Science, 2005. **287**: p. 640-646.

76. Gray, M.R., *Upgrading Petroleum Residues and Heavy Oils*. 1994.

77. Soriano, J.P., *Mass transfer characteristics in an agitated slurry reactor operating under Fischer-Tropsch conditions*, in *Chemical and Petroleum Engineering Department*. 2005, University of Pittsburgh: Pittsburgh. p. 137.

78. Gentzis, T. and P.M. Rahimi, *A microscopic approach to determine the origin and mechanism of coke formation towers.* Fuel, 2003. **82**(1): p. 1531-40.

79. Cai, H.-Y., J.M. Shaw, and K.H. Chung, *Hydrogen solubility measurements in heavy oil and bitumen cuts.* Fuel, 2001. **80**: p. 1055-1063.

80. Aijun, G., et al., *Mechanistic analysis on thermal cracking of petroleum residue using H-donor as a probe*, in *Symposium on Kinetics and Mechanisms of Petroleum Processes*. 2001, American Chemical Society: Chicago, IL

81. Marano, J.J. and G.D. Holder, *General equation for correlating the thermophysical properties of n-paraffins, n-olefins, and other homologous series. 2. Asymptotic behavior correlations for PVT properties.* Industrial & Engineering Chemistry Research, 1997. **36**(5): p. 1895-1907.

82. Marano, J.J. and G.F. Holder, *A general equation for correlating the thermophysical properties of n-paraffins, n-olefins, and other homologous series. 3. Asymptotic behavior correlations for thermal and transport properties.* Industrial & Engineering Chemistry Research 1997. **36**(6): p. 2399-2408.

83. Kudchadker, A.P. and B.J. Zwolinski, *Vapor pressures and boiling points of normal alkanes, C21 to C100.* Journal of Chemical and Engineering Data, 1966. **11**(2).

84. Barnea, E. and J. Mizrahi, *A generalized approach to the fluid dynamics of particulate systems. Part 1. General correlation for fluidization and sedimentation in solid multiparticle systems.* The Chemical Engineering Journal, 1973. **5**: p. 171-189.

85. Lemoine, R., B. Fillion, and B.I. Morsi, *Hydrodynamic and mass transfer parameters in agitated reactors part I: critical mixing speed, induced gas flow rate, and wavy surface in SARs and GIRs.* International Journal of Chemical Reactor Engineering, 2004. **2**.

86. Zwietering, T.N., *Suspension of solid particles in liquid by agitators.* Chemical Engineering Science, 1958. **8**: p. 244-253.

87. Aravinth, S., P.G. Rao, and T. Murugesan, *Critical impeller speeds for solid suspension in turbine agitated contactors.* Bioprocess Engineering, 1996. **14**(2): p. 97-99.

88. Armenante, P.M. and E.U. Nagamine, *Effect of low bottom impeller clearance on the minimum agitation speed for complete suspension of solids in stirred tanks.* Chemical Engineering Science, 1998. **53**(9): p. 1757-1775.

89. Armenante, P.M., E.U. Nagamine, and J. Susanto, *Determination of correlations to predict the minimum agitation speed for complete solid suspension in agitated vessels.* Canadian Journal of Chemical Engineering, 1998. **76**(3): p. 413-419.

90. Narayanan, S., et al., *Suspension of solids by mechanical agitation.* Chemical Engineering Science, 1969. **24**(2): p. 223-230.

91. Sharma, R.N. and A.A. Shaikh, *Solid suspension in stirred tanks with pitched blade turbines.* Chemical Engineering Science, 2003. **58**(10): p. 2123-2140.

92. Murugesan, T., *Critical impeller speed for solid suspension in mechanically agitated contactors.* Journal of Chemical and Engineering of Japan, 2001. **34**(3): p. 423-429.

93. Chang, M.Y., *Mass transfer characteristics of gases in aqueous and organic liquids at elevated pressures and temperatures in agitated reactors*, in *Chemical and Petroleum Engineering Department*. 1993, University of Pittsburgh: Pittsburgh.

94. Chang, M.Y. and B.I. Morsi, *Mass transfer characteristics of gases in aqueous and organic liquids at elevated pressures and temperatures in agitated reactors.* Chemical Engineering Science, 1991. **46**(10): p. 2639-2650.

95. Chang, M.Y. and B.I. Morsi, *Solubilities and mass transfer coefficients of carbon monoxide in a gas-inducing reactor operating with organic liquids under high pressures and temperatures.* Chemical Engineering Science, 1992. **47**(13-14): p. 3541-3548.

96. Tekie, Z., *Mass transfer and modeling of liquid-phase cyclohexane oxidation process in agitated reactors*, in *Chemical and Petroleum Engineering Department*. 1997, University of Pittsburgh: Pittsburgh.

97. Tekie, Z., et al., *Gas-liquid mass transfer in cyclohexane oxidation process using gas-inducing and surface-aeration agitated reactors.* Chemical Engineering Science, 1997. **52**(9): p. 1541-1551.

98. Fillion, B., *Modeling of soybean oil hydrogenation process*, in *Chemical and Petroleum Engineering Department*. 2001, University of Pittsburgh: Pittsburgh.

99. Martinez-Caamano Nieves, B., *Mass transfer of H_2 and N_2 in a slurry agitated reactor operating under industrial conditions with organic liquid mixture*, in *Chemical and Petroleum Engineering Department*. 2000, University of Pittsburgh: Pittsburgh.

100. Alghamdi, A.K.A., *Mass transfer characteristics in a slurry agitated reactor with organic liquid mixtures under high pressures and temperatures*, in *Chemical and Petroleum Engineering Department*. 2001, University of Pittsburgh: Pittsburgh.

101. Lemoine, R., *Hydrodynamics, mass transfer and modeling of the liquid-phase toluene oxidation process*, in *Chemical and Petroleum Engineering Department*. 2005, University of Pittsburgh: Pittsburgh.

102. Tekie, Z., J. Li, and B.I. Morsi, *Mass transfer parameters of O_2 and N_2 in cyclohexane under elevated pressures and temperatures: a statistical approach.* Industrial and Engineering Chemistry Research, 1997. **36**: p. 3879-3888.

103. D. Lal, F.D.O. and A.E. Mather, *Solubility of hydrogen in Athabasca bitumen.* Fuel, 1999. **78**: p. 1437-1441.

104. H.-Y. Cai, J.M.S., K.H. Chung, *The impact of solid additives on the apparent solubility of hydrogen in petroleum fractions and model hydrocarbon liquids.* Fuel, 2001. **80**: p. 1065-1077.

105. Behkish, A., et al., *Mass transfer characteristics in a large-scale slurry bubble column reactor with organic liquid mixtures.* Chemical Engineering Science, 2002. **57**(16): p. 3307-3324.

106. Miller, S.A., A. Ekstrom, and N.R. Foster, *Solubility and mass-transfer coefficients for hydrogen and carbon monoxide in n-octacosane.* Journal of Chemical and Engineering Data, 1990. **35**(2): p. 125-127.

107. Purwanto, P., et al., *Solubility of hydrogen, carbon monoxide, and 1-octene in various solvents and solvent mixtures.* Journal of Chemical and Engineering Data, 1996. **41**(6): p. 1414-1417.

108. Benoit, F. and B.I. Morsi, *Gas-liquid mass-transfer and hydrodynamic parameters in a soybean oil hydrogenation process under industrial conditions.* Industrial and Engineering Chemistry Research, 2000. **39**: p. 2157-2168.

109. Himmelblau, D.M., *Solubilities of inert gases in H_2O: 0 Deg to near the critical point of H_2O.* Journal of Chemical and Engineering Data, 1960. **5**(1): p. 10-15.

110. Xu, Y., R.P. Schutte, and L.G. Hepler, *Solubilities of carbon dioxide, hydrogen sulfide and sulfur dioxide in physical solvents.* Canadian Journal of Chemical Engineering, 1992. **70**(3): p. 569-573.

111. Cai, H.-Y., J.M. Shaw, and K.H. Chung, *The impact of solid additives on the apparent solubility of hydrogen in petroleum fractions and model hydrocarbon liquids.* Fuel, 2001. **80**: p. 1065-1077.

112. Inga, J.R. and B.I. Morsi, *Effect of catalyst loading on gas/liquid mass transfer in a slurry reactor: a statistical experimental approach.* The Canadian Journal of Chemical Engineering, 1997. **75**: p. 872-800.

113. Behkish, A., et al., *Gas holdup and bubble size behavior in a large-scale slurry bubble column reactor operating with an organic liquid under elevated pressures and temperatures.* Chemical Engineering Journal, 2007. **128**: p. 69-84.

114. Lekhal, A., et al., *Gas-liquid mass transfer in gas-liquid-liquid dispersions.* Chemical Engineering Science, 1997. **52**(21/22): p. 4069-4077.

115. Maalej, S., B. Benadda, and M. Otterbein, *Influence of pressure on the hydrodynamics and mass transfer parameters of an agitated bubble reactor.* Chemical Engineering & Technology, 2001. **24**(1): p. 77-84.

116. Chen, J.H., et al., *Application of gas-inducing reactor to obtain high oxigen dissolution in areation process.* Water research, 2003. **37**(12): p. 2919-2928.

117. Hichri, H., et al., *Gas-liquid mass transfer coefficients in a slurry batch reactor equipped with a self-gas-inducing agitator.* Industrial and Engineering Chemistry Research, 1992. **31**(8): p. 1864-7.

118. Behkish, A., et al., *Gas holdup and bubble size behavior in a large-scale slurry bubble column reactor operating with an organic liquid under elevated pressures and temperatures.* Chemical Engineering Journal, 2006. **In Press**.

119. Oguz, H., A. Brehm, and W.D. Deckwer, *Gas/liquid mass transfer in sparged agitated slurries.* Chemical Engineering Science, 1987. **42**(7): p. 1815-22.

120. Joosten, G.E.H., J.G.M. Schilder, and J.J. Janssen, *The influence of suspended solid material on the gas-liquid mass transfer in stirred gas-liquid contactors.* Chemical Engineering Science, 1977. **32**(5): p. 563-6.

121. Kluytmans, J.H.J., et al., *Mass transfer in sparged and stirred reactors: influence of carbon particles electrolyte.* Chemical Engineering Science, 2003. **58**(20): p. 4719-28.

122. Ruthiya, K.C., B.F.M. Kuster, and J.C. Schouten, *Gas-liquid mass transfer enhancement in a surface aeration stirred slurry reactors.* Canadian Journal of Chemical Engineering, 2003. **81**(3-4): p. 632-639.

123. Ruthiya, K.C., et al., *Mechanism of physical and reaction enhancement of mass transfer in a gas inducing stirred slurry reactor.* Chemical Engineering Journal (Amsterdam, Netherlands), 2003. **96**(1-3): p. 55-69.

124. Tatterson, G.B., *Scaleup and Design of Industrial Mixing Processes*, ed. McGraw-Hill Inc. 1994.

125. Kara, M., et al., *Hydrogen Mass Transfer in Liquid Hydrocarbons at Elevated Temperatures and Pressures.* Fuel, 1983. **62** p. 1492-1498.

126. Lee, J.H. and N.R. Foster, *Mass Transfer of Oxygen and Methane in Silicon Fluids and Perfluoroalkyl Polyether.* Industrial Chemical Engineering Research, 1990. **29**: p. 1962-1968.

127. Zlokamik, M., *Sorption Characteristics for Gas-Liquid Contacting in Mixing Vessels.* Advanced in Biochemical Engineering, 1978. **8** p. 133-151.

128. Topiwala, H.H. and G. Hamer, *Mass Transfer and Dispersion Properties in A Fermenter with a Gas-inducing Impeller.* Transaction of the Institute of Chemical Engineers, 1974. **52**: p. 113-120.

129. Chang, M.-Y. and B.I. Morsi, *Mass Transfer in a Three Phase Reactor Operating at Elevated Pressures and Temperatures.* Chemical Engineering Science, 1991. **47**: p. 1779-1790.

130. Chang, M.-Y. and B.I. Morsi, *Mass Transfer Characteristics of Gases in n-Decane at Elevated Pressures and Temperatures in Agitated Reactors* Chemical Engineering Journal, 1991. **47**: p. 33-45.

131. Chang, M.-Y., J.G. Eiras, and B.I. Morsi, *Mass Transfer Characteristics of Gases in n-Hexane at Elevated Pressures and Temperatures in Agitated Reactors.* Chemical Engineering Processing, 1991. **29**: p. 49-60.